INSIGHTS INTO THE PHYSICAL PROPERTIES OF THE MAX PHASES AND MXENES: FROM EXPERIMENTS TO FIRST-PRINCIPLES MODELING

Dissertation présentée en vue de l'obtention du grade de
Docteur en Sciences de l'Ingénieur et Technologie
par

AURÉLIE CHAMPAGNE

PROMOTEUR:

Prof. Jean-Christophe Charlier

MEMBRES DU JURY:

Prof. Michel W. Barsoum
Prof. Benoît Hackens
Prof. Bernard Nysten, président
Prof. Thierry Ouisse
Prof. Gian-Marco Rignanese, secrétaire
Prof. Matthieu J. Verstraete

UCLouvain

Septembre 2020

To my beloved family.

Science is not only a disciple of reason but, also, one of romance and passion.

— S. Hawking

ACKNOWLEDGMENTS

'Voilà', this is the end. I can finally say *'I did it!'* and afterwards I am satisfied to have embarked on the professional and human adventure that is the PhD thesis. I take with me the memory of many hours of hard work, of rich scientific discussions, and the almost daily closing of the lab... but, most importantly, I keep in mind the countless games of cards during lunch breaks, the Friday eves' drinks at Brasse-Temps, and the dozen of conferences in which I had the chance to participate and which allowed me to meet extraordinary people. Now, the time has come to gather these memories and list all the people who contributed, directly, or indirectly, to the accomplishment of this thesis.

En tout premier lieu, je me dois de remercier chaleureusement mon promoteur de thèse Jean-Christophe Charlier. J'ai vraiment pris plaisir à travailler avec toi et à lire tes emails et les bonnes blagues qu'ils pouvaient contenir. Ta passion, ton enthousiasme et ta culture scientifique forment la combinaison parfaite pour encourager et encadrer tes étudiants, dont j'ai eu la chance de faire partie. Je te remercie profusément pour ta confiance et pour la liberté que tu m'as octroyée dans ma recherche, me permettant notamment d'aller me promener dans les laboratoires de temps à autre. Merci aussi pour ta disponibilité et ta réactivité qui m'ont permis de maintenir un bon rythme de travail et une motivation constante. Je te suis également profondément reconnaissante pour ton précieux et éternel soutien; un soutien présent lors de mes participations aux conférences, lors de ma candidature pour partir à Philadelphie, ou encore récemment pour mon futur postdoc. J'ai appris énormément grâce à toi, tant sur le plan professionnel que sur le plan humain et je garderai toujours de très bons souvenirs des moments passés en ta compagnie et celle de ta famille. Je pense notamment aux deux semaines à Cargèse, aux restaurants et bowlings entre charbonniers, et à ce retour de Liège sous la neige animé de conversations intéressantes. Pour tout ça, je te remercie Jean-Christophe et je prendrai plaisir à rester en contact avec

toi ces prochaines années. Et si c'était à refaire, je repartirais volontiers pour 4 années de thèse sous ta supervision.

Besides my thesis advisor, I would like to thank the members of my jury, in alphabetical order: Michel W. Barsoum (Drexel University, USA), Benoît Hackens (UCLouvain, Belgium), Bernard Nysten (UCLouvain, Belgium), Thierry Ouisse (LMGP Grenoble, France), Gian-Marco Rignanese (UCLouvain, Belgium), and Matthieu J. Verstraete (ULiège, Belgium). I am incredibly thankful for your guidance and insightful comments and suggestions which encouraged me to reflect harder, to widen my scientific knowledge, and to improve my thesis manuscript. Apart from being members of my jury, you are true scientists and valuable colleagues with whom I had a lot of pleasure working, discussing, and learning. I sincerely hope to keep in touch with you all in the near future and to collaborate on various research projects.

I would also like to thank my thesis committee members: Benoît Hackens, Jean-Pierre Raskin, and Gian-Marco Rignanese, all from UCLouvain, for their time, availability, constant support, and constructive suggestions.

Much of my work emerges from collaborations, in particular with Michel W. Barsoum (Drexel University, USA), Thierry Ouisse (LMGP Grenoble, France), and Johanna Rosen (Linköping University, Sweden). I have been very fortunate to work with them three and to visit them for a couple of days or even a couple of months.

Michel, I would like to thank you for all the great times we have had, including numerous stimulating discussions, scientific meetings, and delightful activities. I still remember all the times and places we met. It started in Berlin, and then we met at various occasions, *e.g.*, in Perugia, Grenoble, Philadelphia, Linköping, and lastly in Mainz. In particular, the Cimtec congress in Perugia was one of the most instructive congress I have been to, not mentioning the lovely setting, the delightful evening activites, and the delicious dinners. A huge thank to you and your research group for the incredibly warm welcome during my stay in Philly. I have spent three amazing months and had the chance to meet good researchers I have learnt a lot from. Thanks for all your support, motivation, and endless flow of ideas that pushed me to work harder and to publish more. I will definitely come to visit you

soon, I owe you at least one good restaurant, and in return you owe me a catamaran day.

Thierry, je te remercie chaleureusement et profusément pour ces quatre belles années. Je me rends compte de la chance que j'ai eue de travailler avec toi. Nous avons eu de nombreuses discussions scientifiques constructives et j'ai particulièrement apprécié ta franchise, ta disponibilité et ta réactivité. Les centaines d'emails que nous avons échangés m'ont permis de devenir plus méticuleuse et organisée dans ma recherche. Tu m'as gentiment accueillie deux fois à Grenoble et je te remercie sincèrement pour le temps que tu m'as accordé pour me faire visiter ton laboratoire et les équipements qui s'y trouvent. Nous avons également eu l'occasion de nous rencontrer à Louvain-la-Neuve, Cargèse, Pérouse, et Linköping, et c'était toujours un plaisir de discuter avec toi de choses et d'autres, scientifiques ou non. Enfin, je te remercie pour ton soutien lors de mes candidatures pour différents projets et bourses de voyage. J'espère sincèrement que nous resterons en contact.

Johanna, it was a pleasure to collaborate and exchange with you during the various MORE-MXenes meetings. I thank you for the numerous scientific discussions and ideas you provided me. I enjoyed a lot my visit to Linköping, which is a beautiful and green city. I am definitely impressed by the way you manage your private and personal life and I hope we will have the opportunity to meet each other again in the future.

My sincere thanks also go to my collaborators Odette Chaix-Pluchery (Grenoble, France) and Jean-Luc Battaglia (Bordeaux, France) from whom I have learnt a lot regarding experimental characterization techniques, methodologies, and rigor. I also thank all my collaborators from UCLouvain, LMGP Grenoble, University of Linköping, and Drexel University who were involved in the MORE-MXenes project and who provided me with great ideas, motivation, and useful comments.

A huge thank to my colleagues, who even became good friends, Janine George, Matteo Giantomassi, Guido Petretto, and Francesco Ricci, who significantly helped me and contributed to the present thesis. You have always been available to listen, help, and answer my various questions until the last minute before my thesis defense. I take the opportunity here to express you all my gratitude and would love to share a few drinks to your health.

I would like to thank all my colleagues of the MODL division, professors and researchers, for their presence, for the stimulating discussions, and for all the fun we have had during the last four years. Foremost, I would like to thank *'les charbonniers'* of whom I have had the honor to be a part and with whom I have enjoyed chatting and laughing, while sharing the same office.

Je remercie aussi chaleureusement toutes les personnes qui m'ont aidée sur le plan administratif et technique durant ma thèse, en particulier Sadia, Vinciane, Fabienne, Jean-Michel, Matteo et Michiels.

Special thanks to my colleagues and friends, with whom I have spent most of my free time playing board games, going for walks, having drinks, attending basketball games, and taking part in various activities: George, Martha, Sergi, Serena, Sriram, Vishank, Davide, Guido, and Francesco N. I am grateful having developed such a good friendship with you all and I hope to stay in touch with you in the future.

De la même manière, je remercie mes amies et amis fidèles depuis des années, avec qui je passe de bons moments de rires: Carole-Ann, Lucie, Ariane, Laurine, Sébastien et Julien. Nos nombreuses discussions sur nos vies actuelles et futures sont toujours intenses et passionnantes et je ne vous remercierai jamais assez pour votre soutien et vos encouragements.

Enfin, je dois plus que des remerciements envers mon incroyable famille qui me soutient depuis toujours. Je remercie en premier lieu mes parents: merci pour votre présence, votre amour, et votre goût pour les sciences que vous m'avez transmis involontairement peut-être. Merci aussi pour vos conseils et avis toujours judicieux qui m'ont permis d'avancer, de me construire et de grandir. Je remercie ma soeur jumelle Pauline pour tout ce que nous partageons depuis le début. Merci d'être ma plus proche confidente et de toujours me soutenir dans mes projets tout en me remettant sur le droit chemin quand il le faut. Merci également à mon petit frère Alexandre pour ton sourire, ton soutien, et ta disponibilité pour jouer à des jeux de société à tout moment. Je remercie aussi mon beau-frère Guillaume de mettre autant de bonne humeur dans la famille et surtout d'avoir assisté à une de mes présentations en conférence avec autant d'attention. Mille merci à l'ensemble des membres de ma famille pour l'intérêt qu'ils ont pu porter à mon travail et à sa progression au cours de ces dernières an-

nées. Un merci particulier à mes grands-parents pour tout ce qu'ils m'apportent depuis tant d'années.

Pour finir, merci à l'homme qui partage ma vie, Francesco, de me supporter au quotidien sans jamais te plaindre. Merci de partager tes connaissances et ton expérience avec moi. Merci aussi de me soutenir dans mes projets et, surtout, d'en faire partie. Grazie mille ai miei suoceri per la loro accoglienza durante le mie visite in Sardegna e per avermi integrata così bene nella vostra meravigliosa famiglia.

Now I put these four beautiful years and the memories they contain in a corner of my head, because it is time for me to fly to new adventures... Berkeley, I'm coming !

ABSTRACT

The MAX phases are nanolayered transition metal carbides and nitrides characterized by a unique combination of metal and ceramic-like properties. Their high electrical and thermal conductivities, combined to impressive thermal-shock and damage resistances, make them good candidates in electrical contacts, micro-mechanical systems, and high-temperature applications. The recent addition of new MAX compositions and atomic ordering brings the total amount of existing MAX phases to 155, most of which still await both experimental characterization and theoretical investigation of their properties. In this manuscript, the growth of high-quality single-crystals of ternary Cr_2AlC and quaternary rare-earth-containing MAX phases is presented. An experimental study of their vibrational and elastic properties is performed. Additionally, the structural, electronic, vibrational, thermal, and elastic properties of these 3D compounds are calculated from first principles. While the elastic properties of the MAX phases are isotropic, a noticeable anisotropy in their electrical, vibrational, and thermal properties is predicted theoretically and, in some cases, verified experimentally. Finally, a complete analysis of the bonding strengths and exfoliation energies is performed, predicting the potential exfoliation of these 3D systems into 2D ones.

In 2011, the MAX phases have been successfully exfoliated into 2D systems, called MXenes. They draw interest due to their unique properties combining high electrical conductivity, large surface area, and hydrophilicity. Since their introduction, over 2,300 works have been published, half of which are devoted to energy-based applications. While, to date about 30 MXenes have been synthesized, the first reported $Ti_3C_2T_z$ MXene remains the most well-studied. In this manuscript, the structural, electronic, and vibrational properties of the V_2CT_z MXene are computed *ab initio*. In parallel, experiments are conducted to synthesize the 2D V_2CT_z MXene from its parent V_2AlC MAX phase and to characterize its Raman response. A complete analysis of the orbital hybridization gives insight into the bonding character within MXenes. Eventually, the phonon mode wavenumbers, symmetries, activities, and associated atomic displacements are predicted.

CONTENTS

List of Figures xvi
List of Tables xviii
List of Symbols xviii
Acronyms xxii
1 INTRODUCTION 1
2 AN INTRODUCTION TO MAX PHASES 5
2.1 History of the MAX phases 5
2.2 Synthesis of MAX phases 7
2.2.1 MAX polycrystals 7
2.2.2 MAX single crystals 8
2.3 Structure and variety of MAX phases 9
2.3.1 Crystal structure and nomenclature 9
2.3.2 Quaternary MAX phases 12
2.4 Properties of MAX phases and derived applications . . . 15
2.4.1 Electrical and magnetic properties 16
2.4.2 Vibrational properties 18
2.4.3 Elastic and mechanical properties 18
2.4.4 Thermal properties 19
2.4.5 Reactivity 20
2.4.6 Applications 21
3 AN INTRODUCTION TO MXENES 23
3.1 Discovery of MXenes 23
3.2 Synthesis of MXenes 25
3.3 Structure, versatility, and stability of MXenes 27
3.4 Properties of MXenes and derived applications 29
3.4.1 Electronic and transport properties 30
3.4.2 Magnetic properties 34
3.4.3 Vibrational properties 36
3.4.4 Mechanical properties 37
3.4.5 Electrochemical properties 38
3.4.6 Other properties and applications 42
4 THEORY 45
4.1 Introduction 45
4.2 Basics of quantum mechanics 46

4.2.1 The Schrödinger equation and the many-body problem . . . 46
4.2.2 The Born-Oppenheimer approximation . . . 47
4.2.3 Independent-electron approximations . . . 48
4.3 Density functional theory . . . 50
4.3.1 Hohenberg-Kohn theorems . . . 51
4.3.2 Kohn-Sham equations . . . 51
4.3.3 Functionals for exchange and correlation . . . 52
4.4 Solid state theory . . . 54
4.4.1 The plane-wave basis set . . . 55
4.4.2 Pseudopotentials . . . 56
4.4.3 Brillouin zone integration . . . 57
4.5 Density functional perturbation theory . . . 58
4.5.1 Introduction to response functions . . . 58
4.5.2 Basics of the perturbation theory . . . 59
4.5.3 Dynamical matrix and phonon frequencies . . . 59
4.6 Elastic constants . . . 61
4.7 Transport properties . . . 61
4.7.1 Electronic thermal conductivity . . . 62
4.7.2 Lattice thermal conductivity . . . 64
4.8 Conclusions . . . 67
5 CHARACTERIZATION TECHNIQUES 69
5.1 Structure and composition . . . 70
5.1.1 Single-crystal X-ray diffraction . . . 70
5.1.2 Scanning electron microscopy . . . 71
5.1.3 Scanning transmission electron microscopy . . . 72
5.2 Vibrational properties . . . 73
5.2.1 Raman spectroscopy . . . 73
5.2.2 Inelastic neutron scattering . . . 75
5.3 Nanoindentation . . . 77
6 INVESTIGATION OF MAX SINGLE CRYSTALS 81
6.1 Ternary Cr_2AlC MAX phases . . . 81
6.1.1 Structural properties . . . 82
6.1.2 Vibrational properties . . . 84
6.1.3 Electronic properties . . . 88
6.1.4 Thermal transport . . . 91
6.1.5 Elastic properties . . . 97
6.1.6 Conclusions . . . 102
6.2 Rare-earth containing MAX phases . . . 103
6.2.1 Structural properties . . . 104

6.2.2 Vibrational properties 106
6.2.3 Elastic properties 118
6.2.4 Electronic structure and DOS 123
6.2.5 Exfoliation potential 125
6.2.6 Conclusions 129
7 INVESTIGATION OF THE V_2CT_z MXENE 131
7.1 Structural properties 132
7.2 Electronic properties 135
7.3 Vibrational properties 138
7.4 Conclusions 146
8 PERSPECTIVES AND CONCLUSIONS 149
Publications 155
Bibliography 157

LIST OF FIGURES

Figure 1.1 Investigated materials. 3
Figure 2.1 Atomic structure of the 211, 312, and 413 phases. 6
Figure 2.2 Atomic structure of the MAX, o-MAX, and i-MAX phases. 10
Figure 2.3 Crystal structures of the MAX polymorphs. . . . 12
Figure 2.4 MAX phase periodic table of M, A, and X elements. 14
Figure 2.5 Electronic bandstructure of MAX phases. 17
Figure 2.6 Ripplocations in layered materials. 20
Figure 3.1 Etching process of the MAX phases in HF solution. 24
Figure 3.2 Atomic structure and chemical versatility of MXenes. 25
Figure 3.3 Schematic representation of the chemical exfoliation process from AIMD. 27
Figure 3.4 Electronic band structure of the topological insulating $Mo_2HfC_2O_2$ MXene. 32
Figure 3.5 Electronic band structure of the half-metallic Cr_2C MXene. 35
Figure 3.6 Electronic DOS of the Janus Cr_2CFCl MXene. . . 36
Figure 3.7 Theoretical elastic constants of MXenes. 39
Figure 3.8 Theoretical gravimetric capacities of MXenes. . . 41
Figure 4.1 Schematic of a self-consistent Kohn-Sham calculation. 53
Figure 4.2 Schematic of the pseudopotential approximation. 56
Figure 5.1 Stokes and Anti-Stokes Raman scattering. 74
Figure 5.2 Berkovich, spherical, and Vickers indenters. . . . 77
Figure 6.1 Atomic structure and transmission Laue diffraction pattern of Cr_2AlC. 83
Figure 6.2 Phonon spectrum and density of states of Cr_2AlC. 86
Figure 6.3 Schematics of the atomic displacements for the phonon modes in Cr_2AlC. 87
Figure 6.4 Electronic band structure of Cr_2AlC. 89
Figure 6.5 Electrical resistivity of Cr_2AlC and experimental device. 90

Figure 6.6 Thermal conductivity of Cr_2AlC. 92
Figure 6.7 Nanoindentation test on Cr_2AlC single crystals. 101
Figure 6.8 Structure and Laue diffraction pattern of RE-i-MAX phases. 105
Figure 6.9 High resolution STEM images for RE-i-MAX single crystals. 108
Figure 6.10 Raman spectra and computed Raman mode wavenumbers of RE-i-MAX single crystals. . . . 109
Figure 6.11 Schematics of the atomic displacements of the vibrational modes of RE-i-MAX phases. 113
Figure 6.12 Dependence on both experimental and calculated wavenumbers on m_{RE}. 114
Figure 6.13 Evolution of the structural parameters with the effective ionic radius of the RE element in the RE-i-MAX phases. 116
Figure 6.14 Schematic representation of the outlying vibrational modes in the RE-i-MAX phases. 117
Figure 6.15 Computed elastic moduli as a function of m_{RE} for the RE-i-MAX phases. 121
Figure 6.16 Nanoindentation test on RE-i-MAX single crystals. 122
Figure 6.17 Electronic DOS and projected DOS of RE-i-MAX. 124
Figure 6.18 Calculated pCOHP and IpCOHP values of RE-i-MAX. 125
Figure 6.19 IpCOHP values for the series of bonds in RE-i-MAX. 127
Figure 6.20 IpCOHP and exfoliation energies vs. bond length for a series of 90 MAX phases. 127
Figure 7.1 Atomic structure of pristine and functionalized V_2CT_z. 133
Figure 7.2 Electronic band structure of pristine and functionalized V_2CT_z. 135
Figure 7.3 LDOS and pDOS of V_2CT_z. 137
Figure 7.4 Schematic representation of the Raman and IR active modes in V_2C. 139
Figure 7.5 Phonon band structures and density of states of V_2CT_z. 140
Figure 7.6 Experimental Raman spectra of V_2AlC single crystal and exfoliated V_2CT_z. 143

Figure 7.7 Comparison of the computed Raman-active wavenumbers with the experimental Raman spectrum of V_2CT_z. 144

LIST OF TABLES

Table 2.1 Atomic sites and coordinates of the MAX polymorphs. 11
Table 3.1 Atomic sites and coordinates of MXenes. 29
Table 6.1 Structural parameters of Cr_2AlC. 83
Table 6.2 Phonon mode energy, symmetry, and activity in Cr_2AlC. 85
Table 6.3 Elastic properties of Cr_2AlC. 100
Table 6.4 Structural parameters of the RE-i-MAX phases. . 107
Table 6.5 Raman mode wavenumbers of the RE-i-MAX phases. 110
Table 6.6 Calculated elastic properties of the RE-i-MAX phases. 119
Table 6.7 Exfoliation energy of the RE-i-MAX phases. . . . 128
Table 7.1 Structural parameters and formation energies of V_2CT_z. 134
Table 7.2 Computed vibrational mode wavenumbers of V_2CT_z. 139
Table 7.3 Computed vibrational mode wavenumbers of $V_2CF(OH)$. 145
Table 7.4 Experimental and computed Raman peaks positions of terminated V_2CT_z systems. 146

LIST OF SYMBOLS

Γ	k-point at the zone center of the BZ

Δ	Variation, deviation
ϵ_0	Static dielectric constant in vacuum
ε	Charge carrier energy
$\varepsilon_{b,k}$	Energy of band b
ε_i	Mono-electronic energy
ε_j	Small strain component
$\varepsilon_{\mathrm{xc}}$	Exchange-correlation energy per electron
θ	Defracting angle
$\hbar$	Reduced Planck constant
κ	Thermal conductivity
κ_0	Thermal conductivity divided by τ_0
κ_e	Electronic contribution to the thermal conductivity
κ_l	Lattice contribution to the thermal conductivity
λ	Wavelength or Small parameter for small perturbation
$\mathcal{L}^\alpha$	Generalized transport coefficient
μ	Chemical potential
μ_B	Bohr magneton
ν	Poisson ratio
∇	Gradient operator
ϕ_i	Mono-electronic wave function
ρ	Electronic density or Electrical resistivity
$\tilde{\rho}$	Trial electronic density
ρ_0	Electronic density of the ground state
σ	Electrical conductivity
σ_0	Electrical conductivity divided by τ_0
$\sigma(\varepsilon, T)$	Transport distribution function
σ_i	Small stress component
Σ	Summation operator
τ	Relaxation time
τ_0	Constant relaxation time
$\phi(r)$	All-electron wave function
$\phi^{\mathrm{PS}}(r)$	Pseudo wave function
Φ_i^α	First-order Born-von Karman force constants

$\Phi_{ij}^{\alpha\beta}$	Second-order Born-von Karman force constants
$\Phi_{ijk}^{\alpha\beta\gamma}$	Third-order Born-von Karman force constants
Ψ	Many-body wave function
$\tilde{\Psi}$	Trial wave function
ω, ω_{mq}	Phonon frequency
Ω	Unit cell volume
$\Omega^{\star}$	Volume of the first BZ
a, b, c	Lattice constants
a_1, a_2, a_3	Three primitive vectors in the real space
$a_1^{\star}, a_2^{\star}, a_3^{\star}$	Three primitive vectors in the reciprocal space
$A(h_c)$	Area function
B	Bulk modulus
c_{ij}	Elastic constants
c_{ν}	Group velocity of phonon mode ν
C_A	Electrochemical capacity
$C_{\kappa,\alpha,\kappa'\beta}$	Interatomic force constant matrix
$\tilde{C}_{\kappa,\alpha,\kappa'\beta}$	Fourier transform of the IFC matrix
d	Spacing between diffracting planes
$\tilde{D}_{\kappa\alpha,\kappa'\beta}$	Dynamical matrix
e, q	Elementary charge
E	Energy or Young's modulus
E_0	Energy of the ground state
E_{cut}	Kinetic cut-off energy
E_{exf}	Exfoliation energy
E_{tot}	Total energy of a system
E_i	Directional elastic modulus
E_{xc}	Exchange-correlation energy
E_{Br}	Berkovich Young's modulus
E_F	Fermi energy
f	Force
f_F	Fermi distribution function
F	Faraday constant
F_{ν}	Phonon population of mode ν

G	Reciprocal space lattice vector or Shear modulus
h_c	Contact depth
h_{tot}	Indentation depth
H	Hardness
H_{Br}	Berkovich hardness
$\widehat{H}$	Hamiltonian operator
$\widehat{J}_j$	Coulomb operator
k	Electron wave vector or Sampling points in the first BZ
k_B	Boltzmann constant
k_i	Initial neutron wave vector
k_f	Final neutron wave vector
K	Bond stiffness
$\widehat{K}_j$	Exchange operator
L_0	Lorentz number
m_e	Electron mass in vacuum
m_{red}	Reduced mass
M_κ	Atomic mass of atom κ
n	Order of reflection or General index
n_ν	Out-of-equilibrium Bose-Einstein distribution
$\overline{n}_\nu$	Equilibrium Bose-Einstein distribution
n_A	Number of adsorbed metal adatoms
N_{at}	Number of atoms in the primitive cell
P	Load
q	Phonon wave vector
r_c	Cut-off radius
r_i	Coordinates of electrons
R_α	Coordinates of nuclei
R_κ^a	Position vector of atom κ in unit cell a
s_{ij}	Compliance constants
S	Harmonic stiffness or Seebeck coefficient or Surface area
T	Temperature
T_m	Melting temperature
$\widehat{T}_e$	Electronic kinetic energy operator

$\widehat{T}_N$	Nuclear kinetic energy operator
u	Atomic displacement
u_{nk}	Periodic part of the Bloch wave function
U	Potential energy
U_0	Potential energy of the unperturbed lattice
U_{mq}	Phonon eigenvector
v	Sound velocity
$v_{b,k}$	Carrier velocity
$V(r)$	Potential
$V^{\mathrm{PS}}(r)$	Pseudopotential
$\widehat{V}_{ee}$	Electron-electron Coulomb interaction operator
$\widehat{V}_{\mathrm{eff}}$	Effective potential acting on each electron
$\widehat{V}_{eN}$	Electron-nucleus Coulomb interaction operator
$\widehat{V}_{\mathrm{ext}}$	External potential
$\widehat{V}_{\mathrm{H}}$	Hartree potential
V_{KS}	Kohn-Sham potential
$\widehat{V}_{NN}$	Nucleus-nucleus Coulomb interaction operator
V_{xc}	Exchange-correlation potential
X	Any physical quantity
zT	Thermoelectric figure of merit
Z_A	Valence state of metal adatoms

ACRONYMS

2D	Two-dimensional
3D	Three-dimensional
AIMD	Ab Initio Molecular Dynamics
ARPES	Angle-Resolved Photoemission Spectroscopy
BO	Born-Oppenheimer
BTE	Boltzmann Transport Equation

BZ	Brillouin Zone
COHP	Crystal Orbital Hamilton Population
CRTA	Constant Relaxation Time Approximation
DFPT	Density Functional Perturbation Theory
DFT	Density Functional Theory
DOS	Density Of States
EDS	Energy Dispersive Spectroscopy
EDX	Energy Dispersive X-ray spectroscopy
f.u.	formula unit
GGA	Generalized Gradient Approximation
HEG	Homogeneous Electron Gas
HAADF	High Angle Annular Dark Field
IFC	Interatomic Force Constants
INS	Inelastic Neutron Scattering
IR	Infrared
LDA	Local Density Approximation
LOBSTER	Local Orbital Basis Suite Towards Electronic structure
MPTR	Modulated Photothermal Radiometry
NFE	Nearly Free Electron
PAW	Projector Augmented Wave
PBE	Perdew-Burke-Ernzerhof
PC	Polycrystal
PFS	Pulse Flying Spot
PPRT	Periodic Pulse Radiometry Technique
QHA	Quasi-Harmonic Approximation
RE	Rare-Earth
RT	Room Temperature
SC	Single Crystal
SCAN	Strongly Constrained and Appropriately Normed
SE	Secondary Electrons
SEM	Scanning Electron Microscopy

SMA	Single Mode Approximation
SOC	Spin Orbit Coupling
STEM	Scanning Transmission Electron Microscopy
TDEP	Temperature Dependent Energy Potential
VASP	Vienna Ab initio Simulation Package
VESTA	Visualization for Electronic and STructural Analysis
XRD	X-Ray Diffraction

The edifice of science not only requires material, but also a plan. Without the material, the plan alone is but a castle in the air - a mere possibility; whilst the material without a plan is but useless matter.

— D. I. Mendeleev

1 INTRODUCTION

Today, it is undeniable that the 20th century enabled the birth and evolution of a remarkable amount of scientific and technological progress. It includes the first human spaceflight in 1961 and the first moon landing in 1969. It also includes many advances in the medical field with the first organ transplant in 1954, the first heart transplant in 1967, and the first test-tube baby in 1978. Additionally, it concerns a set of technologies present in our daily life, such as the color television (1926), the programmable computer (1936), the electronic mail (1971), the digital camera (1975), and the world wide web (1989). All these scientific and technological developments prove to what extent science plays a fundamental role in a society which is in perpetual quest for a better future.

One can wonder what exactly is science? It is such a large and complete area at the same time. Science is not only chemistry, physics, and biology. Science is also geology, mathematics, computer science, medicine, geography, climathology, environmental management, ecology, etc. Most often research in a specific field involves interactions with other ones.

In the manuscript you are about to read, materials science is at the center of the approach undertaken. Materials science essentially consists in the study of matter at different scales. It is focused on the structural characterization of materials, the study of their properties (*e.g.*, chemical, electrical, thermal, optical, mechanical, ...), and the relationships between the two. Knowledge and control of these relationships and of the microscopic phenomena that govern the response of materials to various external stimuli are the main tools in the development of new electronic, energy, and nanotechnology devices.

One step ahead of materials science is materials engineering, which consists in optimizing the properties of existing materials or even in creating new ones, to meet specific requests in terms of applications. In this context, the trial-and-error procedure in laboratory is often inefficient. In contrast, computational physics plays an essential predictive role in materials engineering. Using *ab initio* calculation methods, it is possible to predict systematically, quickly, and quite accurately, various properties of any material from its composition. Moreover, current high-throughput calculation tools make possible the automation of those calculations and, hence, the fast investigation of large structure and composition databases. However, the usefulness of such a theoretical approach is only real if it reflects the experimental conditions present in laboratory. Indeed, it would be of little utility, if not pointless, to predict exceptional properties for a perfect crystal, if this one is fictitious or infeasible experimentally.

Consequently, interactions between theoretical and experimental research groups are mandatory. A realistic and complete understanding of material physics at the atomic level can only be achieved by effectively combining experimental and theoretical approaches. Therefore, most of the research projects carried out as part of this thesis consist in both theoretical and experimental studies and involve close collaborations with different experimental groups, in particular those of M. W. Barsoum (Drexel University, USA), T. Ouisse (LMPG Grenoble, France), and J. Rosen (Linköping University, Sweden).

This work has four main objectives. The first one is to investigate both experimentally and theoretically the physical properties (*i.e.*, electrical, thermal, vibrational, elastic) of the three-dimensional (3D) MAX phase single crystals and the potential anisotropy thereof. In particular, Cr_2AlC single crystals are studied (left panel in Fig. 1.1). The second goal involves the investigation of the recently discovered rare-earth containing MAX phases, coined RE-i-MAX, and the experimental characterization of monocrystalline samples (central panel in Fig. 1.1). As a third goal, the potential exfoliation of 3D MAX phases into their two-dimensional (2D) counterparts, MXenes, is predicted. Eventually, the fourth goal concerns the 2D MXene systems, in particular the V_2CT_z ones (right panel in Fig. 1.1). It consists in the investigation of their structural, electronic, and vibrational properties, including the establishment of their Raman fingerprint and the study of the influence of the terminal groups T_z thereon.

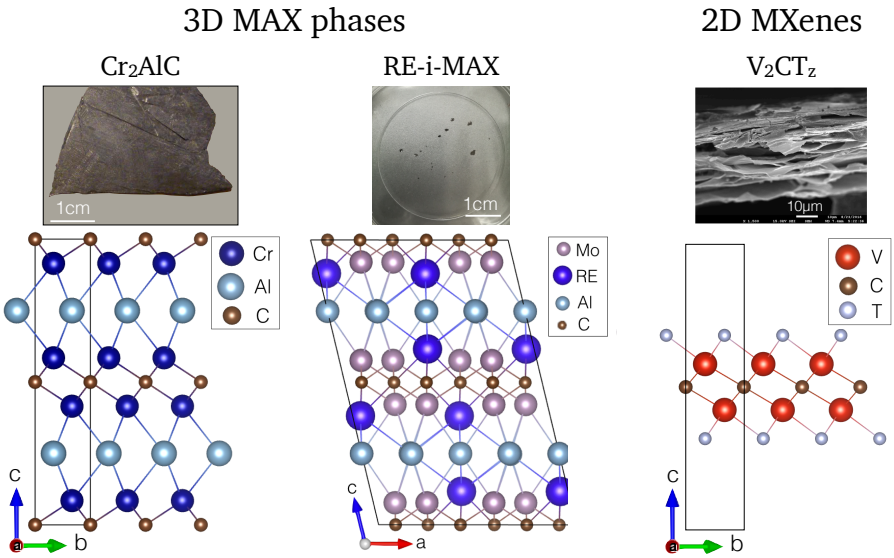

Figure 1.1: Materials investigated in this thesis, including 3D MAX phase single crystals (Cr_2AlC and RE-i-MAX) and 2D MXenes (V_2CT_z).

This thesis consists of 8 chapters. Chapters 2 and 3 focus on the materials studied in this work, *i.e.*, the MAX phases and MXenes, respectively, and present the background and literature survey of their synthesis, structures, properties, and applications. All samples used in this thesis were grown in T. Ouisse's group at LMGP Grenoble in France. Chapters 4 and 5 present the fundamentals of the theoretical concepts and experimental techniques, necessary for the following chapters. Chapter 4 includes a general description of the density functional theory and density functional perturbation theory formalisms used to compute the structural, electronic, vibrational, and elastic properties. In addition, the Boltzmann transport equations for electrons and phonons, respectively used to obtain the electronic and lattice contributions to the thermal conductivity, are detailed. Chapter 5 includes the description of various characterization techniques used to probe the structural, vibrational, and elastic properties of our systems. They include X-ray diffraction (performed in T. Ouisse's group at LMGP Grenoble in France), scanning electron microscopy (performed with H. Badr and M. Sokol at Drexel University in USA and with D. Magnin at UCLouvain in Belgium), scanning transmission electron microscopy (performed in J. Rosen's group at Linköping University in Sweden), Raman spectroscopy (performed together with L. Shi at UCLouvain in

Belgium and by O. Chaix-Pluchery at LMGP Grenoble in France), inelastic neutron scattering (performed by T. Ouisse, F. Bourdarot, and P. Bourges at ILL Grenoble and LLB Paris-Saclay in France), and nanoindentation techniques (performed with H. Badr at Drexel University in USA and with S. Ryelandt at UCLouvain in Belgium). The physical properties of MAX phase single crystals are explored in Chapter 6, while those of two-dimensional MXenes are reported in Chapter 7. They include a complete analysis of the structural, electronic, vibrational, thermal, and elastic properties, combining both theoretical and experimental tools. This highlights the diverse and wide set of skills I have developed during my PhD thesis since I performed all theoretical simulations and was involved in most experimental characterization steps. Finally, conclusions and perspectives for future work are given in Chapter 8.

One of the joys of working with the MAX phases is the ease by which one can change the chemistry, while keeping the structure the same.

— M. W. Barsoum

2 AN INTRODUCTION TO MAX PHASES

2.1 HISTORY OF THE MAX PHASES

The MAX phases have two histories [1]. The first one starts in the early-1960s, when the group of Nowotny in Vienna synthesized a series of ternary carbides and nitrides including about 30 phases with the M_2AX chemistry [2]. At that time, these phases were called 'H-phases' (see Fig. 2.1(a)). In 1967, Nowotny's group synthesized the first two 312 phases, Ti_3SiC_2 [3] and Ti_3GeC_2 [4], with similar layered structures than the H-phases (see Fig. 2.1(b)). In the early-1990s, the same group reported the synthesis of Ti_3AlC_2 [5–7].

Subsequently, these phases remained totally unexplored until the mid-1990s - beginning of the second history of the MAX phases - when Barsoum and El-Raghy synthesized fully dense single-phase Ti_3SiC_2 and revealed its outstanding combination of metallic and ceramic-like properties [8, 9]. The compound was light, relatively soft, and readily machinable, was a good electrical and thermal conductor, and was impressively resistant to thermal shock and oxidation up to 1400°C. Between 1996 and 1997, Barsoum and El-Raghy synthesized and characterized most of the H-phases previously reported by Nowotny and coworkers (*i.e.*, Ti_2AlC, Ti_2AlN, Ti_2GeC, Ti_3GeC_2, V_2AlC, Nb_2AlC, Ta_2AlC, Ti_2SnC, Zr_2SnC, Nb_2SnC, Hf_2SnC, etc.) and surprisingly observed that all of them possessed a similar combination of metallic and ceramic properties [10]. In 1999, Barsoum and El-Raghy synthesized the first 413 phase (see Fig. 2.1(c)), Ti_4AlN_3 [11, 12], and agreed that all 211, 312, and 413 phases form a large family of layered compounds with the general formula $M_{n+1}AX_n$. Today, these phases are commonly referred to as the MAX phases [13].

For the past twenty years, motivated by the intriguing combination of properties observed in such ceramic compounds (see Section 2.4),

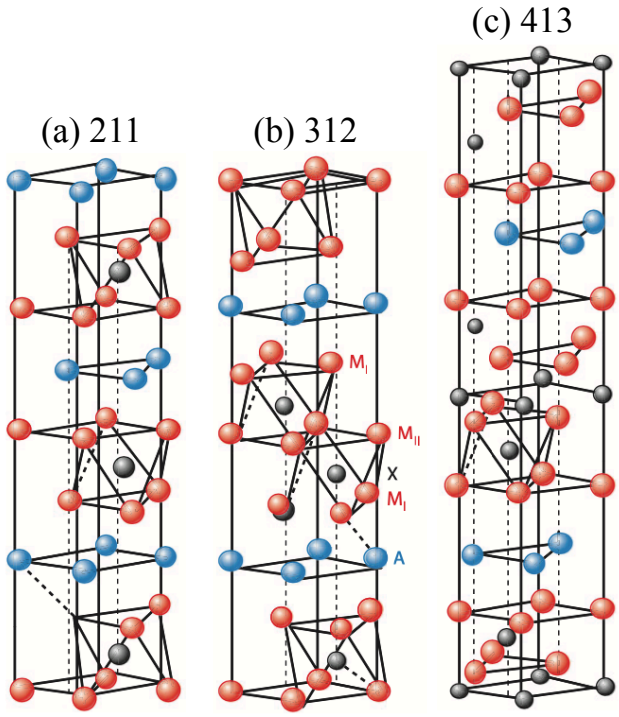

Figure 2.1: Atomic structure of the (a) 211 ('H-phase'), (b) 312, and (c) 413 phases, with the edge-sharing M_6X octahedra highlighted in all three figures and the M, A, and X atoms represented respectively by red, blue, and grey spheres. From [14].

the MAX phase community has been simultaneously working on the discovery of new MAX phases and their characterization. Intensive works have been devoted towards the growth of pure samples, including the optimization of high-temperature synthesis processes and the development of new techniques to produce MAX single crystals (see Section 2.2). Rapidly, a new route to significantly increase the elemental combination of MAX phases was proposed, consisting in the addition of a fourth element, by alloying on the M, A, or X sites. In this regard, many isostructural MAX phase solid solutions have been reported [15–17], together with the more recent reports of chemically ordered quaternaries [18, 19] (see Section 2.3). Eventually, the success of the MAX phases has been maintained by the possibility to use them as 3D precursors to produce 2D crystals, coined MXenes [20] (see Chapter 3).

These last two decades, substantial efforts have been made on the synthesis of MAX phases. Initially, all MAX phases were synthesized in powders, bulk materials, or thin films, corresponding to highly polycrystalline forms. In 2011, Mercier and coworkers [21, 22] reported for the first time on the growth of MAX single crystals, opening the door to a more accurate characterization of the intrinsic MAX phase properties and their anisotropy. This section reviews the various techniques used to synthesize MAX phases in both polycrystalline and mono-crystalline forms.

2.2.1 *MAX polycrystals*

Several methods have been reported regarding the synthesis of MAX polycrystals and can be classified into three main categories.

The first category corresponds to the synthesis of MAX phase powders and includes mechanical alloying [23], self-propagating high-temperature [24, 25], and solid-state reaction pressure-less sintering [26, 27] techniques.

The second category involves physical vapor deposition [28], chemical vapor deposition [29, 30], solid-state reactions [31], thermal spraying [32], and slip casting [33] processes, which result in the production of MAX phase thin films.

The last category involves the synthesis of bulk MAX phases which is achieved through hot isostatic pressing [10, 34–36], hot-pressing [8, 37–39], spark plasma sintering [40], or pulse discharge sintering [41]. In their seminal report [8], Barsoum and El-Raghy fabricated polycrystalline bulk sample of Ti_3SiC_2 using the first two ones. In short, Ti, SiC, and graphite powders are mixed and cold-pressed at 180 MPa. Afterwards, the hot isostatic pressing is achieved using molten glass as the pressure transfer medium, while the hot-pressing is done in a graphite die. In both cases, the system is hot-pressed at 1600°C for 4h under a pressure of 40 MPa. These methods allowed to obtain pure Ti_3SiC_2 crystals in relatively large quantity. Subsequently, these techniques were used to synthesize Ti_3SnC_2, Ti_2SnC, V_2AlC, Cr_2AlC, and Nb_2AlC phases [13].

2.2.2 *MAX single crystals*

Until ten years ago, the lack of large MAX phase single crystals prohibited the experimental investigation of their physical properties and the anisotropy thereof.

In 2011, Mercier and coworkers [21, 22] first reported on the solution growth process used to grow Ti_3SiC_2 single crystals. In short, the solution growth method involves four main steps. First, an appropriate composition of M and A elements is heated up to a temperature T_m above the melting temperature of all elements. This temperature ranges from 1500°C up to 2000°C depending on the nature of the elements or of the starting compounds. In the case of Ti_3SiC_2, carbon incorporation is ensured by the graphite crucible wall dissolution, and the crystals are grown on a carbon rod dipped at a cold point. This allows to get the crystals out of the flux, since the latter cannot be selectively dissolved after the growth. For solutions aimed at producing less refractory compounds and allowing a higher C solubility (*e.g.*, Cr_2AlC), a better control of carbon incorporation is ensured by using an alumina crucible and introducing a well defined volume of a carbon rod until complete dissolution of the latter is achieved. The third step is the spontaneous nucleation in the melted flux, which takes place around some nucleation temperature below T_m, and is crossed by progressively reducing T. The fourth step is crystal growth from the nuclei. In order to decrease the number of crystals and in return increase the crystal size, the system is cooled down very slowly, in order to dissolve the smallest, nucleated crystals into the bigger ones through the Ostwald ripening effect. The cooling step during which crystals are growing can last several hours or days. Once the system is cooled down to room temperature, the solidified flux is taken out from the reactor. Al-based compounds are immersed into HCl acid to dissolve the flux and collect the single crystals. Alternatively, an Al-based solidified flux auto-hydrolyzes and turns into powder at ambient air after a few weeks. However, not all phases lend themselves to such easy crystal extraction, and specific tricks must be developed for most non Al-based compounds (as described above for Ti_3SiC_2).

To date, macroscopic MAX phase single crystals or single crystalline layers have been synthesized only in two research groups including Ouisse's group (Grenoble, France) using the solution growth process, and Rosen's group (Linköping, Sweden) using physical vapor deposition by sputtering. Those are the only two techniques reported so

far to obtain MAX single crystalline samples with large lateral dimensions. Since this first report, several other MAX phases [21, 42, 43], including Cr_2AlC and V_2AlC, were grown and used to study their magneto-transport [44, 45] and electronic [46] properties. In addition, as discussed later, utilizing single crystal palette as precursor for synthesizing large area 2D MXene is also promising.

2.3 STRUCTURE AND VARIETY OF MAX PHASES

2.3.1 *Crystal structure and nomenclature*

The MAX phases are layered hexagonal 3D solids composed of 2D $M_{n+1}X_n$ sheets separated by A layer [13], thus exhibiting a general formula $M_{n+1}AX_n$, where M represents an early transition metal, A is an element from groups 13 to 16, X is either a carbon or a nitrogen atom, and n varies from 1 to 3 [13]. Depending on their n value, the MAX phases can be categorized as 211 phases for M_2AX, 312 phases for M_3AX_2, and 413 phases for M_4AX_3. As depicted in Figs. 2.1 and 2.2, the main difference between the structures of the 211, 312, and 413 phases is the number of M layers separating the A layers. In all systems, edge-sharing M_6X octahedra, identical to those found in the rocksalt structures, are interleaved with layers of A elements (see Fig. 2.1).

All ternary MAX phases crystallize in the $P6_3/mmc$ (#194) hexagonal structure with two formula units per unit cell. Typical lattice parameters are a $\sim$ 3 Å, and c $\sim$ 13, 18, and 23 Å, for the 211, 312, and 413 phases, respectively. Their densities range from 4 to 15 g.cm^{-3}. While the 211 phases exist in a unique polymorph, the extra degree of freedom related to the layer stacking in the 312 and 413 phases respectively results into two (α and β) 312 and three (α, β, and γ) 413 polymorphs (see Fig. 2.3). The atomic sites and idealized reduced coordinates of all known MAX polymorphs are reported in Table 2.1 [1].

So far about 85 ternary MAX carbides and nitrides have been reported, with eleven different elements on the M sites (*i.e.*, Sc, Ti, V, Cr, Mn, Zr, Nb, Mo, Hf, Ta, and Lu) and fifteen elements on the A sites (*i.e.*, Al, Si, P, S, Zn, Ga, Ge, As, Cd, In, Sn, Ir, Au, Tl, and Pb). Regarding the X site, the recent synthesis of the Ti_2InB_2 MAX phase [52] constitutes

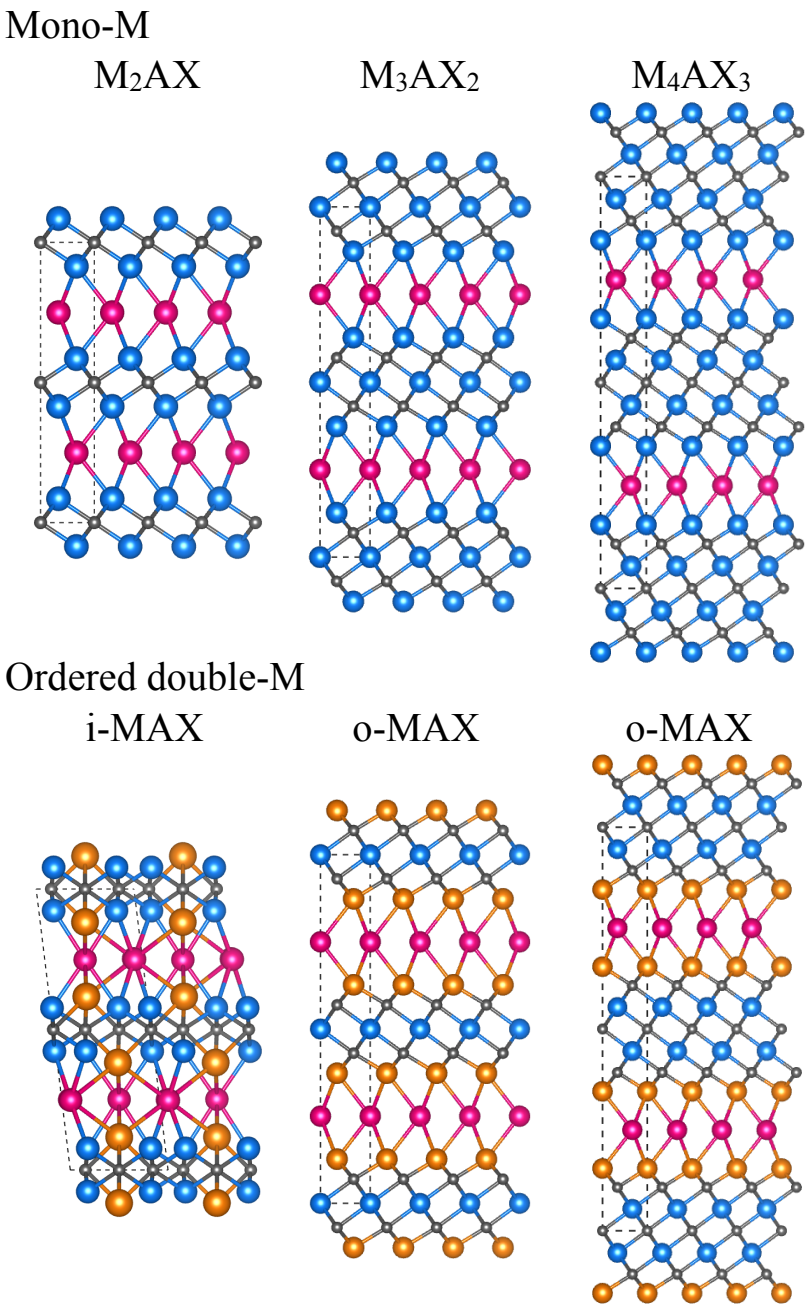

Figure 2.2: Atomic structure of existing MAX phases, including ternary $M_{n+1}AX_n$ ($n = 1, 2, 3$) phases, and quaternary out-of-plane ordered (o-MAX) and in-plane ordered (i-MAX) phases. The unit cells are represented with dashed lines and the M, A, and X elements are respectively represented by small blue/orange, pink, and grey spheres.

Table 2.1: Atomic Wyckoff sites and idealized reduced coordinates of the 211, 312, and 413 MAX phase polymorphs. Adpated from [1].

Atoms	Chemistry/Archetypical phase				Refs.
	Wyckoff	x	y	z_i (canonical)	
M_2AX/Ti_2SC					[47]
A	$2d$	1/3	2/3	3/4	
M	$4f$	2/3	1/3	1/12(0.083)	
X	$2a$	0	0	0	
α-M_3X_2/Ti_3SiC_2					[3]
A	$2b$	0	0	4/16	
M_I	$4f$	1/3	2/3	2/16(0.125)	
M_{II}	$2a$	0	0	0	
X	$4f$	2/3	1/3	1/16(0.0625)	
β-M_3X_2/Ti_3SiC_2					[48]
A	$2d$	1/3	2/3	4/16	
M_I	$4f$	1/3	2/3	2/16(0.125)	
M_{II}	$2a$	0	0	0	
X	$4f$	2/3	1/3	1/16(0.0625)	
α-M_4AX_3/Ti_4AlN_3					[11, 49]
A	$2c$	1/3	2/3	5/20	
M_I	$4e$	0	0	3/20(0.15)	
M_{II}	$4f$	1/3	2/3	1/20(0.05)	
X_I	$2a$	0	0	0	
X_{II}	$4f$	2/3	1/3	2/20	
β-M_4AX_3/Ta_4AlC_3					[50]
A	$2c$	1/3	2/3	5/20	
M_I	$4e$	1/3	2/3	12/20(0.6)	
M_{II}	$4f$	1/3	2/3	1/20(0.05)	
X_I	$2a$	0	0	0	
X_{II}	$4e$	2/3	1/3	2/20	
γ-M_4AX_3/Ta_4GaC_3					[51]
A	$2c$	1/3	2/3	5/20	
M_I	$4e$	0	0	3/20(0.15)	
M_{II}	$4f$	1/3	2/3	1/20(0.05)	
X_I	$2a$	0	0	0	
X_{II}	$4f$	2/3	1/3	2/20	

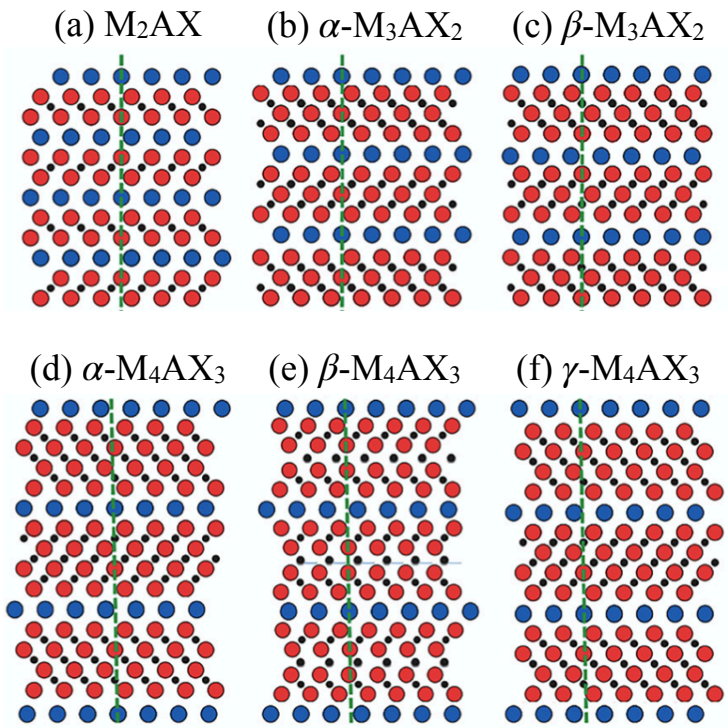

Figure 2.3: Crystal structures of the MAX phase polymorphs: (a) M_2AX, (b) α-M_3AX_2, (c) β-M_3AX_2, (d) α-M_4AX_3, (e) β-M_4AX_3, and (f) γ-M_4AX_3. From [1].

the first report of a MAX phase with neither C nor N element on the X site and opens the door to an important increase of the elemental combinations possible in the MAX phases.

2.3.2 *Quaternary MAX phases*

Recently, a new route to increase the elemental combination of MAX phases and to optimize their performance was proposed, consisting in the addition of a fourth element, by alloying on the M, A, or X sites [15–17]. Historically, most quaternary MAX phases existed as random solid solutions [17].

In 2014, out-of-plane ordered quaternary MAX phases (o-MAX) were discovered [18], with the general formula $M'_2M''AX_2$ for 312 phases and $M'_2M''_2AX_3$ for 413 phases, where M′ and M″ are two different early transition metals. As depicted in Fig. 2.2, two M′ lay-

ers sandwich either one or two layers of M″ elements. Similarly to ternary MAX phases, the o-MAX phases crystallize in the $P6_3/mmc$ (#194) hexagonal structure. It is worth noting that the degree of ordering in each layer is not always perfect and some M′ atoms sometimes occupy the M″ sites and vice versa. Additionally, significant amounts of C vacancies are observed in o-MAX phases, even though all elemental powders are initially added in stoichiometric quantities.

Since 2014, six different o-MAX phases have been synthesized, *i.e.*, Cr_2TiAlC_2 [18], Cr_2VAlC_2 [53], $Cr_2V_2AlC_3$ [53], Mo_2TiAlC_2 [54], $Mo_2Ti_2AlC_3$ [54], and Mo_2ScAlC_2 [55]. The latter Mo_2ScAlC_2 is a unique system because a totally different crystal structure with other type of ordering can be obtained by simply changing the ratio of the initial elemental powders.

In 2017, in-plane ordered quaternary MAX phases (i-MAX) were theoretically predicted and successfully synthesized with the general formula $(M'_{2/3}M''_{1/3})_2AlC$, where M′ and M″ are two different transition metals [19]. As depicted in Fig. 2.2, the two M′ and M″ elements are in-plane ordered with the M′:M″ ratio equal to 2. As described by Dahlqvist et al. [56], a requirement for formation of i-MAX phases is a large difference in atomic size between M′ and M″ elements which allows for the formation of a M′ honeycomb lattice with the M″ atoms at the centers of the hexagons. To minimize in-plane stress, the larger M″ atoms are displaced toward the Al-layer in which the Al atoms redistribute into a Kagome-like lattice [56]. This chemical ordering and atomic arrangement, only observed in 211 systems, lead to $C2/c$ (#15) monoclinic or $Cmcm$ (#63) orthorhombic crystal structure, as opposed to $P6_3/mmc$ hexagonal structure for traditional and o-MAX phases. Interestingly, in some $C2/c$ systems (*e.g.*, $(Cr_{2/3}Sc_{1/3})_2AlC$), the presence of a minority phase whose symmetry corresponds to $Cmcm$ was found. Respectively, in $Cmcm$ crystalline systems (*e.g.*, $(Cr_{2/3}Y_{1/3})_2AlC$), the minority phase has a $C2/c$ symmetry. Although what governs the crystal symmetry in i-MAX phases is not clear yet, Tao *et al.* [19] showed, using DFT calculations, that both $C2/c$ and $Cmcm$ crystal structures are energetically equal.

The first reported i-MAX phase, $(Mo_{2/3}Sc_{1/3})_2AlC$ [19], thus consists in the first report of a MAX phase whose symmetry was not $P6_3/mmc$. Soon thereafter, eleven other i-MAX phases were synthesized, *i.e.*, $(V_{2/3}Zr_{1/3})_2AlC$ [56], $(Mo_{2/3}Y_{1/3})_2AlC$ [56], $(W_{2/3}Sc_{1/3})_2AlC$ [55], $(W_{2/3}Y_{1/3})_2AlC$ [55], $(Cr_{2/3}Sc_{1/3})_2AlC$ [57], $(Cr_{2/3}Y_{1/3})_2Al$ [57],

$(Mo_{2/3}Y_{1/3})_2GaC$ [58], $(Mo_{2/3}Sc_{1/3})_2GaC$ [58], $(Cr_{2/3}Zr_{1/3})_2AlC$ [59], $(Cr_{2/3}Sc_{1/3})_2GaC$ [60], and $(Mn_{2/3}Sc_{1/3})_2GaC$ [60]. Interestingly, this ordering allowed the addition of non-traditional MAX phase elements, such as Sc, Y, and W. Very recently, the existence of rare-earth (RE) containing i-MAX phases, coined RE-i-MAX, with the general formula $(Mo_{2/3}RE_{1/3})_2AC$ (A = Al or Ga), was revealed [61, 62]. Almost simultaneously, a similar layered family with a $M_4RE_4Al_7C_3$ stoichiometry was discovered [63]. Because of their magnetic properties [61, 63], these new phases are expected to attract much attention from the scientific community. Moreover, since most of them are Al based, the Al should, in principle, be selectively etched to create RE-i-MXenes, where the RE elements are ordered in the basal plane. This would significantly increase the palette of available magnetic 2D crystals that could be used in future 2D electronic and spintronic devices.

In total, considering both ternary and quaternary MAX phases, as well as solid solution compounds, there are more than 150 different compositions that have been reported experimentally. The MAX phase periodic table of M, A, and X elements is presented in Fig. 2.4 and highlights the remarkably wide space available to play on the MAX composition and, consequently, on their properties.

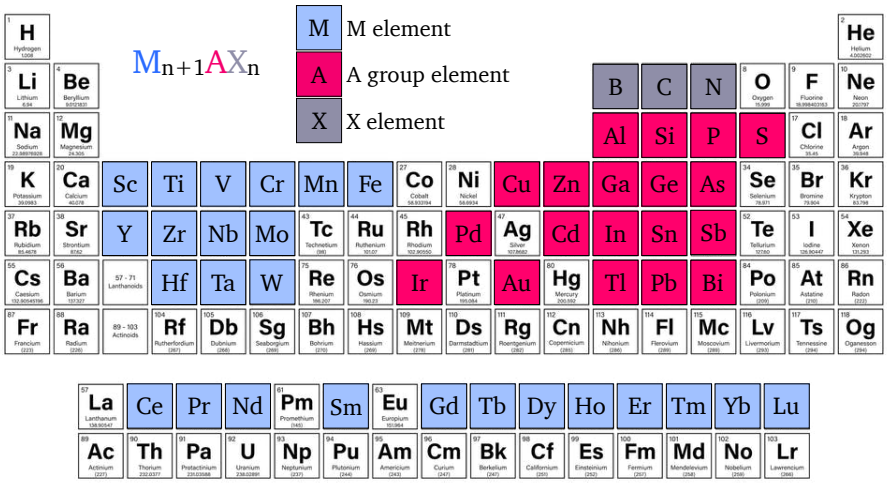

Figure 2.4: Periodic table with all elements experimentally incorporated in ternary and quaternary MAX phases, with M elements highlighted in blue, A elements in pink, and X elements in grey.

By now, it is well established that at least a subset of MAX phases combines some of the best properties of metals and ceramics [1, 13, 64], including high electrical and thermal conductivities, chemical, oxidation, and thermal shock resistances, as well as reversible deformation [65], and bulk ripplocations [66, 67]. Beyond their unique sets of properties, the MAX phases have attracted growing interest for their use as parent materials to produce 2D derivatives MXenes [20] (see Chapter 3).

The best characterized ternaries to date are Ti_3SiC_2, Ti_3AlC_2, and Ti_2AlC. Their transport properties have been intensively studied, including electrical and thermal conductivities, optical and magnetic characteristics, and Hall and Seebeck coefficients. Other physical properties have been measured and accurately modeled, including heat capacities, thermal expansion coefficients, and the temperature dependency thereof. In addition, the elastic and mechanical properties have also been quantified, *i.e.*, elastic moduli, stiffness, hardness, and fracture toughness [1].

In contrast to the ternary phases, the quaternary o-MAX and i-MAX phases still await experimental characterization. Regarding the o-MAX phases, only their structures, magnetic ground states, and electrical conductivities have been characterized. Although only six o-MAX phases have been reported so far, DFT calculations predict the existence of many more. The etching potential of o-MAX phases has also been investigated theoretically and four out of six systems have been successfully etched into 2D MXenes. Regarding the i-MAX phases, the lack of bulk samples with high-enough purity explains their poor characterization so far. However, some of them have been successfully etched into MXenes [19, 55, 68], bringing to four the number of i-MXene compositions. It is nonetheless clear that efforts on both experimental and theoretical sides are needed to more systematically investigate the o-MAX and i-MAX properties and understand the effect of chemical ordering on their properties [69]. As presented in Section 6.2, we greatly contributed to the characterization of the i-MAX phases, in general, and the RE-i-MAX phases, in particular.

As discussed in the following sections, the unusual combination of properties, which give MAX phases their attractive features to bridge

the gap between metals and ceramics, mostly results from their layered structure and the combination of strong metallic M−X bonds with relatively weaker M−A bonds. In Section 2.4.1, the electrical and magnetic properties of the MAX phases are briefly introduced. Section 2.4.2 describes the vibrational properties of the MAX phases including the analysis of the phonon wavenumbers, symmetries, and activities. In Section 2.4.3, the elastic and mechanical properties are presented. Section 2.4.4 sheds light on the good thermal properties of the MAX phases. Eventually, Section 2.4.5 briefly reviews the oxidation and reactivity of the MAX phases with their environment. Potential area where the MAX phases have found or could find applications are discussed in Section 2.4.6.

2.4.1 *Electrical and magnetic properties*

The MAX phases are all good metal-like conductors, with resistivities ranging from 0.07 to 2 $\mu\Omega$m [8, 13, 70] at RT which increase linearly with increasing temperature. In some cases, such as Ti_3SiC_2 and Ti_3AlC_2, their conductivities are higher than the one of pure Ti metal. The density of charge carriers is in the order of $1-3\times10^{27}\mathrm{m}^{-3}$ [1]. Interestingly, many MAX phases appear to be compensated conductors, *i.e.*, the effective concentrations and mobilities of electrons and holes are roughly equal [71–73].

Not surprisingly, the theoretical electronic band structures and densities of states (DOS) of most MAX phases exhibit similar features. As depicted in Fig. 2.5 for the Ti_3AlC_2 system, there is a strong hybridization between the *d* orbitals of the M atoms and the *p* orbitals of the X atoms, approximately around 2 to 5 eV below the Fermi level. This characteristic is common to the MX binaries. The DOS at the Fermi level is dominated by the *d* orbitals of the M elements and is higher than the one of the corresponding binary system. Finally, around 1 eV below the Fermi level, the *p* orbitals of the A atoms and the *d* orbitals of the M atoms overlap, forming M−A bonds that are roughly twice weaker than M−X bonds.

Given that the MAX phases are good electrical conductors, it is not too surprising that they have very low Seebeck coefficients [1].

A magnetic ground state has been predicted theoretically and/or observed experimentally for a large number of MAX phases [74, 75]. Almost all magnetic MAX phases contain Cr and/or Mn elements, in-

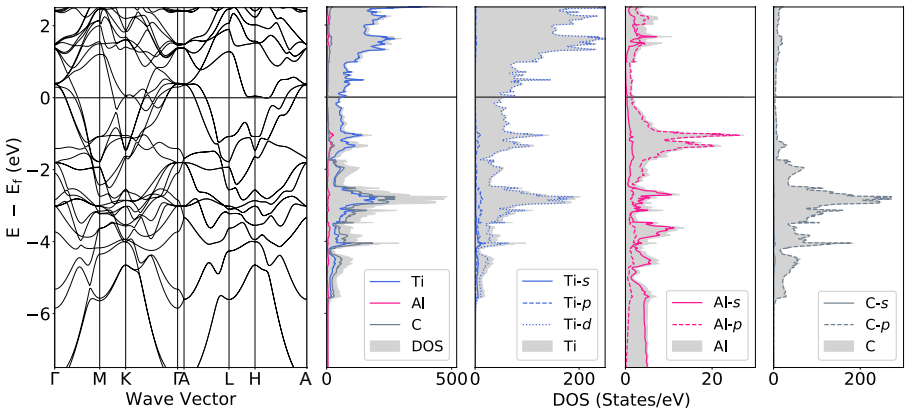

Figure 2.5: Electronic band structure and DOS of Ti_3AlC_2, as a representative member of the MAX family.

cluding Cr_2AlC [76–85], Cr_2GeC [74, 82, 86–88], Cr_2GaC [82, 89, 90], Cr_2AlN [85], Cr_2GaN [89, 91], $Fe_{n+1}AC_n$ ($n = 1, 2, 3$, and A = Al, Si, Ge) [92], Mn_2AlC [78, 85], Mn_2GaC [93–97], $(Cr,Mn)_2AlC$ [56, 84], $(Cr,Mn)_2GeC$ [82], Cr_4AlN_3 [98], $(Cr_2Ti)AlC_2$ [18, 56, 99].

The latest additions to the list of magnetic MAX phases concern the in-plane ordered $(M_{2/3}Sc_{1/3})_2AlC$ (M = Cr, Mn) [60], $(Mo_{2/3}RE_{1/3})_2AlC$ (RE = Ce, Pr, Nd, Sm, Gd, Tb, Dy, Ho, Er, Tm, and Lu) [61], and $(Mo_{2/3}RE_{1/3})_2GaC$ (RE = Gd, Tb, Dy, Ho, Er, Tm, Lu, and Yb) [62] MAX phases, with various magnetic characteristics. More specifically, complex magnetic order, which is characteristic of magnetically frustrated systems due to competing intra- and in-plane magnetic interactions, has been observed experimentally in most RE-containing i-MAX phases [61]. The in-plane ordering in quaternary MAX phases is of particular interest for two main reasons: (i) it allowed the addition of non-traditional MAX phase elements such as the magnetic RE elements, and (ii) a targeted etching process, proposed so far only for i-MAX phases, allowed to produce either ordered-divacancy MXenes or chemically ordered i-MXenes [61, 100].

Eventually, the prospect to convert the magnetic i-MAX phases into magnetic 2D crystals adds up to their remarkable importance for spintronic applications, since it would significantly enlarge the palette of available magnetic 2D crystals.

2.4.2 *Vibrational properties*

The number of phonon modes N depends on the number of atoms N_{at} in the unit cell, such that $N = 3N_{at}$. As mentioned previously, the unit cell of the MAX phases consists of two formula units. Consequently, the 8, 12, and 16 atoms, respectively in the 211, 312, and 413 structures, lead to 24, 36, and 48 phonon modes. Making good use of the group theory allows to predict the Raman and infrared activity of the modes. In addition to the three acoustic modes with symmetry A_{2u} and E_u, there are respectively 21, 33, and 45 optical modes, whose irreducible representations are respectively given by:

$$\Gamma(211) = \underbrace{1A_{1g} + 2E_{2g} + 1E_{1g}}_{\text{Raman}} + \underbrace{2A_{2u} + 2E_{1u}}_{\text{IR}} + \underbrace{2B_{1g} + 2B_{2u} + 2E_{2u}}_{\text{silent}} \quad (2.1)$$

$$\Gamma(312) = \underbrace{2A_{1g} + 3E_{2g} + 2E_{1g}}_{\text{Raman}} + \underbrace{3A_{2u} + 3E_{1u}}_{\text{IR}} + \underbrace{3B_{1g} + 3B_{2u} + 3E_{2u}}_{\text{silent}} \quad (2.2)$$

$$\Gamma(413) = \underbrace{3A_{1g} + 4E_{2g} + 3E_{1g}}_{\text{Raman}} + \underbrace{4A_{2u} + 4E_{1u}}_{\text{IR}} + \underbrace{4B_{1g} + 4B_{2u} + 4E_{2u}}_{\text{silent}} \quad (2.3)$$

where A_{1g}, E_{2g}, and E_{1g} are Raman-active, A_{2u} and E_{1u} are infrared-active, and all remaining modes are silent. The modes with E-symmetry are doubly-degenerate.

From the various experimental and theoretical works reported in the literature [22, 101–105], several conclusions on the Raman-active modes in the MAX phases can be drawn that are valid for all systems. The Raman modes can be classified into two categories. First, the low-wavenumber modes, ranging from 50 to 300 cm^{-1}, involve the vibrations of the M and A atoms and are observed in all 211, 312, and 413 systems. Then, the high-wavenumber modes, ranging from 550 to 660 cm^{-1}, involve the vibrations of the lighter X atoms, and are only observed in the 312 and 413 phases. Remarkably, the agreement between the experimental Raman spectrum and the computed Raman mode wavenumbers of the MAX phases is often good.

2.4.3 *Elastic and mechanical properties*

Similar to the MX binaries, a subset of MAX phases, *e.g.*, Ti_3SiC_2, Ti_3AlC_2, Ti_2AlC, and Cr_2AlC, are elastically stiff with Young's and

shear moduli in the order of 350 and 150 GPa, respectively [1, 72, 73]. Combined with a low density for the MAX phases with light transition metal elements (*e.g.*, Ti, V, Cr), these high elastic moduli lead to high specific stiffness values. For instance, the specific stiffness of Ti_3SiC_2 is comparable to that of Si_3N_4 and is roughly three times that of Ti metal [1]. This subset of Ti-, V-, and Cr-based MAX phases are also slightly refractory with elastic moduli slowly decreasing with the temperature [1]. In general, first-principles calculations of the elastic properties are in good agreement with experimental values [72].

While elastically the MAX phases share many of the features of their respective MX binaries, their mechanical behaviors are totally different. The large hardness values and the good wear resistance of the MX carbides and nitrides make them good candidates for abrasive materials or cutting tools. In strong contradistinction, the MAX phases are relatively soft, with Vickers hardness values ranging from 2 to 8 GPa, and are impressively readily machinable. Remarkably, a simple hack-saw is enough to machine the MAX phases. This makes the most noticeable difference between the MAX phases and all the other stiff ceramic compounds. Additionally, they are damage-tolerant and their good mechanical properties are preserved even at high temperature $> 1000°C$ [64].

Since a couple of years now, it is well-established that the MAX phases all deform under compression via the nucleation of ripplocation boundaries that rapidly propagate away from the indenter in a wavelike manner, leading to kink- and shear-band formation [66, 67, 106, 107], as presented in Fig. 2.6(b). This deformation mechanism, observed using an experimental setup as presented in Fig. 2.6(a), has been extended to many other layered materials, including graphite (Fig. 2.6(d)), steel plates (Fig. 2.6(c)), and geological formations [67].

2.4.4 *Thermal properties*

Thermally, the MAX phases are comparable to their MX counterparts. They are all good thermal conductors, for the most part because they are good electrical conductors, with RT thermal conductivities ranging from 12 to 60 $Wm^{-1}K^{-1}$ [1]. In addition, the MAX phases are thermal-shock resistant and are quite refractory, making them good candidates for high-temperature applications. Some of the MAX phases have a

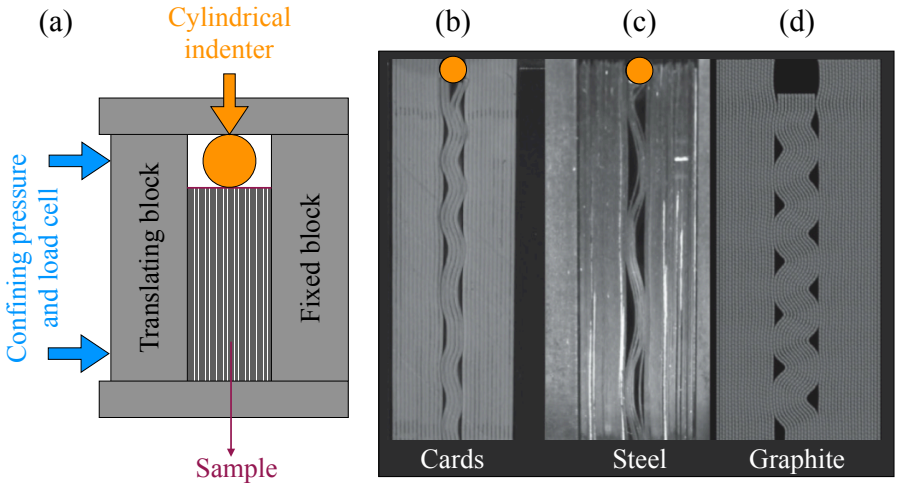

Figure 2.6: (b) Experimental setup with a cylindrical indenter used to observe ripplocation boundaries. Snapshots of ripplocations formed during edge-on loading onto (b) plastic card deck, (c) steel plates, and (d) graphite. The latter is a result of a molecular dynamics simulation. Adpated from [67].

high thermal expansion coefficient, ranging from $5 - 15 \times 10^{-6}\,\mathrm{K}^{-1}$ [1]. Both experimental and computational data agree on the anisotropy observed in the thermal properties of some MAX phases.

More information on the thermal and thermodynamic properties of the MAX phases can be found in Refs. [1, 73, 108], including the quantification of the specific heat, Debye's temperature, atomic displacement parameters, and thermal stability, from both theoretical and experimental approaches.

2.4.5 *Reactivity*

The last property discussed in this section refers to the reactivity of the MAX phases with their environment. In general, the MAX phases are quite stable and react very little with gasses or molecules in their surrounding.

In many cases, the preferred reaction path is that involving the diffusion of the A-group element into the surrounding medium, leaving behind the binary carbides [1]. In some cases, the A-group elements react with the surrounding medium to form intermetallic compounds. This implies the A element to be soluble in the surrounding medium, otherwise no reaction is observed.

Regarding the oxidation resistance of the MAX phases, they do not all behave in the same way, since the nature of the oxides that form mostly depends on the MAX composition. To be used in high-temperature applications, this oxide layer should be protective enough up to high temperature and not degrade with time. In this regard, the most promising MAX phases are the Al-containing ones that form a dense protective alumina (α-Al_2O_3) layer [109–115]. Especially, for the Ti_2AlC system, 8,000 consecutive thermal cycles from RT up to $\sim$ 1350°C result in the formation of a thin ($\sim$ 15 μm), adherent, and protective Al_2O_3 layer [110], which is beneficial for high-temperature structural and non-structural applications.

2.4.6 *Applications*

To summarize, a subset of MAX phases combine some of the best properties of metals and ceramics, including good electrical and thermal conductivities, high damage, thermal-shock, and oxidation resistances, as well as good mechanical properties. Most remarkable is the ease with which they can be machined. This exceptional set of properties observed in some MAX phases can predominantly be understood from their layered structures and the combination of strong metallic and covalent M−X bonds in contrast to the weaker M−A bonds.

Consequently, the MAX phases have been considered for numerous applications. For instance, their good electrical and thermal properties make them good candidates in electrical contacts, sensors, connectors, and many more. Additionally, owing to their excellent mechanical properties, some of the MAX phases find applications in micromechanical systems, protective coatings, and even in daily-life applications such as non-sticky pans and drilling tools. Finally, their excellent high-temperature properties and oxidation resistance make them promising candidates for high-temperature structural and non-structural applications, including heating elements and gas burning applications.

It is worth mentioning here that the list of properties and applications discussed in the previous sections is far from exhaustive and can be considered, at best, as a short overview of what has been reported in the literature in the past twenty years. More information can be found in Barsoum's reference book [1] and in a number of review articles [13, 116–119].

The material that will change the world is the one that will be made, not the one that can be made.

— **S. Curtarolo**

3 AN INTRODUCTION TO MXENES

Since the exfoliation of graphene in 2004 and the characterization of its outstanding properties [120, 121], two-dimensional (2D) materials have received considerable attention in the field of materials science and device processing. 2D crystals are a subclass of nanomaterials that exhibit peculiar physical properties due to the quantum confinement of their electrons [122]. Owing to their large surface areas combined with unique electronic, mechanical, and optical properties, 2D materials have been intensively studied for their possible use in electronic devices, composite materials, and energy-related applications [123–126]. Additionally, they can be employed as building blocks to obtain the so-called van der Waals heterostructures, known to exhibit unusual properties and new phenomena [124]. At present, the existence and stability of a few dozens of 2D crystals have been reported, including hexagonal boron nitride (*h*-BN) [127], transition-metal dichalcogenides (MoS_2, $MoSe_2$, WS_2, WSe_2, $NbSe_2$, ...) [128], thin oxide layers (TiO_2, MoO_3, WO_3, ...), silicene [129], germanene [130, 131], phosphorene [132], etc. Following the technique initially used to isolate a monolayer graphene from its three-dimensional (3D) counterpart, graphite, most 2D materials were obtained from the mechanical exfoliation of a parent 3D phase. This was feasible thanks to the weak van der Waals interlayer interactions intrinsically present in the parent phases.

3.1 DISCOVERY OF MXENES

In 2011, Naguib and coworkers [20] showed that 3D nanolaminate MAX phases with strong interlayer bonds could also be exfoliated into 2D crystals, using a combination of chemical etching and sonication techniques. In the initial work [20], a Ti_3AlC_2 powder sample was immersed in a 50 wt.% concentrated hydrofluoric acid (HF) solution for

2h at RT, resulting in the selective etching of Al planes, as depicted in Fig. 3.1. This successful etching of a strongly-bonded layered compound represents a major breakthrough in the synthesis of novel 2D systems.

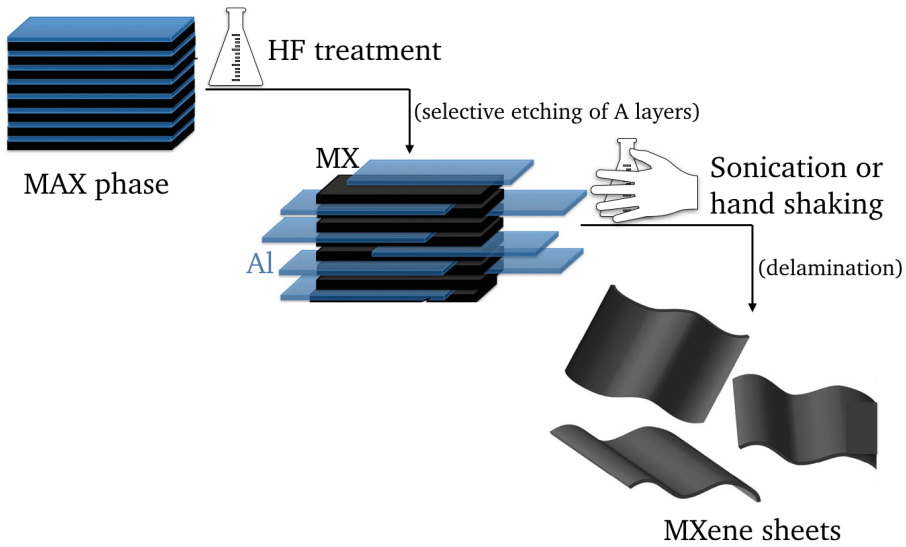

Figure 3.1: Schematic representation of the synthesis process of 2D MXenes, obtained from the selective etching of the Al planes from the parent 3D MAX phases when immersed in HF solution. Adapted from [133].

Since then, about 30 transition-metal carbides and nitrides, called MXenes, with different chemical compositions and orders have been reported [133–135], and up to 70 compositions have been predicted theoretically (see Fig. 3.2) [135, 136]. Depending on the 3D precursor, MXenes materials exhibit the formula $M_{n+1}X_nT_z$ ($n = 1, 2, 3$) or $M_{1.33}XT_z$, where M is an early transition metal (Sc, Y, Ti, Zr, Hf, V, Nb, Ta, Cr, Mo, or W), X represents either a carbon or a nitrogen atom, and T_z are termination groups such as $-$F, $-$OH, $=$O, or $-$Cl, mostly depending on the nature of the chemical environment [134]. This random distribution of the terminal groups was confirmed by electron-energy-loss spectroscopy in transmission electron microscopy [137], nuclear magnetic resonance spectroscopy [138, 139], and x-ray photoelectron spectroscopy [140] for various transition metal carbides. The thickness of the MXene monolayer is about 1 nm and varies with the value of the n index and the nature of the terminal groups [135].

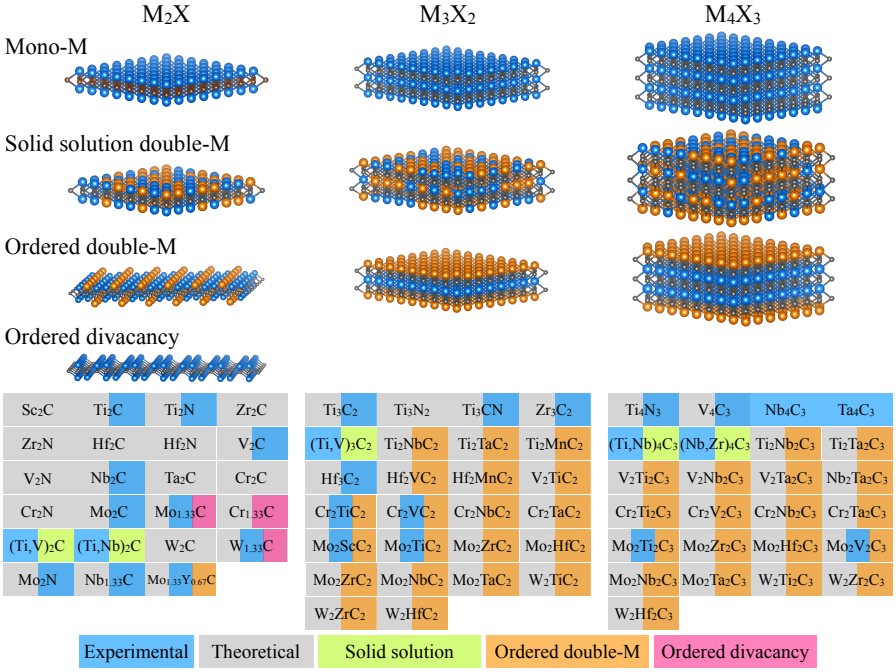

Figure 3.2: Chemical versatility of all existing MXenes systems, including conventional $M_{n+1}X_n$ ($n = 1, 2, 3$), double-M solid solutions, out-of-plane ordered, in-plane ordered double-M, and divacancy ordered MXene systems. M and X elements are respectively represented by blue/orange and grey small spheres. Adapted from [135].

3.2 SYNTHESIS OF MXENES

Most MXenes (25 out of 30) were obtained by selective etching of the Al planes from the MAX phases [141], as illustrated in Fig. 3.1. Since the etching process is kinetically controlled, it is worth mentioning that the etching conditions vary from one system to another, such that the solution concentration, immersion time, and temperature must be individually optimized to achieve a complete etching of the 3D phase into MXenes. To date, only one non-Al-containing MAX phase, Ti_3SiC_2, has been successfully etched into MXene [142]. It should also be noted that MXenes can be synthesized from non-MAX phase precursors, *e.g.*, Mo_2CT_z was obtained by etching Ga layers from Mo_2Ga_2C [143], $Zr_3C_2T_z$ by etching Al_3C_3 layers from $Zr_3Al_3C_5$ [144], and $Hf_3C_2T_z$ by etching $(Al,Si)_4C_4$ layers from $Hf_3(Al,Si)_4C_6$ [145]. Although HF treatment remains the most common synthesis path-

way, it is highly hazardous and often requires a delamination step through the intercalation of metallic cations or organic molecules to separate the MXene sheets. Consequently, various alternatives have been explored, including *in situ* formation of HF via the mixture of HCl and LiF solutions [146], NH_4HF_2 [137, 147], or electrochemical etching [148, 149]. More information can be found in two recent reviews by Verger *et al.* [150, 151].

Theoretically, *ab initio* molecular dynamics (AIMD) calculations have been used to simulate the etching process of Ti_3AlC_2 in HF solution (see Fig. 3.3) [152]. After the spontaneous dissociation of HF molecules, the F ions are attracted by the A and M elements, resulting in a weakening of the M−A bonds. As the HF concentration increases, the M−A bonds are broken and AlF_3 molecules are formed. Progressively, with the removal of the AlF_3 molecules, an interlayer gap is opened, facilitating further insertion of HF molecules. In contrast to F species, H ions are moderately attracted by the MAX phase and form H_2 molecules instead. In the end of the etching process, a fluorinated MXene is formed, together with AlF_3 and H_2 molecules. The preferential etching process and termination of the MXene surface can be summarized as:

$$Ti_3AlC_2 + 3HF \rightarrow Ti_3C_2 + AlF_3 + \frac{3}{2}H_2 \tag{3.1}$$

$$Ti_3C_2 + 2H_2O \rightarrow Ti_3C_2(OH)_2 + H_2 \tag{3.2}$$

$$Ti_3C_2 + 2HF \rightarrow Ti_3C_2F_2 + H_2 \tag{3.3}$$

Additional researches have concluded that the termination process is much more complex and might additionally include =O functional groups [20].

The mechanical exfoliation of the MAX phases into 2D MXenes has also been investigated [153]. Given that, in some cases, the bonding in the *ab*-plane is stronger than the one perpendicular to the plane ($c_{11} > c_{33}$) [154, 155], the theoretical breaking of the M−A bonds upon tensile stress has been revealed, highlighting the possibility to form 2D MXenes through the mechanical exfoliation of 3D MAX phases. This

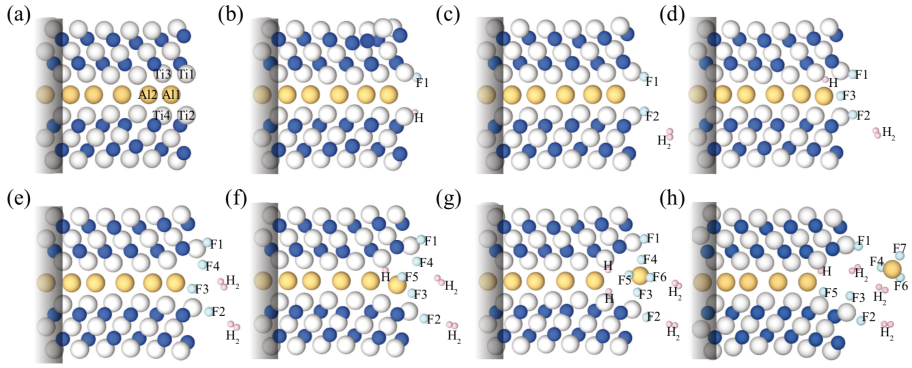

Figure 3.3: Schematic representation of the chemical exfoliation of Ti_3AlC_2 phase in the presence of HF acid, from AIMD simulation. The number of HF molecules increases from (a) zero, (b) one, (c) two, (d) three, (e) four, (f) five, (g) six, and (h) seven molecules. During the exfoliation process, AlF_3 and H_2 molecules are produced. Ti, Al, C, F, and H elements are respectively represented by small white, orange, blue, cyan, and pink spheres. Reprinted with permission from *ACS Applied Materials & Interfaces* 8, 2016 [152]. Copyright (2020) American Chemical Society.

theoretical prediction has been experimentally achieved in a very recent work. Gkountaras and coworkers [156] successfully reported on the mechanical exfoliation of four MAX phase single crystals, using the adhesive tape method. They coined the resulting crystals 'MAXenes', since the presence of the A element in the 2D flakes was confirmed. In contrast with chemically exfoliated flakes that are terminated by $-$F, $-$OH or $=$O anions, the mechanically exfoliated ones are not functionalized since the Al atoms remain. The thickness of the flakes could be reduced down to a monolayer. Most importantly, crystals that were to date chemically "unetchable", such as Cr_2AlC, Ti_2SnC, and even the ferromagnetic $Mo_4Ce_4Al_7C_3$, have been mechanically exfoliated. This opens the door to the formation of less defective crystals and the in-depth characterization of their electronic, magnetic, and optical properties.

3.3 STRUCTURE, VERSATILITY, AND STABILITY OF MXENES

The chemical variety of the MAX phases, with over 150 compositions reported so far [13, 119], explains the resulting chemical versatility in 2D MXenes. Since most of the newly discovered MAX phases are Al-based, the family of 2D MXenes is expected to further expand in the

near future. To date, a few o-MAX phases have already been exfoliated to form out-of-plane ordered double transition metal MXenes, *e.g.*, $Cr_2TiC_2T_z$ [54], $Mo_2TiC_2T_z$ [54], $Mo_2ScC_2T_Z$ [55], and $Mo_2Ti_2C_3T_z$ (Fig. 3.2) [54]. More interestingly, depending on the etching conditions, the i-MAX phases can be exfoliated to form two different types of MXenes. In-plane ordered double transition metal MXenes, such as $(Mo_{2/3}Y_{1/3})_2CT_z$ [157], are obtained from the selective etching of the Al layers in the parent MAX phase, while ordered divacancy MXenes, such as $Mo_{1.33}CT_z$ [19] and $W_{1.33}CT_z$ [55] result from the removal of the minority M element (Sc or Y) together with the Al element (Fig. 3.2). Additionally, Halim *et al.* [68] reported the exfoliation of the $(Nb_{2/3}Sc_{1/3})_2AlC$ solid solution into $Nb_{1.33}CT_z$ with disordered vacancies.

The structure of pristine MXenes can be constructed by removing the A element from the parent MAX phases. The structures of conventional pristine MXenes with the general formula $M_{n+1}X_n$ ($n = 1, 2, 3$) are depicted in Fig. 3.2. Consistent with the symmetry of the precursor MAX phases, the derived MXenes are hexagonal, with space group $P\overline{3}m1$ (#164). The atoms are arranged in a layered structure where the X layers are alternatively sandwiched between the M layers. Atomic Wyckoff sites and reduced coordinates of pristine $M_{n+1}X_n$ systems are listed in Table 3.1. Similarly, the o-MXenes with the general formula $M'_2M''X_2$ or $M'_2M''_2X_3$ also have an hexagonal symmetry (Fig. 3.2). In o-MXenes, the outer-layers are exclusively formed with the M′ element, while the inner-layer(s) consist(s) of M″ element. The exfoliation of the in-plane ordered MAX phases results either in 2D i-MXenes with the general formula $(M'_{2/3}M''_{1/3})_2X$, or in 2D $M_{1.33}X$ systems with ordered divacancies. Their pristine structures are illustrated in Fig. 3.2. The presence of two different transition metal elements in each layer involves a small out-of-plane shift of the larger M″ atoms from their usual positions, which, in turn, results in a change in the system symmetry from hexagonal to monoclinic [158].

As expected from the experimental observations, MXenes become thermodynamically more stable upon surface functionalization, and the stability is further enhanced for fully-terminated MXenes [136]. Based on the unit cell of pristine MXene, functionalized MXene structures are constructed, with the general formula $M_{n+1}X_nT_z$ with T = F, OH, and O terminations. As proposed by Khazaei *et al.* [136], different

Table 3.1: Atomic Wyckoff sites and idealized reduced coordinates of the $M_{n+1}X_n$ ($n = 1, 2, 3$) systems. Adpated from [1].

Atoms	Chemistry/Archetypical phase			
	Wyckoff	x	y	z_i (canonical)
M_2X				
M	$2d$	$2/3$	$1/3$	z
X	$1a$	0	0	0
M_3X_2				
M_I	$2d$	$1/3$	$2/3$	z
M_{II}	$1a$	0	0	0
X	$2d$	$2/3$	$1/3$	z
M_4AX_3				
M_I	$2c$	0	0	z
M_{II}	$2d$	$1/3$	$2/3$	z
X_I	$1a$	0	0	0
X_{II}	$2d$	$2/3$	$1/3$	z

functionalization models can be built depending on the relative positions of the terminal groups. Given that the properties of MXenes can strongly vary with the nature and position of the terminal groups, it is mandatory to systematically investigate all possible configurations and evaluate their respective stability, in order to find the ground-state structure. This will be further discussed in Chapter 7 with the case of V_2CT_z. Although there are much less reports on heterogeneously-terminated MXenes, Hu *et al.* [159] investigated the stability of Ti_2CT_z, $Ti_3C_2T_z$, and $Nb_4C_3T_z$ systems with respect to heterogeneous terminations (T = F, OH, and O). The most stable structure of all three systems corresponds to the fully O-terminated configuration, while the fully OH-terminated configuration is found to be the least energetically favorable.

3.4 PROPERTIES OF MXENES AND DERIVED APPLICATIONS

Since the discovery of MXenes in 2011, several experimental and theoretical studies have been conducted to shed light on their chemical and physical properties. The MXene properties are unique and combine high electrical and thermal conductivities, tunable electronic band

gap, various magnetic ordering, and high Young's modulus. In the following sections, we focus on the electronic, magnetic, vibrational, mechanical, and electrochemical properties of MXenes, predominantly predicted or confirmed by a first-principles approach.

3.4.1 *Electronic and transport properties*

Similar to the MAX phases, the pristine MXenes are predicted to be metallic. The states in the vicinity of the Fermi level correspond to M$-d$ states and are expected to give rise to electrical conductivity in the MXene systems. The electron density of states (DOS) near the Fermi level is predicted to be higher in the bare MXenes than in their parent MAX phases [160].

Upon functionalization, the electronic properties of MXenes vary from metallic to semiconducting, depending on the nature of the M, X, and T groups [136, 161]. While the majority of terminated MXenes retain their metallic character, Sc_2CT_2 [136], Ti_2CO_2 [136], Zr_2CO_2 [136], Hf_2CO_2 [136], Cr_2CF_2 [162], $Cr_2C(OH)_2$ [162], and $(M'_{2/3}M''_{1/3})_2CO_2$ (M′ = Mo, W; M″ = Sc, Y) [163] are predicted to be semiconductors, due to a shift of the Fermi level. Computed electronic band gaps are summarized in Ref. [164] and range from 0.25 to 3.9 eV. All semiconducting MXenes have an indirect band gap, except $Sc_2C(OH)_2$ that has a direct band gap at Γ. Given that both −F and −OH terminal groups can only accept one electron from the surface, they often affect the electronic properties in a similar way. In contrast, =O terminations accept two electrons from the surface [136]. A comprehensive study of the electronic properties of a dozen of M_2XT_2 systems can be found in Ref. [136]. Moreover, a materials database, aNANt, containing the structural and electronic band structure of more than 23,000 MXenes in their pristine and functionalized forms, has recently been released [165, 166].

Interestingly, some MXenes (and o-MXenes) with group VI transition metals (Cr, Mo, W) are predicted to be 2D topological insulators (TI), *i.e.*, to present an insulating gap in the bulk and gapless states at the edges. In these systems, the spin-orbit coupling (SOC) is found to significantly affect the electronic properties. For instance, without the SOC, M_2CO_2 (M = Mo, W, Cr) [167], $M'_2M''C_2O_2$ (M′ = Mo, W; M″ = Ti, Zr, Hf) [168–170], and $Ti_3N_2F_2$ [171] are semiconductors with a zero-energy gap or semimetals with compensated electron and hole Fermi

pockets. As depicted in Fig. 3.4(a) for $Mo_2HfC_2O_2$, the topmost valence band and the lowest conduction band only touch at the Γ point, around which the bands have a parabolic dispersion. These bands mostly correspond to the *d*-states of the M element. The inclusion of the SOC lifts the degeneracy of the bands at the Fermi level and the above-mentioned systems become insulators (see Fig. 3.4(b)), with band gaps evaluated within the hybrid functional HSE06 ranging from 0.05 to 0.47 eV [167–171]. In general, the energy band gap is larger as the SOC is larger [168]. In ordinary insulators, both sides of the edge states dispersion are connected to the same bulk (valence or conduction) band as shown in Fig. 3.4(d). In contrast, the edge states in TI presented in Fig. 3.4(e) connect the bulk valence and conduction bands and, in the particular case of $Mo_2HfC_2O_2$, they only touch at the M point (see Fig 3.4(c)). These edge states, which consist in pairs of states with opposite spins propagating in opposite directions, are perfectly conducting channels (see Fig. 3.4(f)). Large band gap TI are appropriate systems to observe quantum spin Hall effect at RT and above and are therefore potential candidates for electronic and spintronic device applications. It should be noted that other MXenes such as $Sc_2C(OH)_2$ and $M_3N_2F_2$ (M = Zr, Hf) become TI by applying an electric field [172] or a tensile strain of a few percents [171], respectively.

It is important to recall here that most exotic features discussed in this section are theoretical predictions for perfect, defect-free, pristine or homogeneously-terminated MXenes, which are thus far from the experimentally-grown samples. Consequently, in order to observe semiconducting and topological insulating states in MXenes, more work is needed on the experimental side to control the surface termination of MXenes and find new routes to create homogeneously-functionalized MXenes. So far, only the semiconductor-like behavior of Ti_2CO_2 has been observed experimentally, with a band gap of 80 meV [173], which is much smaller than the theoretical prediction.

Regarding the electronic transport in 2D MXenes, coherent transport calculations within the non-equilibrium Green's functions (NEGF) formalism have demonstrated that the metallic MXenes are highly conductive [174, 175]. It was also determined that the electrical character and conductivity of MXenes strongly depend on the surface terminations. For instance, the presence of nearly free electron (NFE) states in the electronic band structure of several OH-terminated MXenes has been evidenced [174]. In particular, in $Ti_2C(OH)_2$, $Zr_2C(OH)_2$,

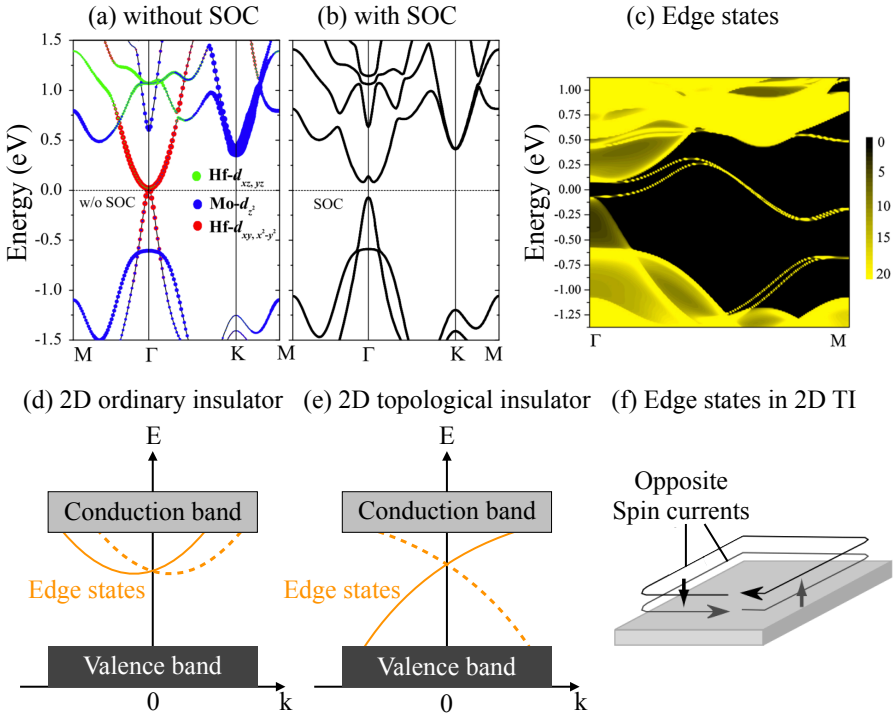

Figure 3.4: Electronic band structure of $Mo_2HfC_2O_2$ computed (a) without SOC and (b) with SOC. Upon including SOC, a gap opens at the Γ point. (c) Edge states connecting the bulk valence and conduction bands and only touching at the M point. General description of the edge states in (d) ordinary insulators and (e) topological insulators. (f) In the latter, the edge states consist in opposite spin currents. Reprinted with permission from *Nano Letters* 16, 2016 [169]. Copyright (2020) American Chemical Society.

$Zr_2N(OH)_2$, $Hf_2C(OH)_2$, $Hf_2N(OH)_2$, $Nb_2C(OH)_2$, and $Ta_2C(OH)_2$ MXenes, the NFE states are close to the Fermi level and their partial occupation contributes to a higher electron conductivity, without atomic scattering with the surface vibrations [174]. In contrast, the NFE states in graphene, *h*-BN, and MoS_2 are located at high energies above the Fermi level, and remain therefore unoccupied. Hu and coworkers [176] reported on the intrinsic electronic conductivity of stacked multilayered $Ti_3C_2(OH)_2$ MXenes. The theoretical calculations of the electronic band structure, band dispersions, and Fermi surface indicate that the charge carriers are preferentially transferred in the plane rather than out-of-plane. Said otherwise, the electronic conduction in stacked $Ti_3C_2(OH)_2$ MXenes is highly anisotropic.

Semiconducting materials are usually good candidates for electronic devices or thermoelectric applications. In this regard, the thermal and thermoelectric properties of a series of semiconducting MXenes have been studied.

The thermoelectric efficiency can be evaluated through the figure of merit zT given by:

$$zT = \frac{S^2\sigma}{\kappa_e + \kappa_l} T \tag{3.4}$$

where S, σ, $\kappa_e + \kappa_l$ are respectively the Seebeck coefficient, electrical conductivity, and thermal conductivity with the electronic κ_e and lattice κ_l contributions. Using the Boltzmann theory, Khazaei *et al.* [136] reported the Seebeck coefficient of the semiconducting Ti_2CO_2 and $Sc_2C(OH)_2$ systems, being as high as 1140 and 2200 μVK^{-1} at 100 K. The thermoelectric performance of Sc_2C-based MXenes has been investigated by Kumar *et al.* [177], based on the explicit calculation of σ, κ_e, and κ_l, using the Boltzmann transport equation for electrons and phonons, respectively. At RT, Seebeck coefficients of 1022, 1036, and 372 μVK^{-1} are obtained, respectively for O-, F-, and OH-terminated Sc_2CT_2 systems. In comparison, Seebeck coefficients of 427 and 350 μVK^{-1} are obtained for 2D $MoSe_2$ and WSe_2, respectively [177]. Power factors, given by $S^2\sigma$, in the range of $1 - 5 \times 10^{-3}\,Wm^{-1}K^{-2}$ are found for the Sc_2CT_2 systems, which is comparable to known thermoelectric materials such as PbTe and Bi_2Te_3 [178, 179]. The lattice thermal conductivities are of 59, 36, and 10 $Wm^{-1}K^{-1}$, respectively for O-, F-, and OH-terminated Sc_2CT_2, while the electronic thermal conductivities range from 3 to 6 $Wm^{-1}K^{-1}$. The quite low thermal conductivity in the $Sc_2C(OH)_2$ system with respect to other semiconducting MXenes leads to a maximal figure of merit of 0.1 at 300 K up to 0.5 at 900 K. The value of the figure of merit could be significantly improved by further reducing the thermal conductivity down to values around 1 to 5 $Wm^{-1}K^{-1}$, which are typical values of efficient thermoelectric materials reported in the literature [180].

Eventually, Zha *et al.* [181] computed the thermal conductivity, thermal expansion coefficient, electronic band gap, and charge carrier mobility of M_2CO_2 (M = Ti, Zr, Hf) systems, by means of DFT, DFPT, and the Klemens theory. In all three systems, the thermal conductivity is found to be highly anisotropic. Among the three compounds, Hf_2CO_2 possesses the highest thermal conductivity of about 86 $Wm^{-1}K^{-1}$ and 36 $Wm^{-1}K^{-1}$ at 300 K for a 5 μm-large crystal, along the armchair and

zigzag direction, respectively [181]. Additionally, it has a low thermal expansion coefficient which guarantees its good structural stability at all temperatures. Given the low thermal expansion coefficient and high thermal conductivity values, Hf_2CO_2 is considered as a promising 2D materials for nanoelectronics.

3.4.2 *Magnetic properties*

A magnetic ground state has been predicted for a large number of MAX phases based on a subtle combination of theoretical and experimental studies [74, 75]. To date, unfortunately, none of them has been etched into 2D MXenes, except Cr_2TiAlC_2 [54]. Nevertheless, the magnetic properties of MXenes have been intensively studied from first-principles calculations. Although the majority of the pristine MXenes are non-magnetic (NM), some of them such as Ti_2C, Ti_2N, Cr_2C, Mn_2C, and Mn_2N have ferromagnetic (FM) ground-states, while V_2C and Cr_2N are antiferromagnetic (AFM). Because of the surface terminations that are inevitably introduced during the synthesis process, none of the magnetic pristine MXenes has been realized in experiment. Interestingly, some functionalized MXenes have been predicted to preserve a magnetic moment, including Ti_2NO_2 [182], Cr_2NO_2 [139], and all Mn_2CT_2 [183] and Mn_2NT_2 [182] systems, regardless of surface functionalization. Magnetic moments up to $3\,\mu_B$ have been predicted in these systems that might retain their magnetism up to near RT. Notwithstanding, large magnetic moments may be induced in 2D MXenes via tensile/compressive strain or via doping with Cr/Mn elements [135, 184, 185]. Eventually, NM, AFM, and FM magnetic behaviors are also found for o-MXenes systems, depending on their composition [186, 187].

Recently, half-metallicity has been predicted in magnetic MXenes. Half-metallicity involves that one spin-channel is metallic, while the other one is insulating [188], resulting in a conductivity solely ensured by a single spin charge carrier channel and a 100% spin-polarization of the electrons at the Fermi level [182]. Si and coworkers [162] first predicted half-metallicity in Cr_2C, with a substantial minority spin gap of 2.85 eV (see Fig. 3.5), computed within HSE. Subsequently, near-half-metallicity has been predicted in Ti_2C and Ti_2N systems, for which true half-metallicity is only observed under biaxial strain [189]. In all three systems, half-metallicity disappears upon functionalization, together with the ferromagnetism. Upon surface passivation with oxygen, Cr_2N

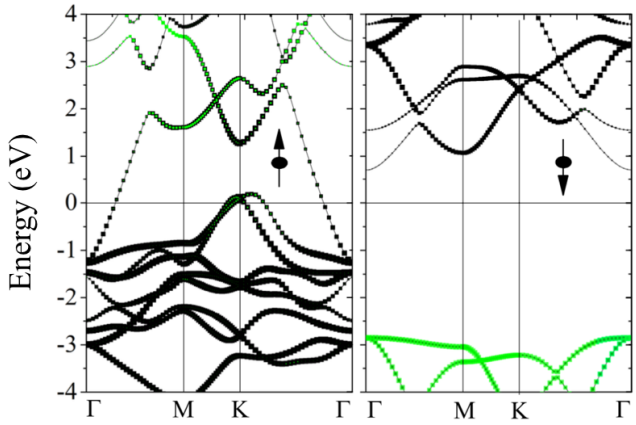

Figure 3.5: Electronic band structure of Cr_2C MXene highlighting its half-metallicity, with a metallic majority spin channel (left panel) and an insulating minority spin channel with a gap of 2.85 eV (right panel). Black and green squares represent the contributions of Cr-*d* and Cr-*p* orbitals respectively. Reprinted with permission from *ACS Applied Materials & Interfaces* 7, 2015 [162]. Copyright (2020) American Chemical Society.

becomes a half-metallic ferromagnetic system, with a computed minority spin gap of 2.79 eV (3.88 eV) within GGA (HSE06) [139]. Similarly, half-metallicity is also predicted in Mn_2CF_2 [183]. It should be noted that all these materials, *i.e.*, Cr_2C, Cr_2NO_2, and Mn_2CF_2, exhibit half-metallicity for none or specific surface terminations, which is currently difficult to achieve experimentally. In contrast, a half-metallic behavior was found in Mn_2NT_2 systems for all kind of surface terminations ($-$F, $-$OH, and $=$O) [182], suggesting great promise for these systems to be used in spintronic devices such as spin filters, spin injectors, and magnetic sensors [182].

Besides the symmetrically-terminated MXenes, a new class of asymetrically-functionalized MXenes, called Janus MXenes, has been intensively studied [190]. As depicted in Fig. 3.6(a), Janus MXenes have distinct terminations on their opposite surfaces. Both intrinsic FM and AFM ordering have been predicted in Janus MXenes, highlighting the possibility to effectively tune the magnetic behavior based on the selected pair of chemical terminations. For instance, it is predicted that all Cr_2CTT' (T,T′ = H, F, Cl, Br, OH) systems are AFM semiconductors with Neel temperatures of $\sim$ 400 K [190]. More precisely, as evidenced in Fig. 3.6(a), they are bipolar magnetic semiconductors with zero-magnetization, as the valence and

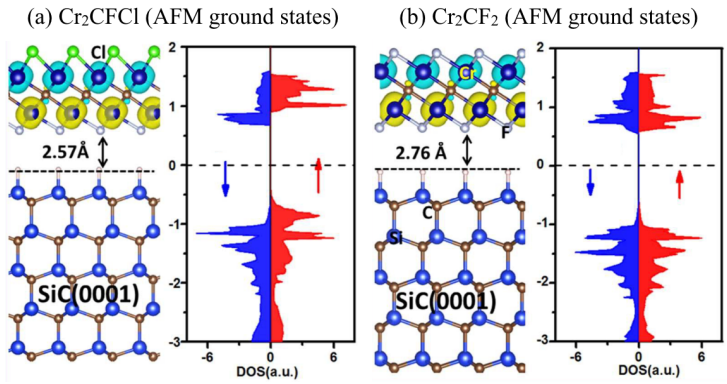

Figure 3.6: Atomic structures and electronic DOS of (a) Cr_2CFCl janus MXene and (b) Cr_2CF_2 MXene, deposited on SiC(0001). Both systems are AFM, with the spin-polarized charge density represented in cyan and yellow for the spin up and spin down, respectively. Reprinted with permission from *Journal of Materials Chemistry C* 4 (2016) [190].

conduction bands are made up of opposite spin channels that are fully compensated [190]. This makes the most noticeable difference between symmetrically-functionalized Cr_2CF_2 with a symmetrical distribution and the asymmetrically-functionalized Cr_2CFCl, as illustrated in Figs. 3.6(b) and 3.6(a), respectively. Similar bipolar magnetic features are also predicted in V-, Mn-, and Ti-based Janus MXenes [135].

3.4.3 *Vibrational properties*

The phonon spectra of various pristine and terminated M_2XT_2 (M = Sc, Ti, Zr, Mo, Hf; X = C, N; T = F, O) systems have been computed confirming some specific stabilities [191]. Due to the similar crystal structure and chemical bonding of M_2C systems, many features are common to all of them, and are even shared by higher-order M_3C_2 and M_4C_3 MXenes [192]. The phonon dispersions have three acoustic modes; two of them exhibit a linear dispersion near Γ and correspond to in-plane rigid-body motions. In contrast, the third acoustic mode corresponding to out-of-plane vibration has a quadratic dispersion close to Γ and a lower energy in the rest of the spectrum. Additionally, a wide phonon band gap is observed separating the low-frequency vibrations of the M element from the high-frequency vibrations of the lighter C element. Upon functionalization, this band gap is filled by additional optical modes [193].

Basics of solid-state physics inform us that $3N_{at}$ phonon modes are observed in a system made of N_{at} atoms. In addition to the 3 acoustic modes, there are therefore $3N_{at} - 3$ optical modes. Based on the crystal structure of the M_2X MXene including 3 atoms, the optical modes at the zone center of the Brillouin zone can be classified with the following irreducible representation:

$$\Gamma(M_2X) = \underbrace{A_{1g} + E_g}_{\text{Raman}} + \underbrace{A_{2u} + E_u}_{\text{IR}} \tag{3.5}$$

where the E-symmetry modes (E_g and E_u) are doubly-degenerate. In the same way, the optical modes of M_3X_2 and M_4X_3 systems with respectively 5 and 7 atoms in their unit cells, have the following irreducible representations:

$$\Gamma(M_3X_2) = \underbrace{2A_{1g} + 2E_g}_{\text{Raman}} + \underbrace{2A_{2u} + 2E_u}_{\text{IR}} \tag{3.6}$$

$$\Gamma(M_4X_3) = \underbrace{3A_{1g} + 3E_g}_{\text{Raman}} + \underbrace{3A_{2u} + 3E_u}_{\text{IR}} \tag{3.7}$$

Upon functionalization, the addition of 2 atoms in the unit cell (for F_2 and O_2 terminations) involves the addition of 6 optical modes, namely $A_{1g} + E_g + A_{2u} + E_u$, and the addition of 4 atoms via $(OH)_2$ terminations results in 12 additional optical modes. Making good use of the group theory, the Raman and infrared (IR) activity of the modes can be predicted. Our study on the vibrational properties of V_2CT_z systems [193] has greatly contributed to the understanding of the vibrational properties in the M_2XT_z MXenes in general. More details on the predicted Raman mode wavenumbers and experimental Raman spectra can be found in Chapter 7.

3.4.4 *Mechanical properties*

Kurtoglu and coworkers [194] first reported on the elastic constants (c_{11}) of a series of pristine MXenes. In average, the elastic constants of 2D MXenes are twice larger than those of the corresponding MAX phases. In addition, in most cases, nitrides are stiffer than the carbide counterparts, as presented in Fig. 3.7(a) [195]. This might be explained by the additional electron provided by N atoms with respect to C

atoms, and hence the formation of stronger M−X bonds in nitride compounds [191, 196]. Based on the c_{11} values, 2D transition metal carbides tend to get stiffer as the atomic mass of the M element increases (see Fig. 3.7(b)). Further computational studies have investigated the effect of terminations on the elastic properties of MXenes [194, 197]. The presence of terminal groups drastically reduces the c_{11} values of all MXenes, as evidenced in Fig. 3.7(b). The general trend is that the smaller lattice parameters in the O-terminated systems result in stronger MXenes with respect to those terminated with −F or −OH groups [197]. The thickness dependence of the elastic constants has also been studied through DFT and AIMD calculations, both predicting M_2X systems stiffer than their M_3X_2 and M_4X_3 counterparts (see Fig. 3.7(a)) [195, 198]. This may be due to the strengthening of the M−X bonds, when the Al atoms are selectively etched and the electron density is further concentrated within the $M_{n+1}X_n$ layers, which is more important in the M_2X systems with respect to the M_3X_2 and M_4X_3 ones [133]. Experimentally, the elastic response of a single layer $Ti_3C_2T_z$ has been measured through nanoindentation technique with an AFM tip [199]. A Young's modulus of 330 ± 30 GPa was found, which is lower than the one of graphene (1000 ± 100 GPa) and *h*-BN (870 ± 70 GPa), but is the highest one reported for a solution-processed 2D material, *e.g.*, MoS_2: 270 ± 100 GPa and graphene oxide: 210 ± 20 GPa [199]. Despite lower Young's modulus than other 2D materials, the higher bending stiffness, hydrophilicity, and high negative zeta potential of MXenes (making MXene colloids highly-stable) make them promising candidates in composites with polymers, oxides, or carbon nanotubes. Experimentally, many polymer-MXene composites have been realized, with enhanced tensile strength, elastic moduli, thermal and electrical conductivities, and electrochemical capacitance, thanks to the presence of 2D MXenes [200, 201].

3.4.5 *Electrochemical properties*

The development of safe and powerful devices is becoming increasingly important for use in a wide variety of applications including smart electronics, electric, and hybrid cars, and storage of renewable energy [146, 202]. In the field of energy storage, two main families of materials arise. On one hand, the electrical double-layer capacitors (EDLCs) store electrical energy via the formation of an electrical double layer at the electrode/electrolyte interface. Their capacitance is pro-

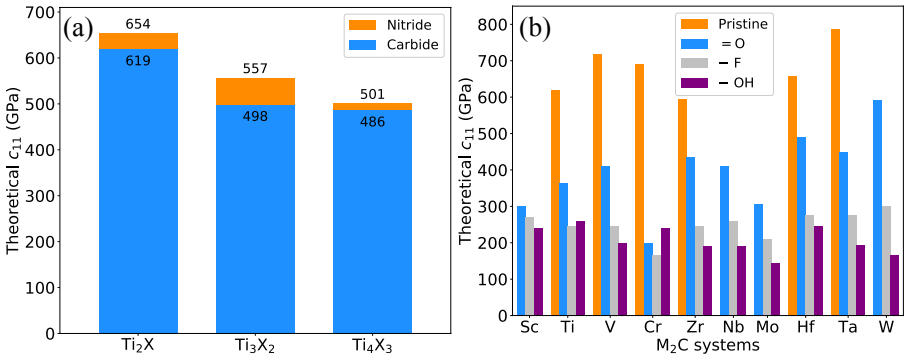

Figure 3.7: Comparison of the theoretical elastic constants c_{11} of (a) pristine $Ti_{n+1}X_n$ carbides and nitrides with $n = 1, 2, 3$, and (b) pristine and functionalized M_2CT_2 systems with T = O, F, and OH. Adapted from [197].

portional to the electrode's surface area available for the ion adsorption [203]. Batteries, on the other hand, rely on electron transfer to metal centers that is made possible by the intercalation of ions such as Li^+ and Na^+ [204]. Electrochemical capacitors (including pseudocapacitors and supercapacitors), which occupy a middle ground between EDLCs and batteries, use either ion adsorption or fast surface redox mechanisms that allow them to store much more energy than EDLCs, within a charging time of seconds to minutes, *i.e.*, much faster than batteries do [204].

In this context, 2D MXenes have shown great promise in energy storage applications, which can be explained by their high electronic conductivity, their redox active surface generated during the etching process, and their 2D morphology optimal for fast ion transport and intercalation [203]. About 50% of the publications on MXenes are on energy-related topics and mostly include experimental works. Nevertheless, the success of MXenes in electrodes for batteries and electrochemical capacitors has also been investigated theoretically, considering MXene systems in both their pristine and functionalized forms.

Mono and multivalent ion batteries

The energy stored in the battery is the product of its operating voltage and its electrochemical capacity [205]. The electrochemical capac-

ity, expressed in $mAhg^{-1}$, basically depends on the amount of charges exchanged between the electrodes and their formula weight:

$$C_A = \frac{n_A Z_A F}{M_{material} + n_A M_A} \tag{3.8}$$

where n_A is the number of adsorbed metal adatoms, Z_A is the valence state of the metal adatoms, F is the Faraday constant, $M_{material}$ is the molar weight of the electrode material, and M_A is the molar weight of metal adatoms. In common commercial Li ion batteries (LIBs), the cathode consists of $LiCoO_2$ spinel compound, while the anode is made of graphite (LiC_6) which has a limited storage capacity of 330 $mAhg^{-1}$ (372 $mAhg^{-1}$, theoretically). The most promising MXenes in battery applications thus correspond to those with suitable anode voltage ($0.2 - 1.0$ V) and high gravimetric capacity (> 372 $mAhg^{-1}$). In the initial report of 2D MXene, a Li capacity of 320 $mAhg^{-1}$ was predicted for the pristine Ti_3C_2 system [20]. Soon afterwards, theoretical simulations of Li storage predicted a diffusion barrier of 0.07 eV in pristine Ti_3C_2 [206], which is much lower than the diffusion barrier in graphite of 0.3 eV [207]. However, in functionalized $Ti_3C_2T_2$, the presence of $-$F, $-$OH, and $=$O groups blocks the Li transport and the computed diffusion barriers become as large as 0.36 [206], 1.02 [206], and 0.62 eV [208], respectively. Since then, the capacities of several 2D MXenes have been predicted theoretically [209, 210] and are presented in Fig. 3.8(a), revealing several trends. First, M_2X systems with light transition metal elements exhibit the highest gravimetric capacities, resulting from their low molar weight. The theoretical Li capacity values of pristine M_2X (M = Sc, Ti, V, Cr) systems are greater than 400 $mAhg^{-1}$. The surface terminations can affect the electrochemical properties of MXenes; O terminations being the most favorable in terms of capacity [209]. From Eq. 3.8, a method to improve the capacity is by transferring more than one electron per ion. This can be achieved by using multivalent cations (Mg^{2+}, Ca^{2+}, Al^{3+}, etc.) instead of monovalent ones (Li^+, Na^+, K^+). The theoretical capacities of multivalent metal ions are shown in Figs. 3.8(a) and 3.8(b), and clearly outperform the values for carbon-based electrodes.

Experimentally, the predicted trends are not always verified due to the complex nature of ion storage, and the highest Li capacity has been reported for V_2CT_z systems (280 $mAhg^{-1}$ at a cycling rate of 1 C and 125 $mAhg^{-1}$ at 10 C). To get in-depth understanding of the ion storage process, Xie and coworkers [210] computed the ion adsorption energies

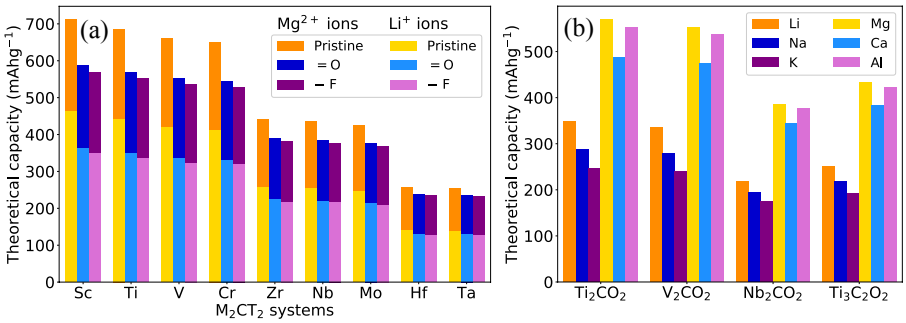

Figure 3.8: (a) Theoretical gravimetric Li and Mg capacities of various M_2CT_2 systems in their pristine, O-, and F-terminated forms, and (b) theoretical gravimetric capacities of monovalent (Li, Na, K) and multivalent (Mg, Ca, Al) metal ions in oxygen-terminated MXenes. The data in (a) are obtained from equation 3.8 considering a full surface coverage (adsorption of the ions), while data in (b) take partial coverage into account, resulting from a systematic study of the ion adsorption energies. Adapted from [209] and [210].

of pristine and O-terminated Ti_2C, V_2C, Nb_2C, and Ti_3C_2 MXenes, considering various metallic ions (Li^+, Na^+, K^+, Mg^{2+}, Ca^{2+}, and Al^{3+}). In some cases (*e.g.*, Al^{3+} ions), positive adsorption energies were obtained before attaining the full coverage of the MXene surface, hence resulting in a favorable partial surface coverage (*e.g.*, of 2/3 for Al^{+3} ions). This partial coverage of the MXene surface is considered in the computed gravimetric capacities presented in Fig. 3.8(b) [210].

Electrochemical capacitors

The 2D morphology of MXenes allows for electrochemical intercalation of large organic molecules or metal ions, which can participate in energy storage. To date, the best volumetric capacitance of carbon-based electrodes is around 300 Fcm^{-3} [211], while volumetric capacitances exceeding 900 Fcm^{-3} have been reported for free-standing $Ti_3C_2T_z$ MXene electrodes [146, 203, 212]. MXenes also exhibit excellent cyclability, with no change in capacitance reported after 10,000 cycles for $Ti_3C_2T_z$ electrodes [146]. Experimentally, several factors can affect the volumetric capacitance of MXenes, including their surface chemistry, hence the synthesis process, and the nature of the electrolyte solution (basic, neutral, or acidic), resulting in different charge-discharge mechanisms. Recent experimental works also pointed out the beneficial effect of divancy ordering in $Mo_{1.33}CT_z$ with a volumetric capacitance

of $\sim$ 1100 Fcm^{-3}, compared to 700 Fcm^{-3} obtained in Mo_2CT_z [19]. A capacitance up to 1500 Fcm^{-3} was even revealed in the ordered $(Mo_{2/3}Y_{1/3})_2CT_z$ MXene used as an electrode in a supercapacitor with basic KOH electrolyte [157]. Promising performances as supercapacitors were finally predicted in MXene-based hybrid materials, polymer-MXene composites, and hydrogels, with volumetric capacitances exceeding 1550 Fcm^{-3} [157, 201, 203, 213–217].

3.4.6 *Other properties and applications*

Even though energy storage has been the first and most studied application for MXenes, there are several other applications where MXenes have shown great promise. Anasori *et al.* [141] reported a comprehensive survey with most of the energy- and non-energy-related applications for MXenes investigated so far. In the search for new potential applications, first-principles calculations are adequate tools, usually less expensive and time-demanding than experimental works.

Thin films of $Ti_3C_2T_z$ are transparent and have a transmission of 97% of visible light per nanometer thickness [147, 218, 219], which is close to the 97.7% transmission of monolayer graphene [220]. Thin films of M_2CT_z (M = Ti, V) are twice as transparent and, given their high electrical conductivity, they are considered as promising materials for transparent conductive electrodes [221, 222]. Similarly to most of the MXenes properties, their optical behavior is affected upon surface termination [175, 223–226] and can be tuned by electrochemical ion intercalation [227, 228].

Another exciting physical property of MXenes is their high electromagnetic interference (EMI) shielding [229]. Thin films of $Ti_3C_2T_z$, $Mo_2TiC_2T_z$, and $Mo_2Ti_2C_3T_z$ showed EMI shielding capacities higher than graphene and other carbon-based materials with comparable thickness [229, 230]. Combined with their good flexibility and lightweight, MXenes are thus promising 2D materials for EMI electronic devices.

MXenes have also shown suitable affinity with various gasses, including CO_2, ethanol, ammonia, etc. [231, 232]. In addition, first-principles calculations have predicted efficient physisorption capability of Ti_2C with respect to several gas molecules. Consequenly, their potential use as gas sensors has also been pointed out [233].

MXenes performances have been tested in several other applications, such as hydrogen storage media [234–237], sensors and mem-

branes [233, 238, 239], biomedical engineering [238, 240–242], thermoelectric materials [177, 181, 243, 244], structural composites [200], catalysts [245], electrocatalysts [246, 247], photocatalysts [247, 248], water purificatants [249, 250], organic photovoltaics [251], flexible photovoltaics [252], and many more.

If you can't explain it simply, you don't understand it well enough.

— A. Einstein

4 THEORY

4.1 INTRODUCTION

The end of the 20th century marks the beginning of the computational investigation, a new powerful approach in materials science allowing to efficiently predict and characterize materials properties. Moreover, first-principles calculations not only allow to investigate all properties of a given material, but also enable the design of new materials with optimized composition with the aim to achieve specific properties required for a given application [253]. Using a computational approach offers several key advantages over laboratory work, as calculations are usually less time-consuming and expensive than experiments, and allow to reach good level of control on the structure and the potential external constraints [205]. Moreover, computations provide insight into fundamental processes that can sometimes not be accessible otherwise.

Since the first implementation of the density functional theory (DFT) in 1964 [254, 255], remarkable advances in the computational research field have been achieved. The combination of more accurate *ab initio* approaches (DFT+U, hybrid functionals), more powerful computational resources (super-computers), and the apparition of several open-source packages for DFT calculations (*e.g.*, Abinit, Quantum Espresso, Siesta, CP2K, Elk, Fleur) has led to tremendous progress in materials science, including computer-assisted design of new materials [205, 253, 256], rapid screening of large materials databases for targeted applications [256], and understanding of various processes on the atomic scales [257].

Today, many essential materials properties can be accurately computed through *ab initio* methods at a reasonable cost.

This chapter aims to quickly recall the foundations required to understand the electronic, dynamical, and transport properties in solids.

At first, Section 4.2 recalls the basics of quantum mechanics, starting from the many-body Schrödinger equation and introducing various approximations required to solve the many-body problem, namely the Born-Oppenheimer approximation and the independent-electron (Hartree and Hartree-Fock) approximations.

Section 4.3 is devoted to the density functional theory and presents the basic theorems of Hohenberg and Kohn and the derived Kohn-Sham equations. A few examples of approximate functionals for exchange and correlation are also presented.

In Section 4.4, basic notions of solid state theory are introduced, including plane-wave basis sets, k-point sampling of the Brillouin zone, and pseudopotentials.

A very complete and detailed introduction to basic theory and methods for electronic structure can be found in the reference book *"Electronic structure: basic theory and practical methods"* by R. Martin [258], which was used to write Sections 4.2- 4.4 of this thesis manuscript.

The formalism of density functional perturbation theory (DFPT) required to calculate the response functions of a system is introduced in Section 4.5, together with the equations used to compute dynamical matrix, phonons, and elastic constants of a system.

Eventually, Section 4.7 is devoted to the Boltzmann transport equation (BTE) for both electrons and phonons, with the aim to compute the thermal conductivity.

4.2 BASICS OF QUANTUM MECHANICS

4.2.1 *The Schrödinger equation and the many-body problem*

A system constituted of N_e electrons and N_N nuclei is completely quantum-mechanically described by its wave function Ψ:

$$\Psi = \Psi\left(r_1, r_2, \ldots, r_{N_e}, R_1, R_2, \ldots, R_{N_N}\right) \tag{4.1}$$

where r_i $(i = 1, \ldots, N_e)$ and R_α $(\alpha = 1, \ldots, N_N)$ are the coordinates of electrons and nuclei, respectively. The square of the amplitude of this wave function gives the density of probability to find a particular configuration of electrons and nuclei. The accurate description of a non-relativistic system requires a quantum approach and the resolution of

the so-called Schrödinger equation. The stationary Schrödinger equation is given by:

$$\widehat{H}\Psi = E\Psi \tag{4.2}$$

where $\widehat{H}$ is the hamiltonian operator defined by:

$$\widehat{H} = \widehat{T}_e + \widehat{T}_N + \widehat{V}_{ee} + \widehat{V}_{eN} + \widehat{V}_{NN} \tag{4.3}$$

Adopting Hartree atomic units $\hbar = m_e = e = \frac{4\pi}{\epsilon_0} = 1$, these operators may be written in their simplest form: the electronic kinetic energy operator $\widehat{T}_e$ is given by:

$$\widehat{T}_e = \sum_i -\frac{1}{2}\nabla_i^2 \tag{4.4}$$

the nuclear kinetic energy operator, by:

$$\widehat{T}_N = \sum_\alpha -\frac{1}{2M_\alpha}\nabla_\alpha^2 \tag{4.5}$$

the electron-electron Coulomb interaction, by:

$$\widehat{V}_{ee} = \frac{1}{2}\sum_{i\neq j}\frac{1}{|r_i - r_j|} \tag{4.6}$$

the electron-nucleus Coulomb interaction, by:

$$\widehat{V}_{eN} = \sum_i\sum_\alpha \frac{-Z_\alpha}{|r_i - R_\alpha|} \tag{4.7}$$

and the nucleus-nucleus Coulomb interaction, by:

$$\widehat{V}_{NN} = \frac{1}{2}\sum_{\alpha\neq\beta}\frac{Z_\alpha Z_\beta}{|R_\alpha - R_\beta|} \tag{4.8}$$

4.2.2 *The Born-Oppenheimer approximation*

As the nuclei are several thousand times heavier, hence slower, than the electrons, the Born-Oppenheimer approximation states that the nuclei positions are fixed and that electrons almost instantaneously conform to the nuclei configuration. This approach allows to split the wave function of the system into its electronic and nuclear components. Therefore, for any fixed nuclei configuration of the system, the Schrödinger

equation for electrons can be solved, considering the following hamiltonian, in which the positions of the nuclei $\{R\}$ are parameters:

$$\widehat{H}^e_{\{R\}} = \widehat{T}_e + \widehat{V}_{ee} + \widehat{V}_{eN} \tag{4.9}$$

The nucleus-electron Coulomb interaction is often denoted as the external potential $V_{\text{ext}}(r_i)$ and the Schrödinger equation simplifies to:

$$\left(-\frac{1}{2}\sum_i \nabla_i^2 + \sum_i V_{\text{ext}}(r_i) + \frac{1}{2}\sum_{i\neq j}\frac{1}{|r_i - r_j|}\right)\Psi^e = E^e_{\{R\}}\Psi^e \tag{4.10}$$

4.2.3 *Independent-electron approximations*

In practice, for systems with more than two electrons, Eq. 4.10 cannot be solved analytically as the problem becomes too complex due to the treatment of the electron-electron Coulomb interaction $\widehat{V}_{ee}$. A first approximation consists in neglecting it and considering non-interacting electrons. Equation 4.10 simplifies to:

$$\left(-\frac{1}{2}\sum_i \nabla_i^2 + \sum_i V_{\text{ext}}(r_i)\right)\Psi^e = E^e_{\{R\}}\Psi^e \tag{4.11}$$

Given the simplification of equations to solve, it is interesting to keep the formalism of independent electrons while reintroducing some interaction between electrons. It can be done by introducing a potential judiciously selected $\widehat{U}(r)$:

$$\widehat{H}^e_{\{R\}} = -\frac{1}{2}\nabla_r^2 + V_{\text{ext}}(r_i) + \widehat{U}(r) \tag{4.12}$$

$$= -\frac{1}{2}\nabla_r^2 + V_{\text{eff}}(r) \tag{4.13}$$

where $V_{\text{eff}}(r)$ is defined as an effective potential acting on each electron at point r.

Different models try to approximate the effective potential $V_{\text{eff}}(r)$ such as the Hartree and Hartree-Fock models.

Hartree approximation

The Hartree approximation [259] assumes that the wave function of a many-body system can be approximated by the product of N_e mono-electronic wave functions, even when the electron-electron interactions are not neglected:

$$\Psi^e(r_1, \ldots, r_{N_e}) = \phi_1(r_1)\,\phi_2(r_2)\ldots\phi_{N_e}(r_{N_e}) \tag{4.14}$$

This wave function is only an approximation of the real wave function and is far simpler. The best solution, for each electron, according to the variational principle (the one minimizing the total energy) is a solution of the equation:

$$\left[-\frac{1}{2}\nabla_i^2 + \sum_\alpha \frac{-Z_\alpha}{|r_i - R_\alpha|} + \sum_{j\neq i} \widehat{J}_j\right] \phi_i\left(r_i\right) = \varepsilon_i \phi_i\left(r_i\right) \tag{4.15}$$

where $\widehat{J}_j$ is the Coulomb operator defined by:

$$\widehat{J}_j(r)\phi_i(r) = \int \frac{\phi_j^\star\left(r'\right)\phi_j\left(r'\right)}{|r - r'|} dr' \phi_i(r) \tag{4.16}$$

In the Hartree model, the effective potential $V_{\text{eff}}(r)$ in Eq. 4.13 is thus approximated as the sum of the external potential $V_{\text{ext}}(r)$ and an average Coulomb interaction generated by all the electrons (seen as an electronic cloud) $V_{\text{H}}(r)$, coined the Hartree potential and defined by:

$$V_{\text{H}}(r) = \int \frac{\rho\left(r'\right)}{|r - r'|} dr' \tag{4.17}$$

with the electronic density $\rho(r)$ defined by:

$$\rho(r) = \sum_i \left|\phi_i\left(r_i\right)\right|^2 \tag{4.18}$$

When including the self-interaction, equation 4.15 becomes:

$$\left[-\frac{1}{2}\nabla^2 + V_{\text{ext}}(r) + V_H(r)\right] \phi_i(r) = \varepsilon_i \phi_i(r) \tag{4.19}$$

which is solved iteratively, starting from a trial electronic density and iterating until self-consistency is reached.

Hartree-Fock approximation

In order to satisfy the Pauli exclusion principle (not satisfied by the Hartree model), which states that "the wave function of an electronic system is antisymmetric regarding the permutation of spin-space coordinates of any pair of particles", the wave function is replaced by a Slater determinant, as suggested by Fock [260]:

$$\Psi^e\left(r_1, \ldots, r_{N_e}\right) = \frac{1}{\sqrt{N_e!}} \begin{vmatrix} \phi_1\left(r_1\right) & \phi_2\left(r_1\right) & \ldots & \phi_{N_e}\left(r_1\right) \\ \phi_1\left(r_2\right) & \phi_2\left(r_2\right) & \ldots & \phi_{N_e}\left(r_2\right) \\ \vdots & \vdots & & \vdots \\ \phi_1\left(r_{N_e}\right) & \phi_2\left(r_{N_e}\right) & \ldots & \phi_{N_e}\left(r_{N_e}\right) \end{vmatrix} \tag{4.20}$$

The Hartree-Fock equation in its canonical form is written:

$$\left[-\frac{1}{2}\nabla^2 + V_{\text{ext}}(r) + \sum_j \left(\widehat{J}_j(r) - \widehat{K}_j(r)\right)\right]\phi_i(r) = \varepsilon_i\phi_i(r) \tag{4.21}$$

where $\widehat{J}_j(r)$ is the Coulomb operator, describing the average coulombian interaction associated to the electronic density, and $\widehat{K}_j(r)$ is the exchange operator. The Coulomb operator $\widehat{J}_j(r)$ defined in equation 4.16 is said local because it does not depend on the orbital (ϕ_i) on which it acts. The exchange operator $\widehat{K}_j(r)$ is defined by:

$$\widehat{K}_j(r)\phi_i(r) = \int \frac{\phi_j^\star(r')\,\phi_i(r')}{|r-r'|}dr'\phi_j(r) \tag{4.22}$$

and is said non-local because it depends on the orbital (ϕ_i) on which it acts. Equation 4.21 can be seen as an eigenvalue problem that must be solved iteratively:

$$\widehat{F}(r)\phi_i(r) = \varepsilon_i\phi_i(r) \tag{4.23}$$

where the Fock operator $\widehat{F}(r)$ is given by:

$$\widehat{F}(r) = -\frac{1}{2}\nabla^2 + V_{\text{ext}}(r) + \sum_j \left(\widehat{J}_j(r) - \widehat{K}_j(r)\right) \tag{4.24}$$

Apart from the indirect correlation effect involved by the Pauli exclusion principle, no correlation is included in the Hartree-Fock model. However, in comparison to the Hartree approximation, the Hartree-Fock equations now involve an exchange term which makes the mathematics more complex and the physics more correct.

4.3 DENSITY FUNCTIONAL THEORY

Since the end of the 20th century, DFT has become the primary theoretical tool to investigate and predict materials properties. Combined to the increase of computational resources and the apparition of several open-source codes, DFT allows an accurate prediction of a wide set of advanced properties, at a reasonable computational cost. While DFT can be efficiently used to study molecules and finite systems, this work is restricted to the treatment of infinite crystalline solids and isolated two-dimensional layers. Besides, for the sake of simplicity, the spin dependence is omitted in the following equations.

4.3.1 *Hohenberg-Kohn theorems*

In principle, DFT can be used to predict the ground-state properties of any system of interacting electrons, in an external potential $V_{\text{ext}}(r)$ generated by nuclei with fixed positions, by solving the Schrödinger equation with the hamiltonian given by:

$$\widehat{H} = -\frac{1}{2}\sum_i \nabla_i^2 + \sum_i V_{\text{ext}}(r_i) + \frac{1}{2}\sum_{i\neq j}\frac{1}{|r_i - r_j|} \tag{4.25}$$

DFT is based upon two theorems proposed by Hohenberg and Kohn in 1964 [254]. The first theorem states that for any system of interacting particles in an external potential $V_{\text{ext}}(r)$, this potential is uniquely determined (modulo a global constant) by the electronic density of the ground-state $\rho_0(r)$. Moreover, if the arbitrary constant for the external potential is fixed, the hamiltonian is uniquely determined and all properties of the system can be computed.

The second theorem proved by Hohenberg and Kohn is called the variational principle and states that for any external potential $V_{\text{ext}}(r)$, a universal functional of the density can be defined for the energy $E[\rho]$. For a particular external potential, the exact ground-state energy E_0 corresponds to the global minimum of this functional and the density minimizing this functional is the exact fundamental density ρ_0. In other words, given the expression of the energy functional:

$$E[\tilde{\rho}] = \left\langle \tilde{\Psi} \left| \widehat{H} \right| \tilde{\Psi} \right\rangle = \left\langle \tilde{\Psi} \left| \widehat{T}_e + \widehat{V}_{ee} + V_{\text{eff}} \right| \tilde{\Psi} \right\rangle \tag{4.26}$$

the ground-state energy corresponds to:

$$E_0\left[\rho_0\right] = \min\left\{E\left[\tilde{\rho}\right]\right\} \tag{4.27}$$

with $\tilde{\Psi}$ a trial wave function and $\tilde{\rho}$ the corresponding trial electronic density.

In summary, the fundamental principle of DFT is that any property of a many-body system is a functional of the ground-state density $\rho_0(r)$ and knowing the energy functional $E[\rho]$ is sufficient to determine the exact ground-state energy and density.

4.3.2 *Kohn-Sham equations*

In 1965, Kohn and Sham established a connection between the original interacting many-body system and an auxiliary system of non-interacting electrons that can be solved more easily [255]. The original

system is replaced by a system of non-interacting electrons with the same electronic density ρ in an effective potential, called the Kohn-Sham potential $V_{\mathrm{KS}}(r)$, expressed by:

$$V_{\mathrm{KS}}[\rho] = V_{\mathrm{ext}}(r) + V_{\mathrm{H}}[\rho] + V_{\mathrm{xc}}[\rho] \tag{4.28}$$

where $V_{\mathrm{H}}[\rho]$ is the Hartree potential from Eq. 4.17 and $V_{\mathrm{xc}}[\rho]$ is the exchange-correlation potential. $V_{\mathrm{xc}}[\rho]$ is obtained from the functional derivative of the exchange-correlation energy $E_{\mathrm{xc}}[\rho]$:

$$V_{\mathrm{xc}}[\rho] = \frac{\delta E_{\mathrm{xc}}[\rho]}{\delta \rho} \tag{4.29}$$

where $E_{\mathrm{xc}}[\rho]$ contains an exchange term, a correlation term, and the difference between the kinetic energies of the systems of interacting and non-interacting electrons. This term is the only unknown in the Kohn-Sham approach and its knowledge would lead to the exact description of the original many-body system.

The ground-state total energy and electronic density are obtained by solving the set of independent-particle Kohn-Sham equations, expressed by:

$$\left[-\frac{1}{2}\nabla^2 + V_{\mathrm{ext}}(r) + V_{\mathrm{H}}[\rho] + V_{\mathrm{xc}}(r)\right]\phi_i(r) = \varepsilon_i \phi_i(r) \tag{4.30}$$

Due to the functional dependence on the density ρ, the equations must be solved by iterating until self-consistence is achieved, following the scheme depicted in Fig. 4.1.

4.3.3 *Functionals for exchange and correlation*

The crucial quantity in the Kohn-Sham equations is the exchange-correlation potential (energy) $V_{\mathrm{xc}}[\rho]$ ($E_{\mathrm{xc}}[\rho]$), which is a functional of the density. The Kohn-Sham equations are independent of any approximation to the exchange-correlation terms and would lead to the exact ground-state electronic density and total energy of the original many-body system if the exact exchange-correlation functionals were known. Unfortunately, in practice, $E_{\mathrm{xc}}[\rho]$ is not known and must be approximated.

In their initial work [255], Kohn and Sham also provided a way to build approximate energy functionals for interacting system and expressed the exchange-correlation energy functional by an integral

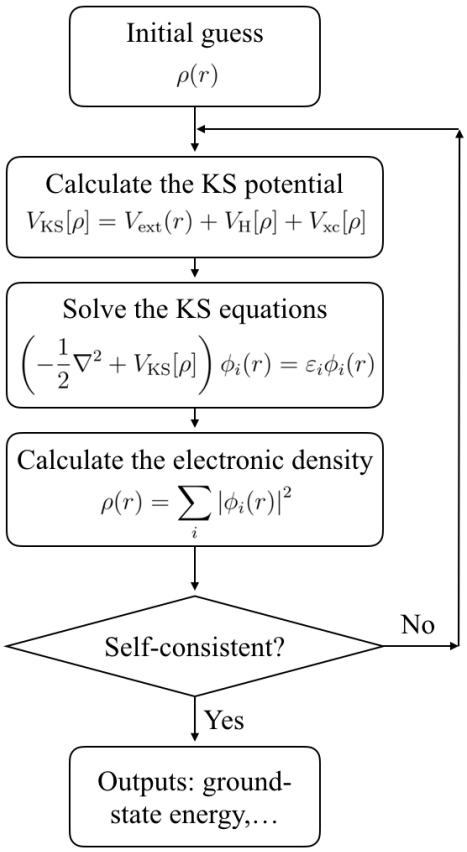

Figure 4.1: Schematic of a self-consistent Kohn-Sham calculation.

over all space of the density multiplied by a (nearly-)local exchange-correlation energy per electron $\varepsilon_{\mathrm{xc}}([\rho], r)$:

$$E_{\mathrm{xc}}[\rho] = \int \rho(r)\varepsilon_{\mathrm{xc}}([\rho], r)\, dr \tag{4.31}$$

The most relevant approximate functionals in condensed matter are known as the local density approximation and the generalized gradient approximation.

The local density approximation

The local density approximation (LDA) assumes that the local exchange-correlation energy per electron corresponds to that of an homogeneous electron gas (HEG) with the same density:

$$E_{\mathrm{xc}}^{\mathrm{LDA}} = \int \rho(r)\varepsilon_{\mathrm{xc}}^{\mathrm{HEG}}([\rho], r)\, dr \tag{4.32}$$

The exchange-correlation energy of the HEG is commonly decomposed into exchange and correlation terms where the exchange term has a simple analytic form, while the correlation term is obtained from a quantum Monte-Carlo simulation. A common LDA parametrization was proposed in 1992 by Perdew and Wang [261]. Although LDA seems rather simple it performs remarkably well.

The generalized gradient approximation

The generalized gradient approximation (GGA) provides a semi-local approximation to the exhange-correlation energy constructed from the local electronic density and its gradients:

$$E_{\mathrm{xc}}^{\mathrm{GGA}} = \int \rho(r)\varepsilon_{\mathrm{xc}}\left(\rho(r), \nabla\rho(r), \nabla^2\rho(r)\right) dr \tag{4.33}$$

GGA functionals are constructed to fulfill a large number of exact constraints for all possible densities. Among the various GGA approximations, the most popular is the one proposed by Perdew, Burke, and Ernzerhof (PBE) in 1996 [262] which satisfies 11 exact constraints.

Beyond GGA

The last decades have seen a tremendous interest in the search for better approximate functionals. While GGA already fulfilled a large number of exact constraints, meta-GGA approximations were developed to satisfy additional constraints. For instance, the strongly-constrained and appropriately-normed (SCAN) meta-GGA, constructed in 2015 [263, 264], respects all 17 known exact constraints that a meta-GGA can satisfy. SCAN has shown improved accuracy in the description of layered materials with diverse kinds of bonding, including intermediate-range many-body van der Waals interactions, at the computational cost of normal GGA approaches. Another alternative consists in mixing the exact Hartree-Fock exchange with a DFT correlation density functional. These approaches are known as hybrid functionals and are mostly used in the chemistry community.

4.4 SOLID STATE THEORY

Up to now, DFT has been considered in its generality and from a theoretical point of view. This part of the work focuses on solid state theory and hence on practical use of DFT to any system.

4.4.1 *The plane-wave basis set*

A crystal can be seen as a periodic structure of repeated unit cells defined by three primitive translation vectors a_1, a_2, and a_3. The vectors of the lattice are thus defined by $R = la_1 + ma_2 + na_3$ where l, m, and n are integers. The reciprocal space is defined by the vectors $G = ua_1^\star + va_2^\star + wa_3^\star$ where u, v, and w are integers and $a_1^\star, a_2^\star$, and $a_3^\star$ are the primitive vectors of the reciprocal space defined by:

$$a_1^\star = \frac{2\pi}{\Omega}\left(a_2 \times a_3\right), \quad a_2^\star = \frac{2\pi}{\Omega}\left(a_3 \times a_1\right), \quad a_3^\star = \frac{2\pi}{\Omega}\left(a_1 \times a_2\right) \tag{4.34}$$

with Ω the volume of the unit cell. The volume defined by the three primitive reciprocal vectors $\Omega^\star$ is called the first Brillouin zone (BZ).

In periodic solids, using the Bloch's theorem, the electronic wave functions can be expressed as a product of a plane wave and a function $u_{nk}(r)$ with the periodicity of the lattice ($u_{nk}(r) = u_{nk}(r + R)$):

$$\phi_{nk}(r) = e^{ik\cdot r} u_{nk}(r) \tag{4.35}$$

where n and k label the band index and the wave vector of the wave functions, respectively. If the periodic part of the Bloch's function is also expanded in terms of plane waves with wave vectors corresponding to reciprocal lattice vectors, G, then the electronic wave functions can be expressed as a sum of plane waves:

$$\phi_{nk}(r) = \frac{1}{\sqrt{N\Omega}} \sum_G e^{i(k+G)\cdot r} u_{nk}(G) \tag{4.36}$$

assuming N to be the number of unit cells repeated in the Born-von Karman periodic box. From Eq. 4.36, a simple set of basis functions to describe a periodic structure is composed of plane waves. To obtain an exact expansion of the electronic wave functions, an infinite number of plane waves is needed. Fortunately, the coefficients $u_{nk}(G)$, used to determine the lowest-energy eigenfunctions, decrease exponentially with the kinetic energy and the plane wave basis set can be truncated using a kinetic cut-off energy, E_{cut}, corresponding to a maximum allowed wave vector:

$$\frac{|k + G|^2}{2} < E_{\text{cut}} \tag{4.37}$$

4.4.2 *Pseudopotentials*

Introduction to pseudopotentials

The major problem is the huge number of plane waves required to properly describe the strong oscillations of highly localized core orbitals (see Fig. 4.2).

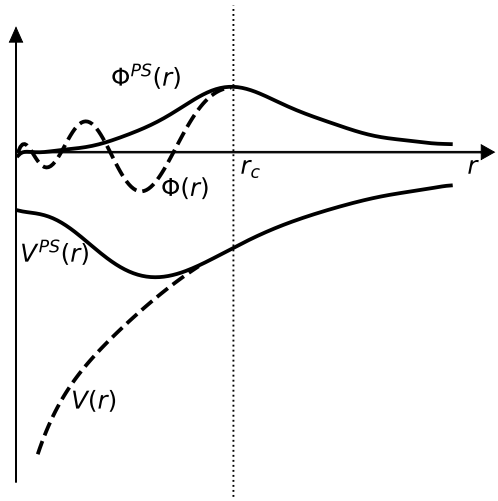

Figure 4.2: Schematic of the pseudopotential approximation, where $\phi(r)$ corresponds to the all-electron wave function, $\phi^{\mathrm{PS}}(r)$ to the pseudo wave function, $V(r)$ to the potential due to the ion with core electrons screening, and $V^{\mathrm{PS}}(r)$ to the pseudopotential.

The idea is to use pseudopotentials to eliminate the low-wavelength strong oscillations. The concept of pseudopotential is based on the frozen-core approximation in which core electrons configurations are considered the same in the atomic environment and in the bonding environment. The core electrons are thus frozen in the nuclei and are not explicitly described by the pseudopotential. For the valence electrons, a pseudo wave function $\phi^{\mathrm{PS}}(r)$, which is a smooth function, is generated to replace the initial all-electron wave function $\phi(r)$ and matches this initial wave function for a radius r higher than a given cut-off radius r_c (see Fig. 4.2). This smooth pseudo wave function can be described by fewer plane waves, thus reducing the computational time. Since the distinction between core and valence electrons is somehow arbitrary, there exist numerous pseudopotentials with different

efficiencies. Moreover, various conditions can be imposed to pseudopotentials.

Norm-conservation

Norm-conserving pseudopotentials exactly describe the atomic potential and, hence, the all-electron wave function, in the region where $r > r_c$. Moreover, they are built upon the condition of integrated charge conservation. This imposes the charge contained inside r_c to be equal between the pseudo and all-electron wave functions, according to:

$$\int_0^{r_c} |\phi(r)|^2 \, dr = \int_0^{r_c} \left|\phi^{\mathrm{PS}}(r)\right|^2 dr \tag{4.38}$$

Considered together, these conditions ensure the continuity at r_c, the conservation of the total charge in the core region, and the exact description of the wave function and potential outside r_c.

Ultrasoft and PAW pseudopotentials

Relaxing the norm-conserving condition allows to build much smoother pseudopotentials and derivative pseudo functions. These smooth pseudopotentials include ultrasoft and projected augmented wave (PAW) pseudopotentials, respectively proposed by Vanderbilt [265] and Blöchl in 1990 [266–268]. The use of these smooth pseudopotentials efficiently reduces the size of the plane wave basis set needed to accurately describe the electronic wave function.

4.4.3 *Brillouin zone integration*

A last point concerns the BZ integration for the calculation of the total energy of a system. In principle, the various terms included in the total energy involve integrals over the whole BZ. For practical reasons, these integrals are replaced by weighted sums over a set of k-points. The k-point grid must be dense enough to accurately capture the wave function variations and usually depends on the symmetry of the system. A popular scheme adopted for the sampling of the BZ is the Monkhorst-Pack grid introduced in 1976 [269].

A global convergence study must be performed both on the kinetic cut-off energy and on the density of the k-point grid, in order to optimize the computational time while preserving a satisfactory accuracy

of the calculations. All computational details related to the calculations performed within this thesis can be found in the chapters dedicated to the results, *i.e.*, Chapters 6 and 7.

4.5 DENSITY FUNCTIONAL PERTURBATION THEORY

4.5.1 *Introduction to response functions*

Many physical properties are derived from total energy variations with respect to external perturbations. These perturbations can be of four types: atomic displacements, static homogeneous electric field, strain, or magnetic field. The response to the first two perturbations allows to compute the phonon dynamical matrices, the dielectric tensor, and the Born effective charges, while the strain perturbation, coupled to phonons and electric field, leads to elastic constant matrices, internal strain, and piezoelectricity. In this manuscript, the perturbation of the phonon type, corresponding to atomic displacements, are predominantly studied.

In practice, the phonon perturbation is characterized by a wave vector q in the reciprocal space. For discrete values of perturbations, the simplest methods are referred to as direct approaches and are based on finite difference calculations. For example, the frozen phonon method [270] considers a small perturbation frozen into the system and calculates all the derivatives of the energy with respect to an approriate set of perturbations. Another direct method consists in extracting phonon eigenfrequencies and eigenvectors from molecular dynamic trajectories [271]. These direct approaches are widely used, though they present a series of limitations regarding the commensurability with the periodic lattice. Calculations for wave vectors different than zero require the use of a supercell, which often increases the computational time, while calculations are even impossible for wave vectors that are incommensurate with the lattice.

In contrast to these direct approaches, perturbation theories can be used with arbitrary wave vector q. The responses to perturbations are mapped onto an equivalent problem presenting the periodicity of the unperturbed system, which suppresses the problem of incommensurability. In the nineties, Baroni, Giannozzi, Testa, Gonze, and others [272–279], popularized perturbative approaches in which responses to external perturbations are calculated self-consistently. Among them, the density functional perturbation theory (DFPT) is the most popular one

thanks to the rapid convergence of the self-consistent loop. DFPT allows to determine the derivatives of the total energy and infers the existence of a variational principle for the second-order derivatives, which can be efficiently used to determine the first-order variation of the wave function, charge density, and potentials.

4.5.2 *Basics of the perturbation theory*

Supposing the perturbation is characterized by a small parameter λ, all physical quantities X, *i.e.*, potentials, energies, wave functions, etc., can be developed into a Taylor series of the perturbation around the unperturbed solution $X^{(0)}$:

$$X(\lambda) = X^{(0)} + \lambda X^{(1)} + \lambda^2 X^{(2)} + \dots \tag{4.39}$$

where $X^{(k)}$ correspond to:

$$X^{(k)} = \frac{1}{k!}\frac{\partial^k X}{\partial \lambda^k} \tag{4.40}$$

It can be demonstrated that the nth order wave function gives access to the $(2n+1)^{\text{th}}$ order energies. This is the so-called "$2n+1$" theorem [280–282].

Making good use of the perturbation theory (not developed herein), the 1st order wave function $\Psi^{(1)}$ can be calculated from the self-consistent solution of the Sternheimer equations given by:

$$\left(\widehat{H}^{(0)} - \varepsilon_i^{(0)}\right)\left|\Psi_i^{(1)}\right\rangle = -\left(\widehat{H}^{(1)} - \varepsilon_i^{(1)}\right)\left|\Psi_i^{(0)}\right\rangle \tag{4.41}$$

where $\widehat{H}^{(0)}$ is the unperturbed hamiltonian, $\widehat{H}^{(1)}$ the 1st order perturbed hamiltonian, $\varepsilon_i^{(0)}$ and $\Psi^{(0)}$ the ground-state eigenenergies and eigenfunctions respectively, and $\varepsilon^{(1)}$ the first-order perturbed eigenenergies.

4.5.3 *Dynamical matrix and phonon frequencies*

Phonons correspond to collective vibrations of a periodic arrangement of atoms or molecules and play a major role especially in thermal and electrical conductivities. Thanks to DFPT, phonon frequencies and associated displacement patterns can be calculated. The second derivative

of the total energy with respect to two atomic displacements corresponds to the interatomic force constant (IFC) matrix [283] expressed by:

$$C_{\kappa\alpha,\kappa'\beta}\left(a,b\right) = \frac{\partial^2 E}{\partial R^a_{\kappa\alpha}\partial R^b_{\kappa'\beta}} \tag{4.42}$$

where α and β refer to cartesian directions, and κ and κ' label atoms in unit cell a and b, respectively. The IFC can thus be seen as the coupling between the displacement of one atom κ from its equilibrium position and the resulting displacement of another atom κ'. For any wave vector q in the reciprocal space, the phonon frequencies ω_{mq}'s and eigenvectors U_{mq}'s of the phonon mode m are determined as solutions of the following eigenvalue problem:

$$\sum_{\kappa'\beta} \tilde{D}_{\kappa\alpha,\kappa'\beta}(q) U_{mq}\left(\kappa'\beta\right) = \omega^2_{mq} U_{mq}(\kappa\alpha) \tag{4.43}$$

The dynamical matrix $\tilde{D}_{\kappa\alpha,\kappa'\beta}(q)$ is connected to the Fourier transform of the IFC, $\tilde{C}_{\kappa\alpha,\kappa'\beta}$, through:

$$\tilde{D}_{\kappa\alpha,\kappa'\beta}(q) = \frac{\tilde{C}_{\kappa\alpha,\kappa'\beta}}{\sqrt{M_\kappa M_{\kappa'}}} \tag{4.44}$$

with M_κ the atomic mass of atom κ.

Equation 4.43 gives rise to 3 acoustic modes, with zero-frequency at the zone-center ($q = 0$), and $3N_{\text{at}} - 3$ optical modes as a function of q with N_{at} the number of atoms in the unit cell. If the dynamical matrix is known for a sufficiently fine grid of wave vectors q, it is possible to calculate the phonon eigenfrequencies for each wave vector in the Brillouin zone, which results in the phonon dispersion band structure.

Phonon frequencies computed for $q = 0$ can be directly compared to Raman and infrared frequencies, while the full phonon spectrum can be obtained experimentally from inelastic neutron scattering. Such direct comparison between theoretical predictions and experiments is performed in Sections 6.1.2, 6.2.2, and 7.3, for three-dimensional and two-dimensional compounds, respectively. Computed phonon frequencies are generally reproduced with $10 - 20\%$ of deviation with respect to the experimental values, depending on the approximate to the exchange-correlation functional.

4.6 ELASTIC CONSTANTS

In principle, as mentioned in section 4.5.1, the elastic constant matrices can be obtained from a DFPT calculation. The strain perturbation can be either uniaxial strain or shear strain. This DFPT approach is the one implemented in the ABINIT software [284, 285].

In the context of this thesis, however, the elastic constants were computed within the finite difference approach, as implemented in the VASP package [286–288]. The reason for this choice comes from the use of the SCAN functional which is, to date, not implemented in ABINIT, but well in VASP. The calculation of the elastic constants requires the computation of the Hessian matrix, *i.e.,* the matrix of second derivatives of the energy with respect to atomic displacements. The Hessian matrix is determined using finite differences by applying a set of inequivalent ionic displacements in each cartesian direction. The 6×6 elastic tensor is determined by applying a set of six homogeneous finite distortions of the lattice ($+1.5\%$ and -1.5% along the three cartesian coordinates) and calculating the associated resulting stress. Elastic constants c_{ij} are then derived from the stress-strain relationship:

$$\sigma_i = \sum_{j=1}^{6} c_{ij}\varepsilon_j \tag{4.45}$$

where σ_i corresponds to a small stress component resulting from the application of a small strain ε_j to the relaxed system [289].

In this work, the elastic constants of several MAX phases are computed *ab initio* and reported in Sections 6.1.5 and 6.2.3. The elastic tensor is calculated both for rigid ions as well as relaxed ionic positions. Only the results for relaxed ionic positions are presented. Usually, elastic constants are reproduced with $\sim 15\%$ of deviation with respect to experimental values, which is comparable to the agreement found for the phonon frequencies.

4.7 TRANSPORT PROPERTIES

The thermal conductivity of the Cr_2AlC MAX phase is investigated in Section 6.1.4. For this purpose, the thermal conductivity is decomposed into its electronic and lattice contributions, such that $\kappa = \kappa_e + \kappa_l$. Both contributions are predicted from first principles by solving the Boltzmann transport equation for electrons and phonons, respectively.

The fundamental theories useful to calculate the electronic and lattice thermal conductivity are presented in Sections 4.7.1 and 4.7.2, respectively.

4.7.1 *Electronic thermal conductivity*

Boltzmann transport equation

From first principles, the electronic contribution to the thermal conductivity κ_e can be obtained by solving the Boltzmann transport equation (BTE) for electrons. The BTE describes the statistical behavior of an out-of-equilibrium system in terms of various scattering processes considering their specific scattering rates. The transport distribution function is defined as:

$$\sigma(\varepsilon, T) = \int \sum_b v_{b,k} \times v_{b,k} \tau_{b,k} \delta\left(\varepsilon - \varepsilon_{b,k}\right) \frac{dk}{8\pi^3} \tag{4.46}$$

where b is a band index, k the conserved wave vector, $v_{b,k}$ the carrier velocities, $\tau_{b,k}$ the relaxation time, and $\varepsilon_{b,k}$ the band energies. $\sigma(\varepsilon, T)$ can be used to compute the moments of the generalized transport coefficients:

$$\mathcal{L}^{\alpha} = q^2 \int \sigma(\varepsilon, T) \left(\varepsilon - \mu\right)^{\alpha} \left(-\frac{\partial f_F(\varepsilon; \mu, T)}{\partial \varepsilon}\right) d\varepsilon \tag{4.47}$$

with f_F the Fermi distribution and μ the chemical potential, that, in turn, are used to access the electronic transport coefficients of interest, namely the electrical conductivity σ and the electronic thermal conductivity κ_e, as:

$$\sigma = \mathcal{L}^{(0)} \tag{4.48}$$

$$\kappa_e = \frac{1}{q^2 T} \left[\frac{\left(\mathcal{L}^{(1)}\right)^2}{\mathcal{L}^{(0)}} - \mathcal{L}^{(2)} \right] \tag{4.49}$$

The integration of the BTE requires an accurate description of the electronic band structure. BoltzTraP2 code [290] provides such a description using an interpolation method based on a Fourier expansion that takes as input the electronic energies for different k-points, previously calculated by a DFT code. The code then computes the Fermi integrals for different temperatures and Fermi levels, and returns as output all the transport coefficients [290, 291].

Relaxation time approximation

The relaxation time $\tau_{b,k}$ typically depends on the temperature T, and on the charge carrier energy ε. All scattering events that can influence the electron conduction such as impurity scattering, phonon scattering, etc., are summed in this parameter according to a Matthiessen law. In many cases, as a first approximation, the relaxation time is often assumed to be constant. Within the constant relaxation time approximation (CRTA), quantities such as $\sigma_0 = \sigma/\tau_0$ and $\kappa_0 = \kappa/\tau_0$ are determined by the band structure where the temperature dependence exclusively comes from the electronic occupation function. This approach is quite efficient in terms of computational time and globally provides satisfactory quantitative agreement with experimental measurements for lightly-doped semiconductors [292] where charge carriers are concentrated in specific bands and wave vectors. However, for highly-doped semiconductors and metals, charge carriers are located at various places (various bands and wave vectors k) and the electronic relaxation time thus varies significantly on the Fermi surface [293]. In these particular cases, the CRTA has shown limitations and more-advanced computational theories or models must be considered.

Besides the CRTA

In order to obtain a good description of the electronic properties of metallic systems, both the temperature- and energy-dependence of $\tau_{b,k}$ must be considered in Eq. 4.46. The temperature and energy dependence is dictated by the scattering mechanisms. The most important mechanisms of electron scattering in metals are (i) defects and charged impurity scattering, dominant at low temperature ($< 100\,\mathrm{K}$), and (ii) electron-phonon scattering, dominant at high-temperature. An analytical model expression for $\tau(T,\varepsilon)$, developed on the basis of known semi-classical theories can be formulated as [294, 295]:

$$\tau(T,\varepsilon) = \tau_{\mathrm{ref}} \left(\frac{T}{T_{\mathrm{ref}}}\right)^{\gamma} \left(\frac{\varepsilon}{\varepsilon_{\mathrm{ref}}}\right)^{\lambda-1/2} \tag{4.50}$$

where τ_{ref} is a suitable reference value of τ at a temperature T_{ref} and $\varepsilon_{\mathrm{ref}}$ is the bottom of the conduction band which, in the case of metallic systems, is taken as the Fermi level energy. At low temperature, γ and λ exponents in Eq. 4.50 are respectively 0 and 2 reflecting the effect of defects and impurities. At high temperature, γ and λ exponents are

respectively equal to -1 and 0 and the linear temperature dependence T^{-1} of the relaxation time reflects the dominance of electron-phonon scattering mechanisms.

The temperature- and energy-dependent relaxation time has been implemented in the BoltzTraP2 code and is used to investigate the electrical and thermal transport in Cr_2AlC single crystals in Section 6.1.4.

4.7.2 *Lattice thermal conductivity*

The lattice thermal conductivity κ_l of a perfect harmonic crystal, which can be considered as an assembly of independent harmonic oscillators, is infinite and not a function of temperature. As a reminder, the harmonic approximation considers that all ions oscillate around their equilibrium positions which correspond to Bravais lattice sites and that the amplitude of the vibrations is small compared to interatomic distances. The lattice thermal resistance is dictated by phonon scattering processes that can be intrinsic, through anharmonic phonon-phonon scattering, or extrinsic, induced by isotopic disorder, point defects, or edge effects. The treatment of these scattering processes is mandatory in order to obtain a good description and temperature-dependence of thermal and thermodynamic properties, especially at high temperature.

Phonon Boltzmann transport equation

When a material is at equilibrium at the temperature T, the equilibrium phonon population $\overline{n}_\nu$ describes the number of phonons for each vibrational mode ν found at energy $\hbar\omega_\nu$. If a gradient of temperature is applied, the phonon population deviates from its equilibrium condition and reaches an out-of-equilibrium condition [296].

The first microscopic description of the lattice thermal conductivity was formulated in 1929 by Peierls [297], and is nowadays known as the phonon BTE. This equation describes how the perturbation due to a gradient of temperature involves a change in the phonon population due to all possible scattering mechanisms. In order to accurately predict thermal transport properties, an accurate description of the equilibrium and perturbed phonon populations is required, as well as of their interactions, and lifetimes [296]. In practice, the harmonic quantities, such as phonon frequencies, group velocities, and phonon populations, can be obtained *ab initio* by computing the second-order IFC

using DFPT. The challenge thus resides in the determination of the anharmonic quantities, such as phonon scattering rates and linewidths. The total out-of-equilibrium distribution n_ν in its linearized form is given by:

$$n_\nu = \overline{n}_\nu \left(\overline{n}_\nu + 1\right) F_\nu \nabla T \tag{4.51}$$

where F_ν corresponds to the deviation of the phonon population with respect to the equilibrium condition. The computation of n_ν, which is the key quantity to be evaluated, requires to solve the linearized BTE for phonons:

$$c_\nu \nabla T \frac{\partial \overline{n}_\nu}{\partial T} = \sum_{\nu'} \Omega_{\nu,\nu'} n_{\nu'} \tag{4.52}$$

where $\Omega_{\nu,\nu'}$ is a matrix of scattering rates acting on the phonon population. The lattice thermal conductivity can be expressed as:

$$\kappa_l = \frac{\hbar^2}{\Omega k_B T^2} \sum_\nu \overline{n}_\nu \left(\overline{n}_\nu + 1\right) c_\nu \omega_\nu F_\nu \tag{4.53}$$

where Ω is the unit cell volume, ω_ν the phonon frequencies, and c_ν the corresponding group velocities.

Additional information on the computation of the lattice thermal conductivity can be found in Ref. [296].

Single mode approximation

In most cases, phonons are treated individually through the single mode approximation (SMA) [298–300]. This relies on the assumption that heat-current is dissipated every time a phonon undergoes a scattering event [301] and approximates F_ν with $c_\nu \omega_\nu \tau_\nu$ where τ_ν is the relaxation time of the phonon mode ν. While the SMA properly describes the depopulation of a phonon mode after any scattering process, the repopulation process is usually poorly described due to a loss of memory of the initial phonon distribution (final states are repopulated isothermally) [301, 302].

TDEP formalism

In 2011, Hellman *et al.* [303–305] introduced the temperature-dependent energy potential (TDEP) formalism for finite temperature lattice dynamics, including the calculation of temperature-dependent

phonon frequencies, anharmonic free energy, and lattice thermal conductivity. In order to understand the basics of the TDEP formalism, the fundamental notions of lattice dynamics are recalled.

When an atom in a crystal is displaced from its equilibrium position, it causes all the atoms in the crystal to be displaced. In Section 4.5, it was shown that the effect of any perturbation can be modeled as a Taylor series of the potential energy U with respect to atomic displacements u:

$$U(\{u\}) = U_0 + \sum_i \sum_\alpha \Phi_i^\alpha u_i^\alpha + \frac{1}{2!} \sum_{ij} \sum_{\alpha\beta} \Phi_{ij}^{\alpha\beta} u_i^\alpha u_j^\beta + \frac{1}{3!} \sum_{ijk} \sum_{\alpha\beta\gamma} \Phi_{ijk} u_i^\alpha u_j^\beta u_k^\gamma + \dots \quad (4.54)$$

where i, j, k label the atoms in the crystal, α, β, γ are cartesian indices, and U_0 is the potential energy of the unperturbed lattice. Coefficients $\Phi_i^\alpha, \Phi_{ij}^{\alpha\beta}, \Phi_{ijk}^{\alpha\beta\gamma}$ are called the Born-von Karman force constants and correspond, respectively, to the first-, second-, and third-order derivatives of the potential energy with respect to atomic displacements at zero-temperature:

$$\Phi_i^\alpha = \left.\frac{\partial U}{\partial u_i^\alpha}\right|_{u=0}, \quad \Phi_{ij}^{\alpha\beta} = \left.\frac{\partial^2 U}{\partial u_i^\alpha \partial u_j^\beta}\right|_{u=0}, \quad \Phi_{ijk}^{\alpha\beta\gamma} = \left.\frac{\partial^3 U}{\partial u_i^\alpha \partial u_j^\beta \partial u_k^\gamma}\right|_{u=0} \quad (4.55)$$

In the harmonic approximation, *i.e.*, for small atomic displacements at constant volume, the problem is solved with the second-order term, while the higher-order terms are treated as perturbations. In the quasi-harmonic approximation (QHA), the volume dependence of the potential energy is taken into account. However, QHA calculations simply consist in the harmonic approximation applied to each volume and therefore neglect the temperature dependence of the potential energy. As a major consequence, the use of harmonic and quasi-harmonic approximation is limited to systems where anharmonicities are negligible.

The TDEP formalism solves this issue and considers force constants that are volume- and temperature-dependent. This is achieved by giving up the constraint that force constants are derivatives of the zero-

temperature configuration (Eq. 4.55). Instead, force constants are considered as parameters in an effective hamiltonian expressed by:

$$\widehat{H} = U_0 + \sum_i \frac{p_i^2}{2m_i} + \frac{1}{2!}\sum_{ij}\sum_{\alpha\beta}\Phi_{ij}^{\alpha\beta}u_i^\alpha u_j^\beta + \frac{1}{3!}\sum_{ijk}\sum_{\alpha\beta\gamma}\Phi_{ijk}^{\alpha\beta\gamma}u_i^\alpha u_j^\beta u_k^\gamma + \dots \quad (4.56)$$

The sampling of the Born-Oppenheimer (BO) surface at finite temperature is achieved with a stochastic sampling. The sampling provides a set of simulated forces f^{BO} and displacements u which is then used to fit the coefficients of the model hamiltonian, through a minimization scheme of the difference between the *ab initio* forces f^{BO} and the forces of the model system f^{M}:

$$f_{i\alpha}^{\mathrm{M}} = -\sum_{j\beta}\Phi_{ij}^{\alpha\beta}u_j^\beta - \frac{1}{2!}\sum_{jk\beta\gamma}\Phi_{ijk}^{\alpha\beta\gamma}u_j^\beta u_k^\gamma + \dots \quad (4.57)$$

The second-order force constants can be used to compute the phonon dispersion, phonon density of states, and some thermodynamic quantities. The third-order force constants are required to compute the lifetime due to anharmonic phonon-phonon scattering, and hence the F_ν term, which is involved in the determination of the lattice thermal conductivity in Eq. 4.53.

4.8 CONCLUSIONS

In this thesis, the structural and electronic properties of various MAX and MXene systems are computed within the DFT framework using either the ABINIT [284, 285, 306] or VASP package [286–288]. The DFPT formalism [272–274, 307, 308] is used to compute the second-order interatomic force constant matrix required to obtain phonon spectra, phonon mode frequencies, and associated eigen-displacements (see Sections 6.1.2, 6.2.2, and 7.3). In addition, the elastic constants of various systems are computed *ab initio* using the stress-strain method based on finite-differences as implemented in the VASP package [286–288] (see Sections 6.1.5 and 6.2.3). The thermal conductivity of Cr_2AlC is evaluated from first principles and reported in Section 6.1.4. In this context, the electronic thermal conductivity is computed by solving the BTE for electrons described in Section 4.7.1, with a temperature-

dependent relaxation time. The lattice thermal conductivity is evaluated within the TDEP formalism via the computation of the second- and third-order interatomic force constant matrices. In addition, various scattering processes are considered in the calculations (see Section 6.1.4).

A theory is something nobody believes, except the person who made it. An experiment is something everybody believes, except the person who made it.

— **A. Einstein**

5 CHARACTERIZATION TECHNIQUES

While, in some cases, theoretical works are used to interpret experimental results afterwards, they can also be used to predict the physical properties of thousands of materials. In this case, experimental works are required to confirm and complement the theoretical predictions and, sometimes, turn to be very useful to set some realistic limits to the materials efficiencies. Experimental measurements are usually conducted in less favorable conditions, *i.e.*, on samples with defects, at ambient air conditions, etc., while *ab initio* predictions deal with perfect samples at zero-temperature. Besides, computational works are still limited regarding the predictive capability in how materials can be synthesized and regarding their stability, safety, and durability, which are major criteria for future applications.

The development of new characterization tools combined with the improvement in image resolution in imaging techniques thanks to the efficient use of various particles (*e.g.*, electrons, photons, X-rays, etc.) have led to tremendous advances in materials characterization, including the accurate measurement of most physical properties, *i.e.*, structural, electronic, vibrational, optical, mechanical, magnetic, and thermal properties.

This chapter aims to quickly recall the basic principles behind various experimental techniques used to characterize materials structures and properties. Specific instrumental details used within the framework of this thesis are also presented.

At first, Section 5.1 recalls the basics of experimental techniques used to probe the structure and composition of materials. These techniques include X-ray diffraction, scanning electron microscopy, and scanning transmission electron microscopy.

Section 5.2 is devoted to experimental techniques used to investigate the vibrational properties, including Raman spectroscopy and inelastic neutron scattering.

Eventually, Section 5.3 details the nanoindentation technique used to characterize materials elastic response.

5.1 STRUCTURE AND COMPOSITION

5.1.1 *Single-crystal X-ray diffraction*

Single-crystal X-ray diffraction (XRD) is a non-destructive technique which reveals information about the unit cell dimensions and the positions and nature of atoms within the unit cell. Information about bond lengths, angles, crystal symmetries, and site-ordering can be deduced from the atomic positions. Most commonly, XRD is coupled to a single-crystal refinement technique to obtain the crystal structure. The physics of diffraction is well-covered in the literature, *e.g.*, in Refs. [309, 310].

Working principle

The working principle of XRD involves three main steps, *i.e.*, the production of the X-ray beam with a specific wavelength, the focus of X-rays on the sample, and the detection of diffracted X-rays. X-rays are produced in an X-ray tube by heating a filament to produce electrons which are then accelerated towards a target material (typically Molybdenum). When the high-energy electrons impact the target material, some inner electrons are ejected and X-rays are produced from the relaxation of outer electrons to inner levels. The wavelength λ of the resulting monochromatic X-ray beam is characteristic of the target material and is typically chosen to be in the same order of magnitude than the interatomic distances in the crystal. X-rays are then directed onto the sample and constructive interferences are observed for X-rays satisfying Bragg's law: $n\lambda = 2d \sin\theta$. The diffraction angle θ is determined by the order of reflection n (which can be any integer), the wavelength of the X-ray beam λ, and the spacing between the diffracting planes d. The specific diffraction directions leading to constructive interferences appear as regularly spaced bright spots on the diffraction pattern, called reflections. From the Fourier transform of the diffraction pattern, information about the unit cell are obtained.

Instrumental details

In this thesis, XRD technique is used to determine the crystalline structure of several $(Mo_{2/3}RE_{1/3})_2AlC$ single crystals (RE = Nd, Gd, Dy, Ho, and Er) (see Section 6.2.1). XRD measurements and single-crystal refinements are performed by T. Ouisse and L. Jouffret respectively at LMGP Grenoble and Institut de Chimie de Clermont-Ferrand in France. X-ray intensity data are measured, in transmission mode, for structural determination using a Bruker APEX2 SC diffractometer. The determination of the final cell constants is based upon the refinement of the XYZ centroids of reflections above $20\sigma(I)$. Data are corrected for absorption effects using the Numerical Mu from formula method (SADABS). The structure is solved, and refined, using the Bruker SHELXTL software package [311]. Several different single crystals for each rare-earth (RE) element are examined in order to ascertain that all give the same structure.

5.1.2 *Scanning electron microscopy*

Scanning electron microscopy (SEM) is a characterization technique used to produce high-resolution images of a sample by scanning the surface with an electron beam, taking advantage of basics principles of electron-matter interaction. Depending on the working mode of the microscope, information about the morphology, topography, chemical composition, and crystalline structure can be obtained. Energy dispersive X-ray spectroscopy (EDX or EDS) is commonly integrated into SEM and is used for elemental analysis. Detailed explanations of the basic concepts and capabilities of the SEM can be found in Ref. [312].

Working principle

A scanning electron microscope consists of four main parts: an electron gun and lenses used to generate and focus an electron beam onto the sample, a sample holder allowing displacements in the three directions, and electron detectors used to collect, amplify, and analyze the emitted electrons from the sample. When a primary electron from the fine electron beam arrives on the sample, it interacts with the atoms at the surface. Part of the energy of the primary electron is transferred to outer electrons that are lightly bound to the atoms, leading to the emission of these electrons, coined secondary electrons (SE). SE generally have low energy and come from the top 10 nm of the sample

surface. An electric signal is recorded at the detector for each impact point, whose intensity depends on the amount of collected SE, and thus on the topography, morphology, and orientation of the surface. By scanning a sample, SEM thus allows to obtain a magnified image of its surface.

Instrumental details

In this thesis, the surface of a Cr_2AlC single crystal is imaged using a scanning electron microscope (Zeiss Supra 50VP) at an accelerating voltage of 20 kV and with a working distance around 11 mm (see Section 6.1.5). All the micrographs are obtained with secondary electrons. Before imaging, the sample is coated with an 8 nm platinum/palladium 80 : 20 layer to prevent spurious reactions with the glue potentially present on the sample edges. Both the sample preparation and microscopy are performed with H. Badr and M. Sokol at Drexel University in USA.

Similarly, the surface of a $(Mo_{2/3}Ho_{1/3})_2AlC$ single crystal is imaged using a field emission gun-scanning electron microscope (JEOL 7600F) at an accelerating voltage of 15 kV and with a working distance around 12 mm (see Section 6.2.3). Before imaging, the sample is coated with an 8 nm gold layer using a Cressington sputter 208HR. Sample preparation and SEM imaging are performed with D. Magnin at UCLouvain in Belgium.

5.1.3 *Scanning transmission electron microscopy*

Scannning transmission electron microscopy (STEM) is an efficient technique to observe the atomic structure of materials as it offers a sub-angstrom spatial resolution suitable to resolve individual atoms. STEM combines the working principles of both scanning electron microscopy and transmission electron microscopy. For more details on the structure and imaging capabilities of a STEM, refer to Refs. [313, 314].

Working principle

An electron beam produced by an electron gun is focused to a small area onto the sample thanks to the use of condenser lenses. Due to electron-matter interactions, electrons propagate through the sample and are scattered along various trajectories. The intensity of high-angle

scattered electrons is recorded, allowing for the construction of a Z-contrast image of the scanned area. This imaging mode refers to the high angle annular dark field imaging (HAADF). In Z-contrast images, the intensity is proportional to the atomic number $Z^{1.64}$, making heavier atoms brighter than lighter atoms.

Instrumental details

In this thesis, STEM combined with HAADF is performed in a double-correlated FEI Titan3, operated at 300 kV, with the aim to confirm the crystal structure of $(Mo_{2/3}RE_{1/3})_2AlC$ single crystals (see Section 6.2.1). STEM analysis is performed in the group of J. Rosen at Linköping University in Sweden.

5.2 VIBRATIONAL PROPERTIES

5.2.1 *Raman spectroscopy*

Elastic and inelastic scattering are two important processes observed when a monochromatic light interacts with matter. While for elastic scattering, the reflected beam has the same energy as the incident one, inelastic scattering involves an energy loss due to lattice vibrations. A common inelastic scattering is the Raman scattering characterizing the energy shifts resulting from the light-matter interaction. Raman spectroscopy is usually used to measure vibrational mode frequencies and to gain insight into the composition and external structural of a sample. More information can be found in the book by H. A. Szymanski [315].

Working principle

Raman spectroscopy is a useful experimental tool to measure vibrational and rotational modes in a material, through the analysis of light frequency shifts. The main idea is that a monochromatic light from a laser, usually in the visible light range, is sent onto a sample and interacts with the atomic lattice through vibrations that change the frequency, energy, and wave vector of the light beam. In particular, when the incident light, made out of photons, hits the material, the energy of the incident photon, $\hbar\omega$, is transfered to the crystal which gets excited to a higher vibrational mode. If the excited crystal then reemits a photon of the same energy $\hbar\omega' = \hbar\omega$, we talk about Rayleigh scattering. If

the crystal relaxes to a vibrational state with an energy different than the energy of the incident photon $\hbar\omega' \neq \hbar\omega$, we talk about Raman scattering. In this case, if the crystal relaxes to a vibrational state with an energy higher than the initial state, the emitted photon has a lower energy than the incident photon $\hbar\omega' < \hbar\omega$ and the crystal additionally emits a phonon of energy $\hbar\omega_p = \hbar\omega - \hbar\omega'$ (see Fig. 5.1(a)). We talk about Stokes Raman scattering. In contrast, if the crystal relaxes to a vibrational state lower in energy than the initial state, the emitted photon has a higher energy than the incident one $\hbar\omega' > \hbar\omega$ and the crystal absorbs a phonon of energy $\hbar\omega_p = \hbar\omega' - \hbar\omega$ (see Fig. 5.1(b)). This corresponds to Anti-Stokes Raman scattering. A schematic representation of the Stokes and Anti-Stokes scattering is provided in Fig. 5.1.

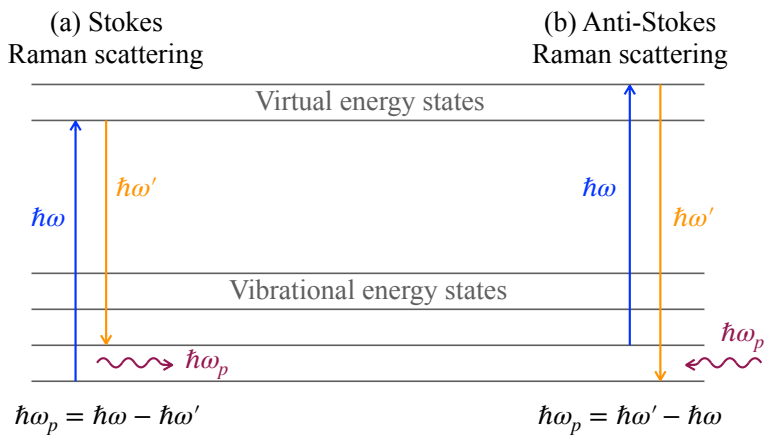

Figure 5.1: Schematic representation of the energy levels for (a) Stokes and (b) Anti-Stokes Raman scattering, where the energies of the incident and scattered photons are respectively $\hbar\omega$ and $\hbar\omega'$, whereas the absorbed/emitted phonon has an energy $\hbar\omega_p$.

The analysis of the diffused beam results in the determination of the frequency/wavenumber shifts associated to the lattice vibrations, often referred to as the phonon mode frequencies/wavenumbers. The vibrational modes observed on an experimental Raman spectrum correspond to the modes that cause a change in the polarizability of the material and that have a wave vector almost equal to zero (Γ point of the BZ). Making good use of the group theory and the crystal symmetry analysis allows to predict the Raman-activity of the computed zone-centered phonon modes.

Instrumental details

In this thesis, the Raman spectra of $(Mo_{2/3}RE_{1/3})_2AlC$ single crystals (RE = Nd, Gd, Dy, Ho, and Er) are recorded using a Horiba/Jobin Yvon LabRam spectrometer equipped with a liquid-nitrogen-cooled charge-coupled device detector (see Section 6.2.2). The measurements are carried out in the micro-Raman mode at RT in a backscattering geometry. The 514.5 nm, or 488 nm (Er-based phase), exciting line of an Ar^+ laser is focused to a spot size of $\sim 1\,\mu$m on the sample surface (*i.e.*, basal plane) with an incident power of 1.8 and 1.1 mW for the Ho and Er-based phases, respectively, and 0.7 mW for the other three phases.

In addition, the V_2C-based MXene flakes are deposited on a glass slide and not transferred on a substrate. Micro-Raman spectroscopy is performed at RT with a LabRam Horiba spectrometer with a laser wavelength of 514.5 nm (see Section 7.3). The laser beam is focused on the sample with a 100× objective (numerical aperture of 0.95) and the incident power is kept below 1 mW. A grating of 2400 lines/mm is used in order to achieve a high spectral resolution.

All Raman spectra are calibrated using a silicon reference spectrum. The Raman spectra of RE-i-MAX phases are collected by O. Chaix-Pluchery from LMGP Grenoble in France, while the one of V_2C-based MXenes are collected with L. Shi at UCLouvain in Belgium.

5.2.2 *Inelastic neutron scattering*

Inelastic neutron scattering (INS) is a technique of choice to study atomic motions in crystalline materials and to determine the energy and associated wave vector q of the phonon modes. INS data are usually presented in the form of a phonon dispersion spectrum, *i.e.*, the phonon energy as a function of the wave vector q along a high-symmetry path. Theoretical and technical details on the INS technique can be found in Ref. [316].

Working principle

The basic idea of INS is that a neutron can interact with a crystalline solid by emitting or absorbing a quantum of phonon energy, $\hbar\omega$. The energy and wave vector of the neutron are thus modified during the inelastic scattering process. Typically, the energy of the emitted/absorbed phonon is determined by the difference between the initial en-

ergy of the neutron E_i and its final energy E_f after scattering. Similarly, the phonon wave vector q is given by $q = k_i - k_f$ with k_i and k_f, the neutron wave vector respectively before and after the scattering event. Several techniques allow to access the neutron wave vector and energy transfer, among which the triple-axis spectrometer is the method of choice. A monochromator is used to selectively choose a neutron beam with a well-defined wave vector k_i (first axis). The incident neutron beam is then scattered by the crystalline sample (second axis), and the scattered neutron beam with a wave vector k_f is reflected by the analyzer (third-axis) onto the neutron detector which determines the energy transfer $\hbar\omega$. By performing a scan on the reciprocal space (q wave vector) or on the energy $\hbar\omega$, keeping the other variable constant, the dispersion relation $\hbar\omega(q)$ of a single crystal can be obtained with good accuracy.

Instrumental details

In this thesis, the dispersion relation of a Cr_2AlC single crystal is determined experimentally by INS (see Section 6.1.2). All measurements are performed by T. Ouisse and supervised by F. Bourdarot and P. Bourges, respectively at ILL (Grenoble, France) and LLB (Paris-Saclay, France). P. Piekark, from INP Krakow in Poland, also helped in the use of the INS technique. The neutron beam slit is around 4 cm $\times$ 2 cm. In the low phonon energy range ($0 - 40$ meV), INS is performed at RT on the thermal neutron three-axis IN22, CRG-CEA spectrometer. The initial beam is provided by a double-focusing pyrolithic graphite (PG) monochromator (PG$(0,0,2)$) and the scattered beam is analyzed by a double-focusing PG analyzer (PG$(0,0,2)$) with fixed $k_f = 2.662$ Å^{-1}. The sample is aligned first in the $[h0l]$ direction and then in the $[hhl]$ direction. For the high phonon energy range ($50 - 100$ meV), the graphite monochromator is replaced by a Cu monochromator. Each phonon wave vector value is selected by choosing a Brillouin zone compatible with the spectrometer configuration range and an acceptable predicted intensity. Spurious resonances are eliminated by checking the configurations leading to higher order parasitic signals and accidental Bragg scattering. The phonon branches of a Cr_2AlC single crystal are measured along three crystallographic directions: $\Gamma-$M, $\Gamma-$A, and M$-$L.

The nanoindentation technique is used to characterize the elastic and mechanical properties of materials, including hardness and Young's modulus.

Working principle

In a nanoindentation test, a load is applied on a tip (indenter), with known geometry and mechanical properties, which penetrates into a sample. The evolution of the penetration depth is recorded as a function of the applied load. A typical nanoindentation test includes a loading part up to a maximal load or penetration depth fixed by the user, and an unloading part corresponding to the retraction of the tip away from the sample. The resulting load versus displacement curve gives information about the elastic and plastic response of the material, and allows the extraction of various materials properties. Typical loads can go up to tens of microNewtons while the penetration depths usually range from tens of nanometers to a few micrometers, depending on the sample thickness. Different indenters are used to perform nanoindentation tests, among which the most used ones are the Berkovich, spherical, and Vickers indenters, depicted in Fig. 5.2. Usually, the Berkovich tip is more readily fashioned to a sharper point than the Vickers one, hence ensuring a more precise control over the indentation process [317].

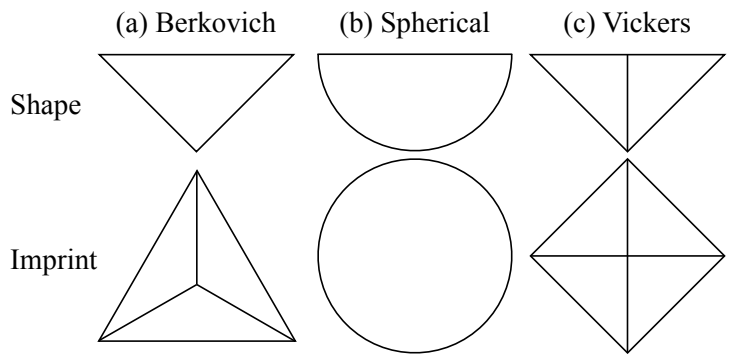

Figure 5.2: Representation of the shape and imprint of a (a) Berkovich, (b) spherical, and (c) Vickers indenter.

In general, the elastic modulus or Young's modulus can be determined from the slope of the stress-strain curve obtained from a tensile

test. In nanoindentation technique, the modulus, called indentation modulus, can be determined from the slope of the unloading part of the load-displacement curve. Ideally, the indentation and Young's modulus have the same meaning and values, but this is not always guaranteed. In fact, the indentation modulus may be affected by the material behavior below the indent where the applied load is not homogeneous.

Oliver and Pharr [318] established analytical models to determine the indentation modulus and hardness from the load-displacement curve recorded during the indentation test. For a Berkovich tip, the contact depth h_c is calculated by:

$$h_c = h_{\text{tot}} - \left(\frac{3P}{4S}\right) \tag{5.1}$$

where h_{tot} is the indentation depth, P is the load, and S is the harmonic stiffness. By defining the area function as:

$$A\left(h_c\right) = C_0 h_c^2 + C_1 h_c + C_2 h_c^{1+2} + C_3 h_c^{1/4} + \ldots \tag{5.2}$$

the Berkovich Young's modulus E_{Br} is calculated from:

$$\frac{1}{E^\star} = \frac{\left(1-\nu^2\right)}{E_{\text{Br}}} + \frac{\left(1-0.07^2\right)}{1140} \tag{5.3}$$

with ν, the Poisson ratio, and $E^\star$ obtained from:

$$E^\star = \frac{S\sqrt{\pi}}{2\sqrt{A\left(h_c\right)}} \tag{5.4}$$

The Berkovich hardness H_{Br} is expressed by:

$$H_{\text{Br}} = \frac{P_{\text{max}}}{A} \tag{5.5}$$

with P_{max}, the maximal load applied on the sample and A, the area function defined in Eq. 5.2.

Instrumental details

In this thesis, the Young's modulus and hardness values of Cr_2AlC single crystals are measured by a nanoindenter with a Berkovich tip in the continuous stiffness measurement mode (see Section 6.1.5). For this purpose, Cr_2AlC single crystals are mounted on a aluminum puck (in

epoxy resin) for indentation perpendicular (parallel) to the *ab*-plane, and polished to a mirror finish. Two configurations are considered for the nanoindentation measurements. The first one consists in the indentation of the sample perpendicularly to the *ab*-plane. The second one consists in the indentation of the sample parallel to the *ab*-plane. In total, 18 and 28 indents are performed perpendicularly and parallel to the *ab*-plane, respectively. The maximal load is set to 150 mN, with a strain rate of $0.05\,\mathrm{s}^{-1}$. The Berkovich tip is calibrated on a standard amorphous silica sample beforehand. Both sample preparation and nanoindentation tests are performed with H. Badr at Drexel University in USA.

In addition, the Young's modulus and hardness values of a $(Mo_{2/3}Ho_{1/3})_2AlC$ single crystal, previously fixed with superglue on an aluminum puck, are measured by a nanoindenter with a Berkovich tip in the continuous stiffness measurement mode (see Section 6.2.3). The indentation depth limit is set to 1 μm, with a strain rate of $0.05\,\mathrm{s}^{-1}$. In total, 15 indents with a spacing of 30 μm between them are performed. The sample preparation and nanoindentation tests are performed with S. Ryelandt at UCLouvain in Belgium.

The most exciting phrase to hear in science, the one that heralds new discoveries, is not 'Eureka!', but 'That's funny'...

— I. Asimov

6 INVESTIGATION OF MAX SINGLE CRYSTALS

Although the MAX phases have been around for more than 20 years [8], the lack of large single crystals has long prohibited a direct assessment of the anisotropy of the physical properties expected from their crystal structure. As a consequence, most of the works on electrical and thermal transport in MAX phases were performed on polycrystals [73, 108]. Since 2011, macroscopic single crystals are available [21, 42, 43], and some of their magneto-transport properties have been investigated [44, 45], as well as their electronic structure [46]. However, given the large diversity in the MAX phase composition, the current amount of experimental measurements performed on single crystal flakes is relatively low. In this context, a first step consists in the growth and characterization of MAX single crystals.

In the following sections, we focus on the properties of the ternary Cr_2AlC MAX phase and of the recently synthesized rare-earth containing MAX phases with the formula $(Mo_{2/3}RE_{1/3})_2AlC$ (RE = Nd, Sm, Gd, Tb, Dy, Ho, Er, Tm, and Lu). In Section 6.1, the structural, electronic, vibrational, thermal, and elastic properties of the Cr_2AlC MAX phase are investigated from both experimental and theoretical approaches. Section 6.2 reports on the growth of $(Mo_{2/3}RE_{1/3})_2$ AlC single crystals and presents their structural, dynamical, electronic, and elastic properties.

6.1 TERNARY CR_2ALC MAX PHASES

Large Cr_2AlC single crystals are grown and used to determine experimentally their structural, dynamical, and elastic properties. Complementarily, phonon dispersion spectra, thermal conductivity, and elastic constants are computed within the DFT and DFPT frameworks. In

Section 6.1.1, the experimental and optimized structural parameters of Cr_2AlC single crystals are reported. In Section 6.1.2, the vibrational properties are investigated, including the description of the phonon dispersion spectra using DFPT calculations and INS measurements. Additionally, the phonon mode symmetry and activity are studied and the sound velocities are evaluated. Section 6.1.3 presents the computed electronic band structure of Cr_2AlC and the experimental curve of the temperature dependence of the electrical resistivity. The electronic and lattice contributions to the thermal conductivity are computed using BoltzTraP2 code [290, 291] and TDEP code [303–305], respectively. The results are discussed in Section 6.1.4. Eventually, in Section 6.1.5, the elastic response of Cr_2AlC single crystals is investigated from both nanoindentation technique and *ab initio* calculations. Main conclusions are drawn in Section 6.1.6.

6.1.1 *Structural properties*

The conventional Cr_2AlC unit cell includes eight atoms - four Cr, two Al, and two C atoms - and crystallizes in the $P6_3/mmc$ (#194) space group with hexagonal symmetry (see Fig. 6.1(a)). The non-equivalent atomic positions are distributed in specific Wyckoff positions: $4f$ for the Cr atoms, $2d$ for the Al atoms, and $2a$ for the C atoms. The structural parameters are optimized within DFT [254, 255] using the ABINIT package [284, 285, 306]. The exchange-correlation functional is approximated using the PBE functional [262] and optimized norm-conserving Vanderbilt pseudopotentials [319] are used to describe core-valence interaction. A plane-wave kinetic energy cut-off of 40 Hartree is used and the first BZ is sampled with a $18 \times 18 \times 6$ Monkhorst-Pack k-point grid [269]. A Gaussian smearing of 1 mHa is used to accelerate the convergence. The complete set of cell parameters resulting from the structural optimization are reported in Table 6.1, together with experimental parameters with optimized atomic positions. The lattice parameter optimization leads to an underestimation of the experimental values, which is quite surprising given that GGA usually overestimates the lattice parameters. However, such underestimation of the lattice parameters of Cr_2AlC was already reported by Sun et al. [76]. Consequently, in order to accurately describe the phonon spectra of Cr_2AlC, we fix the lattice parameters using the experimental values measured from our samples, a = 2.86 Å and c = 12.82 Å, and we fully optimize

the atomic positions inside the cell until the largest force is smaller than 2.5 10^{-4} eV/Å.

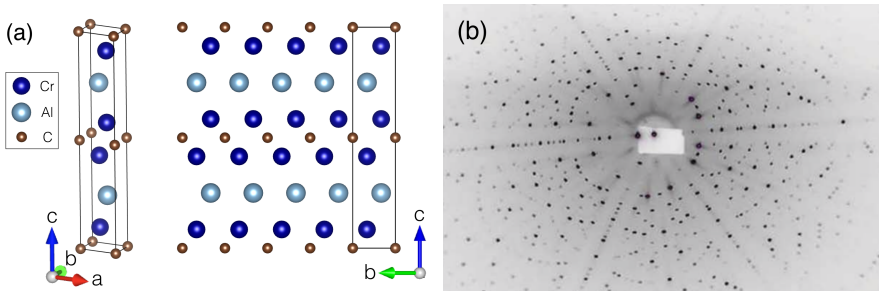

Figure 6.1: (a) Atomic structure of Cr_2AlC ($P6_3/mmc$ space group, a = 0.286 nm, c = 1.282 nm), and (b) transmission Laue diffraction pattern. From [320].

Table 6.1: Structural parameters computed *ab initio* considering a hexagonal $P6_3/mmc$ symmetry ($\alpha = \gamma = 90°$and $\gamma = 120°$) and compared to experimental parameters for single crystals with optimized atomic positions.

	Computed	Experimental
Unit cell dimensions		
a (Å)	2.843	2.860
b (Å)	2.843	2.860
c (Å)	12.708	12.820
Volume (Å^3)	88.955	90.814
Atomic positions		
Cr	$(\frac{1}{3}, \frac{2}{3}, 0.415)$	$(\frac{1}{3}, \frac{2}{3}, 0.414)$
	$(\frac{2}{3}, \frac{1}{3}, 0.915)$	$(\frac{2}{3}, \frac{1}{3}, 0.914)$
	$(\frac{2}{3}, \frac{1}{3}, 0.585)$	$(\frac{2}{3}, \frac{1}{3}, 0.586)$
	$(\frac{1}{3}, \frac{2}{3}, 0.085)$	$(\frac{1}{3}, \frac{2}{3}, 0.086)$
Al	$(\frac{1}{3}, \frac{2}{3}, 0.75)$	$(\frac{1}{3}, \frac{2}{3}, 0.75)$
	$(\frac{2}{3}, \frac{1}{3}, 0.25)$	$(\frac{2}{3}, \frac{1}{3}, 0.25)$
C	$(0, 0, 0)$	$(0, 0, 0)$
	$(0, 0, \frac{1}{2})$	$(0, 0, \frac{1}{2})$

6.1.2 *Vibrational properties*

The investigation of the vibrational properties of Cr_2AlC single crystals includes the description of the phonon dispersion spectra using DFPT calculations and INS measurements, the characterization of the phonon mode symmetry and activity, and the computation of the sound velocities. The dynamical matrix is computed within DFPT, using the ABINIT package [284, 285, 306], on a $6 \times 6 \times 6$ q-point grid in the Brillouin zone. Details regarding the INS measurements can be found in Section 5.2.

To date, experimental investigations of the vibrational modes in MAX phases are limited to the Raman-active modes and no work has reported the experimental phonon spectra by means of INS technique. The Raman-active vibrational modes of several MAX phases have been measured and calculated *ab initio* [22, 101–105]. In all cases, the low-wavenumber modes, that ranged from 5 to 40 meV were assigned to the vibrations of the M and A atoms; the X atoms vibrate at higher wavenumbers, that range from 65 to 85 meV, and were only observed in the 312 and 413 systems. In general, a good agreement was observed between first-principles calculations and experimental measurements.

According to the crystal information of the Cr_2AlC system, the eight atoms in the unit cell give rise to twenty-one optical modes and three acoustic modes at the Γ point. The energy, symmetry, and activity of the twenty-four phonon modes are listed in Table 6.2. Raman frequencies measured in Refs. [42, 102] are all recovered by the theoretical predictions. Additionally, the phonon spectrum computed along a high-symmetry path of the BZ is presented in Fig. 6.2(a) (blue solid lines), together with the experimental points (red dots) obtained from the recorded INS resonances along three crystallographic directions: $\Gamma-A$, $\Gamma-M$, and $M-L$. A very reasonable agreement is obtained. Both measurements and *ab initio* modeling confirm the existence of a substantial phonon gap, separating the first block, B1, of optical modes below 45 meV, from the second block, B2, centered around 80 meV. From Fig. 6.2(b), phonon modes in B1 involve the vibrations of the Cr and Al atoms, while those in B2 mainly involve the vibrations of the C and Cr atoms. A schematic representation of the atomic displacements for the six optical branches of B2 at the zone center is depicted in Fig. 6.3. For these modes, calculations predict that the vibration amplitude of the Al atoms is quite small in comparison with that of the Cr and C

atoms. This can be explained from the weaker Cr−Al bonding strength with respect to the strong Cr−C bonds. Since the Al atoms are almost immobile, the system can be seen as Cr_2C planes vibrating independently from the Al layers. Consequently, for a phonon wave vector close to the Γ point, the mode propagation can only take place in the *ab*-plane, involving the system to behave as a 2D system. This is confirmed by the calculations along the Γ−A, M−L, or H−K directions (along the *c*-axis), which predict very flat dispersion curves and further indicate that the analysis can be extended away from the Γ point (see Fig. 6.2(a)).

Table 6.2: Zone center phonon mode energy, symmetry, and activity.

	Phonon energy (meV)				
Mode no.	DFT	Raman [42, 102]	INS	Symmetry	Activity
1	0	–	–	A_{2u}	Acoustic
2 – 3	0	–	–	E_{1u}	Acoustic
4 – 5	12.14	–	12.45	E_{2u}	Silent
6 – 7	19.22	18.73	18.89	E_{2g}	Raman
8	19.52	–	–	B_{2u}	Silent
9 – 10	22.66	–	–	E_{1u}	IR
11 – 12	30.99	29.53	–	E_{1g}	Raman
13 – 14	31.04	30.77	30.83	E_{2g}	Raman
15	31.59	–	–	B_{1g}	Silent
16	40.55	–	40.00	A_{2u}	IR
17	41.27	41.69	42.13	A_{1g}	Raman
18	43.50	–	45.40	B_{1g}	Silent
19 – 20	78.92	–	77.00	E_{1u}	IR
21 – 22	79.17	–	–	E_{2u}	Silent
23	80.51	–	–	B_{2u}	Silent
24	80.53	–	–	A_{2u}	IR

Such a situation allows to produce a simplified, yet meaningful, analysis of the system. Limiting the system to one Cr_2C plane, two inequivalent Cr atoms and one C atom are identified so that the number of inequivalent atoms is $p = 3$. Consequently, if $d = 3$ is the number

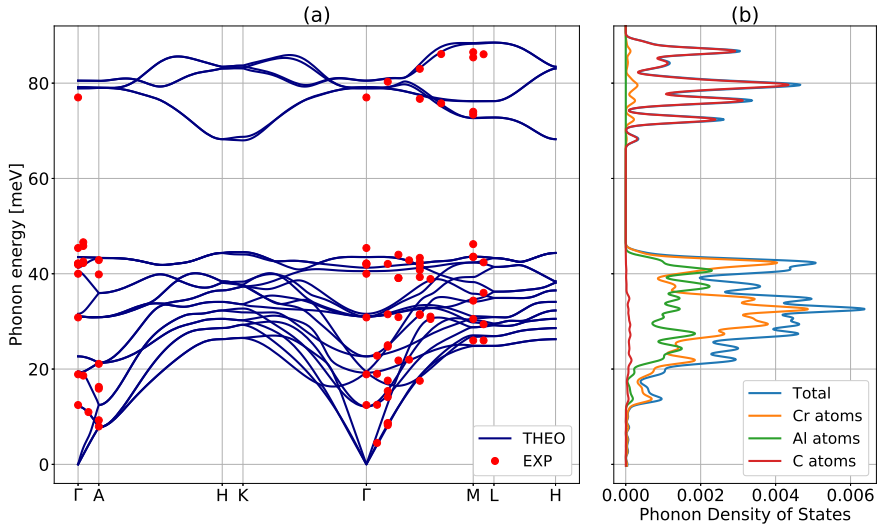

Figure 6.2: (a) First-principles phonon spectrum and experimental phonon energy modes of Cr_2AlC along major crystallographic directions and (b) corresponding theoretical phonon density of states separated among the various atomic constituents. From [320].

of possible directions for the vibrations (two in-plane and one out-of-plane), $d(p-1) = 6$ optical branches are expected. The six optical branches can be decomposed into two transverse optical (TO) in-plane branches, two longitudinal optical (LO) in-plane branches, and two TO out-of-plane branches. DFT calculations predict that the two upper branches are almost degenerate at all wave vectors and correspond to the schematics in Figs. 6.3(e) and 6.3(f). The four remaining in-plane modes can be assigned to the TO modes in Figs. 6.3(a) and 6.3(c), and the LO modes in Figs. 6.3(b) and 6.3(d).

The experimentally investigated acoustic branches along the $\Gamma-M$ direction are in good agreement with theoretical predictions, as evidenced in Fig. 6.2(a). Sound velocities of these acoustic branches can be estimated using the *ab initio* phonon spectrum. It is important to have in mind that both transverse and longitudinal sound velocities depend on the direction since the slope at the Γ point is not the same in every direction. In the ABINIT package, the sound velocities are computed within one of the following approximations: the linear approximation or the gradient method. While the linear approximation simply calcu-

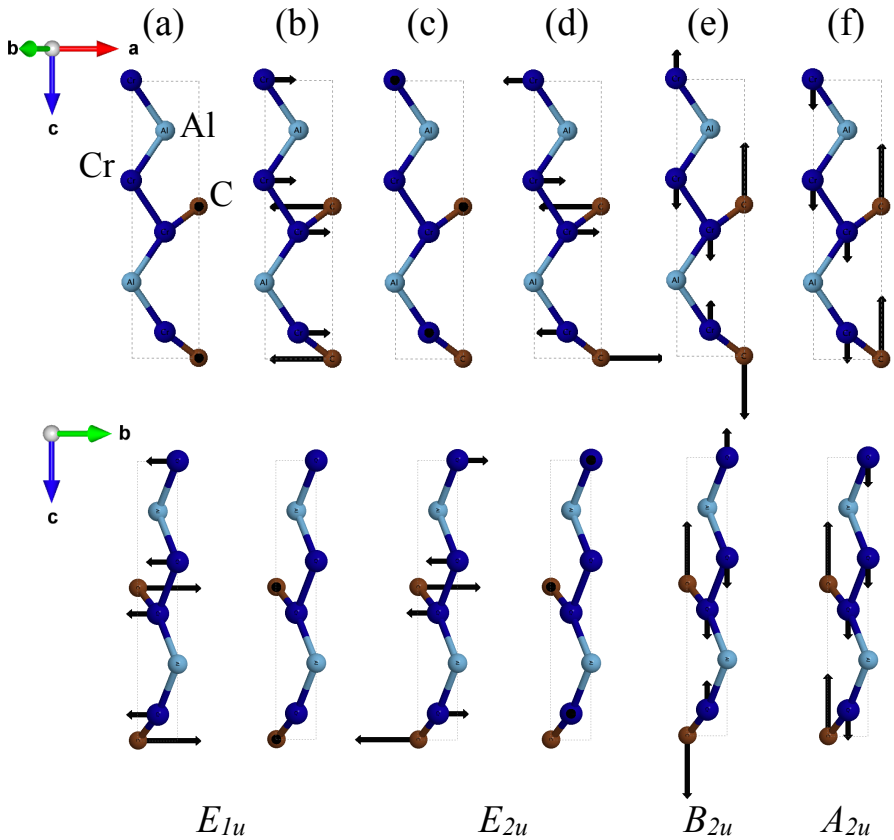

Figure 6.3: Schematic representation of the atomic displacements for the six highest phonon energy modes at Γ. (a) and (c) are in-plane transverse optical modes, (b) and (d), in-plane longitudinal optical modes, and (e) and (f), out-of-plane transverse optical modes. The arrows schematically represent the atomic displacement for the specific vibration mode. From [320].

lates ω/q assuming a linear behavior, the gradient method calculates the gradient of the mode frequency with respect to the vector q:

$$v_g(q\nu) = \nabla_q \omega(q\nu) = \frac{\partial \omega(q\nu)}{\partial q} \tag{6.1}$$

where $\omega(q\nu)$ is the mode frequency of the band index ν at the wave vector q. Using the gradient method, the sounds velocities along the Γ−M direction (in the *ab*-plane) are $v_{\mathrm{TA}_1} = 4.820$, $v_{\mathrm{TA}_2} = 5.216$, and $v_{\mathrm{LA}} = 7.664\,\mathrm{km.s^{-1}}$, for the first transverse, second transverse, and longitudinal acoustic modes, respectively. Similarly, along the

$\Gamma-K$ direction (in the *ab*-plane), $v_{TA_1} = 4.821$, $v_{TA_2} = 5.216$, and $v_{LA} = 7.664\,\mathrm{km.s^{-1}}$ are respectively estimated. At last, along the $\Gamma-A$ direction (along *c*-axis), $v_{TA_1} = 5.057$, $v_{TA_2} = 5.057$, and $v_{LA} = 9.567\,\mathrm{km.s^{-1}}$ are respectively calculated. Values are typical of materials with intermediate bonding strength. From the point of view of sound velocities, the material is almost isotropic. This results from the comparable intra- and inter-plane bonding strengths in the MAX phases.

As a general conclusion regarding the vibrational properties of Cr_2AlC, the agreement between first-principles calculations and INS measurements gives confidence to both these techniques for predicting and measuring the physical properties of nano-lamellar materials such as the MAX phases. In Cr_2AlC, *ab initio* modeling predicts the anisotropy of the phonon branches with a very accurate way. However, from the point of view of sound velocities, the material is almost isotropic. Eventually, the existence of a substantial phonon gap which pushes six optical branches at higher energy is confirmed by both theoretical and experimental approaches. Although the gap is not large enough for prohibiting two-phonons decays [320], the possibility to find large optical phonon lifetimes deserves to be further investigated, as well as their impact on electron–phonon coupling, electrical transport, or heat dissipation.

6.1.3 *Electronic properties*

Similar to all MAX phases, Cr_2AlC exhibits a metallic behavior ensured by the presence of Cr-*d* orbitals at the Fermi level, in agreement with recent ARPES measurements [46]. From Fig. 6.4, some anisotropy in the electronic properties can be predicted. While the branches along the $\Gamma-K$, $\Gamma-M$, and $L-H$ directions (in the *ab*-plane) are very dispersive, those along the $\Gamma-A$, $H-K$, and $M-L$ directions (along the *c*-axis) are almost flat. The anisotropy in the electronic band structure reflects the anisotropy observed experimentally in the conductivity measurements [44].

In order to gain insight into the transport properties of Cr_2AlC single crystals, the in-plane electrical resistivity $\rho_{\parallel}(T)$ is measured experimentally with V. Natu at Drexel University in USA, using a 4-probe configuration as the one depicted in Fig. 6.5(c). For this purpose,

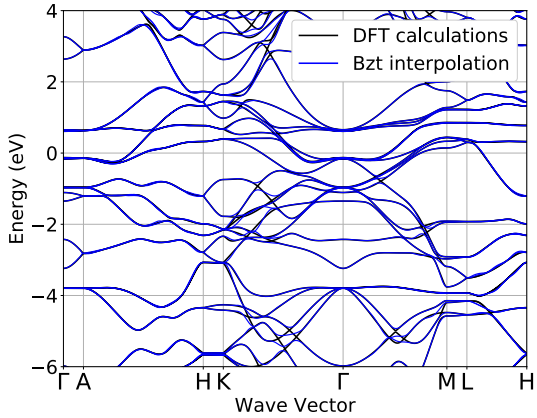

Figure 6.4: First-principles electronic band structure of Cr_2AlC (black lines) compared to the band interpolation achieved with the BoltzTraP2 code (blue lines). The Fermi level is fixed as the reference of zero energy.

Cr_2AlC single crystals are grown following the procedure described in Section 2.2.2 and polished to get a uniform thickness. They are then cut with a diamond wire saw in order to obtain square-shaped samples of about $1-2\,\mathrm{cm}^2$. Four equidistant and parallel Cr/Au contact pads are deposited on the Cr_2AlC single crystals. The initial Cr layer is 10 nm thick followed by 150 nm thick gold layer. Later, silica sheathed copper wires are attached to the gold pads using graphite glue (Ted Pella, USA). The whole assembly is placed inside a furnace under flowing Argon, and the furnace heats up to 700°C using a 5°C/minute ramp rate. The copper wire contacts coming out of the furnace are passed through a rubber stopper to protect the inert atmosphere inside. A 100 mA current is passed through the outer wires using a constant current source (Hewlett-Packard, DC current source, USA) and the voltage at the inner probes is recorded using a voltmeter (Keithley Instruments, USA). The correction factor is calculated according to Ref. [321].

The in-plane electrical resistivity $\rho_{\parallel}(T)$ is depicted in Fig. 6.5(a). Not surprisingly, a linear temperature-dependence is observed, as is usual in metals, due to the linear increase of the phonon occupation with temperature. This experimental curve will be further used to investigate the thermal transport in Cr_2AlC single crystals in Section 6.1.4. A value of $\sim 0.7\,\mu\Omega\mathrm{m}$ is obtained at 50°C, which is in agreement with previous reports for Cr_2AlC polycrystals with electrical resistivities ranging from 0.6 to $0.74\,\mu\Omega\mathrm{m}$ at 300 K [73, 322, 323]. It can be noted here that the electrical resistivity of Cr_2AlC is almost twice higher than

the one of other M_2X systems [1], *e.g.*, Ti_2AlC [324], V_2AlC [73], and Nb_2AlC [73] show electrical resistivities of 0.36, 0.25, 0.29 $\mu\Omega$m, respectively, at 300 K.

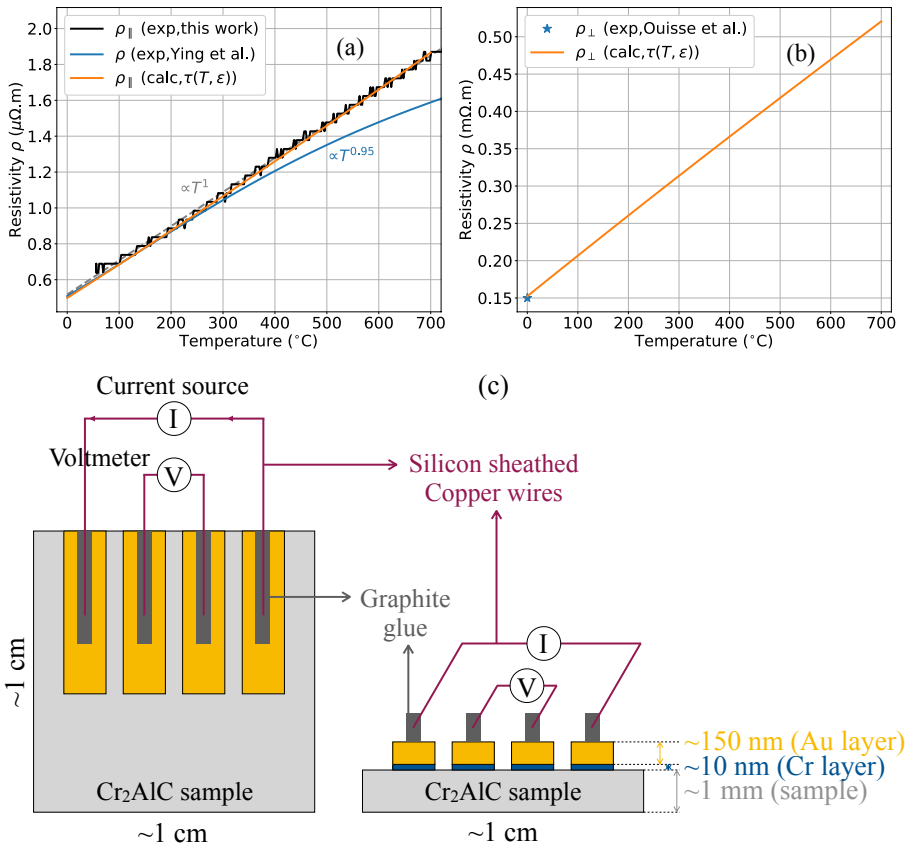

Figure 6.5: (a) Measured in-plane electrical resistivity $\rho_\parallel$ for Cr_2AlC single crystals (black line), compared to experimental data from Ref. [322] for a polycrystalline sample (blue line), and to the computed in-plane resistivity (orange line) using the model relaxation time $\tau(T,\varepsilon)$ defined in Eq. 6.3. The dashed gray line is a guide to the eye, highlighting the linear temperature dependence of the resistivity. (b) Predicted out-of-plane resistivity (orange line) using $\tau(T,\varepsilon)$, compared to experimental data from Ref. [44]. (c) Schematic of the 4-probe configuration, with equidistant pads, used to measure the temperature-dependence of the in-plane resistivity (shown in (a)).

6.1.4 *Thermal transport*

The thermal conductivity can be decomposed into its electronic and lattice contributions, such that $\kappa = \kappa_e + \kappa_l$. The transport theory for electrons is implemented in the BoltzTraP2 code [290, 291] which computes the electronic transport coefficients assuming rigid bands (unchanged either with doping or temperature) and usually a constant relaxation time τ_0 (see Section 4.7.1). The estimation of the lattice contribution implies the inclusion of anharmonic processes and, hence, the computation of the third-order force constant matrix. The effective second- and third-order IFC are obtained at a given temperature from a fit of DFT forces in supercells, with thermally displaced atoms (based on initial DFPT harmonic estimates) using the TDEP code [303–305]. The lattice thermal conductivity tensor and cumulative thermal conductivity are then obtained from the iterative solution of the phonon BTE (see Secion 4.7.2). External and internal scattering processes are also considered, *i.e.*, vacancy, isotope, and grain boundary scattering processes. The isotopic concentrations are chosen to be as close as possible to the natural ones: carbon of 98.93% ^{12}C, 1.07% ^{13}C, aluminum of 100% ^{27}Al, and chromium of 4.35% ^{50}Cr, 83.79% ^{52}Cr, 9.50% ^{53}Cr, 2.36% ^{54}Cr. The determination of the phonon scattering rates due to three-phonon collisions and to extrinsic scattering processes using an *ab initio* approach is described in detail in Refs. [303–305].

Electronic thermal conductivity

As a first approximation, the electronic contribution to the thermal conductivity κ_e can be quickly estimated using the Wiedemann-Franz law as:

$$\kappa_e = \frac{L_0 T}{\rho(T)} \tag{6.2}$$

In this relationship, $L_0 = 2.45 \times 10^{-8}\mathrm{W\Omega K^{-2}}$ is the Lorentz number and $\rho(T)$ is the temperature-dependent electrical resistivity. The experimental in-plane electrical resistivity $\rho_{\parallel}(T)$ depicted in Fig. 6.5(a) is used to compute the in-plane electronic thermal conductivity $\kappa_e^{\parallel}$. As expected from the quasi-linear temperature-dependence of the resistivity, an almost temperature-independent electronic thermal conductivity is observed in Fig. 6.6(a).

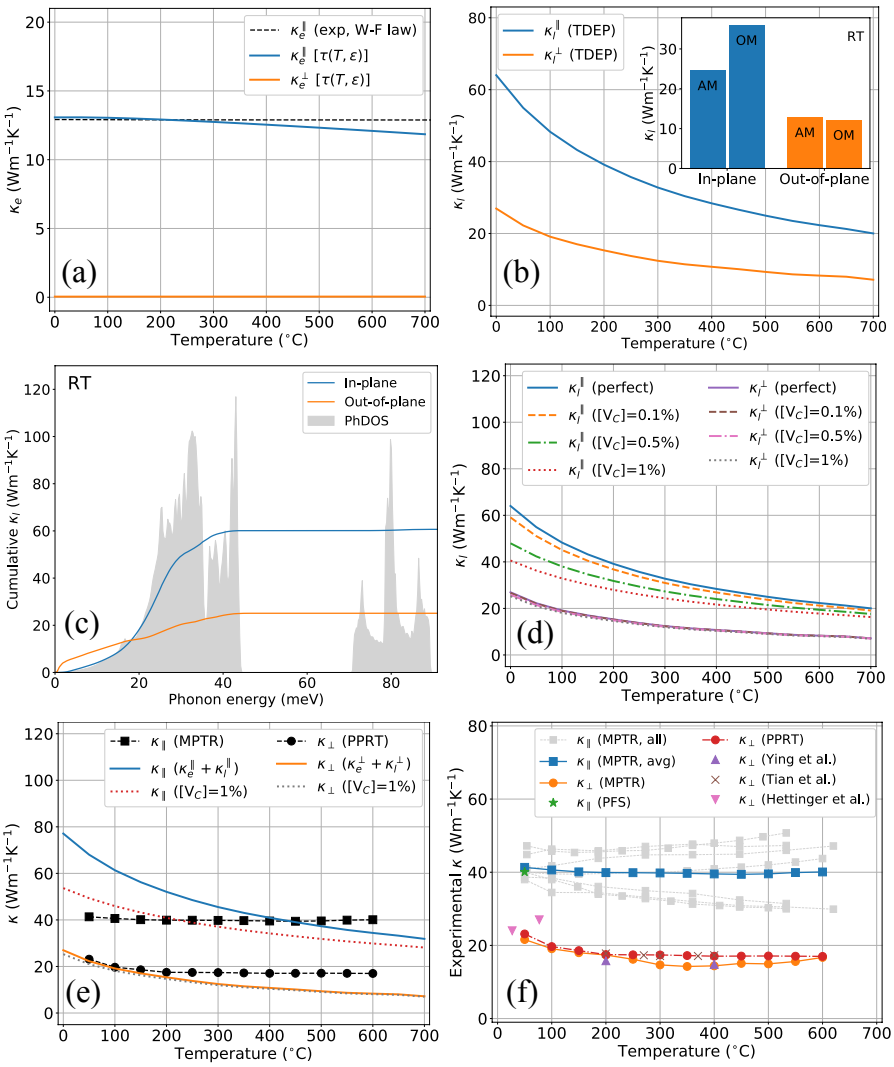

Figure 6.6: (a) In-plane κ_e obtained from the Wiedemann-Franz law considering the experimental electrical resistivity $\rho_{\parallel}(T)$ from Fig. 6.5(a) and κ_e computed with a temperature- and energy-dependent electronic relaxation time defined in Eq. 6.3, (b) κ_l computed with anharmonic phonon-phonon scattering processes, with the contribution from optical and acoustic modes (OM and AM, respectively) at RT shown in the inset, (c) cumulative lattice thermal conductivity at RT, (d) temperature dependence of the lattice thermal conductivity κ_l for various concentrations of C vacancies, (e) total computed thermal conductivity obtained by summing the electronic and lattice contributions: $\kappa = \kappa_e + \kappa_l$, compared to the experimental curves, and (f) measured in-plane and out-of-plane thermal conductivities using various techniques, compared to values found in the literature [73, 322, 323].

From first-principles, the electronic contribution to the thermal conductivity κ_e can be obtained by solving the BTE for electrons (see Section 4.7.1). The integration of the BTE requires an accurate description of the electronic band structure. The BoltzTraP2 code [290] provides such a description using an interpolation method based on a Fourier expansion that takes as input the electronic energies for different k-points, previously calculated by a DFT code (see Fig. 6.4). The code then computes the Fermi integrals for different temperatures and Fermi levels, and returns as output all the transport coefficients $(\sigma, \kappa, ...)$ [290, 291]. Calculations are performed at constant doping (equal to zero). As mentioned in Section 4.7.1, in order to obtain a good description of the electronic properties of metallic systems, a realistic electronic relaxation time must be considered in Eq. 4.46. Therefore, a temperature- and energy-dependent model for the relaxation is defined, implemented in the BoltzTraP2 code, and used herein. Given that we are interested in the $[0-700]$°C temperature range for which the relaxation time is governed by electron-phonon scattering processes, the expression of the relaxation time is given by:

$$\tau\left(T,\varepsilon\right) = \tau_{\text{ref}}\left(\frac{T}{T_{\text{ref}}}\right)^{-1}\left(\frac{\varepsilon}{\varepsilon_{\text{ref}}}\right)^{-1/2} \tag{6.3}$$

where τ_{ref} is a suitable reference value at a temperature T_{ref} and ε_{ref} is taken as the Fermi energy for a metallic system. The T^{-1} dependence in the model relaxation time allows to recover the linear temperature dependence of $\rho_{\parallel}(T)$ in Fig. 6.5(a). A value of $\tau_{\text{ref}} = 5\,\text{fs}$ at $T_{\text{ref}} = 273\,\text{K}$ is chosen to fit the experimental in-plane resistivity curve in Fig. 6.5(a), and is in good agreement with recently determined electronic relaxation times in Cr_2AlC single crystals [325]. Based on the anisotropy ratio $\rho_{\perp}/\rho_{\parallel} \sim 300$ obtained experimentally by Ouisse *et al.* [44], a value of $\tau_{\text{ref}} = 0.06\,\text{fs}$ at $T_{\text{ref}} = 273\,\text{K}$ is chosen to fit the out-of-plane resistivity value of $1.5 \times 10^{-4}\,\Omega\text{m}$ at 273 K (see Fig. 6.5(b)).

In Fig. 6.6(a), $\kappa_e^{\parallel}$ and $\kappa_e^{\perp}$ are reported using the temperature- and energy-dependent relaxation time defined in Eq. 6.3. A value of $13\,\text{Wm}^{-1}\text{K}^{-1}$ ($0.04\,\text{Wm}^{-1}\text{K}^{-1}$) at RT for the in-plane (out-of-plane) direction is obtained, and remains quasi-constant in the whole temperature range. Not surprisingly, the Wiedemann-Franz law gives a good approximation of the electronic thermal conductivity, and leads to results similar to those obtained with the BoltzTraP2 code using a temperature- and energy-dependent relaxation time (see Fig. 6.6(a)).

Lattice thermal conductivity

The lattice thermal conductivity κ_l in a harmonic crystal is infinite and not a function of the temperature. The lattice thermal resistance is dictated by phonon scattering processes that can be intrinsic, through anharmonic phonon-phonon scattering, or extrinsic, induced by isotopic disorder, point defects, or edge effects.

A first microscopic description of the lattice thermal conductivity was formulated in 1929 by Peierls [297], and is nowadays known as the phonon BTE. General details on the phonon BTE can be found in Section 4.7.2, as well as information on the commonly used single mode approximation (SMA) [298–300]. However, the SMA has shown some limitations to accurately describe the lattice thermal conductivity in layered compounds and 2D systems [301].

Recently, Hellman *et al.* [303–305] proposed a formalism to obtain the third-order IFC and to accurately calculate the lattice thermal conductivity from the iterative solution of the phonon BTE (see Section 4.7.2). The first step consists in computing the second- and third-order force constant matrices that are both temperature- and volume-dependent. For this purpose, an ensemble of thirty non-correlated configurations generated from a gaussian distribution of harmonic input phonons is used to sample the Born-Oppenheimer potential energy surface at finite temperature. Then, a minimization scheme between the model forces and the *ab initio* computed forces is used, and leads to the direct determination of the force constant matrices. The second step consists in iteratively solving the phonon BTE in Eq. 4.53, starting from an initial guess F_ν^0 to obtain the non-equilibrium distribution.

Figure 6.6(b) presents the computed lattice thermal conductivities in-plane $\kappa_l^{\parallel}$ and out-of-plane $\kappa_l^{\perp}$ for Cr_2AlC single crystals, when only anharmonic phonon-phonon scattering processes are considered. Both in-plane and out-of-plane κ_l decrease with the temperature, which is a signature of umklapp-dominated scattering processes. Although Cr_2AlC has relatively isotropic sound velocities (see Section 6.1.2), it has a significantly anisotropic lattice thermal conductivity. This can be explained from the cumulative κ_l depicted in Fig. 6.6(c) where the anisotropy clearly starts at energies greater than 20 meV, mostly corresponding to optical modes. The low-lying optical branches - with energy below 40 meV - in the phonon spectrum of Cr_2AlC (see Fig. 6.2(a))

are very dispersive, with higher group velocities in the *ab*-plane (along $\Gamma-$K and $\Gamma-$M) than along the *c*-axis (along $\Gamma-$A). Consequently, the optical modes significantly contribute to κ_l, particularly for the in-plane direction as shown in the inset of Fig. 6.6(b). This decomposition partly explains the intrinsic anisotropy predicted in the MAX phases, in general, and in Cr_2AlC, in particular.

The inclusion of isotopic scattering processes does not modify the lattice thermal conductivity, as expected from the small natural isotopic diversity of Cr, Al, and C elements. Grain boundary scattering processes can play an important role in phonon transport as polycrystallinity tends to drastically decrease the lattice thermal conductivity [326]. However, there is no reason to include these scattering processes since all measurements are performed on single crystals with a single grain of a few cm^2. Phonon scattering from point defects can also play an important role in limiting the thermal conductivity. Since both experimental and theoretical works gave evidence for significant amounts of vacancies in MAX phases [119, 327], these defects are taken into account in the computation of the lattice thermal conductivity. A vacancy can be regarded as a perturbation of the crystal corresponding to the removal of the mass of one atom and the force constants of two atoms [328]. Hence, the energy associated to a vacancy can be treated as equivalent to an isotopic defect corresponding to a change of mass $\Delta M = -3M$ where M is the atomic mass of the missing atom [328], *i.e.*, C atom in Cr_2AlC [327]. Concentrations of C vacancies ranging from 0.1% to 1% are considered. The results are presented in Fig. 6.6(d). While $\kappa_l^{\perp}$ remains almost constant over the whole temperature range, $\kappa_l^{\parallel}$ is reduced, especially in the $[0-300°C]$ temperature range by the inclusion of C vacancies. This can be understood from Fig. 6.2 and the related discussion about high-energy bands (B2 block) and their 2D character presented in Section 6.1.2. In fact, the presence or absence of C atoms only affects the in-plane phonon propagation and lattice thermal conductivity since, for the high-energy C-related modes, there is no phonon propagation feasible perpendicularly to the plane, due to the flatness of the bands.

Total thermal conductivity

The computed total thermal conductivities are presented in Fig. 6.6(e). It is observed that both $\kappa_{\parallel}$ and $\kappa_{\perp}$ slightly decrease with the tempera-

ture. An anisotropy ratio higher than ~ 2.5 is predicted over the whole temperature range.

Experimentally, the thermal conductivity of Cr_2AlC single crystals is measured in Battaglia's group (Bordeaux, France) using various techniques, including the modulated photothermal radiometry (MPTR) [329], the pulsed flying spot (PFS) [330], and the periodic pulse radiometry technique (PPRT) [331]. The temperature-dependent in-plane thermal conductivities $\kappa_{\parallel}$ measured on several Cr_2AlC samples using the MPTR are depicted in gray in Fig. 6.6(f). The deviations between the different gray curves result from the variable quality of the different samples. They still provide results in the same order of magnitude, with an average thermal conductivity curve depicted in blue in the same figure. Using the same technique, the out-of-plane thermal conductivity $\kappa_{\perp}$ of a unique sample is measured and depicted in orange in Fig. 6.6(f). Values of $\kappa_{\parallel} = 41.3\,\mathrm{Wm^{-1}K^{-1}}$ and $\kappa_{\perp} = 21.6\,\mathrm{Wm^{-1}K^{-1}}$ are obtained at RT. In addition, using the PFS, an in-plane thermal diffusivity $a_{\parallel}$ of $11.4\,\mathrm{mm^2s^{-1}}$ is measured at RT, leading to $\kappa_{\parallel} = 40.8\,\mathrm{Wm^{-1}K^{-1}}$. The temperature dependence of $\kappa_{\perp}$ is also measured using the PPRT technique and the results are reported in red in Fig. 6.6(f). These values confirm rather well those obtained with the MPTR technique, although the slight increase at the highest temperatures is not observed anymore. Given the high standard deviation on $\kappa_{\perp}$ using the MPTR technique, we suspect the increase is spurious. Comparisons with values of $\kappa_{\perp}$ in the literature are also reported in Fig. 6.6(f). The measurements obtained by Tian *et al.* [323] in a more narrow temperature range fit rather well with the present measurements. As a global observation, the in-plane thermal conductivity is found to be almost constant in the whole temperature range, whereas the out-of-plane thermal conductivity slightly decreases with the temperature and then saturates from 200°C. More importantly, an anisotropy ratio of about 2 is found over the whole temperature range.

In Fig. 6.6(e), the computed total thermal conductivities are compared to the experimental data. A qualitative agreement is found between experimental and computed thermal conductivity curves, with an overestimation of the experimental $\kappa_{\parallel}$ by 65% and an underestimation of the experimental $\kappa_{\perp}$ by 4% at 50°C. The overestimation of $\kappa_{\parallel}$ can be due to various electron/phonon scattering sources and intrinsic structural defects present in the samples and not taken into account in the calculations. For example, it was shown in Fig. 6.6(d) that the inclusion of C vacancies in our model reduces

$\kappa_{\parallel}$ in the $[0 - 300°C]$ temperature range, while keeping $\kappa_{\perp}$ constant. Consequently, the deviation between the calculated and experimental in-plane thermal conductivities at 50°C goes down to 55% and 19% considering scattering processes with C vacancies, with a concentration of 0.1 and 1%, respectively. This confirms that the overestimation of the in-plane thermal conductivity can be explained by missing scattering processes in the calculations, which can play an important role especially around RT.

The main result is the quantitative analysis of the anisotropy in the thermal conductivity of Cr_2AlC single crystals confirmed by both experimental and theoretical approaches. This anisotropy arises from both the electronic and lattice contributions; the latter being the dominant term. At RT, the lattice contribution represents $\sim$ 81% of the total in-plane thermal conductivity, and decreases with T to reach 63% at 600°C. For the out-of-plane thermal conductivity, the electronic contribution is almost zero and the thermal transport is only feasible through lattice vibrations.

6.1.5 *Elastic properties*

In order to gain insight into the elastic properties of Cr_2AlC single crystals, the full elastic tensor is computed *ab initio* using the VASP package [286–288]. PAW pseudopotentials are used to describe the core-valence interactions [266–268]. A plane-wave kinetic energy cut-off of 520 eV is used and the first Brillouin zone is sampled with a $12 \times 12 \times 4$ Monkhorst-Pack k-point grid [269]. A Gaussian smearing of 0.2 eV is used to accelerate the convergence. The atomic positions are optimized beforehand until the largest force is smaller than 0.1meV/Å. Homogeneous elastic moduli, *i.e.*, bulk, shear, and Young's moduli, are estimated from the elastic constants. Additionally, nanoindentation tests are performed allowing for the experimental determination of elastic constants and hardness. For this purpose, Cr_2AlC single crystals are mounted on a aluminum puck (in epoxy resin) for indentation perpendicular (parallel) to the *ab*-plane, and polished to a mirror finish.

First-principles calculations

For hexagonal symmetry, five non-zero independent elastic constants c_{ij} are defined, namely c_{11}, c_{12}, c_{13}, c_{33}, and c_{44} [332]. The elastic con-

stant c_{66} is given by $c_{66} = (c_{11} - c_{12})/2$. The single crystal elastic constants can be determined from the computation of the stress associated to a set of six imposed homogeneous finite deformations of $\pm 1.5\%$ along the three cartesian coordinates (see Section 4.6). In Table 6.3, the elastic constants c_{ij} computed at zero pressure and zero temperature are listed for the Cr_2AlC system. It is observed that the diagonal c_{11} and c_{33} values are larger than all other constants, with $c_{11} > c_{33}$.

From the calculated c_{ij}, the homogenized polycrystalline elastic properties, including the bulk modulus B, the shear modulus G, the Young's modulus E, and the Poisson's ratio ν, are computed. For hexagonal systems, the Voigt bulk and shear moduli (upper bound) can be obtained, respectively, assuming [332]:

$$B_V = \frac{1}{9}\left[2\left(c_{11} + c_{12}\right) + 4c_{13} + c_{33}\right] \tag{6.4}$$

$$G_V = \frac{1}{15}\left(2c_{11} + c_{33} - c_{12} - 2c_{13}\right) + \frac{1}{5}\left[2c_{44} + \frac{1}{2}\left(c_{11} - c_{12}\right)\right] \tag{6.5}$$

The Reuss bulk and shear moduli (lower bound) are given, respectively, by [332]:

$$B_R = \frac{c^2}{c_{11} + c_{12} + 2c_{33} - 4c_{13}} \tag{6.6}$$

$$G_R = \frac{5}{2}\left[\frac{c^2 c_{44} c_{66}}{3B_V c_{44} c_{66} + c^2\left(c_{44} + c_{66}\right)}\right] \tag{6.7}$$

with $c^2 = \left(c_{11} + c_{12}\right) c_{33} - 2c_{13}^2$. The arithmetic averages of Voigt and Reuss moduli are known as Hill moduli given by [333]:

$$B_H = \frac{B_V + B_R}{2} \tag{6.8}$$

$$G_H = \frac{G_V + G_R}{2} \tag{6.9}$$

Using the calculated values of B_H and G_H, the average Young's modulus E and the Poisson's ratio ν can be obtained, respectively, assuming [333]:

$$E_H = \frac{9B_H G_H}{3B_H + G_H} \tag{6.10}$$

$$\nu = \frac{3B_{\mathrm{H}} - 2G_{\mathrm{H}}}{2\left(3B_{\mathrm{H}} + G_{\mathrm{H}}\right)} \tag{6.11}$$

The values of the elastic properties reported in Table 6.3 are in good agreement with computed values previously reported [334].

Eventually, the directional elastic moduli are given by:

$$\frac{1}{E_i} = s_{11}l_1^4 + 2s_{12}l_1^2l_2^2 + s_{22}l_2^4 + 2s_{23}l_2^2l_3^2 + s_{33}l_3^4 + 2s_{13}l_1^2l_3^2 + s_{44}l_2^2l_3^2 + s_{55}l_1^2l_3^2 + s_{66}l_1^2l_2^2 \tag{6.12}$$

where s_{ij} are the compliance constants obtained by inverting the 6×6 elastic tensor, and l_1, l_2, and l_3 are the directional cosines of angles between the three principal directions (x, y, and z) [335]. The E_i's reported in Table 6.3 are very close to another showing limited anisotropy in the elastic properties.

Nano-indentation

In order to evaluate the accuracy of the present theoretical data, the elastic response of a Cr_2AlC single crystal is measured experimentally using nanoindentation. Nanoindentation tests are performed at RT using a Berkovich tip calibrated on a standard amorphous silica sample (see Section 5.3). Eighteen indents are performed perpendicularly to the *ab*-plane while twenty-eight indents are performed parallel to the *ab*-plane. Representative load-displacement curves for both indentation configurations are depicted in Fig. 6.7(a). In both cases, a load of 150 mN is required to indent the sample $\sim$ 900 nm. From Fig. 6.7(a), we also observe a series of small and discontinuous pop-ins, which are mostly evident for the indentation normal to the basal plane (blue curve). Typical SEM micrographs of indents made on Cr_2AlC are shown in Figs. 6.7(b) and 6.7(c), respectively for indentation tests performed perpendicularly and parallel to the *ab*-plane. Interestingly, short cracks confined to the indenter imprint are observed in both micrographs, and well-defined piles-up around the indenter are more evident in case of indentation perpendicularly to the *ab*-plane, coincident with the pop-ins in Fig. 6.7(a). Both deformation responses are common features to most MAX phases [336]. In fact, the combination of large pileups (buckling marks) and delamination cracks are the signatures of deformation by ripplocations [66, 67].

Table 6.3: Theoretical elastic constants and moduli (in GPa) for the Cr_2AlC system computed at experimental lattice parameters with optimized atomic positions. For comparison, previous theoretical results are presented [334]. In addition, experimental elastic constants obtained from nanoindentation are reported in the fourth column.

	DFT		Nano-
	PBE	PW91 [334]	indentation
c_{11}	347.03	365	317 ± 10
c_{12}	77.15	84	–
c_{13}	91.21	102	–
c_{33}	332.49	369	320 ± 9
c_{44}	129.49	140	–
B_H	171.75	186	–
G_H	129.81	138	–
E_H	311.06	332	–
ν	0.20	0.20	–
E_1	347.03	–	317 ± 10
E_2	342.95	–	–
E_3	332.50	–	320 ± 9

Using the Oliver and Pharr method [318, 338], the average value of E_3 is evaluated from the 18 indents performed perpendicularly to the *ab*-plane to be 320 ± 9 GPa. Similarly, the average value of E_1, from the 28 indents performed parallel to the *ab*-plane is found to be 317 ± 10 GPa. In comparison, the computed values of E_3 and E_1 of Cr_2AlC are respectively 332 and 347 GPa. This 10% overestimation is reasonable and is typical of DFT calculations [1], considering that both defects and temperature are not included in the calculations. For MAX phases in general, an increase of the temperature by 500°C can result in a decrease by up to 10% of the Young's modulus [1]. Noteworthy, both experimental and theoretical approaches predict that Cr_2AlC single crystals are isotropic from the point of view of their elastic properties. This is consistent with theoretical [339] and experimental [340, 341] works identifying the Ti_3SiC_2 MAX phase as elastically isotropic. The isotropy of the MAX phase elastic properties is in contrast to most known layered solids, *e.g.*, graphite and mica, which are highly

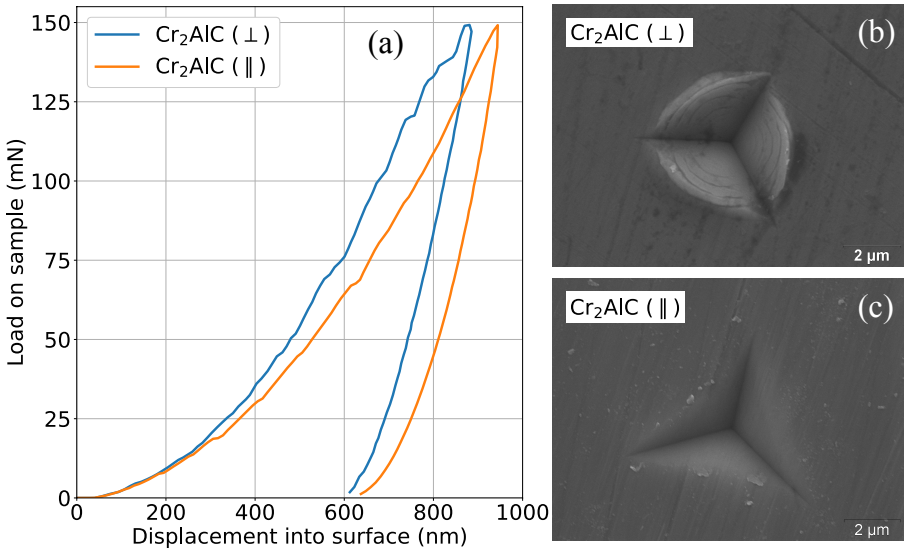

Figure 6.7: (a) Representative load−displacement curves from the nanoindentation of the top surface and sample side of a Cr_2AlC single crystal and scanning electron microscope images of the indentation marks of indent performed (b) perpendicularly to the *ab*-plane and (c) parallel to the *ab*-plane of a Cr_2AlC single crystal. Adapted from [337].

anisotropic. Such isotropy in the elastic properties, as well as in the sound velocities, results from the similar and comparable intra- and inter-layer bonding strengths in the MAX phases, in contrast to the weak van der Waals interlayer bonds in graphite-like materials.

Eventually, another fundamental physical parameter that can be determined from nanoindentation is the hardness H. Using the Oliver and Pharr method [318, 338], the Berkovich hardness of Cr_2AlC single crystal is evaluated to 9.7 ± 0.3 GPa (8.4 ± 0.4 GPa) in a direction perpendicular (parallel) to the *ab*-plane. In comparison, the Vickers hardness values of polycrystalline Cr_2AlC MAX phases range from 6 to 9 GPa [336]. The small, but present, anisotropy in the hardness values of Cr_2AlC highlights the interesting and unique feature of the MAX phases, which respond in an isotropic way to elastic deformation and anisotropically to plastic deformation. This is further evidenced in the SEM micrographs (Figs. 6.7(b) and 6.7(c)) where, as mentioned previously, some pileups and delamination cracks are respectively observed upon loading perpendicular and parallel to the basal plane.

6.1.6 *Conclusions*

In conclusion, the structural, electronic, vibrational, thermal, and elastic properties of Cr_2AlC single crystals are reported, combining experimental and theoretical approaches. The anisotropy observed in many physical properties of Cr_2AlC single crystals presumably results from the intrinsic structural anisotropy prevailing in these layered compounds.

Regarding the electronic properties, Cr_2AlC is electrically conductive with the Cr-4*d* electrons occupying the bands at the Fermi level, similarly to all MAX phases. The investigation of the vibrational properties includes the characterization of the phonon spectrum of Cr_2AlC, and the *ab initio* determination of phonon mode wavenumbers, symmetries, activities, and relative atomic displacements. The *ab initio* modeling and analysis of the band dispersion predicts the anisotropy of both electronic structure and phonon dispersion spectrum with a very satisfactory accuracy when compared to experiment. The existence of a substantial phonon gap in the phonon spectrum of Cr_2AlC, evidenced both experimentally and computationally, pushes 6 optical phonon branches at higher energy. Additionally, the in-plane and out-of-plane thermal conductivities of Cr_2AlC single crystals are predicted from first-principles calculations. An accurate microscopic description of heat transport is achieved and the electronic contribution to thermal conductivity is determined using a temperature-dependent electronic relaxation time. Solving iteratively the BTE for phonons, the lattice thermal conductivity is estimated. The inclusion of scattering processes by C vacancies slightly reduces the thermal conductivity with a more noticeable impact on the in-plane component. An anisotropy of about 2.5 is found between the in-plane and out-of-plane conductivities and seems to mainly arise from the lattice contribution. A similar anisotropy in the transport properties is expected for other MAX phases with identical layered structures. Finally, the elastic response of Cr_2AlC is investigated using both first-principles approach and nanoindentation technique. In contrast to most physical properties of Cr_2AlC single crystals, the elastic properties are found to be isotropic, with a Young's modulus around $\sim 320 \pm 10$ GPa, accurately predicted *ab initio* within 10% of deviation.

The high electronic, thermal, and elastic properties of Cr_2AlC presented in the previous sections confirm that MAX phases are good candidates for high-temperature structural applications, micromechan-

ical systems, or electrical contacts. We believe that the combination of first-principles and experimental approaches can be effectively applied in the future to investigate the anisotropy in the physical properties of layered systems, in general, and MAX phases, in particular.

6.2 RARE-EARTH CONTAINING MAX PHASES

Recently, a new route to increase the elemental combination of MAX phases and to optimize their performance was proposed, consisting in the addition of a fourth element, by alloying on the M, A, or X sites [15–17]. In particular, the existence of RE-i-MAX phases, with the general formula $(Mo_{2/3}RE_{1/3})_2AC$, was recently revealed [61, 62]. Because of their complex magnetic order, characteristic of magnetically frustrated systems due to competing intra- and in-plane magnetic interactions [61], these new phases are expected to attract much attention from the scientific community. Moreover, since some of these new systems are Al-based, the Al should, in principle, be selectively etched to create RE-i-MXenes, where the RE elements are ordered in the basal plane. This may significantly enlarge the palette of magnetic 2D crystals for spintronic applications.

Motivated by these recent discoveries and the possibility to use these magnetic phases as precursor layered compounds to synthesize 2D magnetic MXenes, we investigate their structural, vibrational, elastic, and electronic properties, using both experimental and theoretical approaches. In Section 6.2.1, we report on the growth of single crystals of various $(Mo_{2/3}RE_{1/3})_2$ AlC (RE = Nd, Sm, Gd, Tb, Dy, Ho, Er, Tm, and Lu) phases and their optimized structural parameters. STEM images are used to confirm the crystal structure. In Section 6.2.2, using first-principles, the wavenumbers of the various phonon modes and their relative atomic displacements are calculated and compared to experimental results. Twelve high-intensity Raman peaks are identified as the fingerprint of this new family of RE-i-MAX phases, thus being a useful tool to investigate their corresponding composition and structural properties. Additionally, a complete classification of bond stiffnesses is achieved based on the direct dependence of a phonon mode wavenumber with respect to the bond stiffness. In Section 6.2.3, first-principles calculations are performed to investigate the elastic response of $(Mo_{2/3}RE_{1/3})_2AlC$ single crystals. The Voigt-Reuss-Hill bulk, shear, and Young's moduli are compared along the series of RE = Nd,

Sm, Gd, Tb, Dy, Ho, Er, Tm, and Lu, and the global trend is found to depend on the unit cell volume. Additionally, single crystals of these novel systems are characterized through nanoindentation to determine the elastic and hardness response. Section 6.2.4 investigates the electronic properties and bonding characters within RE-i-MAX phases via the computation of the projected density of states, projected crystal orbital Hamilton population, and integrated projected crystal orbital Hamilton population. Finally, in order to gain insight into the exfoliation potential of the RE-i-MAX phases, their static exfoliation energies are computed and compared to the values for conventional MAX phases. Results are presented and discussed in Section 6.2.5. Section 6.2.6 summarizes our studies conducted on the RE-i-MAX phases.

6.2.1 *Structural properties*

A typical X-ray Laue diffraction pattern of a Ho-based single crystal is shown in Fig. 6.8(a), with a pole figure corresponding to a reflection orientation $[\bar{1}\bar{1}8]$. The conventional $(Mo_{2/3}RE_{1/3})_2AlC$ unit cell includes 48 atoms - 16 Mo, 8 RE, *i.e.*, Nd, Sm, Gd, Tb, Dy, Ho, Er, Tm, or Lu, 12 Al, and 12 C atoms - and crystallizes in the $C2/c$ space group. The nonequivalent atomic positions are distributed in specific Wyckoff positions: $8f$ (two Mo, one RE, one Al, and one C), $4e$ (one Al), and $4d$ (one C). Considering their similar structures, a schematic representation valid for any RE element is used in Figs. 6.8(b)– 6.8(d) [61].

The atomic structure of the nine $(Mo_{2/3}RE_{1/3})_2AlC$ compounds are optimized *ab initio* using DFT [254, 255] as implemented in the VASP package [286–288]. The exchange-correlation functional is approximated in two ways. In the first we used the PBE [262], and in the second we used the SCAN approximation [263, 264]. PAW pseudopotentials [266–268] are used with the $4f$ electrons of the RE elements frozen in the core. A plane-wave kinetic energy cutoff of 520 eV is used. The first Brillouin zone is sampled with a $11 \times 11 \times 4$ Monkhorst-Pack k-point grid [269] and a Gaussian smearing of 0.2 eV is used to accelerate the convergence. For all systems, the unit cell parameters and the atomic positions are fully optimized until the largest force is smaller than 0.1 meV/Å. All atomic models are rendered using VESTA [344].

The theoretically predicted lattice parameters of the optimized monoclinic structures are listed in Table 6.4 and compared to the refined experimental parameters of both monocrystalline [342] and

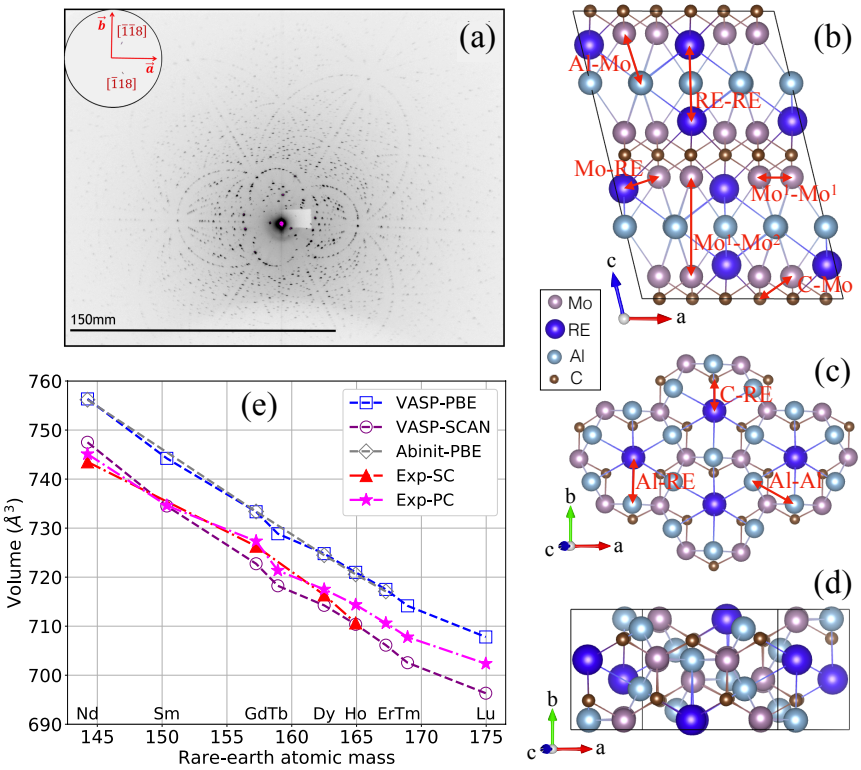

Figure 6.8: (a) Laue diffraction pattern of a $(Mo_{2/3}Ho_{1/3})_2$ AlC single crystal, obtained in transmission, along with a pole figure; schematic representation of the conventional monoclinic $C2/c$ cell of $(Mo_{2/3}RE_{1/3})_2AlC$, RE = Nd, Sm, Gd, Tb, Dy, Ho, Er, Tm, or Lu, along the (b) [010], and (c) and (d) [103] zone axes. Some specific interatomic bonds are defined with red arrows. RE, Mo, Al, and C atoms are represented by dark blue, purple, light blue, and brown spheres, respectively. (e) Dependence of the conventional cell volume on RE atomic mass, computed with PBE (squares - blue dashed line) and SCAN functionals (circles - violet dashed line) within the VASP package and with PBE (diamonds, grey dashed line) within ABINIT package, compared to experimental volumes extracted from Refs. [342] and [61] for single crystals (SC, triangles - red dotted dashed line) and polycrystals (PC, stars - pink dotted dashed line), respectively. From [342] and [343].

polycrystalline samples [61]. Note that, following experimental convention, the structural parameters in Table 6.4 are for the conventional unit cell, corresponding to twice the primitive cell. From the values listed in Table 6.4 and plotted in Fig. 6.8(e), the agreement between

the theoretical and experimental parameters is good, and is further improved by switching from the PBE to the SCAN functional. The increase of the RE atomic mass leads to reduced lattice parameters, as expected from the decrease of the covalent atomic radius when moving from left to right on the lanthanide row.

Figures 6.9(a)−6.9(c) show STEM images of the $(Mo_{2/3}Dy_{1/3})_2AlC$ single-crystal sample along [010], [110], and [100] zone axes, respectively. In these micrographs, the Dy atoms appear as bright dots due to their large atomic number (Z contrast), the Mo atoms are less bright, the Al are almost invisible, and lastly, the C atoms are not visible. Line profiles in the insets of Figs. 6.9(b) and 6.9(c) show the Z contrast variation. In Fig 6.9(b), the alternation of one strong peak and two weak peaks corresponds to the alternation of one RE atom and two Mo atoms. Schematics are shown to the left of each image. The structure is consistent with $C2/c$ space group. Most of the studied regions are free of faults as shown in Figs. 6.9(a)−6.9(c). The main defects observed in this family of materials are stacking faults. Figure 6.9(d) shows a region with stacking faults. As discussed in Ref. [61], in the $C2/c$ structure, every metal carbide layer is rotated by 60° with respect to others. In the $Cmcm$ structures, on the other hand, layers are rotated by 180° with respect to each other. In the stacking fault region, several layers are rotated by 180°, which reflects the structural similarity between the two structures.

6.2.2 *Vibrational properties*

The dynamical properties of five $(Mo_{2/3}RE_{1/3})_2AlC$ (RE = Nd, Gd, Dy, Ho, Er) systems are computed *ab initio* within the DFPT formalism [272–274, 307, 308] implemented in the ABINIT package [284, 285, 306]. For this purpose, the unit cell and atomic positions of the five systems are optimized *ab initio* using the ABINIT package. Optimized parameters are plotted in Fig. 6.8 and are very close to those obtained with VASP. PBE [262] is used to approximate the exchange-correlation functional and ONCVPSP pseudopotentials [319] are used to describe core-valence interaction. A plane-wave kinetic cut-off of 40 Ha is used and the first BZ is sampled with a $12 \times 12 \times 12$ Monkhorst-Pack k-point grid [269].

Table 6.4: Structural parameters of the RE-i-MAX phases computed with both PBE and SCAN functionals considering a monoclinic $C2/c$ symmetry ($\alpha = \gamma = 90°$), and compared to refined experimental parameters for single crystals (SC) [342] and polycrystals (PC) [61].

	a (Å)	b (Å)	c (Å)	β (°)	V (Å^3)	Description
$(Mo_{2/3}Nd_{1/3})_2AlC$	9.69	5.61	14.31	103.48	756.35	PBE
	9.67	5.59	14.21	103.54	747.51	SCAN
	9.66	5.59	14.16	103.47	743.51	SC
	9.67	5.59	14.17	103.48	745.11	PC
$(Mo_{2/3}Sm_{1/3})_2AlC$	9.64	5.58	14.25	103.54	744.23	PBE
	9.61	5.56	14.15	103.61	734.51	SCAN
	9.62	5.56	14.12	103.52	734.61	PC
$(Mo_{2/3}Gd_{1/3})_2AlC$	9.59	5.55	14.18	103.58	733.34	PBE
	9.55	5.53	14.08	103.64	722.74	SCAN
	9.57	5.54	14.09	103.53	726.31	SC
	9.58	5.54	14.09	103.53	727.34	PC
$(Mo_{2/3}Tb_{1/3})_2AlC$	9.57	5.54	14.16	103.59	728.86	PBE
	9.53	5.52	14.06	103.63	718.18	SCAN
	9.55	5.52	14.07	103.54	721.36	PC
$(Mo_{2/3}Dy_{1/3})_2AlC$	9.55	5.53	14.13	103.60	724.80	PBE
	9.51	5.51	14.03	103.63	714.25	SCAN
	9.52	5.51	14.04	103.56	716.38	SC
	9.53	5.51	14.05	103.54	717.51	PC
$(Mo_{2/3}Ho_{1/3})_2AlC$	9.53	5.52	14.11	103.60	720.98	PBE
	9.49	5.49	14.01	103.62	710.38	SCAN
	9.49	5.50	14.02	103.56	710.66	SC
	9.51	5.50	14.04	103.54	714.37	PC
$(Mo_{2/3}Er_{1/3})_2AlC$	9.51	5.51	14.09	103.61	717.50	PBE
	9.47	5.48	13.99	103.61	706.13	SCAN
	9.49	5.49	14.02	103.53	710.62	PC
$(Mo_{2/3}Tm_{1/3})_2AlC$	9.40	5.50	14.07	103.61	714.15	PBE
	9.45	5.47	13.98	103.61	702.55	SCAN
	9.48	5.49	14.00	103.51	707.77	PC
$(Mo_{2/3}Lu_{1/3})_2AlC$	9.46	5.48	14.04	103.60	707.80	PBE
	9.42	5.46	13.94	103.59	696.33	SCAN
	9.45	5.47	13.97	103.48	702.36	PC

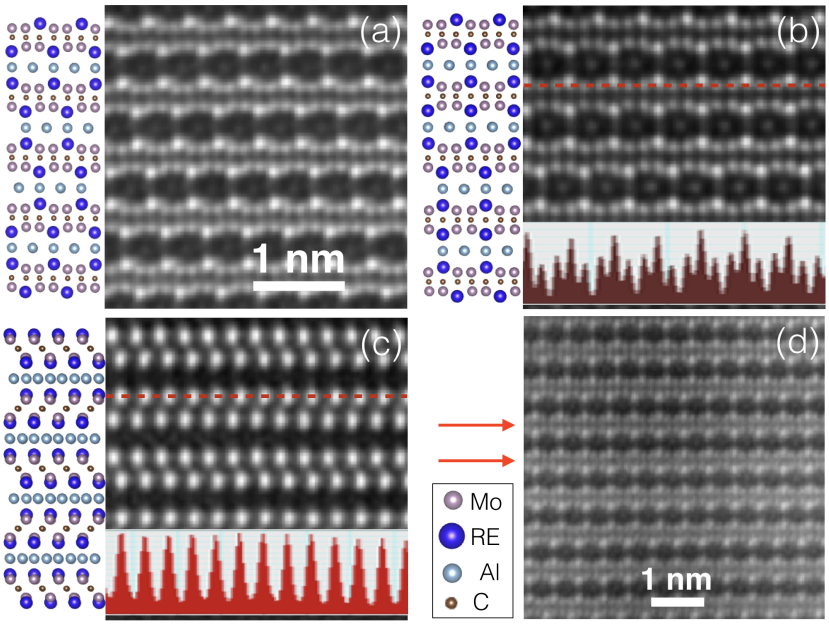

Figure 6.9: High resolution STEM images for $(Mo_{2/3}Dy_{1/3})_2AlC$ single crystals along (a) [010], (b) [110], and (c) [100] zone axes, with corresponding schematics for the $C2/c$ monoclinic structure. Insets in (b) and (c) show line-profiles of the Z contrast along the red dashed lines. (d) Region with stacking faults pointed out by red arrows. From [342].

With 24 atoms in the primitive cell, group theory predicts 3 acoustic modes and 69 optical modes at the Γ point of the BZ. Group theory can also determine which of these modes are Raman-active. The optical phonon modes can be classified with the following irreducible representation:

$$\Gamma_{\text{optical}} = \underbrace{16A_g + 17B_g}_{\text{Raman}} + \underbrace{18A_u + 18B_u}_{\text{IR}} \tag{6.13}$$

where A_g and B_g modes are Raman-active and A_u and B_u modes are IR-active.

Typical Raman spectra of $(Mo_{2/3}RE_{1/3})_2AlC$ crystals (RE = Nd, Gd, Dy, Ho, Er) are presented in Fig. 6.10 and the complete set of Raman peak positions are reported in Table 6.5. Not surprisingly, the spectra are similar in shape and relative line intensities. As shown in Table 6.5, the 33 expected Raman modes are observed for the Ho-based phase, while 31, 30, 29, and 30 modes are observed for the Nd-, Gd-, Dy-,

and Er-based phases, respectively. In all spectra, a majority of lines are located below 300 cm^{-1} and are distributed above a broad band. They are close to each other and most of them are well-defined intense lines, whereas the seven last lines appear more dispersed over the $350 - 650\,cm^{-1}$ range with rather weaker intensities.

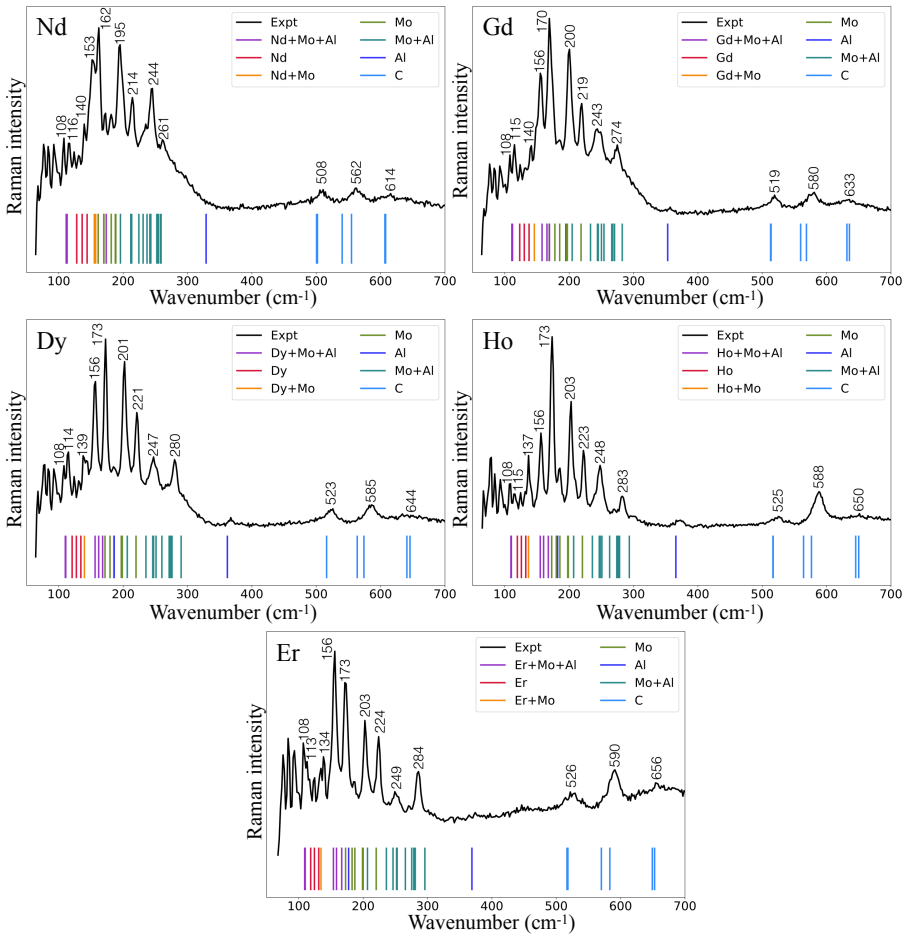

Figure 6.10: Typical single-crystal $(Mo_{2/3}RE_{1/3})_2AlC$ (RE = Nd, Gd, Dy, Ho, Er) Raman spectra collected at RT. The 33 calculated Raman-active modes are represented at the bottom of each graph, and classified according to the atoms involved in the vibrational modes (see colored lines in the inset). From [342].

The positions of the 33 Raman modes obtained theoretically by the *ab initio* calculations are also reported in Table 6.5 and represented

Table 6.5: Experimentally observed (ω_{exp}) and calculated (ω_{calc}) Raman mode wavenumbers in $(Mo_{2/3}RE_{1/3})_2AlC$, with RE = Nd, Gd, Dy, Ho, Er. The symmetry of each mode is mentioned, as well as the atoms involved in the vibrations. Atoms in between brackets state for the Nd-based system, and atoms in between squared brackets for the four other systems. Wavenumbers of intense peaks are highlighted in bold. These peaks form the Raman fingerprint of RE-i-MAX phases.

		Nd		Gd		Dy		Ho		Er	
Symm.	Atoms	ω_{exp}	ω_{calc}	ω_{exp}	ω_{calc}	ω_{exp}	ω_{calc}	ω_{exp}	ω_{calc}	ω_{exp}	ω_{calc}
$A_g(1)$	RE+Mo+Al	**108**	111.5	**108**	111.2	**108**	110.1	**108**	109.5	**108**	109.1
$B_g(1)$	RE+Mo+Al	**116**	112.9	**115**	112.0	**114**	110.8	**115**	110.2	**113**	110.0
$B_g(2)$	RE	124	127.9	124	123.2	124	120.7	124	119.5	124	118.5
$A_g(2)$	RE	131	136.3	132	130.3	131	127.3	132	125.8	130	124.3
$B_g(3)$	RE	**140**	144.0	**140**	137.7	**139**	134.3	**137**	132.6	**134**	131.0
$A_g(3)$	RE+Mo	147	155.2	148	145.9	144	139.8	140	136.8	139	134.5
$A_g(4)$	RE+Mo[+Al]	**153**	157.2	**156**	157.9	**156**	156.4	**156**	155.1	**156**	153.8
$B_g(4)$	RE+Mo+Al	160	170.0	–	165.5	151	162.0	152	160.3	152	158.6
$A_g(5)$	RE+Mo+Al	172	173.7	165	169.4	–	168.1	169	167.6	–	166.7
$B_g(5)$	Mo	**162**	161.2	**170**	169.0	**173**	171.8	**173**	172.9	**173**	172.7
$A_g(6)$	Mo	–	170.1	173	177.8	–	179.6	178	180.0	186	181.8
$B_g(6)$	Mo	181	181.5	182	185.3	185	185.6	190	185.9	191	187.1
$A_g(7)$	Al(+Mo)	211	213.3	187	194.7	188	186.1	185	182.1	–	177.4
$B_g(7)$	Mo	**195**	187.8	**200**	195.2	**201**	197.1	**203**	197.8	**203**	199.0
$A_g(8)$	Mo	192	188.6	–	197.2	–	198.6	205	198.7	–	200.0
$B_g(8)$	Mo+Al	200	195.8	205	204.7	208	206.4	210	207.0	209	206.7
$A_g(9)$	Mo(+Al)	**214**	211.9	**219**	218.5	**221**	220.0	**223**	220.6	**224**	220.8
$B_g(9)$	Mo+Al	228	224.4	232	233.2	237	235.4	239	236.1	240	236.1
$A_g(10)$	Mo+Al	235	231.0	240	244.0	243	246.0	244	246.8	245	246.4
$B_g(10)$	Mo+Al	**244**	241.5	**243**	245.2	**247**	247.3	**248**	248.3	**249**	251.9
$A_g(11)$	Mo+Al	241	243.0	249	250.2	252	251.2	253	250.9	255	252.8
$B_g(11)$	Mo+Al	238	237.1	255	254.1	259	260.2	262	262.9	259	265.6
$B_g(12)$	Mo+Al	256	254.6	271	266.2	266	271.5	270	274.0	272	275.5
$A_g(12)$	Mo+Al	249	252.3	278	267.7	270	273.8	275	276.3	280	278.7
$A_g(13)$	Mo+Al	**261**	257.8	**274**	270.5	**280**	275.9	**283**	278.3	**284**	281.0
$B_g(13)$	Mo+Al	263	258.9	285	282.5	293	290.1	296	293.5	297	295.9
$B_g(14)$	Al	–	328.9	357	353.1	367	361.9	372	365.8	376	369.0
$B_g(15)$	C	500	500.5	509	513.0	514	516.1	516	516.6	517	516.7
$A_g(14)$	C	**508**	501.9	**519**	513.7	**523**	516.1	**525**	517.0	**526**	518.1
$A_g(15)$	C	549	540.3	559	559.7	566	563.7	571	564.2	574	570.1
$B_g(16)$	C	**562**	554.8	**580**	568.7	**585**	574.1	**588**	576.5	**590**	583.3
$B_g(17)$	C	603	606.7	–	631.6	–	640.9	638	645.2	644	649.3
$A_g(16)$	C	**614**	607.8	**633**	635.5	**644**	645.7	**650**	649.9	**656**	652.8

using vertical lines under each experimental spectrum in Fig. 6.10. These vertical lines correspond to the atoms involved in the vibrational modes and are color coded (key is shown in insets). The comparison between experimental and calculated values in Table 6.5 indicates a quite good agreement for all the systems reported, with a maximal deviation of $10\,\mathrm{cm}^{-1}$ corresponding to 7% for the low-wavenumber range (mode $B_g(4)$) and $12\,\mathrm{cm}^{-1}$ corresponding to 2% for the high-wavenumber range (mode $B_g(16)$). Such discrepancies can be linked to the differences between experimental and theoretical atomic structures. Assignment of the computed Raman-active modes with the experimental peaks is almost straightforward even though no information regarding the peak intensities has been predicted theoretically.

By analyzing the symmetry of the vibrational modes (A_g and B_g modes listed in Table 6.5) together with the atomic vibrations (eigen-displacements), a correspondence between the Raman-active modes of the five systems under study can be done. While the Gd-, Dy-, Ho-, and Er-based phases possess very similar Raman behaviors including peaks positions, intensities, symmetries, and atomic displacements, the Raman spectrum of the Nd-based phase is slightly different. Twelve relatively high-intensity peaks, present in the Raman spectra of all five systems, are identified as the fingerprint of the RE-i-MAX phases. These peaks are pointed out in the experimental spectra in Fig. 6.10 and are highlighted in bold in Table 6.10. Moreover, they are schematically depicted in Fig. 6.11. Some weak additional lines are observed in the Raman spectra of all the compounds, although not predicted by theory. Typically, two to four additional lines are observed in the spectra depending on the RE element in the mid-wavenumber range, *i.e.*, between modes $B_g(13)$ and $B_g(14)$, and one (Dy-, Ho-based phases) or two (Nd-, Gd-, Er-based phases) additional lines in the higher wavenumber part of the spectra. These lines remain presently unassigned and could possibly be due to other undefined phases present in the samples. In the same way, four low-wavenumber peaks respectively located around 67, 77, 84, and $93\,\mathrm{cm}^{-1}$ are observed in the experimental spectra of the five systems and not predicted theoretically. Even though Raman measurements were performed under atmosphere, we are not sure at this stage whether this explains the presence of these low-wavenumber Raman peaks. Mercier *et al*. [22] reported the Raman spectrum of Ti_3SiC_2 and assigned the nonpredicted low-wavenumber modes to the presence of air, including one peak at $83\,\mathrm{cm}^{-1}$ and another at $92\,\mathrm{cm}^{-1}$. Even with

this assumption, the first two peaks observed in the Raman spectra of the RE-i-MAX phases remain unassigned. These peaks may be due to other undefined phases present in the samples.

In order to understand the effects of mass and bond stiffness on the Raman peak positions, we use the conventional expression for vibrational wavenumbers, assuming harmonic oscillation, given by [101]:

$$\omega = \sqrt{\frac{K}{m_{\text{red}}}} \tag{6.14}$$

where K is the bond stiffness, or more exactly an effective stiffness obtained from the stiffnesses of the different atomic bonds, and m_{red} is the reduced mass of the atomic masses of the species involved in the vibrations. Because C atoms are light, and as typical of the MAX phases in general [22, 101–105], they tend to form strong covalent bonds with Mo, and their vibrations are exclusively located in the high-wavenumber ($\omega \geq 500\,\text{cm}^{-1}$) range. Due to the lower symmetry of the i-MAX phases, this is the first time C atom vibrations are involved in Raman-active modes in a 211 MAX phase [101, 104]. The relative positions of the vibrational modes involving the RE, Mo, and Al atoms exhibit a less clear trend and vary from one phase to another. Nevertheless, the vibrational modes involving the RE atoms - because of their mass and the weaker bonds they form with Al and C - are mostly located in the low-wavenumber ($\omega \leq 180\,\text{cm}^{-1}$) range. A detailed analysis of bond strengths in $(\text{M}'_{2/3}\text{M}''_{1/3})_2\text{AlC}$ has been reported by Dahlqvist *et al.* [158] leading to the following classification: M′−C > M″−C > M′−Al > M″−Al, where M′ and M″ would respectively correspond to Mo and RE elements in our systems. The fact that the Sc atoms are readily etched from the $(\text{Mo}_{2/3}\text{Sc}_{1/3})_2\text{AlC}$ i-MAX phase to form the $\text{Mo}_{1.33}\text{C}$ MXene [19] supports this assumption.

To further explore the specific role of the RE atomic mass, m_{RE}, and bond stiffness, K, on the Raman peak positions, the evolution of the mode wavenumbers as a function of m_{RE} is presented in Fig. 6.12. In this figure, the data points are those obtained experimentally and the lines are obtained from a least squares polynomial fit of the theoretical values. In Fig. 6.12(a), the first nine modes are associated with the vibrations of the RE atoms. The next eight - with the exception of $A_g(7)$ where Al predominates - relate to the vibrations of the Mo atoms. Similarly, the set of lines in the $220 - 300\,\text{cm}^{-1}$ range in

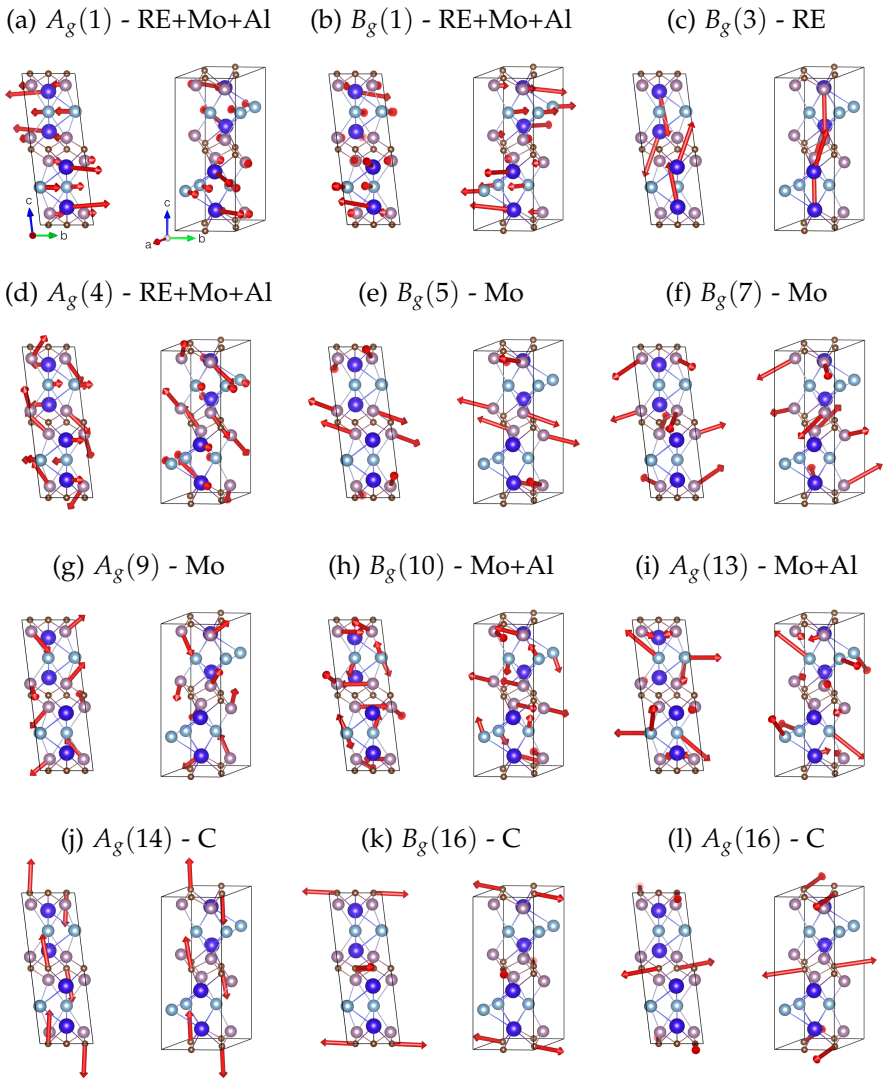

Figure 6.11: Schematics of the atomic displacements (red arrows) of the representative vibrational modes of $(Mo_{2/3}RE_{1/3})_2AlC$ i-MAX phases: (a) $A_g(1)$, (b) $B_g(1)$, (c) $B_g(3)$, (d) $A_g(4)$, (e) $B_g(5)$, (f) $B_g(7)$, (g) $A_g(9)$, (h) $B_g(10)$, (i) $A_g(13)$, (j) $A_g(14)$, (k) $B_g(16)$, and (l) $A_g(16)$. Atomic vibrations are similar for the five systems with RE = Nd, Gd, Dy, Ho, and Er, except for the modes $A_g(4)$, $A_g(7)$, and $A_g(9)$, as mentioned in Table 6.5. The size of the arrows is proportional to the vibration amplitude and varies very slightly from one system to another. The vibrations in the Dy-based system are used for the schematics. Dy, Mo, Al and C atoms are presented using dark blue, purple, light blue, and brown spheres, respectively. From [342].

Fig. 6.12(b) relate to the Mo atoms, while the isolated one above $320\,\mathrm{cm}^{-1}$ is due to Al atom vibrations alone. Lastly, Fig. 6.12(c) plots the six highest energy modes that involve the C atoms. Some of these modes are schematically illustrated in Fig. 6.11. When analyzing the results in Fig. 6.12, the following observations are salient: (i) With one notable exception, *viz.* $A_g(7)$ discussed below, above $\sim 160\,\mathrm{cm}^{-1}$ the experimental points and the slopes of the lines predicted by DFT, change from negative to positive (see Fig. 6.12(a)). (ii) For some of the modes between 100 and $200\,\mathrm{cm}^{-1}$, the experimental results are not as well captured by theory. For example, experimentally the first four modes are flat, while DFT predicts a slightly negative slope. Others are flat and then drop off, *e.g.*, $B_g(3)$, $A_g(3)$ in Fig 6.12(a). It appears that at the lowest wavenumbers, the DFT calculations either overestimate or underestimate K. (iii) Above $\sim 220\,\mathrm{cm}^{-1}$ (see Figs. 6.12(b) and 6.12(c)), the agreement between theory and experiment can be considered qualitatively satisfactory in that the slopes of the lines faithfully reproduce those of experimental data points. With a few exceptions - *e.g.*, $A_g(12)$ and $B_g(16)$ - the quantitative agreement is also quite correct.

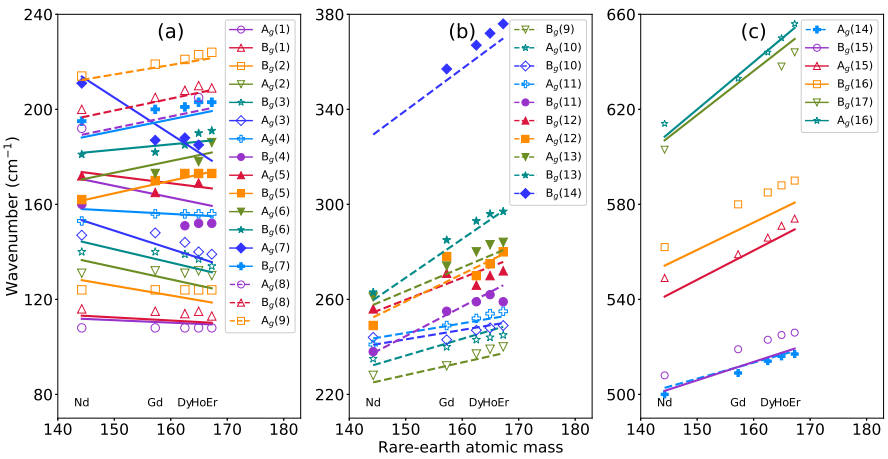

Figure 6.12: Dependence of both experimental and calculated wavenumbers on m_{RE} for the 33 Raman-active modes. For each mode, the experimental data are represented by markers of the same color for the five RE-i-MAX phases. Moreover, a least squares polynomial fit of the theoretical DFT (not shown here) is represented by a straight line with the same color as the markers related to the experimental data. These lines allow for a better understanding of the evolution of the wavenumbers with m_{RE}. From [342].

According to Eq. 6.14, if K were not a function of composition, then the mode energies should decrease with increasing m_{RE}. In contrast, if K increases faster than m_{RE}, then the slopes should be positive. Lastly, if the ratio K/m_{RE} remains constant, the energies should not vary with composition. How this concept in essence explains the trends observed in Fig. 6.12 is discussed below.

More specifically, according to Table 6.5, the heavy RE elements participate in the first nine modes, where presumably mass is important. It is thus not a coincidence that the energies of these modes are either not a function of m_{RE} or they decrease with increasing m_{RE}. This agreement can thus be taken as an independent confirmation of, at least, the correctness of assigning the first nine modes with vibrations of the RE elements.

Before discussing the rest of the modes, refer to Fig. 6.13, where the experimental (solid lines) and optimized (dashed lines) lattice parameters, and various bond distances are plotted as a function of the effective ionic radii of the RE^{3+} cations. Given that shorter bonds are stronger, as verified through *ab initio* calculations by considering different volumes for the systems under study (results not shown here), then, from Fig. 6.13(b), we conclude that: (i) the RE−RE bonds are strongest for Nd and weakest for Er. It is thus not too surprising that the modes involving Nd atoms have higher wavenumbers with respect to the others, in Fig. 6.12(a). (ii) the Mo−Mo, Al−Al, Mo−Al, and, especially, the RE−C bonds, are weakest for Nd and strongest for Er, which explains the increasing wavenumbers (again with a notable exception) going from the left to right in Figs. 6.12(a)−6.12(c).

We now focus on modes $A_g(7)$ and $B_g(14)$ involving only the Al atoms. To understand their evolutions it is important to consider the respective directions of the vibrations with respect to the bond directions. This is important because for vibrations involving more than one bond, the contribution to the energy of the bond parallel to the vibrational direction is larger than the one perpendicular to it. As a consequence, for similar bond stiffnesses, the first type influences K more, and concomitantly ω, than the second one.

Mode $A_g(7)$ corresponds to the well-known torsional mode observed in 2D Kagome lattices [345–347]. As depicted in Fig. 6.14(a), the Al atoms are vibrating in the *ab*-plane with a vibrational direction parallel to the projection of the RE−Al bonds and perpendicular

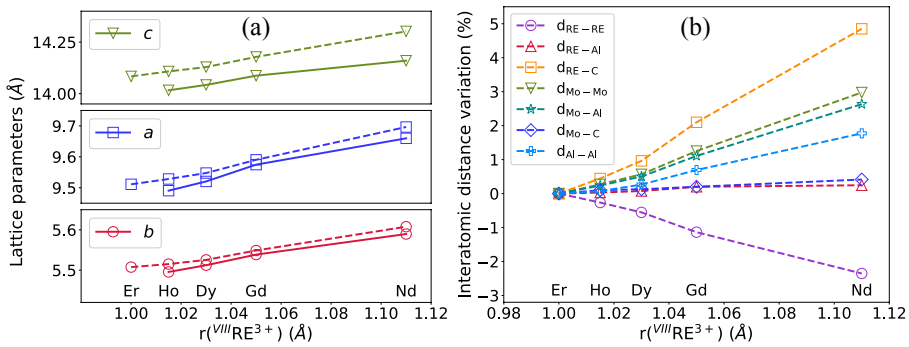

Figure 6.13: Evolution of (a) lattice parameters and (b) interatomic distances with the effective ionic radius of the RE element at valence +3 and coordination VIII. The variations of interatomic distances are normalized using those of the Er-based phase, and expressed in %. Solid and dashed lines correspond to the parameters for the experimental and relaxed structures, respectively. From [342].

to the projection of the Mo−Al bonds in the *ab*-plane. Therefore the bonding governing the stiffness is mostly that of the RE−Al one. Since the RE−Al distance is not a function of composition (see Fig. 6.13(b)) then K should not be either. Therefore the only variable here is the vibrational direction. Based on previous results by Dahlqvist *et al.* [58], a difference in atomic radii between the Mo and RE atoms induces a displacement of RE atoms towards the Al plane, in order to minimize the in-plane stress. The larger the RE ionic radius, the larger the out-of-plane shift. Hence, the out-of-plane RE−RE distance decreases when increasing RE ionic radii, as depicted in Fig. 6.13(b). Furthermore, as the unit cell expands when the atomic radius of the RE element increases (see Fig. 6.13(a)), the in-plane spacing between Al atoms increases. As a consequence, RE−Al bonding lengths are comparable for the five systems, but the angle between the Al plane and the RE−Al bonds decreases when increasing ionic radii. This probably explains the decreasing wavenumbers observed for mode $A_g(7)$ going from left to right in Fig. 6.12(a).

Mode $B_g(14)$ also involves in-plane vibrations of Al atoms, as presented in Fig. 6.14(b). In contrast with mode $A_g(7)$, here the motion of the Al atoms is parallel to the projection of the Mo−Al bonds in the *ab*-plane and perpendicular to the one of the RE−Al bonds. Therefore the Mo−Al bond stiffness should prevail in the K factor. The positive slope in Fig. 6.12(b) of this mode thus indirectly

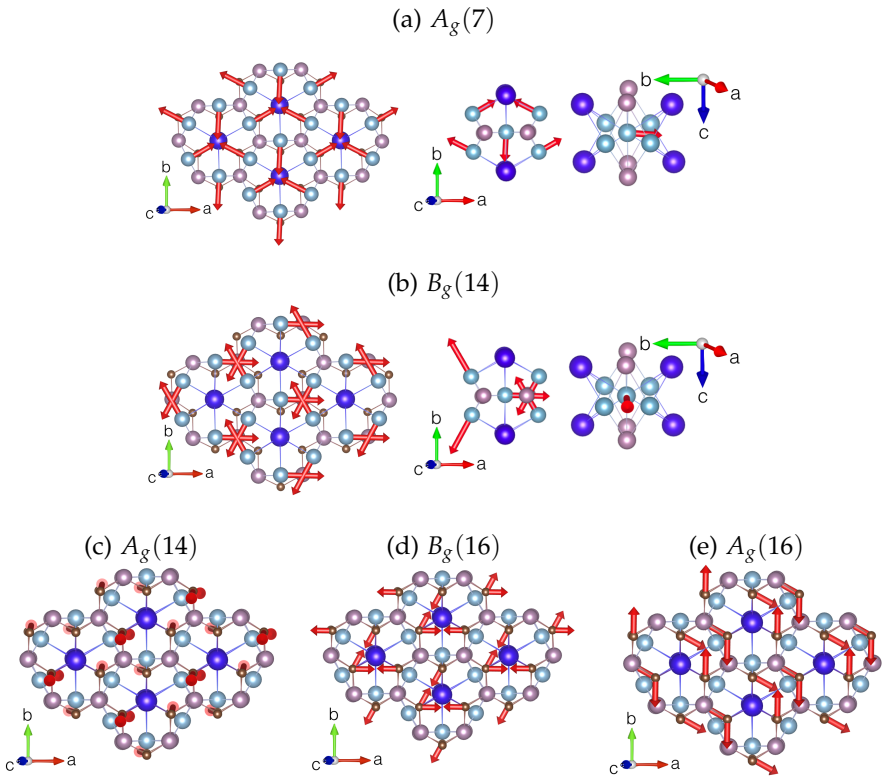

Figure 6.14: Representation of the outlying Al modes: (a) $A_g(7)$ and (b) $B_g(14)$, and C-related modes: (c) $A_g(14)$, (d) $B_g(16)$, and (e) $A_g(16)$, aiming at better visualizing the direction of the vibrations with respect to the direction of the various bonds. The vibrations in the Dy-based system are used for the schematics. Dy, Mo, Al and C atoms are presented using dark blue, purple, light blue, and brown spheres, respectively. From [342].

confirms the increasing value of Mo−Al bond stiffnesses with the RE atomic mass.

Eventually, the dispersion from 500 to 650 cm^{-1} observed in Fig. 6.12(c) for the six C-related modes can be assigned to the various directionalities of the C vibrations with respect to atomic bonds. Modes $B_g(15)$ and $A_g(14)$ correspond to out-of-plane vibrations of C atoms (see Fig. 6.11(j)), perpendicular to both Mo−C and RE−C bonds, as depicted in Fig. 6.14(c). Therefore, the stiffness factor only slightly reflects the stiffness of Mo−C and RE−C bonds. Modes $A_g(15)$ and $B_g(16)$ correspond to in-plane vibrations of C atoms (see Fig. 6.11(k)), with a vibrational direction almost parallel to the projection of the

RE−C bonds and perpendicular to the projection of the Mo−C bonds in the *ab*-plane, as presented in Fig. 6.14(d). Consequently, the bonding governing the stiffness is that of the RE−C one. In contrast, in modes $B_g(17)$ and $A_g(16)$, C atoms are vibrating in a direction parallel to Mo−C bonds and perpendicular to RE−C bonds (see Fig. 6.14(e)). Therefore, the bonding governing the stiffness is that of the Mo−C one. Since Mo−C bonds are stronger than RE−C bonds [158, 343], it is not surprising to find the modes governed by the Mo−C bond stiffnesses at higher wavenumbers than those governed by the RE−C ones.

6.2.3 *Elastic properties*

First-principles calculations

The elastic constants of a crystalline solid are important parameters providing information on its stiffness, stability, and anisotropy. They provide a fundamental insight into the nature of the forces acting in the material and can be seen as a link between a material's dynamical behavior and its mechanical and thermal properties. For monoclinic crystals, 13 non-zero independent elastic constants c_{ij} are defined, namely c_{11}, c_{12}, c_{13}, c_{15}, c_{22}, c_{23}, c_{25}, c_{33}, c_{35}, c_{44}, c_{46}, c_{55}, and c_{66} [332]. The single crystal elastic constants are determined from the computation of the stress associated with a set of six imposed homogeneous finite deformations (±1.5%), as implemented in the VASP code [286–288] (see Section 4.6). For all systems, the elastic tensor is computed within the SCAN functional at the corresponding optimized lattice parameters. Table 6.6 lists the elastic constants c_{ij} of the $(Mo_{2/3}RE_{1/3})_2AlC$ quaternaries calculated at zero pressure and zero temperature. All RE-*i*-MAX phases considered herein fulfill the mechanical stability criteria for monoclinic crystals [348]. Moreover, in all cases, it is observed that the diagonal c_{11}, c_{22}, and c_{33} values are larger than all other constants. While for the first five systems with RE = Nd, Sm, Gd, Tb or Dy, the principal elastic constants are classified as $c_{33} < c_{11} < c_{22}$, $(Mo_{2/3}Ho_{1/3})_2AlC$ is the only one with $c_{11} < c_{33} < c_{22}$, and the last three $(Mo_{2/3}RE_{1/3})_2AlC$ systems with RE = Er, Tm or Lu, exhibit $c_{11} < c_{22} < c_{33}$.

From the calculated c_{ij}, the homogenized polycrystalline elastic properties including the bulk modulus B, shear modulus G, Young's modulus E, and Poisson's ratio are computed. For monoclinic systems,

Table 6.6: Calculated elastic constants c_{ij} and Voigt (V), Reuss (R) and Hill (H) moduli (in GPa) of RE-i-MAX.

	Nd	Sm	Gd	Tb	Dy	Ho	Er	Tm	Lu
c_{11}	262.09	274.09	278.28	280.40	282.16	283.20	282.68	284.41	287.62
c_{12}	86.71	86.83	88.88	90.82	92.05	92.71	91.75	94.09	90.61
c_{13}	97.29	102.18	106.56	109.45	112.01	113.49	114.44	117.86	117.99
c_{15}	1.44	2.57	5.03	5.44	5.72	6.19	6.23	6.03	8.04
c_{22}	270.81	280.62	283.61	286.27	288.97	290.22	290.10	291.77	293.08
c_{23}	98.22	102.54	105.16	107.40	109.75	111.35	112.76	115.74	115.32
c_{25}	0.55	2.23	5.18	6.18	6.53	6.54	5.96	5.81	7.10
c_{33}	223.79	249.04	266.05	274.26	280.79	286.21	291.25	297.15	300.23
c_{35}	−13.41	−10.21	−6.05	−4.46	−3.93	−3.79	−4.16	−3.23	−1.66
c_{44}	96.06	99.39	101.22	102.04	102.92	103.52	104.02	103.94	104.05
c_{46}	−0.48	−0.54	−1.16	−1.49	−1.59	−1.45	−1.24	−1.26	−0.44
c_{55}	86.29	90.42	92.52	93.04	93.93	94.58	95.57	95.51	95.06
c_{66}	97.83	102.01	103.35	103.83	104.37	104.80	105.16	105.11	106.38
B_V	146.79	154.10	158.79	161.81	164.39	166.08	166.88	169.86	169.86
B_R	145.96	153.93	158.73	161.66	164.15	165.74	166.40	169.24	168.99
B_H	146.37	154.02	158.76	161.73	164.27	165.91	166.64	169.55	169.42
G_V	87.67	92.51	94.57	95.33	96.12	96.72	97.29	97.29	98.23
G_R	85.27	90.84	93.20	94.03	94.84	95.47	96.08	96.11	97.03
G_H	86.47	91.67	93.89	94.68	95.48	96.10	96.68	96.70	97.63
ν	0.25	0.25	0.25	0.26	0.26	0.26	0.26	0.26	0.26
E_H	216.73	229.49	235.28	237.66	239.95	241.64	243.05	243.76	245.70
E_1	262.09	274.09	278.28	280.40	282.16	283.20	282.68	284.41	287.62
E_2	270.81	280.62	283.61	286.27	288.97	290.23	290.10	291.77	293.08
E_3	217.20	243.98	263.79	272.93	279.69	284.96	289.45	295.85	299.99

the Voigt bulk and shear moduli (upper bound) can be obtained, respectively, assuming [332]:

$$B_V = \frac{1}{9}\left(c_{11} + c_{22} + c_{33}\right) + \frac{2}{9}\left(c_{12} + c_{13} + c_{23}\right) \tag{6.15}$$

$$G_V = \frac{1}{15}\left[\left(c_{11} + c_{22} + c_{33}\right) - \left(c_{12} + c_{13} + c_{23}\right) + 3\left(c_{44} + c_{55} + c_{66}\right)\right] \tag{6.16}$$

while the Reuss bulk and shear moduli (lower bound) are given, respectively, by [332]:

$$B_R = \frac{1}{(s_{11} + s_{22} + s_{33}) + 2\,(s_{12} + s_{13} + s_{23})} \tag{6.17}$$

$$G_R = \frac{15}{4\,(s_{11} + s_{22} + s_{33}) - 4\,(s_{12} + s_{13} + s_{23}) + 3\,(s_{44} + s_{55} + s_{66})} \tag{6.18}$$

where the s_{ij}'s are compliance constants obtained by inverting the 6×6 elastic constant matrix. The arithmetic averages of Voigt and Reuss moduli are known as the Hill moduli given by [333]:

$$B_H = \frac{B_V + B_R}{2} \tag{6.19}$$

$$G_H = \frac{G_V + G_R}{2} \tag{6.20}$$

In contrast with the results reported by Dahlqvist *et al.* [158] for $(W_{2/3}Sc_{1/3})_2AlC$ and $(W_{2/3}Y_{1/3})_2AlC$ i-MAX systems, it is noted here that the Voigt and Reuss approximations give similar values of both bulk and shear moduli (see Table 6.6). Consequently, the Hill averages are close to these two limits. Using the calculated values of B_H and G_H, the average Young's modulus E_H, measuring the response under uniaxial tension conditions averaged over all directions, and the Poisson ratio ν, providing information about the bonding forces and reflecting the stability of a material against shear, can be obtained, respectively, assuming [333]:

$$E_H = \frac{9B_H G_H}{3B_H + G_H} \tag{6.21}$$

$$\nu = \frac{3B_H - 2G_H}{2\,(3B_H + G_H)} \tag{6.22}$$

The values of the elastic properties reported in Table 6.6 and presented in Fig. 6.15 suggest that an increase of the rare-earth atomic mass, when moving from left to right on the lanthanide row, results in an increase of all elastic moduli. In other words, RE-i-MAX phases with heavier RE elements are stiffer, which is not too surprising since the

unit cell, and hence the atomic bonds, tend to shrink with increasing RE atomic mass. This is consistent with the bonding strength analysis described in Ref. [342], and with the basic idea that shorter bonds are stiffer. Additionally, from Table 6.6, the value of the Poisson ratio of all RE-i-MAX phases is almost constant to ~ 0.26. Since the obtained values fall in the range of $0.25 - 0.5$, it is reasonable to assume that the interatomic forces can be considered as central forces [349].

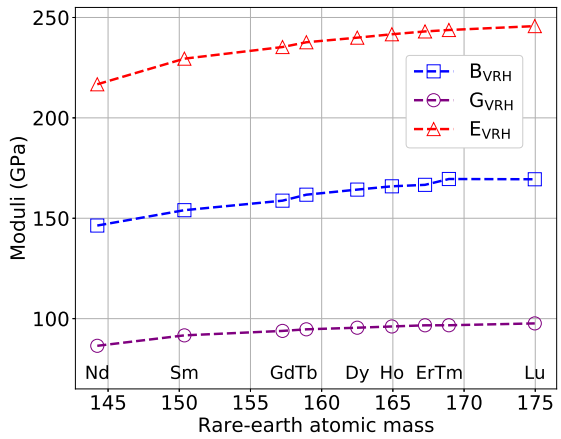

Figure 6.15: Bulk (B), shear (G), and Young's (E) moduli in the Voigt-Reuss-Hill approximation, as a function of the rare-earth atomic mass. From [343].

Other properties computed *ab initio* are the directional elastic moduli:

$$\frac{1}{E_i} = s_{11}l_1^4 + 2s_{12}l_1^2l_2^2 + s_{22}l_2^4 + 2s_{23}l_2^2l_3^2 + s_{33}l_3^4 + 2s_{13}l_1^2l_3^2 + s_{44}l_2^2l_3^2 + s_{55}l_1^2l_3^2 + s_{66}l_1^2l_2^2 \quad (6.23)$$

where l_1, l_2, and l_3 are the directional cosines of angles between the three principal directions (x, y, and z) [335]. The E_i's are very close to another showing limited anisotropy.

Nanoindentation

The elastic properties of RE-i-MAX phases are reported for the first time. Therefore, in order to evaluate the accuracy of the present theoretical data, the elastic response of a $(Mo_{2/3}Ho_{1/3})_2AlC$ single crystal is also measured experimentally using nanoindentation.

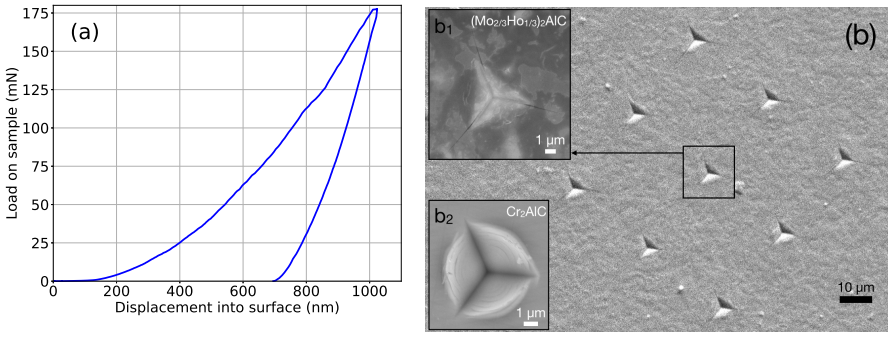

Figure 6.16: (a) Representative load−displacement curve from the nanoindentation of the top surface of a Ho-based single crystal, and (b) a scanning electron microscope image of the indentation marks, with a zoom on one of these indents in inset b_1 (top left). Inset b_2 (bottom left) corresponds to a SEM image of an indent performed on a Cr_2AlC single crystal for comparison. From [343].

A Berkovich tip is used to indent the surface of the Ho-based single crystal, perpendicularly to its *ab*-plane. Fifteen indents are performed and a representative load-displacement curve is depicted in Fig. 6.16(a). A load of about 175 mN is required to indent the sample by 1 μm. A typical SEM micrograph of an indent made on $(Mo_{2/3}Ho_{1/3})_2AlC$ is shown in Fig. 6.16(b). Consistent with the brittle character of RE-i-MAX phases, small cracks are observed from the corners of the indentations, with an emanated crack length of $\sim 7\,\mu$m. From this point of view, RE-i-MAX phases differ from conventional M_2AlC phases, where the indentation induces delaminations, kinking, grain pushouts and pullouts [336], and only short cracks confined to the indenter imprint (see inset b_2 in Fig. 6.16(b) and refer to Section 6.1.5). The presence of long cracks reflects the less ductile response to deformation of the RE-i-MAX phases compared to the ternary MAX phases.

Using the Oliver and Pharr method [318, 338], the average value of E_{Br} is calculated from the 15 indents to be 220 ± 8 GPa. In comparison, the computed value of the isotropic Young's modulus of $(Mo_{2/3}Ho_{1/3})_2AlC$ is 242 GPa. Even though the indentation direction is along axis 3, indentation involves a triaxial loading mode with significant compressive stresses building up in directions 1 and 2. Hence the comparison with an average isotropic modulus is appropriate. This 10% overestimation is reasonable and is typical of DFT calculations [1],

considering that both defects and temperature are not taken into account in the calculations.

Another fundamental physical parameter that can be determined from nanoindentation is the hardness H. Using the Oliver and Pharr method [318, 338], we calculate the Berkovich hardness of $(Mo_{2/3}Ho_{1/3})_2AlC$ to be 9.8 ± 0.4 GPa. In comparison, the Berkovich hardness of a Cr_2AlC single crystal was about 9.7 GPa, while the Vickers hardness values of polycrystalline MAX phases usually range from 2 to 9 GPa [336].

6.2.4 *Electronic structure and DOS*

The electronic DOS and the crystal orbital Hamilton population (COHP) of each system are computed on a $11 \times 11 \times 4$ Monkhorst-Pack k-point grid, using the LOBSTER code [350–352], with the pbeVaspFit2015 basis set [353]. In the present calculations, only the nearest-neighbor interactions are considered: C−Mo, C−RE, Al−Mo, Al−RE, Al−Al, Mo−Mo, and Mo−RE, as depicted in Figs. 6.8(b) and 6.8(c).

Information on the electronic properties can be obtained from the computation of the DOS. In Fig. 6.17, and similar to all conventional MAX and i-MAX phases [1, 163], the RE-i-MAX systems exhibit a metallic behavior mostly ensured by the presence of Mo-d orbitals at the Fermi level. In addition, the projected COHP (pCOHP), and integrated pCOHP (IpCOHP) presented in Fig. 6.18, can be used to shed light on the nature of the bonding. Given the similarities between the nine studied systems, both Figs. 6.17 and 6.18 corresponding to the Dy-based system can be taken as references.

The projected DOS presented in Fig. 6.17 highlights the overlap between the atomic orbitals of each element, while the −pCOHP presented in Fig. 6.18(a) explicitly gives information on the bonding types. In Fig. 6.17, the states between −13 eV and −11 eV can be regarded as bonding between the C-2s and Mo-4d or RE-5d orbitals. The projected DOS of Al-2s and Al-2p orbitals are mainly distributed between −9 and −6.5 eV, and between −6.5 and −3 eV, respectively, corresponding to Al−Al bonding. Also, from −6.5 to −3 eV, C-2p orbitals overlap the d orbitals of both Mo and RE atoms, hence forming the C−Mo and C−RE bonds. The states located between −3 and −1 eV can be assigned to bonding states between the Al-2p and the Mo-4d and RE-5d orbitals. Finally, the states in the vicinity of the Fermi level (from −1 eV and above) correspond mainly to Mo-4d and slightly to RE-5d orbitals.

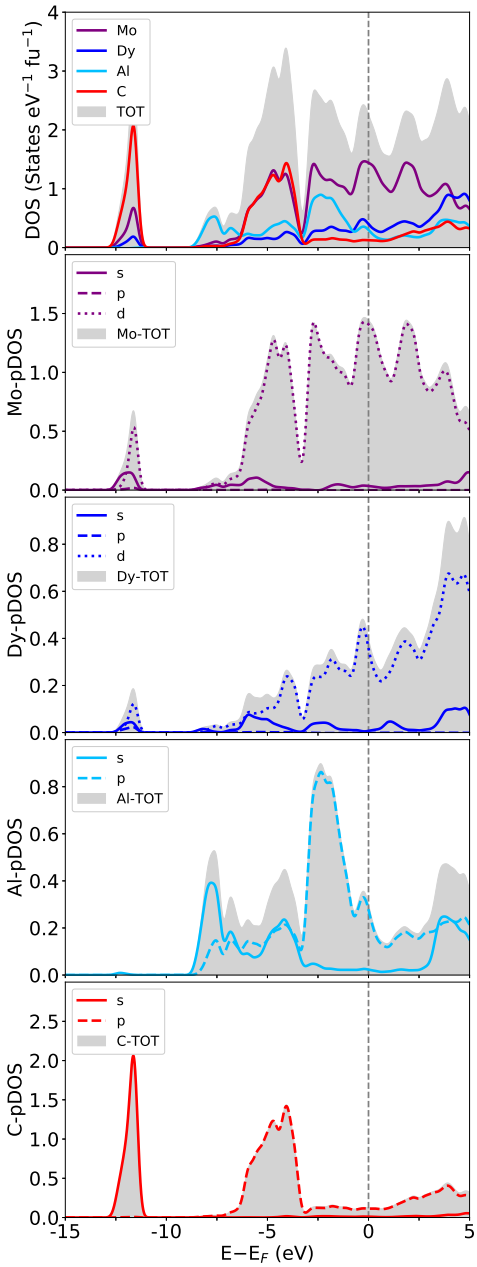

Figure 6.17: Calculated electronic density of states of $(Mo_{2/3}Dy_{1/3})_2AlC$ and projected density of states on the atomic orbitals of each element, expressed in states/eV per formula unit. From [343].

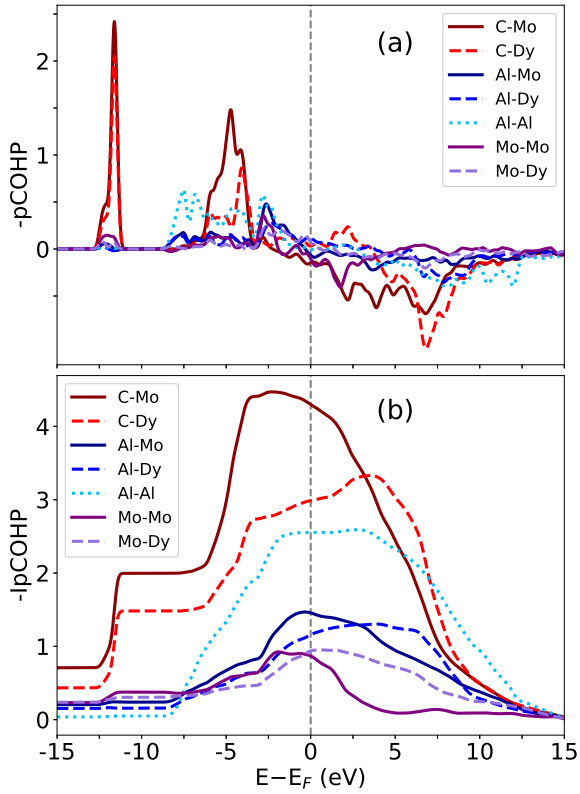

Figure 6.18: Calculated (a) pCOHP and (b) IpCOHP of $(Mo_{2/3}Dy_{1/3})_2AlC$. From [343].

Consequently, the metallic character of all studied RE-i-MAX phases, characterized by a total DOS at the Fermi level of $\sim$ 2.5 states/eV per formula unit (f.u.), arises from the *d* electrons. For this last region from -1 eV and above, the computed $-$pCOHP shown in Fig. 6.18(a) indicates that the *d* electrons of Mo and RE atoms can be seen as nonbonding electrons.

6.2.5 *Exfoliation potential*

While the experimental process used to convert MAX phases into MXenes is quite complex (see Chapter 3), two main criteria, previously exploited by Khazaei and coworkers [354, 355], can be used to evaluate their exfoliation potential: bonding strength and exfoliation energy. For the RE-i-MAX to be successfully etched into RE-i-MXenes, only the

Al bonds, *viz.* Al−Mo and Al−RE, need to be broken. This would only occur if the C−Mo and C−RE bonds are stronger than the Al−Mo and Al−RE ones.

Bonding analysis

By integrating −pCOHP up to E_F, it is possible to assess the relative bond strengths within the RE-i-MAX phases [350–352]. Even though no absolute value for the bond strength can be obtained, the bonds can be classified according to their −IpCOHP curve. From Figs. 6.18(b) and 6.19, the atomic interactions defined in Figs. 6.8(b) and 6.8(c) are ranked as follows: C−Mo > C−RE > Al−Al > Al−Mo > Al−RE > Mo−Mo ≈ Mo−RE. This classification is consistent with the one for conventional MAX phases, where M−X bonds are stronger than M−A bonds (see Fig. 6.20(a)) [69, 354], and presumably indicates the exfoliation potential of RE-i-MAX phases. Recently, Dahlqvist *et al.* [158] reported a similar theoretical investigation about the bonding strengths within the $(W_{2/3}Y_{1/3})_2AlC$ system, where they concluded that C−W > Al−Al > C−Y > Al−W ≈ Al−Y. The etching of the latter resulted in $W_{1.33}C$ with ordered divacancies [55]. Consequently, the fact that C−RE bonds are strictly stronger than Al−Al ones in the RE-i-MAX systems investigated here may prevent the dissolution of the RE element together with the Al. These comments notwithstanding, it is hereby acknowledged that the etching process is much more complicated than simply breaking bonds and what is presented is at best a comparison of the RE-i-MAX systems with respect to previous reports for regular i-MAX phases [19, 55].

Exfoliation energy

The second criterion used to determine whether a RE-i-MAX phase could be successfully etched is its exfoliation energy [354]. The exfoliation energy E_{exf} can be evaluated as:

$$E_{exf} = -\frac{E_{tot}(\text{RE-}i\text{-MAX}) - 2E_{tot}(\text{RE-}i\text{-MXene}) - 12E_{tot}(\text{Al})}{4S} \quad (6.24)$$

where S is the surface area determined from the structural parameters listed in Table 6.4. E_{tot}(RE-*i*-MAX), E_{tot}(RE-*i*-MXene), and E_{tot}(Al) respectively correspond to the ground-state energy of RE-i-MAX, RE-i-MXene, and bulk aluminum per atom. E_{tot}(RE-*i*-MXene) is computed for the pristine MXene system with optimized atomic positions inside

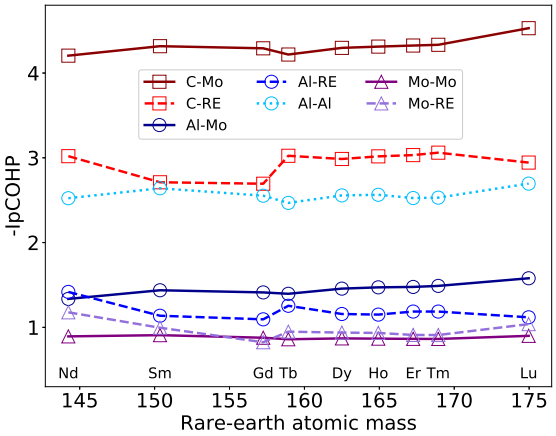

Figure 6.19: −IpCOHP values at the Fermi level as a function of the rare-earth atomic mass. The relative order of bond strengths is almost unchanged with the RE atomic mass. From [343].

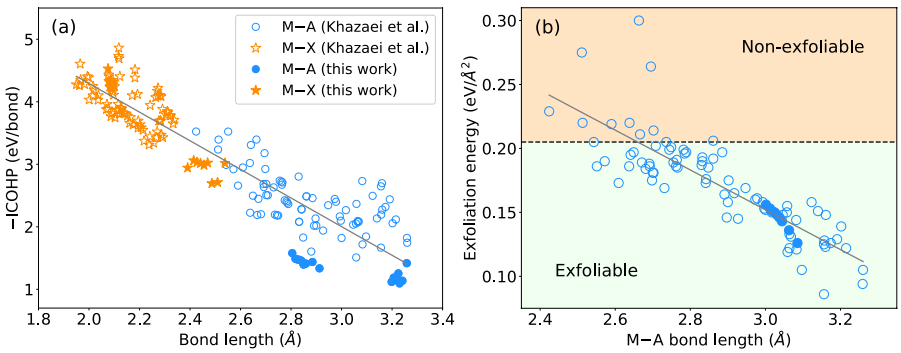

Figure 6.20: (a) Integrated COHP (bond strength) for both M−A and M−X bonds, and (b) computed static exfoliation energy as a function of the bond length, for a series of 82 MAX phases (empty markers) [354] plus the 9 considered RE-i-MAX phases (full markers). The grey lines are guides to the eyes. From [164].

the cell. Since two RE-i-MXene sheets are produced from the etching of the parent RE-i-MAX phase, the total energy is divided by four times the surface area. The computed exfoliation energies of the various RE-i-MAX phases are listed in Table 6.7.

Since no experimental exfoliation data can be found in the literature, the best we can do is compare these theoretical predictions to values for conventional MAX phases, reported by Khazaei *et al.* [354]. Among

Table 6.7: Exfoliation energy E_{exf} (eV/Å^2) for 9 different RE-i-MAX phases with RE = Nd, Sm, Gd, Tb, Dy, Ho, Er, Tm, and Lu, calculated using Eq. 6.24. For comparison, exfoliation energies of three conventional MAX phases are listed [354].

Compound	E_{exf} (eV/Å^2)
$(Mo_{2/3}Nd_{1/3})_2AlC$	0.126
$(Mo_{2/3}Sm_{1/3})_2AlC$	0.136
$(Mo_{2/3}Gd_{1/3})_2AlC$	0.143
$(Mo_{2/3}Tb_{1/3})_2AlC$	0.146
$(Mo_{2/3}Dy_{1/3})_2AlC$	0.148
$(Mo_{2/3}Ho_{1/3})_2AlC$	0.150
$(Mo_{2/3}Er_{1/3})_2AlC$	0.151
$(Mo_{2/3}Tm_{1/3})_2AlC$	0.153
$(Mo_{2/3}Lu_{1/3})_2AlC$	0.156
Ti_2AlC	0.164
Nb_2AlC	0.185
V_2AlC	0.205

the successfully etched MAX phases, V_2AlC has the largest theoretical exfoliation energy of 0.205 eV/Å^2. Therefore, from the computed values in Table 6.7, that are all smaller than the one of V_2AlC, we expect that RE-i-MAX phases could *a priori*, be successfully etched into RE-i-MXenes.

Combining the analysis of the bonding strength (Fig. 6.19) with the computed exfoliation energy in Table 6.7, the exfoliation potential of RE-i-MAX phases is confirmed. Since no major difference is observed in the classification of the bonding strength for the various RE-i-MAX systems, the exfoliation energy values are used to sort the nine systems studied herein. The Nd-based compound is the most promising candidate for exfoliation, because the ease of exfoliation decreases with the RE atomic mass. This trend can be related to the M−A interatomic distance, as presented in Fig. 6.20. The smaller the M−A bond lengths, the stronger the system, and hence the larger the exfoliation energy. This is consistent with the data reported for conventional MAX phases presented in Fig. 6.20 for a series of 82 MAX phases.

6.2.6 *Conclusions*

In summary, we report on the growth and characterization of nine representative members of the new family of rare-earth containing i-MAX single crystals, *viz.* $(Mo_{2/3}RE_{1/3})_2AlC$ with RE = Nd, Sm, Gd, Tb, Dy, Ho, Er, Tm, and Lu.

The structure determined by XRD is confirmed by STEM images as well as by a good agreement between experimental and computed Raman wavenumbers. The *ab initio* calculations of the vibrational properties include the determination of phonon mode wavenumbers, symmetries, and relative atomic displacements. A full analysis of the results is provided, as well as a comparison of the Raman spectra of five of the nine systems. In this framework, the changes in mode wavenumbers are explained by changes in RE mass and bond stiffnesses. From this analysis, twelve high-intensity Raman peaks, present in the five experimental spectra, are identified as the Raman fingerprint of the RE-i-MAX phases, thus allowing for the identification of i-MAX phases and the possible detection of defects, in future work.

Additionally, the electronic, elastic, and hardness properties of nine RE-i-MAX systems are addressed and their exfoliation potential into 2D RE-i-MXenes is investigated, via a complete analysis of both bond strengths and exfoliation energies. Similar to regular MAX phases, RE-i-MAX phases are quite stiff, with Young's moduli ranging from 215 to 245 GPa, as confirmed also by nanoindentation tests on a $(Mo_{2/3}Ho_{1/3})_2$ AlC single crystal. All bulk, shear, and Young's moduli increase with the mass of the RE element, which is consistent with the shrinking of the unit cell induced when moving from left to right on the lanthanide row. Considering that the theoretical values are obtained from first-principles calculations without taking either the temperature or the presence of defects into account, the agreement with the experimental values is remarkable. The *ab initio* calculations of the electronic properties reveal the metallic character of all the systems under investigation and the complete analysis of the bonding strengths leads to the major conclusion that C−Mo and C−RE bonds are stronger than the Al−Mo and Al−RE ones. Finally, the computation of the exfoliation energy confirms the exfoliation potential of the RE-i-MAX phases into RE-i-MXenes.

We believe that this experimental and theoretical study of the physical properties of the recently discovered RE-i-MAX phases will guide further research works to predict potential applications for these sys-

tems. Overall, we believe that the theoretical prediction of the exfoliation potential of the RE-i-MAX phases represents a promising breakthrough for future experimental exfoliation of the presented nine RE-based systems, and their potential use in applications where 2D magnetic materials are desired.

Details matter, it's worth waiting to get it right.

— **S. Jobs**

7 INVESTIGATION OF THE V_2CT_z MXENE

Since the discovery of the first MXene less than 10 years ago, remarkable progress has been made in the synthesis process, in the characterization of the structural and physical properties, and in the search for potential applications. Additionally, MXenes have been investigated intensively from first-principles calculations which play an important role in understanding and predicting the MXenes properties. However, among the several dozens of MXenes predicted to date, the first reported $Ti_3C_2T_z$ system has attracted most attention, with about half of the works dedicated to it.

In this chapter, we focus on the vanadium-based MXenes and investigate the structural, electronic, and vibrational properties of both pristine V_2C and fully-terminated V_2CT_2 (T = F, OH) monolayers using first-principles DFT techniques. In Section 7.1, the atomic structures of V_2C-based MXene phases are optimized, and their respective dynamical stabilities are discussed. In Section 7.2, electronic band structures are computed and indicate that V_2C is metallic as well as all the corresponding functionalized systems. Section 7.3 reports on the vibrational properties of V_2C-based MXenes, including phonon frequencies and spectra, respectively computed within DFPT and measured through Raman spectroscopy. Both Raman-active (E_g, A_{1g}) and infrared-active (E_u, A_{2u}) vibrational modes are predicted *ab initio* with the aim to correlate the experimental Raman peaks with the calculated vibrational modes and to assign them to specific atomic motions. The effect of the terminal groups on the vibrational properties is emphasized, along with the effect on the presence and position of the corresponding Raman peaks. Our results provide insights for the identification and characterization of V_2C-based samples using Raman spectroscopy. Conclusions are drawn in Section 7.4.

The structural properties of V_2C are computed *ab initio* within the ABINIT package [284, 285], using the PBE approximation to the exchange-correlation functional [262]. ONCVPSP pseudopotentials [319] are used to describe the core-valence interaction. A plane-wave basis set with a converged energy cutoff of 80 Ry is used to represent the wave functions. The first Brillouin zone is sampled with an $18 \times 18 \times 1$ Monkhorst-Pack k-point grid [269]. The atomic positions are optimized until the largest force is smaller than 2.5 10^{-4} eV/Å. To prevent an undesired interaction between isolated monolayers, a vacuum spacing of at least 10 Å is introduced. Atomic models are rendered using VESTA [344].

The ground state structure of the pristine V_2C with fully relaxed geometry is found to be hexagonal. The unit cell includes three atoms, two vanadium and one carbon, and resides in the $P\bar{3}m1$ (#164) space group. The V atoms are located at $\left(\frac{1}{3}, \frac{2}{3}, z\right)$ and $\left(\frac{2}{3}, \frac{1}{3}, -z\right)$ on the $2d$ Wyckoff sites, and the C atom is located at $(0, 0, 0)$ on the $1a$ Wyckoff site. These atoms are therefore arranged in a triple-layer structure where the C layer is sandwiched between the two V layers, as illustrated in Fig. 7.1(a). The lattice constant a is equal to 2.89 Å, and the layer thickness d equals 2.18 Å (see Fig. 7.1(a)).

Based on the unit cell of pristine V_2C, functionalized V_2CT_2 MXene structures with terminations T = F and OH are constructed. Two types of hollow sites on the surface of V_2C can be distinguished: A sites correspond to *fcc* sites for which no C atom is present under the V atoms, while B sites correspond to *hcp* sites located on the top of a C atom, as depicted in Fig. 7.1(a). As previously proposed by Khazaei *et al.* [136], different functionalization models can be built according to the positions of the termination groups. Four models are proposed here and are represented in Figs. 7.1(b)−7.1(e). In model 1 (MD1), two functional groups of the same type are positioned on the top of the two transition metal atoms V (see Fig. 7.1(b)). In the case of model 2 (MD2), the two functional groups are located on the top of the hollow sites A (see Fig. 7.1(c)). Model 3 (MD3) considers one functional group on the top of hollow site A and a second functional group of the same type on the top of hollow site B (see Fig. 7.1(d)). Last, model 4 (MD4) presents two functional groups located on the top of hollow sites B

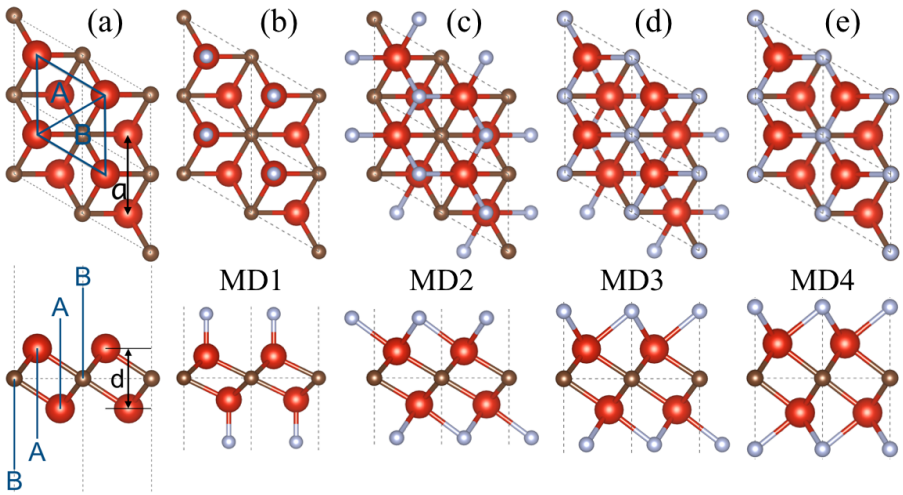

Figure 7.1: Atomic structures of (a) pristine V_2C and four models for terminated V_2CT_2: (b) MD1, (c) MD2, (d) MD3, and (e) MD4 - top and side views. Vanadium and carbon atoms are respectively in red and brown, while the functional groups (T = F, OH) are in blue. In (a), A and B indicate the two types of hollow sites and a and d are the lattice constant and the layer thickness, respectively. From [193].

(see Fig. 7.1(e)). For each type of functionalization, the four configurations are systematically investigated and their respective stabilities are compared. The relative structural stability of the four models usually depends on the possibility for the transition metal to provide sufficient electrons to both the carbon atoms and the functional groups [136]. Table 7.1 summarizes the structural parameters computed *ab initio* for the four models. To ascertain the stability of the functionalized V_2CT_2 MXene monolayers and in order to determine the most stable configuration for each system, the formation energies are computed, according to the following formula [356]:

$$\Delta H_f = E_{tot}\left(V_2CT_2\right) - E_{tot}\left(V_2C\right) - E_{tot}\left(T_2\right) - 2\mu_T \tag{7.1}$$

where $E_{tot}(V_2C)$ and $E_{tot}(V_2CT_2)$ stand for the total energy of the pristine and terminated MXene, respectively. Depending on the terminal groups, $E_{tot}(T_2)$ corresponds to the total energy of F_2 or O_2+H_2 and μ_T is the chemical potential of the chemisorbed groups which can vary as a function of temperature and pressure. For all the terminated structures, the MXene surfaces are assumed to be fully-terminated with no dangling bond remaining, as suggested by Khazaei *et al.* [136]. Results of formation energy calculations at $\mu_T = 0.0\,\text{eV}$, consistently with

previous works [136], are presented in Table 7.1. The large negative values for the formation energies of all V_2CT_2 systems reported in Table 7.1 indicate the spontaneous and exothermic formation of strong ionic bonds between vanadium atoms and terminal groups [136].

Table 7.1: Structural parameters and formation energies for pristine V_2C and MD1−MD4 functionalized systems.

	Model	a (Å)	V−V (Å)	d (Å)	ΔH_f (eV)
V_2C		2.89	2.18	2.18	0
V_2CF_2	MD1	3.20	1.79	5.28	−8.65
	MD2	2.99	2.04	4.59	−9.45
	MD3	2.89	2.24	4.90	−8.94
	MD4	2.80	2.49	5.12	−9.10
$V_2C(OH)_2$	MD1	3.22	1.78	7.24	−7.98
	MD2	3.00	2.06	6.54	−9.41
	MD3	2.93	2.24	6.77	−9.02
	MD4	2.85	2.45	6.94	−9.16
$V_2CF(OH)$	MD1	3.21	1.79	6.26	−8.39
	MD2	2.99	2.05	5.58	−9.46
	MD3	2.91	2.24	5.86	−8.96
	MD4	2.83	2.47	6.04	−9.14

In addition, it is found that the energetically favored structures for V_2C-based systems functionalized with −F and −OH groups correspond to MD2, where the terminal groups occupy *fcc* sites. As a general trend for M_2XT_2 systems, MD1 is generally less stable than the other three models. Depending on the ionic state of the transition-metal element and the nature of the terminal group, either MD2, MD3, or MD4 is found as the most stable configuration [136]. The following sections deal with pristine V_2C and functionalized V_2CF_2 and $V_2C(OH)_2$ systems in their energetically favored configurations, *i.e.*, MD2.

High-symmetry points in the BZ of hexagonal systems include Γ $(0,0,0)$, M $(1/2,0,0)$, and K $(1/3,1/3,0)$ points, with Γ−M and Γ−K respectively along the armchair and zigzag direction, as represented in Fig. 7.2(a). According to its electronic band structure, the V_2C monolayer exhibits a metallic behavior (see Fig. 7.2(b)). In contrast with the well-studied Ti_3C_2 MXene system which undergoes a metallic to indirect band gap semiconductor transition [192], V_2CT_2 structures preserve their metallic character. Figures 7.2(b)−7.2(d) show the calculated band structures of V_2C, V_2CF_2, and $V_2C(OH)_2$, respectively, which are in agreement with previous calculations [174, 189, 357]. At first sight, these band structures show some similarities, and, as both −F and −OH groups are able to catch only one electron from the pristine surfaces, they seem to affect the electronic band structure of V_2C in a similar way. However, in order to better understand the role played by the terminal groups on the electronic bandstructure and DOS, a precise analysis of the position and origin of the different orbitals in the DOS is provided.

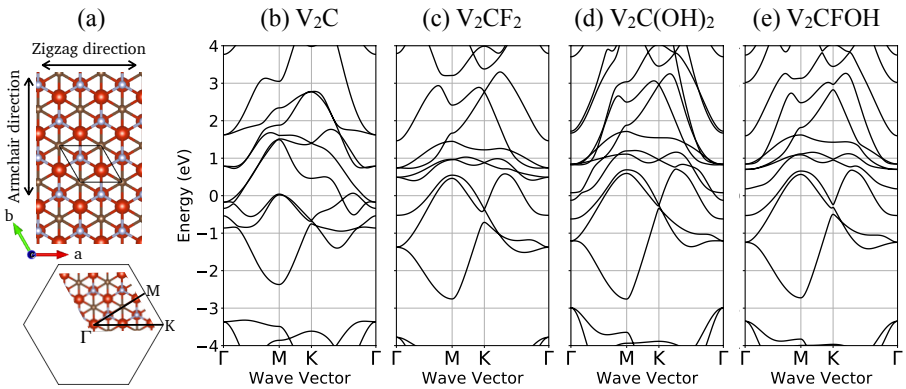

Figure 7.2: (a) V_2CT_2 atomic structure, unit cell, and Brillouin zone, including Γ, M, and K points, with Γ−M and Γ−K respectively along the armchair and zigzag direction. Electronic band structure of (b) V_2C, (c) V_2CF_2, (d) $V_2C(OH)_2$, and (e) $V_2CF(OH)$ in their high-symmetric configuration. The Fermi level is fixed as the reference of zero energy. Adapted from [193].

For both V_2C and V_2CT_2 (T = F, OH) systems, the local density of states (LDOS) for each atom is computed and plotted in Fig. 7.3. More-

over, in order to investigate the contribution of each atomic orbital in the LDOS, the projected densities of states (pDOS) are also calculated.

When bringing atoms in close proximity, strong chemical bonds such as ionic and covalent bonds are formed, respectively, from the transfer and sharing of electrons between atoms. The two electrons involved in bonding are coupled together with a bond strength depending on the overlap between their atomic orbitals. Metal atoms usually take part in bonding via their partially filled valence orbitals. Therefore, in V_2C-based systems, the C atom is involved in the bonding states through its outmost 2*s* and 2*p* orbitals, and V atoms are mainly involved through their 3*d* orbitals. In Fig. 7.3(a), both LDOS and pDOS of pristine V_2C are presented and information on the hybridization of V-3*d*, C-2*p*, and C-2*s* orbitals can be used to discuss the nature of the bonding states. In the lowest-energy region, the states around 11 and 13 eV below the Fermi level can be regarded as bonding states between the C-2*s* and the V-3*d* orbitals. The pDOS of C-2*p* orbitals are mainly distributed between -6 and -3 eV. These states can clearly be assigned to bonding states between the C-2*p* and the V-3*d* orbitals. Given the low electronegativity difference between C and V elements ($\Delta\chi = 0.93 < 1.7$), the V$-$C bond is assumed to be covalent. Around -3 eV, there is a pseudogap of about 1 eV which can be seen as the separation between the bonding and antibonding states. Finally, the states in the vicinity of the Fermi level (from -2 eV and above) correspond to V-3*d* states and are expected to give rise to electrical conductivity in the V_2C system. Upon functionalization, the atomic orbitals from the terminal groups add up in the LDOS and pDOS features. In the pDOS of V_2CF_2 presented in Fig. 7.3(b), the F-2*p* orbitals are mainly located between -8 and -4 eV and can be attributed to bonding states between V-3*d* and F-2*p* orbitals. Given the large electronegativity difference between V and F atoms ($\Delta\chi = 2.35 > 1.7$), the V$-$F bonds consist in ionic bonds. Some F-2*p* states are also found near the Fermi energy and ensure the metallic character of V_2CF_2. In the pDOS of $V_2C(OH)_2$, the O-2*p* orbitals are mainly distributed between -8 and -4 eV and can be assigned to bonding states between V-3*d* and O-2*p* orbitals (see Fig. 7.3(c)). Similarly to V$-$F bonds, V$-$O bonds are ionic with an electronegativity difference $\Delta\chi = 1.81 > 1.7$ between V and O atoms. Due to the presence of H atoms, some bonding states between O-2*p* and H-1*s* orbitals are found in the energy range between -10 and -9 eV. As a consequence, the general bonding character of both V_2C and V_2CT_2 systems thus involve strong covalent V$-$C bonds and

ionic V−T bonds which stabilize the systems. In addition, the metallic character of the system is explained by the presence of the 3*d* orbitals of the V atoms around the Fermi level [358]. Finally, upon adsorption of −F or −OH groups onto the V_2C surfaces, each F or OH group obtains one electron from V_2C leading to a slight shift of the Fermi level and of the V-3*d*, C-2*s* and C-2*p* bands. This shift is small and indicates that the V−C bonds in the different V_2C-based systems are relatively similar, explaining also the very similar V−V distances $\sim 2.0 - 2.2$ Å, (Table 7.1).

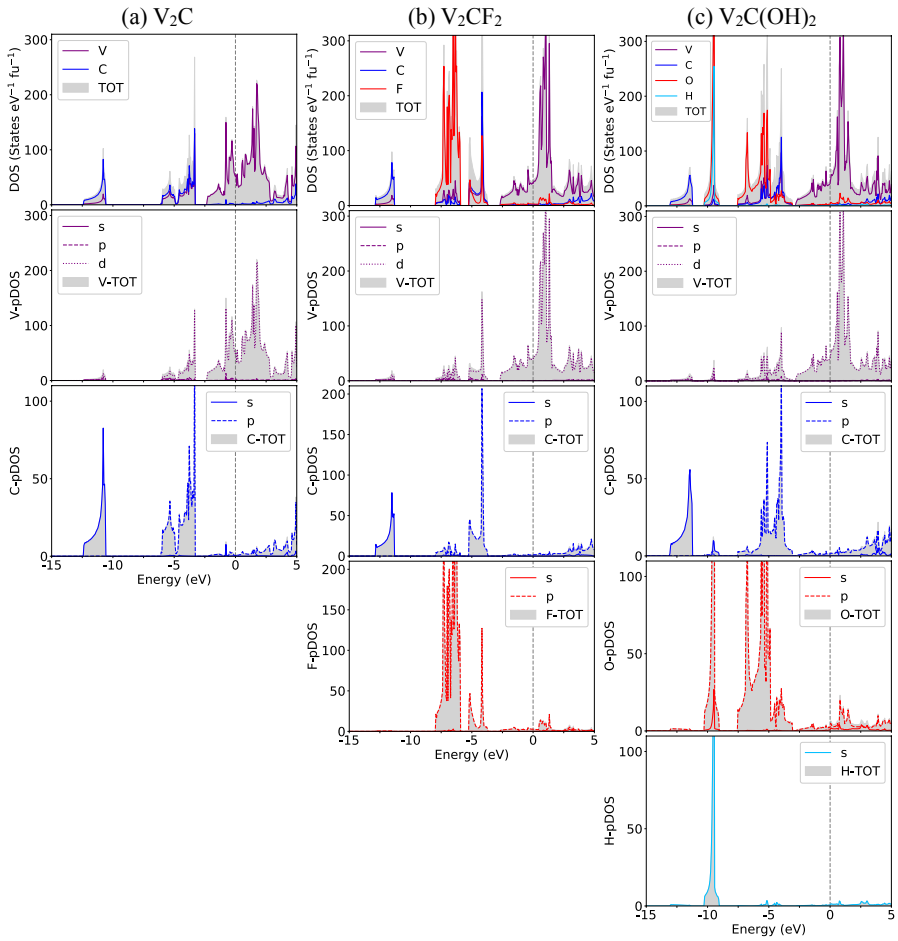

Figure 7.3: Local and projected density of states of (a) V_2C, (b) V_2CF_2, and (c) $V_2C(OH)_2$ in their high-symmetric configuration. The Fermi level is positioned at zero energy. Adapted from [193].

Our theoretical prediction of the metallic character of V_2C-based systems has been confirmed by electrical measurements on exfoliated V_2CT_z MXene flakes [359]. Although the electrical measurements were conducted on multilayered ($\sim$ 20 nm thick) samples with mixed terminations, they can be considered as a first reliable confirmation of the metallic character of the V-based systems.

7.3 VIBRATIONAL PROPERTIES

The vibrational properties and dynamical stability of V_2C-based MXenes are studied for different functionalization configurations within the DFPT framework [272, 273]. Based on the crystal structure of the V_2C and V_2CT_2 systems, the three atoms of the primitive cell in V_2C monolayer give rise to six optical modes and three acoustic modes at the Γ point of the BZ. In V_2CF_2, the five atoms of each primitive cell lead to twelve optical modes and three acoustic modes at the Γ point of the BZ. In the $V_2C(OH)_2$, the seven atoms of each primitive cell lead to eighteen optical modes and three acoustic modes at the Γ point of the BZ. The optical phonons in the center of the BZ can be classified with the following irreducible representations:

$$\Gamma_{\text{optical}}\left(V_2C\right) = \underbrace{A_{1g} + E_g}_{\text{Raman}} + \underbrace{A_{2u} + E_u}_{\text{IR}} \tag{7.2}$$

$$\Gamma_{\text{optical}}\left(V_2CF_2\right) = \underbrace{2A_{1g} + 2E_g}_{\text{Raman}} + \underbrace{2A_{2u} + 2E_u}_{\text{IR}} \tag{7.3}$$

$$\Gamma_{\text{optical}}\left(V_2C(OH)_2\right) = \underbrace{3A_{1g} + 3E_g}_{\text{Raman}} + \underbrace{3A_{2u} + 3E_u}_{\text{IR}} \tag{7.4}$$

where E-symmetry modes (E_g and E_u) are doubly-degenerate. Making good use of the group theory, the Raman and IR activity of the mode can be predicted. Phonon modes with symmetry E_g and A_{1g} are found to be Raman-active, while E_u and A_{2u} are IR-active. In the case of pristine V_2C, the Raman-active modes correspond to the low-frequency optical modes (at 224 and 359 cm^{-1}) while the IR-active modes correspond to the high-frequency modes (at 610 and 701 cm^{-1}). The Raman- and IR-active mode frequencies for all considered V_2C-based systems are reported in Table 7.2.

Table 7.2: Vibrational mode wavenumbers of the stable V_2C-based monosheets. E_g and E_u modes are doubly-degenerate.

	Raman modes					
	$E_g(1)$	$A_{1g}(1)$	$E_g(2)$	$A_{1g}(2)$	$E_g(3)$	$A_{1g}(3)$
V_2C	224.4	358.9	–	–	–	–
V_2CF_2	197.8	289.6	281.6	525.6	–	–
$V_2C(OH)_2$	214.3	301.1	296.6	530.2	443.2	3613.3
	IR modes					
	$A_{2u}(1)$	$E_u(1)$	$E_u(2)$	$A_{2u}(2)$	$E_u(3)$	$A_{2u}(3)$
V_2C	610.4	700.8	–	–	–	–
V_2CF_2	636.0	761.0	221.3	442.8	–	–
$V_2C(OH)_2$	627.4	757.5	285.5	446.7	435.7	3600.0

The correspondence between the vibrational modes of the three systems is determined according to the direction of the vibrations and the nature of the contributing atoms. Schematic representations of the Raman- and IR-active modes of the pristine V_2C are illustrated in Fig. 7.4.

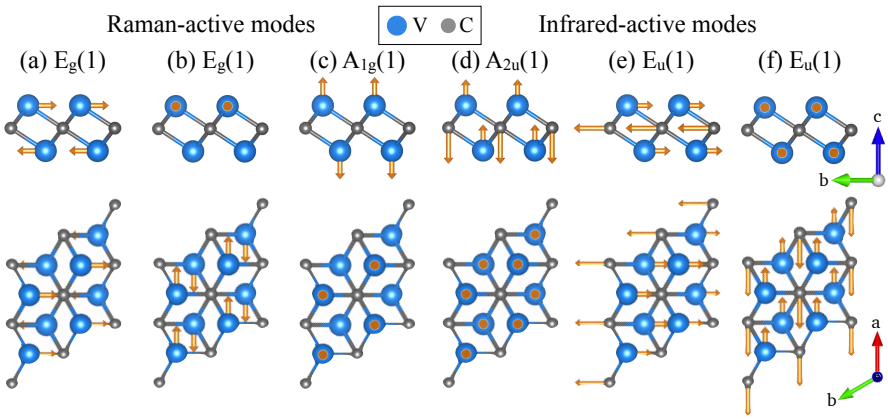

Figure 7.4: Schematic representations of the Raman-active (a)–(b) degenerate $E_g(1)$ mode at 224 cm^{-1} and (c) $A_{1g}(1)$ mode at 359 cm^{-1}; and IR-active (d) $A_{2u}(1)$ mode at 610 cm^{-1} and (e)–(f) degenerate $E_u(1)$ mode at 701 cm^{-1}, of pristine V_2C MXene. The arrows represent the eigen-displacements on each atom. Adapted from [193].

Knowledge of the phonon spectrum of a material is essential to understand a wide set of macroscopic properties, including the electrical and thermal conductivities. The phonon spectrum of V_2C has been reported by Gao *et al.* [189], highlighting the stability of the system. Phonon dispersions and phonon densities of states for the V_2C, V_2CF_2, and $V_2C(OH)_2$ monolayers are presented in Figs. 7.5(a)−7.5(c).

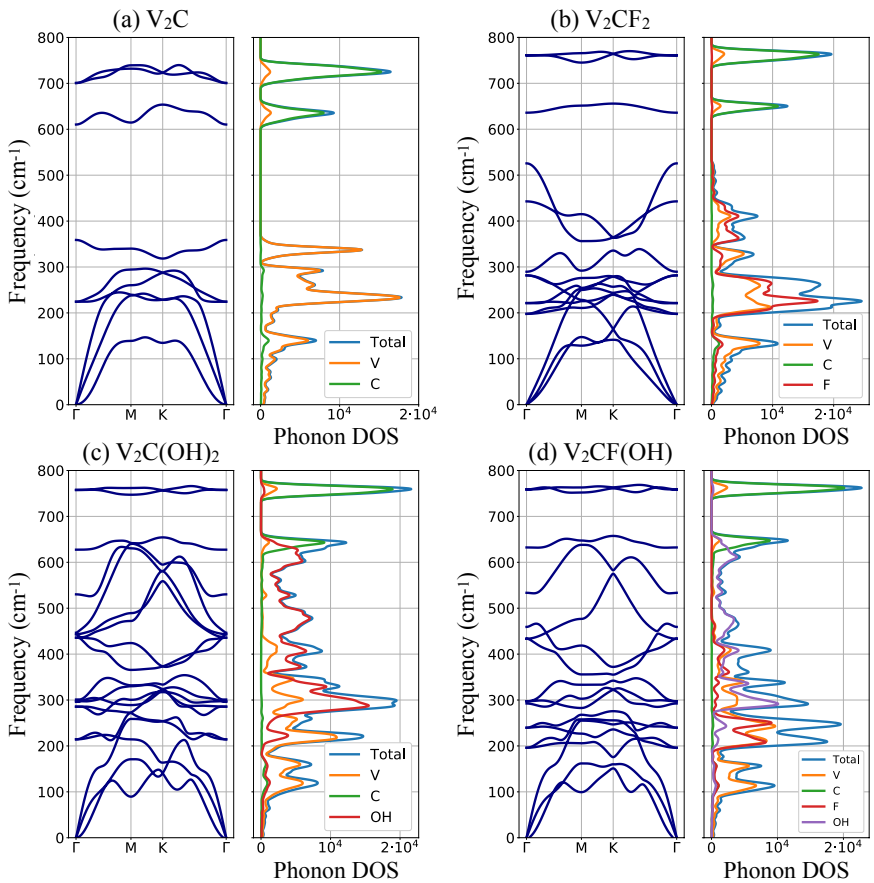

Figure 7.5: Phonon band structures and density of states of (a) V_2C, (b) V_2CF_2, (c) $V_2C(OH)_2$, and (d) $V_2CF(OH)$ in their high-symmetric nonmagnetic configuration. For the three systems, the phonon density of states for each atom is also plotted allowing for a better visualization of the contributing atoms in each normal mode. For (c) and (d), the high-frequency branches at around $3600\,\mathrm{cm}^{-1}$, arising from OH-vibrations, are not shown. From [193].

The phonon dispersions have three acoustic modes. Two of them exhibit a linear dispersion near Γ and correspond to in-plane rigid-body motions. In contrast, the third acoustic mode corresponding to

out-of-plane vibration has a quadratic dispersion close to Γ and a lower energy in the rest of the spectrum. This quadratic dependence is analogous to the one observed in graphene [360] and in MoS_2 [361], and was originally demonstrated by Lifshitz [362]. In Fig. 7.5(a), the vibrations of the V_2C system are below 750 cm^{-1}. The highest peaks in energy in the phonon DOS have a large intensity due to the flatness of the bands around Γ. Moreover, the first three optical branches in the phonon spectrum demonstrate significantly lower frequencies close to the three acoustic phonon branches, thus inducing a phonon gap of about 250 cm^{-1} between the lower three and the upper three optical branches. This is a general property of MXenes and has already been observed previously in several MXene systems [191]. For the functionalized forms, the phonon gap between optical phonons is filled by additional optical phonon branches. This makes the most noticeable difference between pristine and terminated MXene systems. The phonon spectra of the terminated V_2CT_2 systems presented in Figs. 7.5(b) and 7.5(c) reveal that the highest optical phonon frequencies are between 750 cm^{-1} and 800 cm^{-1}, slightly larger than for the pristine case.

To further understand the role played by the surface functionalization in the MXene layer and its influence on the vibrational properties, the Raman- and infrared-active frequencies of the three monolayers are compared.

First of all, as presented in Table 7.2, all terminal atoms strongly influence the normal-mode frequencies calculated for pristine V_2C. Regarding the Raman-active frequencies, the doubly-degenerate $E_g(1)$ modes at 224 cm^{-1} and the $A_{1g}(1)$ mode at 359 cm^{-1} in the pristine V_2C monolayer correspond respectively to in-plane and out-of plane vibrations of V atoms, and are represented in Figs. 7.4(a)−7.4(c). The $E_g(1)$ frequency shifts to lower wavenumbers upon terminating with −F and −OH functional groups. The $A_{1g}(1)$ mode is softened to 290 and 301 cm^{-1} upon functionalization with −F and −OH groups. Since their main contributions are from vibrations of V atoms, it can be inferred that the terminal groups at the surface add up to the reduced mass in Eq. 6.14, hence reducing the mode wavenumber ω. The IR-active frequencies located at 610 and 701 cm^{-1} correspond predominantly to out-of-plane motions of C atoms ($A_{2u}(1)$ mode) and in-plane motion of C atoms (doubly degenerate $E_u(1)$ modes), respectively, as depicted in Figs. 7.4(d)−7.4(f). The former mode at 610 cm^{-1} shifts

to 636 and 627 cm^{-1}, while the latter one at 701 cm^{-1} is shifted to 761 and 758 cm^{-1} when terminating with $-$F and $-$OH groups, respectively. Therefore, the addition of the functional groups, which are not directly bonded to the C atoms, involves a strengthening of the V$-$C bonds, which, from Eq. 6.14, results in an increase of the mode wavenumber.

The remaining modes are attributed to the in-plane and out-of-plane vibrations of $-$F and $-$OH groups. The phonon modes at about 3600 cm^{-1} in the $V_2C(OH)_2$ monolayer ($A_{1g}(3)$ and $A_{2u}(3)$ modes) are dominated by the vibration of the $-$OH terminal groups. In the V_2CF_2 monolayer, the frequencies around 500 cm^{-1} ($A_{1g}(2)$ and $A_{2u}(2)$ modes) are due to collaborative vibrations of V and F atoms. Collaborative vibrations of V and OH are also observed around 500 cm^{-1} in $V_2C(OH)_2$ ($A_{1g}(2)$, $E_g(3)$, $A_{2u}(2)$, and $E_u(3)$ modes). As the terminal $-$F and $-$OH groups strongly bond with V, the band gap centered around 500 cm^{-1} in the V_2C monolayer disappears in V_2CT_2 (T = F, OH). Lower-wavenumber phonons in Figs. 7.5(a)$-$7.5(c) are due to collaborative motion of all atoms in the layers.

Thanks to its sensitivity to very small changes in crystal structures, Raman spectroscopy is used to characterize the composition and the quality of samples. However, before it can be used for this purpose, it is fundamental to properly define the peak positions and to assign them to the phonons computed at the Brillouin zone center (Γ point). This allows us to identify the contribution of each atom and group of atoms in the various vibrational modes corresponding to the reported peaks.

The Raman spectrum of V_2C-based samples simply deposited on a glass slide is presented in Fig. 7.6(b). The comparison between the Raman spectrum of the 3D V_2AlC MAX phase and the corresponding 2D V_2CT_z MXene system indicates a global reduction of the peak intensities and a broadening of the peaks, probably due to the larger defects concentration in the 2D system with respect to its 3D counterpart. Globally speaking, the two Raman spectra are very different, with sharp and well-defined peaks in the Raman spectrum of V_2AlC in contrast to those observed in the Raman spectrum of V_2C (see Fig. 7.6(b)). Four peaks are identified in the V_2AlC spectrum at 158 cm^{-1} (E_{2g}), 240 cm^{-1} (E_{1g}), 257 cm^{-1} (E_{2g}), and 361 cm^{-1} (A_{1g}) [104]. The first two peaks, corresponding to in-plane vibrations of V and Al atoms, seem to completely disappear, due to the removal of Al atoms, as confirmed by our

EDX measurements [359]. The other two peaks, corresponding, respectively, to in-plane and out-of-plane vibrations of V atoms, can still find an equivalence in the V_2C spectrum, as confirmed by our theoretical prediction of an E_g mode around 224 cm^{-1} ($E_g(1)$) and an A_{1g} mode around 359 cm^{-1} ($A_{1g}(1)$) for the V_2C system. In addition, as the etching process involves the substitution of Al atoms with lighter elements (F, OH), additional peaks can be observed at higher frequencies. These features make us confident with the achievement of the etching process and the resulting removal of the Al atoms from the V_2AlC sample. This was further verified through EDX measurements. Results are not discussed here but can be found in Ref. [359].

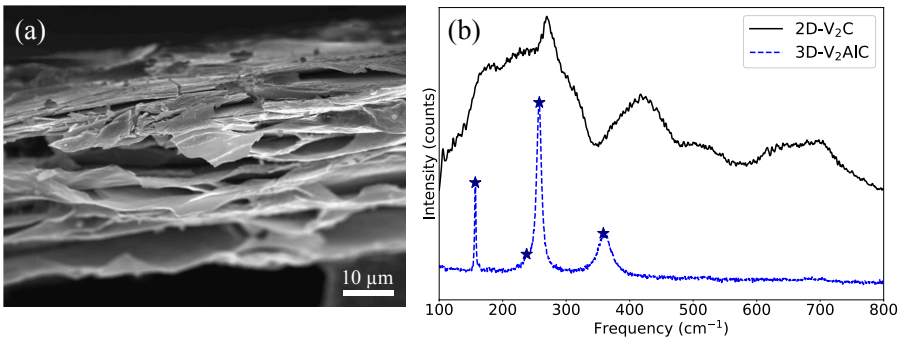

Figure 7.6: (a) SEM image and (b) Raman spectrum of the 3D MAX V_2AlC and the 2D MXene produced by HF-etching of V_2AlC sample. Note the sample consists in the stacking of numerous 2D layers, with curved paper-like morphology. From [193].

The calculated Raman-active frequencies of both V_2C and V_2CT_2 systems are reported in Table 7.2 and also illustrated in Fig. 7.7. The predicted peak positions for the V_2C monolayer are not sufficient to describe the experimental Raman spectrum, especially above 400 cm^{-1}. Upon termination with $-F$ and $-OH$ groups, additional Raman frequencies appear around 525 cm^{-1} and around 443, 530, and 3613 cm^{-1}, respectively. These frequencies roughly match most of the bands in the collected spectrum and it turns out that the peaks around 430 and 530 cm^{-1} are clearly indicative of terminated V_2CT_2 MXene. The peak around 3600 cm^{-1} in the experimental spectrum (not shown here) confirms the presence of $-OH$ terminal groups at the sample surface. However, there are still some discrepancies between the theoretical predictions and the experimental Raman frequencies, as some predicted frequencies do not correspond to

any Raman bands and vice versa. More specifically, the theoretical simulations of both pristine and terminated V_2CT_z MXenes are not able to describe the hump between 600 and 700 cm^{-1}. Different factors can explain these deviations. First, the calculations are performed for homogeneous terminal groups, while the surface of our exfoliated sample is randomly terminated with both $-F$ and $-OH$ groups [138]. Second, the calculations deal with flat monolayers, while our sample consists in a stacking of sheets including stress and corrugations, as highlighted in Fig. 7.6(a). For instance, the presence of intrinsic defects such as vacancies and adatoms was evidenced in $Ti_3C_2T_z$ systems [137].

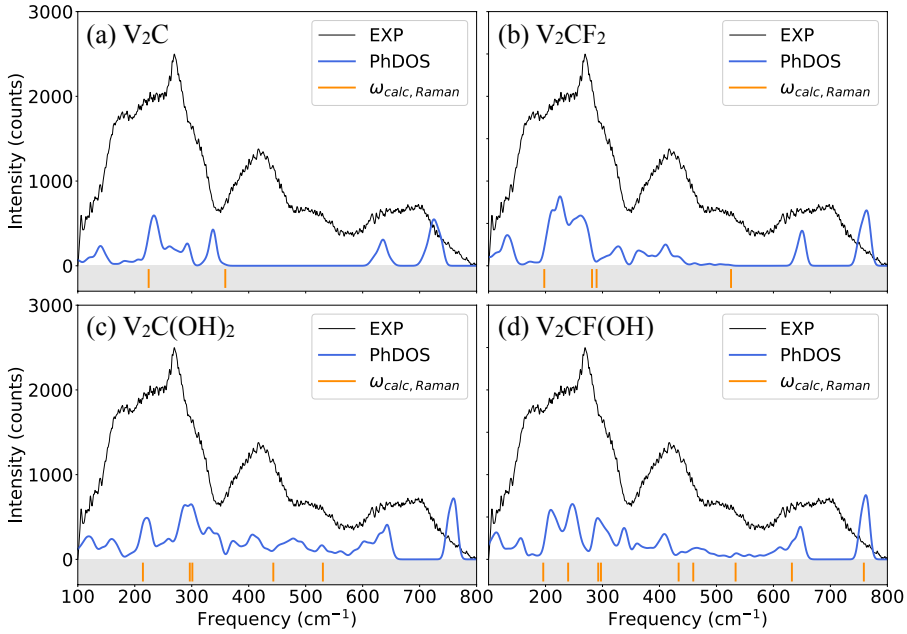

Figure 7.7: Raman spectrum of the exfoliated V_2C-based sample collected at room temperature. The calculated Raman-active wavenumbers and the total phonon densities of states of the (a) V_2C, (b) V_2CF_2, (c) $V_2C(OH)_2$, and (d) $V_2CF(OH)$ mono-sheets are also included under the experimental spectrum for comparison. The matching between the predicted normal mode wavenumbers and the experimental spectrum confirms the presence of heterogeneous terminal groups randomly distributed at the V_2C surface. Adapted from [193].

With the hope to improve the agreement between the experiment and the theoretical predictions, we investigate the effect of heterogeneous termination on the Raman-active modes. Using the same principles as for the homogeneous functionalization, the $V_2CF(OH)$ monolayer (F terminated on one side while OH terminated on the other side of the layer) is built. The four models (MD1−MD4) are tested and it is found that an equivalent of MD2 is the most energetically favorable configuration (Table 7.1). As presented in Fig. 7.2(e), $V_2CF(OH)$ is electrically conductive. The heterogeneity of the terminal groups induces a difference in the V−T bonding lengths on both sides of the MXene layer. As the reduced coordinates are modified, the Wyckoff positions are influenced and, hence, the space group is moved to $P3m1$ (#156). For such configuration, the irreducible representation is given by:

$$\Gamma_{\text{optical}}\left(V_2CF(OH)\right) = \underbrace{5A_1 + 5E}_{\text{Raman+IR}} \tag{7.5}$$

where both A_1 and E modes are Raman- and infrared-active. The predicted normal-mode frequencies of $V_2CF(OH)$ are listed in Table 7.3 and are compared to the experimentally collected Raman spectrum in Fig. 7.7(d).

Table 7.3: Vibrational mode wavenumbers (in cm^{-1}) of the stable heterogeneously-terminated $V_2CF(OH)$ system. All A_1 and E vibrational modes are Raman- and IR-active. E modes are doubly-degenerate.

Raman and IR active modes of $V_2CF(OH)$									
$E(1)$	$E(2)$	$A_1(1)$	$E(3)$	$E(4)$	$A_1(2)$	$A_1(3)$	$A_1(4)$	$E(5)$	$A_1(5)$
196.0	239.7	292.5	297.3	433.6	459.3	533.6	632.4	758.7	3616.6

There are four main additional Raman-active modes at 434, 459, 632, and 759 cm^{-1} with respect to the homogeneous situations. The first two peaks match well with the band around 430 cm^{-1}, and the last two peaks with the hump centered at 650 cm^{-1} in the experimental spectrum. This close matching between the theoretically predicted positions of the Raman-active peaks and the experimental Raman spectrum reflects the fact that the terminal groups are actually heterogeneous and most likely randomly distributed at the V_2C surface.

Table 7.4 summarizes the assignment of the experimental peaks to the theoretical predictions. These results suggest that the presence of Raman peaks between 400 and 550 cm^{-1} is indicative of terminated

V_2CT_2 systems, while the peak centered at $650\,cm^{-1}$ seems to originate from the presence of heterogeneous functional groups at the sample surface. The presence of $-OH$ groups gives rise to a peak around $3600\,cm^{-1}$ in the experimental spectrum. The deviations between the computed and collected Raman frequencies are reported in Table 7.4 and indicate that the experimental Raman frequencies are correctly predicted, with maximal deviations of 15% and 3% in the low- and high-wavenumber ranges, respectively.

Table 7.4: Experimental Raman peaks positions compared to the predicted Raman active wavenumbers computed for V_2C, V_2CF_2, $V_2C(OH)_2$ and $V_2CF(OH)$ mono-sheets. The last row corresponds to the maximal deviation (in %) of the computed frequencies for $V_2CF(OH)$ with respect to the experimental data. The symmetries of the modes assigned to the experimental peaks are indicated and correspond either to E_g or A_{1g} for the homogeneoulsy-terminated systems, or to E or A_1 for the heterogeneously-terminated system.

	Raman wavenumbers (cm^{-1})						
Exp.	~ 170	~ 230	~ 270	~ 430	~ 540	~ 650	~ 3600
	–	E_g	$A_{1g} + E_g$	E_g	A_{1g}	–	A_{1g}
V_2C	–	224	359	–	–	–	–
V_2CF_2	–	198	282, 290	–	526	–	–
$V_2C(OH)_2$	–	214	297, 301	443	530	–	3613
	E	E	$A_1 + E$	$E + A_1$	A_1	A_1	A_1
$V_2CF(OH)$	196	240	293, 297	434, 459	534	632	3617
Δ_{max}(%)	15	4	10	7	1	3	0.5

7.4 CONCLUSIONS

In conclusion, the static and dynamical properties of pristine bare V_2C and terminated V_2CT_2 (T = F and OH) monolayers have been investigated using first-principles techniques. The results discussed in the previous sections give insights into the structural, electronic, and vibrational properties of an emerging family of 2D material, MXene.

The optimized crystal structure of V_2C is dynamically stable and the surface functionalization with $-F$ and $-OH$ groups is energetically favorable. Regarding the electronic properties, both V_2C and V_2CT_2 (T = F, OH) systems are metallic. The electronic bands crossing the Fermi

level come from V-3*d* orbitals. The analysis of the phonon dispersion and phonon DOS of the bare V_2C monolayer demonstrates the presence of a phonon gap between the three lowest and the three highest optical branches. Upon functionalization, such a phonon band gap disappears as the gap is bridged by vibrations of the terminal groups (F and OH). It was shown that the terminal atoms weaken the motions in which the V atoms are involved while strengthening the vibrations of the C atoms. The corresponding vibrational frequencies are drastically changed when the nature of the functional group is modified. Vibrational properties were computed with the aim to understand and characterize the origin of the Raman-active peaks in the experimental spectrum. A first attempt to assign the atomic motions to the experimental Raman peaks was proposed. The comparison of our theoretical predictions with the experimental Raman spectrum gives a relatively good agreement, as both the number of peaks and their positions are well described, especially when considering mixed terminal groups at the MXene's surface. The list of central peak frequencies for each hump in the experimental spectrum reported in Table 7.4 can thus be considered a signature of V_2C samples with different chemical terminations.

The results presented here form a prerequisite to experimental non-destructive identification and synthesis of V_2C-based 2D materials, in particular, and M_2XT_z Mxenes, in general.

Everything will be ok in the end. If it's not ok, it's not the end.

— J. Lennon

8 PERSPECTIVES AND CONCLUSIONS

With roughly 2,000 publications on the MAX phases, and over 2,300 ones on the MXenes, it is clear that both MAX and MXenes have considerably attracted and are still attracting attention from the scientific community. Without exception, our group has jumped into this exciting field and, during four years, I have been fortunate to work on MAX and MXenes and to meet the related amazing community.

In summary, this thesis has been devoted to the investigation of the structural, electronic, vibrational, thermal, and elastic properties of the 3D MAX phase single crystals and the derived 2D MXenes. The approach adopted throughout these four years consisted in a subtle combination of theoretical predictions and experimental measurements. Most of the projects have involved strong collaborations with both experimental and theoretical groups worldwide, especially with the groups of Prof. M. W. Barsoum (Drexel University, USA), Prof. T. Ouisse (Grenoble, France), and Prof. J. Rosen (Linköping, Sweden). Among others, this work allowed to gain insight into the anisotropy present in the MAX phase properties, to understand the bonding nature and strength within quaternary RE-i-MAX phases, and to predict their potential exfoliation into RE-i-MXenes. Additionally, the Raman fingerprint of RE-i-MAX phases has been established and a complete analysis of the relative atomic displacements has been proposed. Finally, the electronic and vibrational properties of V_2CT_z MXenes functionalized either with homogeneous or heterogeneous terminal groups have been studied theoretically and compared to experimental measurements, *i.e.*, to experimental Raman spectra. This led to the main conclusion that heterogeneous terminal groups must be considered in the calculations in order to more accurately reproduce the experimental conditions and recover the experimental results. In the following paragraphs, some of the most important challenges and scientific concerns that still need to be addressed for both

MAX and MXenes are discussed, some avenues to characterize these systems in future experimental and theoretical works are proposed, and eventually some concluding remarks on the work achieved in this thesis are drawn.

The considerable success of the MAX phases mostly results from their unique combination of metal and ceramic-like properties. Most remarkable is the ease with which they can be machined. This exceptional set of properties observed in the MAX phases can predominantly be understood from their layered structures and the combination of strong M−X bonds in contrast to the weaker M−A bonds. Another important advantage of the MAX phases is the ease by which one can change their chemistry and, consequently, tune their properties, while keeping their structure the same. In total, more than 150 MAX phases with different compositions and atomic ordering have been reported experimentally, while the stability of many others has been established theoretically. As outlined in this thesis, the understanding of the properties of the MAX phases has considerably evolved in 20 years. However, there are still important challenges that need to be overcome and many scientific questions that need to be answered.

On the experimental side, while the ternary MAX phases have been intensively studied, most of the recently discovered quaternary phases, including solid solutions and ordered phases, have not been characterized yet. This can be explained by the lack of pure quaternary phases. However, as presented in this thesis, we recently reported on the growth of nine RE-i-MAX single crystals and characterized experimentally their structures, Raman spectra, and elastic properties. We strongly believe that this will stimulate the MAX community to grow other pure quaternary single crystals and systematically characterize them. A second point regards the characterization of the defects present in the MAX phases, *e.g.*, vacancies, grain boundaries, lack of stoichiometry, and their impact on the MAX phase properties. For instance, while the presence of C vacancies has been evidenced in many systems, their effect on the electrical and thermal transport and on the mechanical response is still not fully understood. Eventually, with the possibility to grow large single crystals since 2011 comes the possibility to investigate the potential anisotropy of their physical properties. Until now, only the anisotropy in the magneto-transport and electronic properties of a few ternary MAX phases has been evidenced experimentally via transport or ARPES measurements, respectively. From the

results presented in this thesis for Cr_2AlC single crystals, the electronic structure, phonon branches, and thermal conductivity are significantly anisotropic. In contrast, from the point of view of their elastic properties, MAX single crystals are isotropic.

Theoretically, understanding the role played by the chemistry and chemical ordering on the transport, magnetic, vibrational, and elastic properties of the MAX phases is fundamental. In this context, exploring the large compositional space available for the MAX phases and comparing their physical properties in a more systematic way would be beneficial. For many ternary MAX phases, the theoretical investigation includes the prediction of their electronic, vibrational, magnetic, thermal, thermodynamic, and elastic properties. For the most part, and when experimental data are available, *ab initio* calculations and experiments are in good agreement. This is especially true for the vibrational properties and the elastic constants, which are within $10 - 15\%$ of relative difference. In the same way the experimental characterization is lacking for solid solutions, there is also less DFT work in the literature. This reflects the challenge, in terms of computational time, to perform calculations on large, disordered, or randomly-ordered solid-solution systems. Consequently, efforts must be done in this regard with the aim to fully understand the effect of both defects and disorder on MAX properties. In contrast, the electronic, vibrational, and elastic properties of many quaternary ordered MAX phases, *i.e.*, i-MAX, o-MAX, and RE-i-MAX phases, have been studied from first principles, including this thesis. As highlighted in this thesis, the agreement between experiments and theoretical predictions is decent, which should stimulate the MAX community to use DFT calculations to investigate MAX properties and screen the results to find some outlier systems.

It goes without saying that the current success of the MAX phases can, at least in part, also be attributed to the possibility to use them as 3D precursors to obtain 2D MXenes. Since the discovery of the first MXene in 2011, remarkable progress has been made in the synthesis process, in the characterization of the structural and physical properties, and in the search for potential applications. In total, about 30 MXenes have been successfully produced. Considering the versatility in both elemental composition and surface termination of MXenes, hundreds of them could potentially be formed. Additionally, MXenes have been investigated intensively from first-principles calculations which play an

important role in understanding and predicting the MXenes properties. However, several challenges must be overcome on both experimental and theoretical sides before promoting their use in next-generation applications.

The experimental challenges can be summarized into three main points: (i) Only 20% of the existing MAX phases have been exfoliated, which leaves a lot of space for future experimental work. Besides, many MXenes have been investigated theoretically for which the MAX precursors have not been produced yet. Therefore, the synthesis of new MAX phases is an important research direction to increase the number of available 2D MXenes. Additionally, the mechanism that governs MAX phase etchability still needs to be clarified. In this context, *ab initio* calculations could help to gain insight into the exfoliation process and find new routes for efficient etching of non-Al elements. (ii) The lack of large defect-free monolayer MXenes prevents the experimental measurement of their intrinsic mechanical response. Indeed, most reports of the mechanical properties of MXenes are theoretical works. Similarly, the electrical, thermoelectric, and magnetic properties have been intensively studied from first-principles approaches and await experimental verification. Given that most of the exotic electrical (semiconductor, topological insulator) and magnetic properties (half-metallicity, large magnetic moment) have been predicted for pristine or homogeneously-terminated systems, an essential challenge consists in the synthesis of MXenes with none or uniform surface terminations. In this context, it is highly desirable to develop new etching routes or post-processing techniques with better control of the surface functionalization. Alternatively, more efforts should be focused on the study of the CVD growth of MXenes. (iii) Eventually, most experimental works have been conducted on the first MXene, $Ti_3C_2T_z$, while very few other MXenes have been characterized to date. Among others, the freshly discovered o-MXenes, i-MXenes, and ordered divacancy systems await for experimental characterization of their electronic, magnetic, and transport properties.

Theoretically, understanding the role played by the chemistry and structure on the transport, magnetic, and electrochemical properties of MXenes is fundamental and would ultimately allow to build a material with the desired properties for a targeted application. In this context, the theoretical approach should be as realistic as possible. To date, an accurate modeling of the experimental conditions is still lacking, since most works are dedicated to pristine

or homogeneously-functionalized MXenes, which is not the case experimentally. In this thesis, we highlighted the necessity to include heterogeneous terminal groups in the simulations in order to match better with the real situation and recover the experimental Raman data. Besides, most theoretical works use DFT calculations, and only few AIMD or more advanced simulations have been reported. In the future, more robust tools should be used or developed with the aim to study the transport properties, including electronic band gap, thermoelectric power factor, and thermal transport. In general, the rich chemistry and versatility of MXenes offer a wide area for theoretical works. With the constant discovery of new MAX phases, the amount of potential predictive works continuously increases, and can be extended to the investigation of their 2D counterparts. Notwithstanding, the recent discovery of RE-i-MAX phases with various magnetic ordering, and the prediction of their potential exfoliation in the present thesis, could potentially enlarge the palette of intrinsic magnetic 2D crystals. However, more work is needed in order to assess whether these systems keep, or not, their magnetic properties once exfoliated. More generally, the optical, electrochemical, and thermal properties of all MXenes have not been well described yet.

In conclusion, considering that the MAX community came back to life about 20 years ago while the first MXene has been produced less than 10 years ago, the amount of information already available in the literature, regarding the synthesis and properties of both these families, is remarkable. However, proportionally to the amount of predicted MAX and MXene compositions and accessible properties, there is still a large space for future experimental and theoretical works. With the significant role played nowadays by machine learning in the discovery of new systems and the prediction of their properties, it is reasonable to expect it to be used in the field of MAX and MXenes in the near future.

PUBLICATIONS

1. A. Champagne, J.-L. Battaglia, T. Ouisse, F. Ricci, A. Kusiak, C. Pradere, V. Natu, A. Dewandre, M. J. Verstraete, M. W. Barsoum, and J.-C. Charlier, Heat capacity and anisotropic thermal conductivity in Cr_2AlC single crystals at high temperature, in preparation (2020)

2. H. O. Badr, A. Champagne, T. Ouisse, J.-C. Charlier, and M. W. Barsoum, Elastic properties and hardness of V_2AlC and Cr_2AlC MAX phase single crystals, Phys. Rev. Materials **4**, 083605 (2020)

3. A. Champagne and J.-C. Charlier, Physical properties of 2D MXenes: from a theoretical perspective, J. Phys. Mater. **3**, 032006 (2020)

4. A. Champagne, S. Dechamps, S. M.-M. Dubois, A. Lherbier, V.-H. Nguyen, and J.-C. Charlier, Computational atomistic modeling in carbon flatland and other 2D nanomaterials, Appl. Sci. **10** (5), 1724 (2020)

5. A. Champagne, F. Ricci, M. Barbier, T. Ouisse, D. Magnin, S. Ryelandt, T. Pardoen, G. Hautier, M. W. Barsoum, and J.-C. Charlier, Insights into the elastic properties of RE-i-MAX phases and their potential exfoliation into two-dimensional RE-i-MXenes, Phys. Rev. Materials **4**, 013604 (2020)

6. A. Champagne, O. Chaix-Pluchery, T. Ouisse, D. Pinek, I. Gélard, L. Jouffret, M. Barbier, F. Whilhelm, Q. Tao, J. Lu, J. Rosen, M. W. Barsoum, and J.-C. Charlier, First-order Raman scattering of rare-eartj containing i-MAX single crystals $(Mo_{2/3}RE_{1/3})_2AlC$ (RE = Nd, Gd, Dy, Ho, Er), Phys. Rev. Materials **3**, 053609 (2019)

7. Q. Tao, T. Ouisse, D. Pinek, O. Chaix-Pluchery, F. Whilhelm, A. Rogalev, C. Opagiste, L. Jouffret, A. Champagne, J.-C. Charlier, J. Lu, L. Hultman, M. W. Barsoum, and J. Rosen, Rare-earth (RE) nanolaminates $Mo_4RE_4Al_7C_3$ featuring ferromagnetism and mixed-valence states, Phys. Rev. Materials **2**, 114401 (2018)

8. A. Champagne, F. Bourdarot, P. Bourges, P. Piekarz, D. Pinek, I. Gélard, J.-C. Charlier, and T. Ouisse, Phonon dispersion curves in Cr_2AlC single-crystals, Mater. Res. Lett. **6**, 378 – 383 (2018)

9. A. Champagne, L. Shi, T. Ouisse, B. Hackens, and J.-C. Charlier, Electronic and vibrational properties of V_2C-based MXenes: From experiments to first-principles modeling, Phys. Rev. B **97**, 115439 (2018)

BIBLIOGRAPHY

[1] M. W. Barsoum. *MAX Phases*. 1st ed. Wiley-Blackwell, 2013. DOI: 10.1002/9783527654581.

[2] V. H. Nowotny. *Progress in Solid State Chemistry* 5 (1971), pp. 27 –70. DOI: 10.1016/0079-6786(71)90016-1.

[3] W. Jeitschko and H. Nowotny. *Monatsh. Chem.* 98 (1967), pp. 329–337. DOI: 10.1007/BF00899949.

[4] H. Wolfsgruber, H. Nowotny, and F. Benesovsky. *Monatsh. Chem.* 98 (1967), pp. 2403–240. DOI: 10.1007/BF00902438.

[5] M. A. Pietzka and S. J. *Journal of Phase Equilibria* 15 (1994), pp. 392–400. DOI: 10.1007/BF02647559.

[6] M. A. Pietzka and S. J. *Journal of the American Ceramic Society* 79.9 (1996), pp. 2321–2330. DOI: 10.1111/j.1151-2916.1996.tb08979.x.

[7] J. Schuster and H. Nowotny. *Zeitschrift fuer Metallkunde* 71.6 (1980), pp. 341–346.

[8] M. W. Barsoum and T. El-Raghy. *Journal of the American Ceramic Society* 79.7 (1996), pp. 1953–1956. DOI: 10.1111/j.1151-2916.1996.tb08018.x.

[9] M. W. Barsoum, D. Brodkin, and T. El-Raghy. *Scripta Materialia* 36.5 (1997), pp. 535 –541. DOI: 10.1016/S1359-6462(96)00418-6.

[10] T. El-Raghy, S. Chakraborty, and M. W. Barsoum. *Journal of the European Ceramic Society* 20.14 (2000), pp. 2619 –2625. DOI: 10.1016/S0955-2219(00)00127-8.

[11] M. W. Barsoum, L. Farber, I. Levin, et al. *Journal of the American Ceramic Society* 82.9 (1999), pp. 2545–2547. DOI: 10.1111/j.1151-2916.1999.tb02117.x.

[12] M. W. Barsoum, T. El-Raghy, and A. Procopio. *Metallurgical and Materials Transactions A* 31.2 (2000), pp. 333 –337. DOI: 10.1007/s11661-000-0268-y.

[13] M. W. Barsoum. *Progress in Solid State Chemistry* 28.1 (2000), pp. 201 –281. DOI: 10.1016/S0079-6786(00)00006-6.

[14] M. Barsoum and M. Radovic. *Annual Review of Materials Research* 41 (2011), pp. 195–227. DOI: 10.1146/annurev-matsci-062910-100448.

[15] F. Meng, Y. Zhou, and J. Wang. *Scripta Materialia* 53.12 (2005), pp. 1369 –1372. DOI: 10.1016/j.scriptamat.2005.08.030.

[16] T. Cabioch, P. Eklund, V. Mauchamp, et al. *Journal of the European Ceramic Society* 33.4 (2013), pp. 897 –904. DOI: 10.1016/j.jeurceramsoc.2012.10.008.

[17] A. Mockute, J. Lu, E. J. Moon, et al. *Materials Research Letters* 3.1 (2015), pp. 16–22. DOI: 10.1080/21663831.2014.944676.

[18] Z. Liu, E. Wu, J. Wang, et al. *Acta Materialia* 73 (2014), pp. 186 –193. DOI: 10.1016/j.actamat.2014.04.006.

[19] Q. Tao, M. Dahlqvist, J. Lu, et al. *Nature Communications* 8 (2017), pp. 1–7. DOI: 10.1038/ncomms14949.

[20] M. Naguib, M. Kurtoglu, V. Presser, et al. *Advanced Materials* 23.37 (2011), pp. 4248–4253. DOI: 10.1002/adma.201102306.

[21] F. Mercier, T. Ouisse, and D. Chaussende. *Phys. Rev. B* 83.7 (2011), p. 075411. DOI: 10.1103/PhysRevB.83.075411.

[22] F. Mercier, O. Chaix-Pluchery, T. Ouisse, et al. *Applied Physics Letters* 98.8 (2011), p. 081912. DOI: 10.1063/1.3558919.

[23] J.-F. Li, T. Matsuki, and R. Watanabe. *Journal of Materials Science* 38.12 (2003), pp. 2661 –2666. DOI: 10.1023/A:1024490720287.

[24] M. Lopacinski, J. Puszynski, and J. Lis. *Journal of the American Ceramic Society* 84.12 (2001), pp. 3051–3053. DOI: 10.1111/j.1151-2916.2001.tb01138.x.

[25] C. Yeh and Y. Shen. *Journal of Alloys and Compounds* 470.1 (2009), pp. 424 –428. DOI: 10.1016/j.jallcom.2008.02.086.

[26] J. Yang, S. Dong, Y. Ding, et al. *Journal of the American Ceramic Society* 93.8 (2010), pp. 2117–2120. DOI: 10.1111/j.1551-2916.2010.03672.x.

[27] S. Yang, Z. M. Sun, and H. Hashimoto. *Journal of Alloys and Compounds* 368.1 (2004), pp. 312 –317. DOI: 10.1016/j.jallcom.2003.07.018.

[28] H. Högberg, P. Eklund, J. Emmerlich, et al. *Journal of Materials Research* 20.4 (2005), pp. 779–782. DOI: 10.1557/JMR.2005.0105.

[29] J. Nickl, K. Schweitzer, and P Luxenberg. *Journal of the Less Common Metals* 26.3 (1972), pp. 335 –353. DOI: 10.1016/0022-5088(72)90083-5.

[30] S. Jacques, H. Di-Murro, M.-P. Berthet, et al. *Thin Solid Films* 478.1 (2005), pp. 13 –20. DOI: 10.1016/j.tsf.2004.09.043.

[31] C. Höglund, M. Beckers, N. Schell, et al. *Applied Physics Letters* 90.17 (2007), p. 174106. DOI: 10.1063/1.2731520.

[32] M. Sonestedt, J. Frodelius, M. Sundberg, et al. *Corrosion Science* 52.12 (2010), pp. 3955–3961. DOI: 10.1016/j.corsci.2010.08.004.

[33] Z. Sun, M. Li, L. Hu, et al. *Journal of the American Ceramic Society* 92.8 (2009), pp. 1695–1702. DOI: 10.1111/j.1551-2916.2009.03136.x.

[34] X. Wang and Y. Zhou. *J. Mater. Chem.* 12.3 (2002), pp. 455–460. DOI: 10.1039/B108685E.

[35] S. Gupta and M. W. Barsoum. *Journal of The Electrochemical Society* 151.2 (2004), p. D24. DOI: 10.1149/1.1639160.

[36] S. Dubois, T. Cabioc'h, P. Chartier, et al. 'A New Ternary Nanolaminate Carbide: Ti3SnC2.' *Progress in Nanotechnology*. John Wiley & Sons, Ltd, 2014, pp. 401–403. DOI: 10.1002/9780470588246.ch54.

[37] N. V. Tzenov and M. W. Barsoum. *Journal of the American Ceramic Society* 83.4 (2000), pp. 825–832. DOI: 10.1111/j.1151-2916.2000.tb01281.x.

[38] Z. Lin, Y. Zhou, Y. Zhou, et al. *Zeitschrift für Metallkunde* 96.3 (2005), pp. 291 –296. DOI: 10.3139/146.101033.

[39] W. Zhang, N. Travitzky, C. Hu, et al. *Journal of the American Ceramic Society* 92.10 (2009), pp. 2396–2399. DOI: 10.1111/j.1551-2916.2009.03187.x.

[40] N. Gao, J. Li, D Zhang, et al. *Journal of the European Ceramic Society* 22.13 (2002), pp. 2365 –2370. DOI: 10.1016/S0955-2219(02)00021-3.

[41] Z. Sun, H. Hashimoto, W. Tian, et al. *International Journal of Applied Ceramic Technology* 7.6 (2010), pp. 704–718. DOI: 10.1111/j.1744-7402.2010.02555.x.

[42] T. Ouisse, E. Sarigiannidou, O. Chaix-Pluchery, et al. *Journal of Crystal Growth* 384 (2013), pp. 88–95. DOI: 10.1016/j.jcrysgro.2013.09.021.

[43] L. Shi, T. Ouisse, E. Sarigiannidou, et al. *Acta Materialia* 83 (2015), pp. 304 –309. DOI: 10.1016/j.actamat.2014.10.018.

[44] T. Ouisse, L. Shi, B. A. Piot, et al. *Phys. Rev. B* 92.4 (2015), p. 045133. DOI: 10.1103/PhysRevB.92.045133.

[45] T. Ouisse and M. W. Barsoum. *Materials Research Letters* 5.6 (2017), pp. 365–378. DOI: 10.1080/21663831.2017.1333537.

[46] T. Ito, D. Pinek, T. Fujita, et al. *Phys. Rev. B* 96.19 (2017), p. 195168. DOI: 10.1103/PhysRevB.96.195168.

[47] H. Kudielka and H. Rohde. *Zeitschrift für Kristallographie* 114.1-6 (1960), p. 44456. DOI: 10.1524/zkri.1960.114.1-6.447.

[48] L. Farber, I. Levin, M. W. Barsoum, et al. *Journal of Applied Physics* 86.5 (1999), pp. 2540–2543. DOI: 10.1063/1.371089.

[49] C. Rawn, M. Barsoum, T El-Raghy, et al. *Materials Research Bulletin* 35.11 (2000), pp. 1785 –1796. ISSN: 0025-5408. DOI: 10.1016/S0025-5408(00)00383-4.

[50] P. Eklund, J.-P. Palmquist, J. Höwing, et al. *Acta Materialia* 55.14 (2007), pp. 4723 –4729. ISSN: 1359-6454. DOI: 10.1016/j.actamat.2007.04.040.

[51] J. Etzkorn, M. Ade, D. Kotzott, et al. *Journal of Solid State Chemistry* 182.5 (2009), pp. 995 –1002. ISSN: 0022-4596. DOI: 10.1016/j.jssc.2009.01.003.

[52] J. Wang, T.-N. Ye, Y. Gong, et al. *Nature Communications* 10.2284 (2019), pp. 2041–1723. DOI: 10.1038/s41467-019-10297-8.

[53] E. N. Caspi, P. Chartier, F. Porcher, et al. *Materials Research Letters* 3.2 (2015), pp. 100–106. DOI: 10.1080/21663831.2014.975294.

[54] B. Anasori, Y. Xie, M. Beidaghi, et al. *ACS Nano* 9.10 (2015), pp. 9507–9516. DOI: 10.1021/acsnano.5b03591.

[55] R. Meshkian, M. Dahlqvist, J. Lu, et al. *Advanced Materials* 30.21 (2018), p. 1706409. DOI: 10.1002/adma.201706409.

[56] M. Dahlqvist, J. Lu, R. Meshkian, et al. *Science Advances* 3.7 (2017), pp. 1 –9. DOI: 10.1126/sciadv.1700642.

[57] J. Lu, A. Thore, R. Meshkian, et al. *Crystal Growth & Design* 17.11 (2017), pp. 5704–5711. DOI: 10.1021/acs.cgd.7b00642.

[58] M. Dahlqvist, A. Petruhins, J. Lu, et al. *ACS Nano* 12.8 (2018), pp. 7761–7770. DOI: 10.1021/acsnano.8b01774.

[59] L. Chen, M. Dahlqvist, T. Lapauw, et al. *Inorganic Chemistry* 57.11 (2018), pp. 6237–6244. DOI: 10.1021/acs.inorgchem.8b00021.

[60] A. Petruhins, M. Dahlqvist, J. Lu, et al. *Crystal Growth & Design* 20.1 (2020), pp. 55–61. DOI: 10.1021/acs.cgd.9b00449.

[61] Q. Tao, J. Lu, M. Dahlqvist, et al. *Chemistry of Materials* 31.7 (2019), pp. 2476–2485. DOI: 10.1021/acs.chemmater.8b05298.

[62] A. Petruhins, J. Lu, L. Hultman, et al. *Materials Research Letters* 7.11 (2019), pp. 446–452. DOI: 10.1080/21663831.2019.1644684.

[63] Q. Tao, T. Ouisse, D. Pinek, et al. *Phys. Rev. Materials* 2.11 (2018), p. 114401. DOI: 10.1103/PhysRevMaterials.2.114401.

[64] M. W. Barsoum and T. El-Raghy. *American Scientist* 89 (2001), p. 334. DOI: 10.1511/2001.4.334.

[65] M. Nelson, M. T. Agne, B. Anasori, et al. *Materials Science and Engineering: A* 705 (2017), pp. 182 –188. DOI: 10.1016/j.msea.2017.08.068.

[66] M. Barsoum and G. Tucker. *Scripta Materialia* 139 (2017), pp. 166 –172. DOI: 10.1016/j.scriptamat.2017.04.002.

[67] M. W. Barsoum, X. Zhao, S. Shanazarov, et al. *Phys. Rev. Materials* 3.1 (2019), p. 013602. DOI: 10.1103/PhysRevMaterials.3.013602.

[68] J. Halim, J. Palisaitis, J. Lu, et al. *ACS Applied Nano Materials* 1.6 (2018), pp. 2455–2460. DOI: 10.1021/acsanm.8b00332.

[69] M. Dahlqvist and J. Rosen. *Phys. Chem. Chem. Phys.* 17.47 (2015), pp. 31810–31821. DOI: 10.1039/C5CP06021D.

[70] X. Wang and Y. Zhou. *Journal of Materials Science & Technology* 26.5 (2010), pp. 385 –416. DOI: 10.1016/S1005-0302(10)60064-3.

[71] P. Finkel, J. D. Hettinger, S. E. Lofland, et al. *Phys. Rev. B* 65.3 (2001), p. 035113. DOI: 10.1103/PhysRevB.65.035113.

[72] S. E. Lofland, J. D. Hettinger, K. Harrell, et al. *Applied Physics Letters* 84.4 (2004), pp. 508–510. DOI: 10.1063/1.1641177.

[73] J. D. Hettinger, S. E. Lofland, P. Finkel, et al. *Phys. Rev. B* 72.11 (2005), p. 115120. DOI: 10.1103/PhysRevB.72.115120.

[74] A. S. Ingason, A. Mockute, M. Dahlqvist, et al. *Phys. Rev. Lett.* 110.19 (2013), p. 195502. DOI: 10.1103/PhysRevLett.110.195502.

[75] A. S. Ingason, M Dahlqvist, and J Rosen. *Journal of Physics: Condensed Matter* 28.43 (2016), p. 433003. DOI: 10.1088/0953-8984/28/43/433003.

[76] Z. Sun, R. Ahuja, S. Li, et al. *Applied Physics Letters* 83.5 (2003), pp. 899–901. DOI: 10.1063/1.1599038.

[77] J. M. Schneider, Z. Sun, R. Mertens, et al. *Solid State Communications* 130.7 (2004), pp. 445 –449. DOI: 10.1016/j.ssc.2004.02.047.

[78] M. Dahlqvist, B. Alling, I. A. Abrikosov, et al. *Phys. Rev. B* 84.22 (2011), p. 220403. DOI: 10.1103/PhysRevB.84.220403.

[79] Y. L. Du, Z. M. Sun, H. Hashimoto, et al. *Journal of Applied Physics* 109.6 (2011), p. 063707. DOI: 10.1063/1.3562145.

[80] M. Ramzan, S. Lebègue, and R. Ahuja. *physica status solidi (RRL) - Rapid Research Letters* 5.3 (2011), pp. 122–124. DOI: 10.1002/pssr.201004508.

[81] M. Dahlqvist, B. Alling, and J. Rosén. *Journal of Applied Physics* 113.21 (2013), p. 216103. DOI: 10.1063/1.4808239.

[82] M Dahlqvist, B Alling, and J Rosen. *Journal of Physics: Condensed Matter* 27.9 (2015), p. 095601. DOI: 10.1088/0953-8984/27/9/095601.

[83] W. Sun, W. Luo, and R. Ahuja. *Journal of Materials Science* 47.21 (2012), pp. 7615–7620. DOI: 10.1007/s10853-012-6609-6.

[84] A. Mockute, M. Dahlqvist, J. Emmerlich, et al. *Phys. Rev. B* 87.9 (2013), p. 094113. DOI: 10.1103/PhysRevB.87.094113.

[85] M. Dahlqvist, B. Alling, and J. Rosén. *Phys. Rev. B* 81.22 (2010), p. 220102. DOI: 10.1103/PhysRevB.81.220102.

[86] M. Ramzan, S. Lebègue, and R. Ahuja. *Solid State Communications* 152.13 (2012), pp. 1147 –1149. DOI: 10.1016/j.ssc.2012.03.044.

[87] N. Li, C. Dharmawardhana, K. Yao, et al. *Solid State Communications* 174 (2013), pp. 43 –45. DOI: 10.1016/j.ssc.2013.09.014.

[88] M. Mattesini and M. Magnuson. *Journal of Physics: Condensed Matter* 25.3 (2012), p. 035601. DOI: 10.1088/0953-8984/25/3/035601.

[89] Z. Liu, T. Waki, Y. Tabata, et al. *Phys. Rev. B* 88.13 (2013), p. 134401. DOI: 10.1103/PhysRevB.88.134401.

[90] A. Petruhins, A. S. Ingason, M. Dahlqvist, et al. *physica status solidi (RRL) - Rapid Research Letters* 7.11 (2013), pp. 971–974. DOI: 10.1002/pssr.201308025.

[91] M. Benouis, Y. Azzaz, M. Ameri, et al. *Journal of Superconductivity and Novel Magnetism* 29.5 (2016), pp. 1267–1272. DOI: 10.1007/s10948-016-3387-4.

[92] W Luo and R Ahuja. *Journal of Physics: Condensed Matter* 20.6 (2008), p. 064217. DOI: 10.1088/0953-8984/20/6/064217.

[93] A. Ingason, A. Petruhins, M. Dahlqvist, et al. *Materials Research Letters* 2.2 (2014), pp. 89–93. DOI: 10.1080/21663831.2013.865105.

[94] A. Thore, M. Dahlqvist, B. Alling, et al. *Journal of Applied Physics* 116.10 (2014), p. 103511. DOI: 10.1063/1.4894411.

[95] M. Dahlqvist, A. S. Ingason, B. Alling, et al. *Phys. Rev. B* 93.1 (2016), p. 014410. DOI: 10.1103/PhysRevB.93.014410.

[96] A. S. Ingason, G. K. Pálsson, M. Dahlqvist, et al. *Phys. Rev. B* 94.2 (2016), p. 024416. DOI: 10.1103/PhysRevB.94.024416.

[97] A. Thore, M. Dahlqvist, B. Alling, et al. *Phys. Rev. B* 93.5 (2016), p. 054432. DOI: 10.1103/PhysRevB.93.054432.

[98] C. Li, Z. Wang, D. Ma, et al. *Intermetallics* 43 (2013), pp. 71 –78. DOI: 10.1016/j.intermet.2013.07.015.

[99] Z. Liu, L. Zheng, L. Sun, et al. *Journal of the American Ceramic Society* 97.1 (2014), pp. 67–69. DOI: 10.1111/jace.12731.

[100] I. Persson, A. el Ghazaly, Q. Tao, et al. *Small* 14.17 (2018), p. 1703676. DOI: 10.1002/smll.201703676.

[101] N. J. Lane, M. Naguib, V. Presser, et al. *Journal of Raman Spectroscopy* 43.7 (2012), pp. 954–958. DOI: 10.1002/jrs.3101.

[102] O. D. Leaffer, S. Gupta, M. W. Barsoum, et al. *Journal of Materials Research* 22.10 (2007), pp. 2651–2654. DOI: 10.1557/JMR.2007.0376.

[103] V. Presser, M. Naguib, L. Chaput, et al. *Journal of Raman Spectroscopy* 43.1 (2012), pp. 168–172. DOI: 10.1002/jrs.3036.

[104] J. E. Spanier, S. Gupta, M. Amer, et al. *Phys. Rev. B* 71.1 (2005), p. 012103. DOI: 10.1103/PhysRevB.71.012103.

[105] J. Wang, Y. Zhou, Z. Lin, et al. *Applied Physics Letters* 86.10 (2005), p. 101902. DOI: 10.1063/1.1873057.

[106] J. Gruber, A. C. Lang, J. Griggs, et al. *Scientific Reports* 6.1 (2016), p. 33451. DOI: 10.1038/srep33451.

[107] J. Griggs, A. C. Lang, J. Gruber, et al. *Acta Materialia* 131 (2017), pp. 141 –155. DOI: 10.1016/j.actamat.2017.03.055.

[108] M. K. Drulis, H. Drulis, S. Gupta, et al. *Journal of Applied Physics* 99.9 (2006), p. 093502. DOI: 10.1063/1.2191744.

[109] L. Verger, C. Xu, V. Natu, et al. *Oxidation of Metals* 59.3 (2019), pp. 303 –320. DOI: 10.1023/A:1023092027697.

[110] M. Sundberg, G. Malmqvist, A. Magnusson, et al. *Ceramics International* 30.7 (2004). 3rd Asian Meeting on Electroceramics, pp. 1899 –1904. DOI: 10.1016/j.ceramint.2003.12.046.

[111] J. W. Byeon, J. Liu, M. Hopkins, et al. *Oxidation of Metals* 68.1 (2007), pp. 97 –111. DOI: 10.1007/s11085-007-9063-0.

[112] Z. Lin, M. Li, J. Wang, et al. *Scripta Materialia* 58.1 (2008), pp. 29 –32. DOI: 10.1016/j.scriptamat.2007.09.011.

[113] S. Basu, N. Obando, A. Gowdy, et al. *Journal of The Electrochemical Society* 159.2 (2011), pp. C90–C96. DOI: 10.1149/2.052202jes.

[114] D. J. Tallman, B. Anasori, and M. W. Barsoum. *Materials Research Letters* 1.3 (2013), pp. 115–125. DOI: 10.1080/21663831.2013.806364.

[115] M. Haftani, M. S. Heydari], H. R. Baharvandi, et al. *International Journal of Refractory Metals and Hard Materials* 61 (2016), pp. 51 –60. DOI: 10.1016/j.ijrmhm.2016.07.006.

[116] P. Eklund, M. Beckers, U. Jansson, et al. *Thin Solid Films* 518.8 (2010), pp. 1851 –1878. DOI: 10.1016/j.tsf.2009.07.184.

[117] Z. M. Sun. *International Materials Reviews* 56.3 (2011), pp. 143–166. DOI: 10.1179/1743280410Y.0000000001.

[118] P. Eklund, J. Rosen, and P. O. Å. Persson. *Journal of Physics D: Applied Physics* 50.11 (2017), p. 113001. DOI: 10.1088/1361-6463/aa57bc.

[119] M. Sokol, V. Natu, S. Kota, et al. *Trends in Chemistry* 1.2 (2019), pp. 210 –223. DOI: 10.1016/j.trechm.2019.02.016.

[120] K. S. Novoselov, A. K. Geim, S. V. Morozov, et al. *Science* 306.5696 (2004), pp. 666–669. DOI: 10.1126/science.1102896.

[121] K. S. Novoselov, A. K. Geim, S. V. Morozov, et al. *Nature* 438 (2005), pp. 197–200. DOI: 10.1038/nature04233.

[122] K. S. Novoselov. *Angewandte Chemie International Edition* 50.31 (2011), pp. 6986–7002. DOI: 10.1002/anie.201101502.

[123] L. Yu, Y.-H. Lee, X. Ling, et al. *Nano Letters* 14.6 (2014), pp. 3055–3063. DOI: 10.1021/nl404795z.

[124] A. K. Geim and I. V. Grigorieva. *Nature* 499.7459 (2013), pp. 419–425. DOI: 10.1038/nature12385.

[125] E. Pomerantseva, F. Bonaccorso, X. Feng, et al. *Science* 366.6468 (2019), pp. 1–12. DOI: 10.1126/science.aan8285.

[126] A. Champagne, S. Dechamps, S. M.-M. Dubois, et al. *Applied Sciences* 10.1724 (2020), pp. 1–19. DOI: 10.3390/app10051724.

[127] L. Song, L. Ci, H. Lu, et al. *Nano Letters* 10.8 (2010), pp. 3209–3215. DOI: 10.1021/nl1022139.

[128] Q. H. Wang, K. Kalantar-Zadeh, A. Kis, et al. *Nature Nanotechnology* 7.11 (2012), pp. 699–712. DOI: 110.1038/nnano.2012.193.

[129] B. Lalmi, H. Oughaddou, H. Enriquez, et al. *Applied Physics Letters* 97.22 (2010), p. 223109. DOI: 10.1063/1.3524215.

[130] S. Cahangirov, M. Topsakal, E. Aktürk, et al. *Phys. Rev. Lett.* 102.23 (2009), p. 236804. DOI: 10.1103/PhysRevLett.102.236804.

[131] M. E. Dávila, L Xian, S Cahangirov, et al. *New Journal of Physics* 16.9 (2014), p. 095002. DOI: 10.1088/1367-2630/16/9/095002.

[132] H. Liu, A. T. Neal, Z. Zhu, et al. *ACS Nano* 8.4 (2014), pp. 4033–4041. DOI: 10.1021/nn501226z.

[133] M. Naguib, O. Mashtalir, J. Carle, et al. *Acs Nano* 6.2 (2012), pp. 1322–1331. DOI: 10.1021/nn204153h.

[134] M. Naguib, V. N. Mochalin, M. W. Barsoum, et al. *Advanced Materials* 26.7 (2014), pp. 992–1005. DOI: 10.1002/adma.201304138.

[135] B. Anasori and Y. Gogotsi. *2D Metal Carbides and Nitrides (MXenes)*. 1st ed. Springer International Publishing, 2019. DOI: 10.1007/978-3-030-19026-2.

[136] M. Khazaei, M. Arai, T. Sasaki, et al. *Advanced Functional Materials* 23.17 (2013), pp. 2185–2192. DOI: 10.1002/adfm.201202502.

[137] L. H. Karlsson, J. Birch, J. Halim, et al. *Nano Letters* 15.8 (2015), pp. 4955–4960. DOI: 10.1021/acs.nanolett.5b00737.

[138] K. J. Harris, M. Bugnet, M. Naguib, et al. *Journal of Physical Chemistry C* 119.24 (2015), pp. 13713–13720. DOI: 10.1021/acs.jpcc.5b03038.

[139] G. Wang. *The Journal of Physical Chemistry C* 120.33 (2016), pp. 18850–18857. DOI: 10.1021/acs.jpcc.6b05224.

[140] J. Halim, K. M. Cook, M. Naguib, et al. *Applied Surface Science* 362 (2016), pp. 406 –417. DOI: 10.1016/j.apsusc.2015.11.089.

[141] B. Anasori, M. R. Lukatskaya, and Y. Gogotsi. *Nature Reviews Materials* 2.2 (2017), p. 16098. DOI: 10.1038/natrevmats.2016.98.

[142] M. Alhabeb, K. Maleski, T. S. Mathis, et al. *Angewandte Chemie International Edition* 57.19 (2018), pp. 5444–5448. DOI: 10.1002/anie.201802232.

[143] R. Meshkian, L. Åke Näslund, J. Halim, et al. *Scripta Materialia* 108 (2015), pp. 147 –150. DOI: 10.1016/j.scriptamat.2015.07.003.

[144] J. Zhou, X. Zha, F. Y. Chen, et al. *Angewandte Chemie International Edition* 55.16 (2016), pp. 5008–5013. DOI: 10.1002/anie.201510432.

[145] J. Zhou, X. Zha, X. Zhou, et al. *ACS Nano* 11.4 (2017), pp. 3841–3850. DOI: 10.1021/acsnano.7b00030.

[146] M. Ghidiu, M. R. Lukatskaya, M. Q. Zhao, et al. *Nature* 516.7529 (2014), pp. 78–81. DOI: 10.1038/nature13970.

[147] J. Halim, M. R. Lukatskaya, K. M. Cook, et al. *Chemistry of Materials* 26.7 (2014), pp. 2374–2381. DOI: 10.1021/cm500641a.

[148] W. Sun, S. A. Shah, Y. Chen, et al. *J. Mater. Chem. A* 5.41 (2017), pp. 21663–21668. DOI: 10.1039/C7TA05574A.

[149] S. Yang, P. Zhang, F. Wang, et al. *Angewandte Chemie International Edition* 57.47 (2018), pp. 15491–15495. DOI: 10.1002/anie.201809662.

[150] L. Verger, V. Natu, M. Carey, et al. *Trends in Chemistry* 1.7 (2019), pp. 656 –669. DOI: 10.1016/j.trechm.2019.04.006.

[151] X. Wang and Y. Zhou. *Current Opinion in Solid State and Materials Science* 23.3 (2019), pp. 149 –163. DOI: 10.1016/j.cossms.2019.02.001.

[152] P. Srivastava, A. Mishra, H. Mizuseki, et al. *ACS Applied Materials & Interfaces* 8.36 (2016), pp. 24256–24264. DOI: 10.1021/acsami.6b08413.

[153] Z. Guo, L. Zhu, J. Zhou, et al. *RSC Adv.* 5.32 (2015), pp. 25403–25408. DOI: 10.1039/C4RA17304J.

[154] M. Khazaei, M. Arai, T. Sasaki, et al. *Journal of Physics: Condensed Matter* 26.50 (2014), p. 505503. DOI: 10.1088/0953-8984/26/50/505503.

[155] M. Khazaei, M. Arai, T. Sasaki, et al. *Science and Technology of Advanced Materials* 15.1 (2014), p. 014208. DOI: 10.1088/1468-6996/15/1/014208.

[156] A. Gkountaras, Y. Kim, J. Coraux, et al. *Small* 16.4 (2020), p. 1905784. DOI: 10.1002/smll.201905784.

[157] I. Persson, A. el Ghazaly, Q. Tao, et al. *Small* 14.17 (2018), p. 1703676. DOI: 10.1002/smll.201703676.

[158] M. Dahlqvist, A. Thore, and J. Rosen. *Journal of Physics: Condensed Matter* 30.30 (2018), p. 305502. DOI: 10.1088/1361-648x/aacc19.

[159] T. Hu, M. Hu, B. Gao, et al. *The Journal of Physical Chemistry C* 122.32 (2018), pp. 18501–18509. DOI: 10.1021/acs.jpcc.8b04427.

[160] M. Naguib, J. Halim, J. Lu, et al. *Journal of the American Chemical Society* 135.43 (2013), pp. 15966–15969. DOI: 10.1021/ja405735d.

[161] M. Khazaei, A. Mishra, N. S. Venkataramanan, et al. *Current Opinion in Solid State and Materials Science* 23.3 (2019), pp. 164 –178. DOI: 10.1016/j.cossms.2019.01.002.

[162] C. Si, J. Zhou, and Z. Sun. *ACS Applied Materials & Interfaces* 7.31 (2015), pp. 17510–17515. DOI: 10.1021/acsami.5b05401.

[163] M. Khazaei, V. Wang, C. Sevik, et al. *Phys. Rev. Materials* 2.7 (2018), p. 074002. DOI: 10.1103/PhysRevMaterials.2.074002.

[164] A. Champagne and J.-C. Charlier. *Journal of Physics: Materials* 3.3 (2020), p. 032006. DOI: 10.1088/2515-7639/ab97ee.

[165] *aNANt: a functional materials database*. URL: http://anant.mrc.iisc.ac.in/.

[166] A. C. Rajan, A. Mishra, S. Satsangi, et al. *Chemistry of Materials* 30.12 (2018), pp. 4031–4038. DOI: 10.1021/acs.chemmater.8b00686.

[167] H. Weng, A. Ranjbar, Y. Liang, et al. *Phys. Rev. B* 92.7 (2015), p. 075436. DOI: 10.1103/PhysRevB.92.075436.

[168] M. Khazaei, A. Ranjbar, M. Arai, et al. *Phys. Rev. B* 94.12 (2016), p. 125152. DOI: 10.1103/PhysRevB.94.125152.

[169] C. Si, K.-H. Jin, J. Zhou, et al. *Nano Letters* 16.10 (2016), pp. 6584–6591. DOI: 10.1021/acs.nanolett.6b03118.

[170] C. Si, J. You, W. Shi, et al. *J. Mater. Chem. C* 4.48 (2016), pp. 11524–11529. DOI: 10.1039/C6TC04560J.

[171] Y. Liang, M. Khazaei, A. Ranjbar, et al. *Phys. Rev. B* 96.19 (2017), p. 195414. DOI: 10.1103/PhysRevB.96.195414.

[172] E. Balci, U. O. Akkus, and S. Berber. *Applied Physics Letters* 113.8 (2018), p. 083107. DOI: 10.1063/1.5042828.

[173] S. Lai, J. Jeon, S. K. Jang, et al. *Nanoscale* 7.46 (2015), pp. 19390–19396. DOI: 10.1039/C5NR06513E.

[174] M. Khazaei, A. Ranjbar, M. Ghorbani-Asl, et al. *Phys. Rev. B* 93.20 (2016), p. 205125. DOI: 10.1103/PhysRevB.93.205125.

[175] G. R. Berdiyorov. *EPL (Europhysics Letters)* 111.6 (2015), p. 67002. DOI: 10.1209/0295-5075/111/67002.

[176] T. Hu, H. Zhang, J. Wang, et al. *Scientific Reports* 5.1 (2015), p. 16329. DOI: 10.1038/srep16329.

[177] S. Kumar and U. Schwingenschlogl. *Phys. Rev. B* 94.3 (2016), p. 035405. DOI: 10.1103/PhysRevB.94.035405.

[178] J. Sootsman, H. Kong, C. Uher, et al. *Angewandte Chemie International Edition* 47.45 (2008), pp. 8618–8622. DOI: 10.1002/anie.200803934.

[179] D. LI, R. rui SUN, and X. ying QIN. *Progress in Natural Science: Materials International* 21.4 (2011), pp. 336 –340. DOI: 10.1016/S1002-0071(12)60066-5.

[180] G. J. Snyder and E. S. Toberer. *Materials for Sustainable Energy* 7 (2010), pp. 101–110. DOI: 10.1142/9789814317665_0016.

[181] X.-H. Zha, Q. Huang, J. He, et al. *Scientific Reports* 6.1 (2016), p. 27971. DOI: 10.1038/srep27971.

[182] H. Kumar, N. C. Frey, L. Dong, et al. *ACS Nano* 11.8 (2017), pp. 7648–7655. DOI: 10.1021/acsnano.7b02578.

[183] J. He, P. Lyu, and P. Nachtigall. *J. Mater. Chem. C* 4.47 (2016), pp. 11143–11149. DOI: 10.1039/C6TC03917K.

[184] M. Je, Y. Lee, and Y.-C. Chung. *Thin Solid Films* 619 (2016), pp. 131 –136. DOI: 10.1016/j.tsf.2016.11.014.

[185] J. Yang, X. Luo, S. Zhang, et al. *Phys. Chem. Chem. Phys.* 18.18 (2016), pp. 12914–12919. DOI: 10.1039/C6CP00138F.

[186] J. Yang, X. Zhou, X. Luo, et al. *Applied Physics Letters* 109.20 (2016), p. 203109. DOI: 10.1063/1.4967983.

[187] L. Dong, H. Kumar, B. Anasori, et al. *The Journal of Physical Chemistry Letters* 8.2 (2017), pp. 422–428. DOI: 10.1021/acs.jpclett.6b02751.

[188] R. A. de Groot, F. M. Mueller, P. G. v. Engen, et al. *Phys. Rev. Lett.* 50.25 (1983), pp. 2024–2027. DOI: 10.1103/PhysRevLett.50.2024.

[189] G. Gao, G. Ding, J. Li, et al. *Nanoscale* 8.16 (2016), pp. 8986–8994. DOI: 10.1039/C6NR01333C.

[190] J. He, P. Lyu, L. Z. Sun, et al. *J. Mater. Chem. C* 4.27 (2016), pp. 6500–6509. DOI: 10.1039/C6TC01287F.

[191] U. Yorulmaz, A. Özden, N. K. Perkgöz, et al. *Nanotechnology* 27.33 (2016), p. 335702. DOI: 10.1088/0957-4484/27/33/335702.

[192] T. Hu, J. Wang, H. Zhang, et al. *Phys. Chem. Chem. Phys.* 17.15 (2015), pp. 9997–10003. DOI: 10.1039/C4CP05666C.

[193] A. Champagne, L. Shi, T. Ouisse, et al. *Phys. Rev. B* 97.11 (2018), p. 115439. DOI: 10.1103/PhysRevB.97.115439.

[194] M. Kurtoglu, M. Naguib, Y. Gogotsi, et al. *MRS Communications* 2.4 (2012), pp. 133–137. DOI: 10.1557/mrc.2012.25.

[195] N. Zhang, Y. Hong, S. Yazdanparast, et al. *2D Materials* 5.4 (2018), p. 045004. DOI: 10.1088/2053-1583/aacfb3.

[196] J. C. Lei, X. Zhang, and Z. Zhou. *Front. Phys.* 10 (2015), pp. 276–286. DOI: 10.1007/s11467-015-0493-x.

[197] X.-H. Zha, K. Luo, Q. Li, et al. *Europhysics Letters* 111.2 (2015), p. 26007. DOI: 10.1209/0295-5075/111/26007.

[198] V. N. Borysiuk, V. N. Mochalin, and Y. Gogotsi. *Nanotechnology* 26.26 (2015), p. 265705. DOI: 10.1088/0957-4484/26/26/265705.

[199] A. Lipatov, H. Lu, M. Alhabeb, et al. *Science Advances* 4.6 (2018), pp. 1 –7. DOI: 10.1126/sciadv.aat0491.

[200] Z. Ling, C. E. Ren, M.-Q. Zhao, et al. *Proceedings of the National Academy of Sciences* 111.47 (2014), pp. 16676–16681. DOI: 10.1073/pnas.1414215111.

[201] M. Boota, B. Anasori, C. Voigt, et al. *Advanced Materials* 28.7 (2016), pp. 1517–1522. DOI: 10.1002/adma.201504705.

[202] C. J. Zhang and V. Nicolosi. *Energy Storage Materials* 16 (2019), pp. 102 –125. DOI: 10.1016/j.ensm.2018.05.003.

[203] M. R. Lukatskaya, S. Kota, Z. Lin, et al. *Nature Energy* 2 (2017), p. 17105. DOI: 10.1038/nenergy.2017.105.

[204] Y. Gogotsi and R. M. Penner. *ACS Nano* 12.3 (2018), pp. 2081–2083. DOI: 10.1021/acsnano.8b01914.

[205] G. Hautier, A. Jain, and S. P. Ong. *Journal of Materials Science* 47.21 (2012), pp. 7317–7340. DOI: 10.1007/s10853-012-6424-0.

[206] Q. Tang, Z. Zhou, and P. Shen. *Journal of the American Chemical Society* 134.40 (2012), pp. 16909–16916. DOI: 10.1021/ja308463r.

[207] K. Persson, Y. Hinuma, Y. S. Meng, et al. *Phys. Rev. B* 82.12 (2010), p. 125416. DOI: 10.1103/PhysRevB.82.125416.

[208] M. Ashton, R. G. Hennig, and S. B. Sinnott. *Applied Physics Letters* 108.2 (2016), p. 023901. DOI: 10.1063/1.4939745.

[209] C. Eames and M. S. Islam. *Journal of the American Chemical Society* 136.46 (2014), pp. 16270–16276. DOI: 10.1021/ja508154e.

[210] Y. Xie, Y. Dall'Agnese, M. Naguib, et al. *ACS Nano* 8.9 (2014), pp. 9606–9615. DOI: 10.1021/nn503921j.

[211] S. Murali, N. Quarles, L. L. Zhang, et al. *Nano Energy* 2.5 (2013), pp. 764 –768. DOI: 10.1016/j.nanoen.2013.01.007.

[212] M. R. Lukatskaya, O. Mashtalir, C. E. Ren, et al. *Science* 341.6153 (2013), pp. 1502–1505. DOI: 10.1126/science.1241488.

[213] L. Qin, Q. Tao, A. El Ghazaly, et al. *Advanced Functional Materials* 28.2 (2018), p. 1703808. DOI: 10.1002/adfm.201703808.

[214] R. Meshkian, H. Lind, J. Halim, et al. *ACS Applied Nano Materials* 2.10 (2019), pp. 6209–6219. DOI: 10.1021/acsanm.9b01107.

[215] M.-Q. Zhao, C. E. Ren, Z. Ling, et al. *Advanced Materials* 27.2 (2015), pp. 339–345. DOI: 10.1002/adma.201404140.

[216] F. Feng, J. Wu, C. Wu, et al. *Small* 11.6 (2015), pp. 654–666. DOI: 10.1002/smll.201402346.

[217] E. Kayali, A. VahidMohammadi, J. Orangi, et al. *ACS Applied Materials & Interfaces* 10.31 (2018), pp. 25949–25954. DOI: 10.1021/acsami.8b07397.

[218] A. D. Dillon, M. J. Ghidiu, A. L. Krick, et al. *Advanced Functional Materials* 26.23 (2016), pp. 4162–4168. DOI: 10.1002/adfm.201600357.

[219] M. Mariano, O. Mashtalir, F. Q. Antonio, et al. *Nanoscale* 8.36 (2016), pp. 16371–16378. DOI: 10.1039/C6NR03682A.

[220] R. R. Nair, P. Blake, A. N. Grigorenko, et al. *Science* 320.5881 (2008), pp. 1308–1308. DOI: 10.1126/science.1156965.

[221] G. Ying, A. D. Dillon, A. T. Fafarman, et al. *Materials Research Letters* 5.6 (2017), pp. 391–398. DOI: 10.1080/21663831.2017.1296043.

[222] G. Ying, S. Kota, A. D. Dillon, et al. *FlatChem* 8 (2018), pp. 25 –30. DOI: 10.1016/j.flatc.2018.03.001.

[223] G. R. Berdiyorov. *AIP Advances* 6.5 (2016), p. 055105. DOI: 10.1063/1.4948799.

[224] Y. Bai, K. Zhou, N. Srikanth, et al. *RSC Adv.* 6.42 (2016), pp. 35731–35739. DOI: 10.1039/C6RA03090D.

[225] H. Zhang, G. Yang, X. Zuo, et al. *J. Mater. Chem. A* 4.33 (2016), pp. 12913–12920. DOI: 10.1039/C6TA04628B.

[226] J. Guo, Y. Sun, B. Liu, et al. *Journal of Alloys and Compounds* 712 (2017), pp. 752 –759. DOI: 10.1016/j.jallcom.2017.04.149.

[227] K. Hantanasirisakul, M.-Q. Zhao, P. Urbankowski, et al. *Advanced Electronic Materials* 2.6 (2016), p. 1600050. DOI: 10.1002/aelm.201600050.

[228] K. Hantanasirisakul and Y. Gogotsi. *Advanced Materials* 30.52 (2018), p. 1804779. DOI: 10.1002/adma.201804779.

[229] F. Shahzad, M. Alhabeb, C. B. Hatter, et al. *Science* 353.6304 (2016), pp. 1137–1140. DOI: 10.1126/science.aag2421.

[230] M. Han, X. Yin, H. Wu, et al. *ACS Applied Materials & Interfaces* 8.32 (2016), pp. 21011–21019. DOI: 10.1021/acsami.6b06455.

[231] I. Persson, J. Halim, H. Lind, et al. *Advanced Materials* 31.2 (2019), p. 1805472. DOI: 10.1002/adma.201805472.

[232] E. Lee, A. VahidMohammadi, B. C. Prorok, et al. *ACS Applied Materials & Interfaces* 9.42 (2017), pp. 37184–37190. DOI: 10.1021/acsami.7b11055.

[233] X.-f. Yu, Y.-c. Li, J.-b. Cheng, et al. *ACS Applied Materials & Interfaces* 7.24 (2015), pp. 13707–13713. DOI: 10.1021/acsami.5b03737.

[234] M. R. Lukatskaya, B. Dunn, and Y. Gogotsi. *Nature Communications* 7 (2016), pp. 1–13. DOI: 10.1038/ncomms12647.

[235] Q. Hu, D. Sun, Q. Wu, et al. *Journal of Physical Chemistry A* 117 (2013), p. 14253. DOI: 10.1021/jp409585v.

[236] Q. Hu, H. Wang, Q. Wu, et al. *International Journal of Hydrogen Energy* 39.20 (2014), pp. 10606 –10612. DOI: 10.1016/j.ijhydene.2014.05.037.

[237] J. Pang, R. G. Mendes, A. Bachmatiuk, et al. *Chem. Soc. Rev.* 48.1 (2019), pp. 72–133. DOI: 10.1039/C8CS00324F.

[238] H. Liu, C. Duan, C. Yang, et al. *Sensors and Actuators B: Chemical* 218 (2015), pp. 60 –66. DOI: 10.1016/j.snb.2015.04.090.

[239] G. Liu, J. Shen, Q. Liu, et al. *Journal of Membrane Science* 548 (2018), pp. 548 –558. DOI: 10.1016/j.memsci.2017.11.065.

[240] K. Chen, Y. Chen, Q. Deng, et al. *Materials Letters* 229 (2018), pp. 114 –117. DOI: 10.1016/j.matlet.2018.06.063.

[241] F. Wang, C. Yang, C. Duan, et al. *Journal of The Electrochemical Society* 162.1 (2014), B16 –B21. DOI: 10.1149/2.0371501jes.

[242] H. Lin, Y. Chen, and J. Shi. *Advanced Science* 5.10 (2018), p. 1800518. DOI: 10.1002/advs.201800518.

[243] M. Khazaei, M. Arai, T. Sasaki, et al. *Phys. Chem. Chem. Phys.* 16.17 (2014), pp. 7841–7849. DOI: 10.1039/C4CP00467A.

[244] A. N. Gandi, H. N. Alshareef, and U. Schwingenschlögl. *Chemistry of Materials* 28.6 (2016), pp. 1647–1652. DOI: 10.1021/acs.chemmater.5b04257.

[245] X. Xie, Y. Xue, L. Li, et al. *Nanoscale* 6.19 (2014), pp. 11035–11040. DOI: 10.1039/C4NR02080D.

[246] Z. W. Seh, K. D. Fredrickson, B. Anasori, et al. *ACS Energy Letters* 1.3 (2016), pp. 589–594. DOI: 10.1021/acsenergylett.6b00247.

[247] H. Wang, Y. Wu, X. Yuan, et al. *Advanced Materials* 30.12 (2018), p. 1704561. DOI: 10.1002/adma.201704561.

[248] O. Mashtalir, K. M. Cook, V. N. Mochalin, et al. *J. Mater. Chem. A* 2.35 (2014), pp. 14334–14338. DOI: 10.1039/C4TA02638A.

[249] M. E. Suss, S. Porada, X. Sun, et al. *Energy Environ. Sci.* 8.8 (2015), pp. 2296–2319. DOI: 10.1039/C5EE00519A.

[250] Q. Peng, J. Guo, Q. Zhang, et al. *Journal of the American Chemical Society* 136.11 (2014), pp. 4113–4116. DOI: 10.1021/ja500506k.

[251] Y. Liu, Q. Tao, Y. Jin, et al. *ACS Applied Electronic Materials* 2.1 (2020), pp. 163–169. DOI: 10.1021/acsaelm.9b00668.

[252] L. Qin, J. Jiang, Q. Tao, et al. *J. Mater. Chem. A* 8.11 (2020), pp. 5467–5475. DOI: 10.1039/D0TA00687D.

[253] G. Ceder. *Science* 280.5366 (1998), pp. 1099–1100. DOI: 10.1126/science.280.5366.1099.

[254] P. Hohenberg and W. Kohn. *Phys. Rev.* 136.3B (1964), B864–B871. DOI: 10.1103/PhysRev.136.B864.

[255] W. Kohn and L. J. Sham. *Phys. Rev.* 140.4A (1965), A1133–A1138. DOI: 10.1103/PhysRev.140.A1133.

[256] A. Jain, S. P. Ong, G. Hautier, et al. *APL Materials* 1.1 (2013), p. 011002. DOI: 10.1063/1.4812323.

[257] A. Urban, D.-H. Seo, and G. Ceder. *npj Computational Materials* 2.16002 (2016), pp. 1–13. DOI: 10.1038/npjcompumats.2016.2.

[258] R. M. Martin. *Electronic Structure: Basic Theory and Practical Methods*. 1st ed. Cambridge University Press, 2004.

[259] D. R. Hartree. *Mathematical Proceedings of the Cambridge Philosophical Society* 24.1 (1928), pp. 89–110. DOI: 10.1017/S0305004100011919.

[260] V. Fock. *Zeitschrift für Physik* 61.1 (1930), p. 148. DOI: 10.1007/BF01340294.

[261] J. P. Perdew and Y. Wang. *Phys. Rev. B* 45.23 (1992), pp. 13244–13249. DOI: 10.1103/PhysRevB.45.13244.

[262] J. P. Perdew, K. Burke, and M. Ernzerhof. *Phys. Rev. Lett.* 77.18 (1996), pp. 3865–3868. DOI: 10.1103/PhysRevLett.77.3865.

[263] J. Sun, A. Ruzsinszky, and J. P. Perdew. *Phys. Rev. Lett.* 115.3 (2015), p. 036402. DOI: 10.1103/PhysRevLett.115.036402.

[264] J. Sun, R. C. Remsing, Y. Zhang, et al. *Nature Chemistry* 8 (2016), p. 831. DOI: 10.1038/nchem.2535.

[265] D. Vanderbilt. *Phys. Rev. B* 41.11 (1990), pp. 7892–7895. DOI: 10.1103/PhysRevB.41.7892.

[266] P. E. Blöchl. *Phys. Rev. B* 41.8 (1990), pp. 5414–5416. DOI: 10.1103/PhysRevB.41.5414.

[267] P. E. Blöchl. *Phys. Rev. B* 50.24 (1994), pp. 17953–17979. DOI: 10.1103/PhysRevB.50.17953.

[268] G. Kresse and D. Joubert. *Phys. Rev. B* 59.3 (1999), pp. 1758–1775. DOI: 10.1103/PhysRevB.59.1758.

[269] H. J. Monkhorst and J. D. Pack. *Phys. Rev. B* 13.12 (1976), pp. 5188–5192. DOI: 10.1103/PhysRevB.13.5188.

[270] K. M. Ho and K. P. Bohnen. *Phys. Rev. Lett.* 56.9 (1986), pp. 934–937. DOI: 10.1103/PhysRevLett.56.934.

[271] T. A. Arias, M. C. Payne, and J. D. Joannopoulos. *Phys. Rev. Lett.* 69.7 (1992), pp. 1077–1080. DOI: 10.1103/PhysRevLett.69.1077.

[272] S. Baroni, P. Giannozzi, and A. Testa. *Phys. Rev. Lett.* 58.18 (1987), pp. 1861–1864. DOI: 10.1103/PhysRevLett.58.1861.

[273] X. Gonze. *Phys. Rev. A* 52.2 (1995), pp. 1086–1095. DOI: 10.1103/PhysRevA.52.1086.

[274] S. Baroni, S. de Gironcoli, A. Dal Corso, et al. *Rev. Mod. Phys.* 73.2 (2001), pp. 515–562. DOI: 10.1103/RevModPhys.73.515.

[275] R. D King-Smith, R. J Needs, V Heine, et al. *Europhysics Letters (EPL)* 10.6 (1989), pp. 569–574. DOI: 10.1209/0295-5075/10/6/011.

[276] P. Giannozzi, S. de Gironcoli, P. Pavone, et al. *Phys. Rev. B* 43.9 (1991), pp. 7231–7242. DOI: 10.1103/PhysRevB.43.7231.

[277] X. Gonze, D. C. Allan, and M. P. Teter. *Phys. Rev. Lett.* 68.24 (1992), pp. 3603–3606. DOI: 10.1103/PhysRevLett.68.3603.

[278] R. W. Nunes and D. Vanderbilt. *Phys. Rev. Lett.* 73.5 (1994), pp. 712–715. DOI: 10.1103/PhysRevLett.73.712.

[279] P. Ordejón, D. A. Drabold, R. M. Martin, et al. *Phys. Rev. Lett.* 75.7 (1995), pp. 1324–1327. DOI: 10.1103/PhysRevLett.75.1324.

[280] A. Debernardi, S. Baroni, and E. Molinari. *Phys. Rev. Lett.* 75.9 (1995), pp. 1819–1822. DOI: 10.1103/PhysRevLett.75.1819.

[281] M. Lazzeri and S. de Gironcoli. *Phys. Rev. B* 65.24 (2002), p. 245402. DOI: 10.1103/PhysRevB.65.245402.

[282] G. Deinzer, G. Birner, and D. Strauch. *Phys. Rev. B* 67.14 (2003), p. 144304. DOI: 10.1103/PhysRevB.67.144304.

[283] R. M. Pick, M. H. Cohen, and R. M. Martin. *Phys. Rev. B* 1.2 (1970), pp. 910–920. DOI: 10.1103/PhysRevB.1.910.

[284] X Gonze, G Rignanese, M Verstraete, et al. *Zeitschrift für Kristallographie (Special number on Computational Crystallography)* 220 (2005), pp. 558–562.

[285] X. Gonze, B. Amadon, P.-M. Anglade, et al. *Computer Physics Communications* 180.12 (2009), pp. 2582 –2615. DOI: 10.1016/j.cpc.2009.07.007.

[286] G. Kresse and J. Hafner. *Phys. Rev. B* 47.1 (1993), pp. 558–561. DOI: 10.1103/PhysRevB.47.558.

[287] G. Kresse and J. Furthmüller. *Computational Materials Science* 6.1 (1996), pp. 15 –50. DOI: 10.1016/0927-0256(96)00008-0.

[288] G. Kresse and J. Furthmüller. *Phys. Rev. B* 54.16 (1996), pp. 11169–11186. DOI: 10.1103/PhysRevB.54.11169.

[289] Y. Le Page and P. Saxe. *Phys. Rev. B* 65 (2002), p. 104104. DOI: 10.1103/PhysRevB.65.104104.

[290] G. K. Madsen, J. Carrete, and M. J. Verstraete. *Computer Physics Communications* 231 (2018), pp. 140–145. DOI: 10.1016/j.cpc.2018.05.010.

[291] G. K. Madsen and D. J. Singh. *Computer Physics Communications* 175.1 (2006), pp. 67–71. DOI: 10.1016/j.cpc.2006.03.007.

[292] F. Ricci, W. Chen, U. Aydemir, et al. *Scientific Data* 4 (2017), p. 170085.

[293] J. I. Mustafa, M. Bernardi, J. B. Neaton, et al. *Phys. Rev. B* 94 (2016), p. 155105. DOI: 10.1103/PhysRevB.94.155105.

[294] P. Delugas, A. Filippetti, M. J. Verstraete, et al. *Phys. Rev. B* 88.4 (2013), p. 045310. DOI: 10.1103/PhysRevB.88.045310.

[295] R Farris, M. B. Maccioni, A Filippetti, et al. *Journal of Physics: Conference Series* 1226 (2019), p. 012010. DOI: 10.1088/1742-6596/1226/1/012010.

[296] G. Fugallo and L. Colombo. *Physica Scripta* 93.4 (2018), p. 043002. DOI: 10.1088/1402-4896/aaa6f3.

[297] R. Peierls. *Annalen der Physik* 395.8 (1929), pp. 1055–1101. DOI: 10.1002/andp.19293950803.

[298] P. Klemens. *Solid State Phys. - Adv. Res. Appl.* 7 (1958), pp. 1–98.

[299] J. Callaway. *Phys. Rev.* 113.4 (1959), pp. 1046–1051. DOI: 10.1103/PhysRev.113.1046.

[300] J. F. Ziman. *Electrons and phonons: the theory of transport phenomena in solids*. Oxford University Press, Oxford, 2001.

[301] A. Cepellotti, G. Fugallo, L. Paulatto, et al. *Nature Communications* 6 (2015), p. 6400.

[302] G. Fugallo, A. Cepellotti, L. Paulatto, et al. *Nano Letters* 14.11 (2014), pp. 6109–6114. DOI: 10.1021/nl502059f.

[303] O. Hellman, I. A. Abrikosov, and S. I. Simak. *Phys. Rev. B* 84.18 (2011), p. 180301. DOI: 10.1103/PhysRevB.84.180301.

[304] O. Hellman, P. Steneteg, I. A. Abrikosov, et al. *Phys. Rev. B* 87.10 (2013), p. 104111. DOI: 10.1103/PhysRevB.87.104111.

[305] O. Hellman and I. A. Abrikosov. *Phys. Rev. B* 88.14 (2013), p. 144301. DOI: 10.1103/PhysRevB.88.144301.

[306] X. Gonze, J.-M. Beuken, R. Caracas, et al. *Computational Materials Science* 25.3 (2002), pp. 478 –492. DOI: 10.1016/S0927-0256(02)00325-7.

[307] X. Gonze. *Phys. Rev. B* 55.16 (1997), pp. 10337–10354. DOI: 10.1103/PhysRevB.55.10337.

[308] X. Gonze and C. Lee. *Phys. Rev. B* 55.16 (1997), pp. 10355–10368. DOI: 10.1103/PhysRevB.55.10355.

[309] B. E. Warren. *X-ray diffraction*. 1st ed. Dover Publications, 1990. ISBN: 978-0486663173.

[310] S. Hendricks and E. Teller. *The Journal of Chemical Physics* 10.3 (1942), pp. 147–167. DOI: 10.1063/1.1723678.

[311] G. M. Sheldrick. *Acta Crystallographica Section C* 71.1 (2015), pp. 3–8. DOI: 10.1107/S2053229614024218.

[312] *Scanning Electron Microscopy: Physics of image formation and microanalysis, publisher = Springer, year = 1998, edition = 2, author = "Ludwig Reimer", doi = 10.1007/978-3-540-38967-5,*

[313] D. B. Williams and C. B. Carter. *Transmission Electron Microscopy: A textbook for materials science*. 1st ed. Springer, 2009. DOI: 10.1007/978-0-387-76501-3.

[314] M. D. Graef. *Introduction to conventional transmission electron microscopy*. 1st ed. Cambridge University Press, 2003. DOI: 10.1017/CBO9780511615092.

[315] H. A. Szymanski. *Raman spectroscopy, theory, and practice*. 1st ed. Plenum Press, 1967. DOI: 10.1007/978-1-4684-3024-0.

[316] G. Shirane, S. M. Shapiro, and J. M. Tranquada. *Neutron Scattering with a Triple-Axis Spectrometer: Basic Techniques*. Cambridge University Press, 2002. DOI: 10.1017/CBO9780511534881.

[317] A. C. Fischer-Cripps. *Nanoindentation*. 2nd ed. Springer, 2004. DOI: 10.1007/978-1-4757-5943-3.

[318] W. C. Oliver and G. M. Pharr. *Journal of Materials Research* 7.6 (1992), pp. 1564–1583. DOI: 10.1557/JMR.1992.1564.

[319] D. R. Hamann. *Phys. Rev. B* 88.8 (2013), p. 085117. DOI: 10.1103/PhysRevB.88.085117.

[320] A. Champagne, F. Bourdarot, P. Bourges, et al. *Materials Research Letters* 6.7 (2018), pp. 378–383. DOI: 10.1080/21663831.2018.1463298.

[321] L. J. Swartzendruber. *Technical note* 6 (1964), p. 43.

[322] G. Ying, X. He, M. Li, et al. *Journal of Alloys and Compounds* 509.31 (2011), pp. 8022–8027. DOI: 10.1016/j.jallcom.2011.04.134.

[323] W. Tian, P. Wang, G. Zhang, et al. *Scripta Materialia* 54.5 (2006). Viewpoint set no. 39: Statistical mechanics and coarse graining of dislocation behavior for continuum plasticity, pp. 841 –846. ISSN: 1359-6462. DOI: 10.1016/j.scriptamat.2005.11.009.

[324] T. Scabarozi, A. Ganguly, J. D. Hettinger, et al. *Journal of Applied Physics* 104.7 (2008), p. 073713. DOI: 10.1063/1.2979326.

[325] T. Ouisse, D. Pinek, and M. Barsoum. *Ceramics International* 45.17, Part B (2019), pp. 22956 –22960.

[326] M. B. Maccioni, R. Farris, and V. Fiorentini. *Phys. Rev. B* 98.22 (2018), p. 220301. DOI: 10.1103/PhysRevB.98.220301.

[327] S. H. Shah and P. D. Bristowe. *Scientific Reports* February (2017), pp. 1–8. DOI: 10.1038/s41598-017-10273-6.

[328] C. A. Ratsifaritana and P. G. Klemens. *International Journal of Thermophysics* 8.6 (1987), pp. 737–750. DOI: 10.1007/BF00500791.

[329] A. Kusiak, J. Martan, J.-L. Battaglia, et al. *Thermochimica Acta* 556 (2013), pp. 1 –5. DOI: 10.1016/j.tca.2013.01.010.

[330] L. Gaverina, J. C. Batsale, A. Sommier, et al. *Journal of Applied Physics* 121.11 (2017), p. 115105. DOI: 10.1063/1.4978919.

[331] E. Ruffio, C. Pradere, A. Sommier, et al. *International Journal of Thermal Sciences* 129 (2018), pp. 385 –395. DOI: 10.1016/j.ijthermalsci.2018.03.011.

[332] Z.-j. Wu, E.-j. Zhao, H.-p. Xiang, et al. *Phys. Rev. B* 76.5 (2007), p. 054115. DOI: 10.1103/PhysRevB.76.054115.

[333] R. Hill. *Proceedings of the Physical Society A* 65 (1952), pp. 349–354. DOI: 10.1088/0370-1298/65/5/307.

[334] M. F. Cover, O Warschkow, M. M. M. Bilek, et al. *Journal of Physics: Condensed Matter* 21.30 (2009), p. 305403. DOI: 10.1088/0953-8984/21/30/305403.

[335] J. F. Nye. *Physical Properties of Crystals: their Representation by Tensors and Matrices*. Oxford University Press, 1985.

[336] M. W. Barsoum and M. Radovic. *Annual Review of Materials Research* 41.1 (2011), pp. 195–227. DOI: 10.1146/annurev-matsci-062910-100448.

[337] H. O. Badr, A. Champagne, T. Ouisse, et al. *Phys. Rev. Materials* 4.8 (2020), p. 083605. DOI: 10.1103/PhysRevMaterials.4.083605.

[338] I. C. Albayrak, S. Basu, A. Sakulich, et al. *Journal of the American Ceramic Society* 93.7 (2010), pp. 2028–2034. DOI: 10.1111/j.1551-2916.2010.03669.x.

[339] B. Holm, R. Ahuja, and B. Johansson. *Applied Physics Letters* 79.10 (2001), pp. 1450–1452. DOI: 10.1063/1.1392981.

[340] B. Kooi, R. Poppen, N. Carvalho, et al. *Acta Materialia* 51.10 (2003), pp. 2859 –2872. DOI: 10.1016/S1359-6454(03)00091-0.

[341] A. Murugaiah, M. Barsoum, S. Kalidindi, et al. *Journal of Materials Research* 19.4 (2004), pp. 1139–1148. DOI: 10.1557/JMR.2004.0148.

[342] A. Champagne, O. Chaix-Pluchery, T. Ouisse, et al. *Phys. Rev. Materials* 3.5 (2019), p. 053609. DOI: 10.1103/PhysRevMaterials.3.053609.

[343] A. Champagne, F. Ricci, M. Barbier, et al. *Phys. Rev. Materials* 4.1 (2020), p. 013604. DOI: 10.1103/PhysRevMaterials.4.013604.

[344] K. Momma and F. Izumi. *Journal of Applied Crystallography* 44.6 (2011), pp. 1272–1276. DOI: 10.1107/S0021889811038970.

[345] B. York, S. Solin, N. Wada, et al. *Solid State Communications* 54.6 (1985), pp. 475 –478. DOI: 10.1016/0038-1098(85)90650-7.

[346] T. C. Lubensky, C. L. Kane, X. Mao, et al. *Reports on Progress in Physics* 78.7 (2015), p. 073901. DOI: 10.1088/0034-4885/78/7/073901.

[347] T. Björkman, V. Skakalova, S. Kurasch, et al. *ACS Nano* 10.12 (2016), pp. 10929–10935. DOI: 10.1021/acsnano.6b05577.

[348] F. Mouhat and F. m.c.-X. Coudert. *Phys. Rev. B* 90.22 (2014), p. 224104. DOI: 10.1103/PhysRevB.90.224104.

[349] H. Fu, D. Li, F. Peng, et al. *Computational Materials Science* 44.2 (2008), pp. 774 –778. DOI: 10.1016/j.commatsci.2008.05.026.

[350] R. Dronskowski and P. E. Bloechl. *The Journal of Physical Chemistry* 97.33 (1993), pp. 8617–8624. DOI: 10.1021/j100135a014.

[351] V. L. Deringer, A. L. Tchougréeff, and R. Dronskowski. *The Journal of Physical Chemistry A* 115.21 (2011), pp. 5461–5466. DOI: 10.1021/jp202489s.

[352] S. Maintz, V. L. Deringer, A. L. Tchougréeff, et al. *Journal of Computational Chemistry* 34.29 (2013), pp. 2557–2567. DOI: 10.1002/jcc.23424.

[353] S. Maintz, V. L. Deringer, A. L. Tchougréeff, et al. *Journal of Computational Chemistry* 37.11 (2016), pp. 1030–1035. DOI: 10.1002/jcc.24300.

[354] M. Khazaei, A. Ranjbar, K. Esfarjani, et al. *Phys. Chem. Chem. Phys.* 20.13 (2018), pp. 8579–8592. DOI: 10.1039/C7CP08645H.

[355] M. Khazaei, J. Wang, M. Estili, et al. *Nanoscale* 11.23 (2019), pp. 11305–11314. DOI: 10.1039/C9NR01267B.

[356] M. Ashton, K. Mathew, R. G. Hennig, et al. *The Journal of Physical Chemistry C* 120.6 (2016), pp. 3550–3556. DOI: 10.1021/acs.jpcc.5b11887.

[357] X. Ji, K. Xu, C. Chen, et al. *J. Mater. Chem. A* 3.18 (2015), pp. 9909–9914. DOI: 10.1039/C5TA01003A.

[358] J. M. Schneider, R. Mertens, and D. Music. *Journal of Applied Physics* 99.1 (2006), p. 013501. DOI: 10.1063/1.2150601.

[359] L. Shi. 'From MAX phases to MXenes: synthesis, characterization and electronic properties.' PhD thesis. Ecole Polytechnique de Louvain, Université catholique de Louvain, 2017.

[360] M. S. Dresselhaus and P. C. Eklund. *Advances in Physics* 49.6 (2000), pp. 705–814. DOI: 10.1080/000187300413184.

[361] A. Molina-Sánchez and L. Wirtz. *Phys. Rev. B* 84.15 (2011), p. 155413. DOI: 10.1103/PhysRevB.84.155413.

[362] I. M. Lifshitz. *Zh. Eksp. Teor. Fiz.* 22.4 (1952), pp. 475 –486.